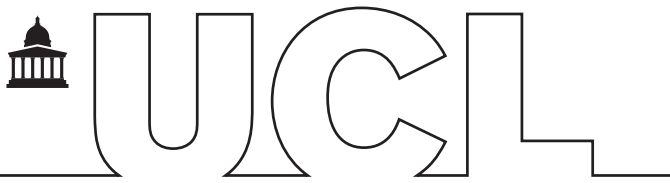

University College London

Department of Physics & Astronomy

Optomechanics with an electrodynamically levitated oscillator

Author:
Nathanaël P. Bullier

Supervisor:
Prof. Peter F. Barker

Submitted in partial fulfilment for the degree of **Doctor of Philosophy**

November 15, 2020

I, Nathanaël P. Bullier, confirm that the work presented in this thesis is my own. Where information has been derived from other sources, I confirm that this has been indicated in the thesis.

Signature

November 15, 2020

Date

À mes parents
To Emily

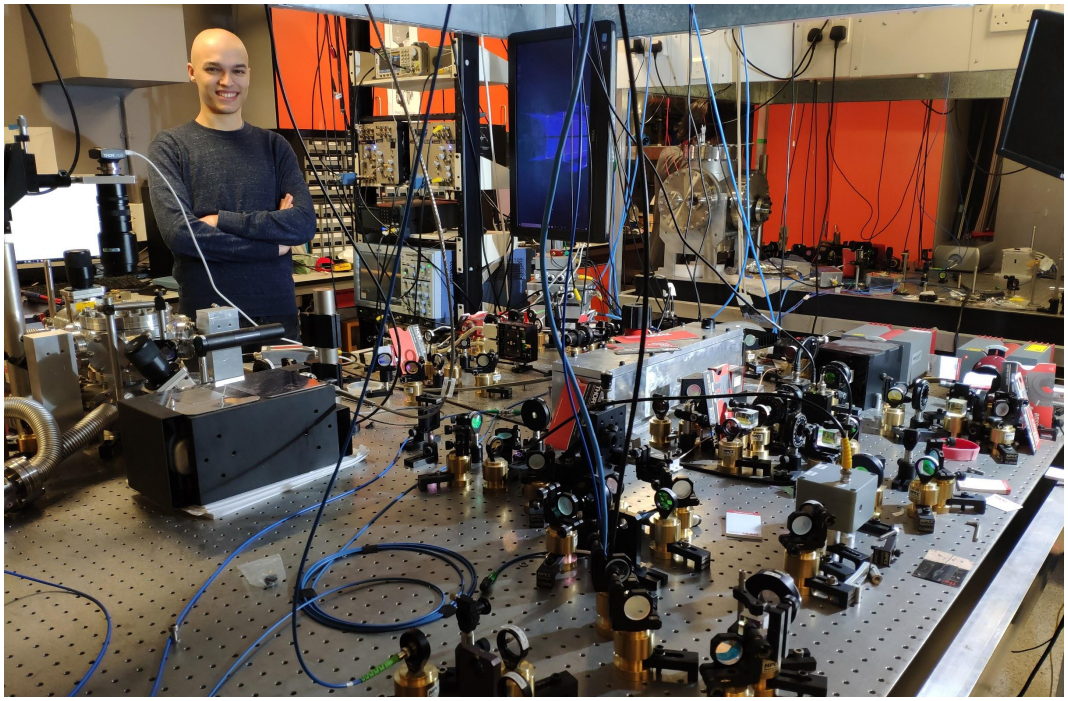

Figure 1: The experimentalist in its environment. Credits: picture taken by Dr. Vincenzo Monachello, lights by Dr. Antonio Pontin.

Abstract

In this work I report on a hybrid trap platform for sensitive optomechanics experiments with applications in quantum physics, thermodynamics and material science. We characterise a miniature linear Paul trap which can be used in combination with an optical cavity. The low-frequency harmonic motion of a nanoparticle levitated in a Paul trap can be detected with competitive sensitivities using a super-resolution imaging technique. This same method can be applied to characterise trap stability and nanosphere parameters such as mass with a 3% uncertainty. Using this same method at room temperature and at a pressure of 3×10^{-7} mbar, we were able to measure an ultra-narrow mechanical linewidth of $\sim 80\,\mu$Hz with a novel phase sensitive scheme which removes slow drifts in the mechanical frequency. We used this measurement to place new bounds on dissipative versions of wavefunction collapse models. Using two optical cavity modes with different frequencies interacting with a nanoparticle levitated within a Paul trap realises a versatile optomechanical system, which can be operated in regimes dominated by either linear or quadratic optomechanical coupling. We demonstrated cooling of the centre-of-mass motion of the nano-oscillator exclusively provided by the quadratic coupling. This nonlinear interaction gives rise to a highly non-thermal state of motion which matches well with theoretical predictions. In the linear regime, we report cooling down to $T_{eff} = 21 \pm 4$ mK limited by Paul trap noise, demonstrating stable trapping in the cavity standing-wave down to pressures $\sim 10^{-6}$ mbar. Using the same technique, we show that in theory, near ground state cooling could be achieved with better electronics used in conjunction with the filtering cavity developed as part of this work.

Impact Statement

The work presented here offers a wide variety of applications within and outside academic research. There is recently significant interest within the research community to levitate nanoparticles in Paul traps. We have reported a novel miniature linear Paul trap with a reliable loading mechanism. The hybrid electro-optical platform presented here could be used for further experiments in levitated optomechanics with potential broad research applications. A super-resolution imaging method was developed to monitor the motion of low-frequency oscillators. Also reported is a method to measure the intrinsic mechanical linewidth of the oscillator in the presence of drifts in the frequency of oscillation. Those two techniques have potential applications in many fields of research. In this work, the first method is used among others to evaluate the nanoparticle mass and the gas damping. The second one is used here extensively to estimate the effective mechanical damping acting on the nanosphere. We have demonstrated a regime where the optomechanical interaction is dominated by the quadratic optomechanical coupling, which leads to a highly non-thermal state of motion with potential application to test quantum mechanics at the nanoscale. We presented as well measurements of the nanoparticle polarisability, little discussed in the literature, which could be used to allow more control over the fabrication of Stöber silica. One major obstacle of working with low frequency oscillators is the strong effect of laser frequency noise. We have designed and characterised a filtering cavity to reduce its effect on both the nanoparticle motion and detection sensitivity. Lastly, we present in this work different ways of testing wavefunction collapse models which offer a phenomenological response to conciliate the measurement postulate and Schrödinger dynamics. This last work can be of particular interest to a broad audience [1].

List of publications

N. P. Bullier, A. Pontin, and P. F. Barker. Cavity cooling of a levitated nano-oscillator in an electro-optical trap with two optical modes. *Manuscript in preparation.*

N. P. Bullier, A. Pontin, and P. F. Barker. Quadratic optomechanical cooling of a cavity-levitated nanosphere. *arXiv:* 2006.16103 (2020).

A. Pontin, N. P. Bullier, M. Toroš, and P. F. Barker. Ultranarrow-linewidth levitated nano-oscillator for testing dissipative wave-function collapse. *Physical Review Research*, **2**, 023349 (2020).

N. P. Bullier, A. Pontin, and P. F. Barker. Characterisation of a charged particle levitated nano-oscillator. *Journal of Physics D: Applied Physics*, **53**, 175302 (2020).

N. P. Bullier, A. Pontin, and P. F. Barker. Super-resolution imaging of a low frequency levitated oscillator. *Review of Scientific Instruments*, Editor's Pick, **90**, 093201 (2019).

M. J. Akram, E. B. Aranas, N. P. Bullier, J. E. Lang, and T. S. Monteiro. Two-timescale stochastic Langevin propagation for classical and quantum optomechanics. *Physical Review A*, **98**, 063827 (2018).

N. P. Bullier, A. Pontin, and P. F. Barker. Millikelvin cooling of the center-of-mass motion of a levitated nanoparticle. *Proceedings SPIE* 10347, Optical Trapping and Optical Micromanipulation XIV, 103471K (2017).

Acknowledgements

Doing an experimental PhD has been an incredible experience, valuable at many levels. I found the scope of the day-to-day tasks very satisfying: debugging in the lab, designing the experiment, analysing data and carrying out simulations. On a personal level, the PhD has enabled me to learn more about myself, how to make decisions and deal with stress effectively. Many people have contributed to the work presented here, from day-to-day collaborators to family and friends. I would like to thank them all very much for their kind help and support over these years.

I would first like to thank my supervisor Prof. Peter Barker, who gave me the opportunity to do research in his group. I am very thankful and indebted. I chose this PhD without any hesitation as it was attractive on many levels, crossing over different areas of physics and using a variety of experimental skills. In the end, I have not been disappointed at all. Peter though incredibly busy has always been available to discuss the experiment, providing me with invaluable help and sharing his extensive knowledge and passion for physics. Moreover, I admire his creativity in coming up with new and exciting ideas and experimental proposals. When discussing problems, Peter never offers one but multiple solutions to choose from. I very much appreciate the fact that he has always left me with some flexibility over which solution to implement, and trusted my judgment throughout the PhD process, while showing incredible patience and understanding at times of slower progress. Something else I valued while working under Peter's supervision was his ability to look at the bigger picture, always thinking about applications and modifications to the current set-up and potential avenues for future experiments, something very challenging to do as a PhD student.

Little of the work presented here would have come to fruition without the hard work, help, teaching and guidance of Dr. Antonio Pontin. Antonio has been the best lab partner I could have ever wished for. I am very thankful and indebted for having been able to work with him. Antonio often gave up his time to teach me a lot of

his amazing experimental and analytical skills. Moreover, he has always answered (fully) my numerous questions with great patience. The long discussions we had always ended up being very useful for me and to come up with new ideas. I very much enjoyed working with him and appreciated his approach towards experimental physics, where spending a bit of extra time modelling the experiment always pays off. Finally, and maybe most important, it has been great working with someone fully committed (and genuinely interested) in the project. This helped me stay motivated at challenging times and, when things were progressing quickly, drove my excitement.

I had the luck of sharing space in the lab with Dr. Vincenzo Monachello. It was greatly motivating and enriching to discuss with someone working on a different (but fascinating) project and who had an incredible scientific knowledge and passion for it. I also benefited from Vincenzo's great experimental expertise and his kind willingness and availability to always help me and cheer me up during tough times. I enjoyed very much the late evenings spent in the lab working on our respective experiments while discussing about physics, consciousness, science-(fiction?), movies...

I am thankful for having been part of a friendly research group, with benevolent members always happy to help, share and discuss ideas. I would like to thank Prof. Tania Monteiro, Dr. Sofia Qvarfort, Abel Beregi, Dr. Marko Toroš, Javed Akram, Hayden Fu, Thomas Penny, Dr. Piergiacomo Fonseca, Dr. Erika Aranas, Dr. Anis Rahman, Dr. Ying Lia Li, Joel Morley, Dr. Anas Almuqhim, Markus Rademacher, Jonathan Gosling and Amy Hopper.

As part of the EPSRC CDT in Delivering Quantum Technologies, I would like to thank particularly Prof. Dan Browne and Prof. Andrew Fisher for putting together such a rich and amazing MRes program. Though incredibly busy, they always found the time to give us tutorials, discuss projects and advise us on PhD plans. Their involvement and commitment to the CDT truly shone on the program and made it an amazing experience from our prospective. In practice, Lopa Murgai organised the program and was an amazingly efficient bridge between us and the professors. She always took the time to help, and her top priority was to ensure that we were always comfortable. I would like to thank her very much for her involvement, which made the program and the experience great.

I had the chance during the MRes year of meeting and working with extraordinarily friendly and clever course mates. I am amazed at what everyone of them has been able to achieve from an academic prospective, on the professional side and on a personal level. I would like to particularly thank my *course buddy* Dr. Alexandre Morgan who has been a great friend. I enjoyed working closely with him during the MRes year and discussing about everyday PhD matters. I would like to thank as well all my amazing course mates: Dan, David, Gavin, James, Mike, Padraic, Paul, Simon and Sofia.

Needless to say my parents Françoise and Antoine have been a big part of my studies. I do not really know where to start since I owe them so much on so many levels. My parents have always believed in me and pushed me to achieve my best. I am grateful and indebted for the way they have raised me, providing me with unconditional financial and psychological support, and love. Relevant to the work presented here, my parents who are also academics are extremely curious and cultivated. They have always encouraged me to observe, question and read, which is a short summary of what research is all about. I am very thankful to my mum, who spent so much time, though I believe (hope) enjoyed it, bringing me to science shows when I was a kid, particularly the fantastic National Science Show in Paris, *Fête de la Science* which was held every year, as well as buying me amazing popular science magazines. Those little things, as a child, truly marked me and expanded my curiosity and excitement towards science, most specifically physics. I dedicate this thesis to them.

Lastly, I would like to thank my amazing partner and best friend Emily. Her help, support and love throughout the MRes and PhD journeys have been invaluable. Those five years (time flies) have been rich, but at times overwhelming. Emily, always showed great patience, took the time to help me and was there to comfort me. Moreover, she always pushed me to do my best, truly believing in my abilities, my studies, and my PhD project in particular. She has always been happy to discuss about it and help me to make the right decisions. I am actually astonished at how much she knows and understands about the experiment. As we joked so many times, she really deserves an associate PhD degree for this work! I also dedicate this thesis to her.

Contents

List of Figures

Chapter 1

Introduction

Cavity optomechanics is the study of the interaction between optical fields and mechanical motion [2, 3]. This interaction has been demonstrated at vastly different scales with experiments ranging from cold atoms [4], to the Laser Interferometer Gravitational-Wave Observatory (LIGO) [5]. While quantum mechanics has been validated more than any other physical theory at the microscopic scale, its lack of clear signatures at macroscopic scales is puzzling. Manipulating mechanical motion at micrometer and nanometer scales using optomechanical methods is seen as a promising way to study quantum behaviours at intermediate scales [6–8]. Furthermore, studying those oscillators has led to new research activities in thermodynamics at small scales, sensing and material science. After briefly reviewing some achievements in the field of cavity optomechanics I will outline the motivation for specific research in levitated optomechanics. The work presented in this thesis is then motivated. Finally, I provide a summary of each chapter in the thesis.

1.1 Standard optomechanics

Cavity optomechanics has greatly benefited from the Laser Interferometer Gravitational-Wave Observatory (LIGO) and Virgo collaborations [5, 9], which have recently been celebrated for the discovery of gravitational waves [10]. The two LIGO observatories consist of two giant Michelson interferometers with arms, 4 km long, terminated by 40 kg test mass mirrors. In order to detect the displacement made by gravitational waves, a strain sensitivity of $10^{-22}/\sqrt{\text{Hz}}$ had to be reached in the audio band. For a 4 km interferometer this is equivalent to a displacement sensitivity of 10^{-19} m$/\sqrt{\text{Hz}}$. With standard interferometric measurements (by opposition to more sophisticated methods such as in Ref. [11]), the maximum sensitivity

for an interferometer is achieved at the standard quantum limit (SQL) [12], which corresponds to the level saturating the uncertainty principle for the test mass of the interferometers. In practice, there is an optimum laser power at which the two main noise sources in the interferometer are equal: shot-noise (imprecision noise) and radiation pressure noise which drives the mechanical motion of the test mass (back-action noise). The main challenge for LIGO has been to reach this level. It has required a high level of mechanical isolation of the test mass, reduction in classical laser noise, and improvements in optics coatings technologies to reduce Brownian noise.

The first protocol which can be realised in an optomechanical system is laser cooling of the mechanical motion. The radiation pressure force can be engineered to cool the centre-of-mass motion of a mechanical mode. One of the first objects showing successful sideband cooling was a silicon beam used as an end-mirror of an optical cavity [13]. In order to cool the oscillator, the laser frequency is red-detuned with respect to the cavity resonance. The time at which the radiation pressure force is applied in the mechanical cycle can be controlled with the input beam detuning. Amplification of the motion can be achieved by blue detuning the laser. In order for this force to extract work and therefore cool the motion, it has to be in phase quadrature with the motion (delayed by a quarter of cycle), which is realised in practice by the finite cavity response time. Cavity cooling can also be understood in a frequency-domain picture. The mechanical motion creates sidebands on the optical field. By red-detuning the input field, the blue sideband is enhanced which makes the mechanical system lose energy [14]. In order to be effective, a high finesse cavity is required (in the paper cited above, the finesse was 30 000 [13]) to operate in the sideband-resolved regime where the cavity linewidth is small in comparison to the mechanical frequency. On top of this, the high finesse cavity leads to a stronger radiation pressure force used for cooling and enhances the sensitivity for the detection of the mechanical motion. Cavity sideband cooling to the ground state was achieved in 2011 in two different experiments. The first system consisted of a nanophotonic crystal with frequency of 3.7 GHz, operated in a 20 K cryostat [15]. The cooling led to a 0.85 final occupation number. The second system consisted of a LC superconducting microwave resonator placed in a cryostat at 20 mK [16]. A

drum-mode of a capacitor-plate at 10 MHz was cooled down to 0.34 phonons.

When the radiation pressure force noise dominates over other noises, it can lead to squeezing of the optical cavity field [17]. In this case, the mechanical motion introduces correlations between the amplitude and phase quadratures of the optical field. This leads to a so-called ponderomotive squeezing where the noise in one quadrature exhibits sub shot-noise fluctuations.

By measuring one quadrature of the motion, at the price of losing any information on the other quadrature, one can perform a so-called quantum nondemolition measurement [18]. Using a similar scheme, a mechanical drum has been squeezed and therefore exhibits quantum fluctuations smaller than its zero-point fluctuations in one of the two quadratures [19]. Recently, two groups have demonstrated entanglement between two remote macroscopic mechanical modes [20, 21]. These recent examples show that mesoscopic oscillators have been demonstrated to exhibit quantum behaviours.

1.2 Levitated optomechanics

1.2.1 Motivation

Arthur Ashkin has been a pioneer in trapping dielectric nanospheres in optical tweezers [22], a tool for which he was awarded the 2018 physics Nobel prize. He showed that stable optical trapping was the result of the right balance between scattering and gradient force [23]. The trapping potential defined by the gradient force gives typical mechanical frequencies ranging from 10 kHz to 200 kHz. Using such a levitated oscillator has been motivated in Ref. [24–27] for cavity cooling experiments and as potential platforms to demonstrate macroscopic quantum behaviours. The main advantage over most clamped systems discussed in the previous section is the very high Q-factor (10^{12} at 10^{-8} mbar for a $\sim$100 nm radius silica particle) and therefore ultra-narrow mechanical linewidths of 0.1 μHz those systems can exhibit [24]. This leads to a very high level of decoupling between the oscillator and the bath which implies possible long-life times for non-classical states of motion. One practical consequence is that there is no need to operate the system in a cryogenic environment to reach the ground state of the centre-of-mass motion. Another advantage of those systems is that they only have a few mechanical modes.

This very high Q-factor is very attractive to many experiments ranging from

small force detection to thermodynamics and even quantum foundations. Because of their small mass and mechanical damping, levitated spheres in vacuum have been shown to reach force sensitivities down to 6 zN [28]. This sensitivity could be used to test non-Newtonian gravity models as well as measure Casimir forces [29]. It could also be used to probe high-frequency gravitational waves [30, 31].

As mentioned above, a strong motivation for studying levitated nanospheres is testing quantum mechanics at the mesoscopic scales. There has been several proposals discussing how a mechanical superposition could be formed and probed, with matter-wave interferometry experiments [6, 32–34]. Similar experiments could be as well used to measure signatures of quantum gravity [7]. In order to further reducing effects of decoherence, the MAQRO collaboration plans to perform these experiments in space where free-fall time is increased and both lower bath temperature ($\sim 20\,\mathrm{K}$) and pressure ($\sim 10^{-15}\,\mathrm{mbar}$) are easily achieved [35]. Lastly, these platforms can be used to probe models of the wave-function collapse [36, 37]. A larger account of experimental proposals using levitated nanospheres can be found in Ref. [8].

1.2.2 Cooling levitated nanospheres

In order to perform the experiments discussed in the previous section, the thermal variance of the nanoparticle motion needs to be greatly reduced and, in some instances, reach the ground state. Two main schemes have been used so far to cool the centre-of-mass motion of levitated nanospheres. The first one is feedback cooling. The second one is cavity sideband cooling already mentioned above. In feedback cooling, a damping force can be engineered by measuring the particle position and then applying a force proportional to the particle velocity (cold damping). It has successfully been demonstrated in an optical tweezer where three orthogonal beams were used to cool the three centre-of-mass modes with the scattering force. Cooling down to 1.5 mK for a $3\,\mu$m diameter silica sphere was observed [38] and down to 400 mK with 300 nm spheres [28]. By using the Coulomb force on charged particles, velocity damping down to 4 phonons has been demonstrated [39, 40]. Another approach, widely used by the community, has been parametric feedback cooling where the trapping potential is directly modulated at twice the frequency of oscillation [41]. Intuitively, as the particle climbs the potential, the trap is stiffened and in-

versely when the particle falls back. The record so far with this approach has been 63 phonons [42].

The other approach, mentioned already in the previous section, is cavity cooling. As a dielectric moves within the cavity standing wave, it gets more or less polarised which in turn changes the cavity resonance frequency, hence the optomechanical coupling. The first demonstration of cavity cooling of nanospheres consisted of slowing them down when crossing the cavity field [43]. A first endeavour of cooling a trapped particle in an optical cavity was reported down to 64 K using two optical modes [44]. Further cooling was later demonstrated by using a Paul trap to enhance the linear optomechanical coupling [45, 46]. Finally, the combination of an optical tweezer with an optical cavity was recently used to demonstrate cooling down to ~ 10 mK, limited by laser frequency noise [47]. Coherent scattering has recently been spotlighted within the community as a new approach of cavity cooling [48, 49]. Here, the nanosphere is positioned on a dark fringe of the cavity with an optical tweezer and the cavity is solely pumped by the tweezer scattered light. This method offers numerous advantages. The optomechanical coupling has been demonstrated to be ~ 40 times larger than with previous schemes [50]. Moreover, it enables full 3D-cavity cooling. Last, the small number of intracavity photons combined with the particle position at the cavity node reduces the effect of frequency noise by more than 40 dB [49], which has previously been a major obstacle in cavity cooling [47]. Using this scheme, the centre-of-mass motion of a silica nanosphere has been brought to the ground-state [51].

1.3 This work

The work presented here is centred around levitation in a hybrid trap consisting of the overlap between the field provided by a Paul trap and an optical standing-wave. This was initially studied in Refs. [45, 46]. The Paul trap offers the advantage of having a broad and deep potential, unlike a tweezer or an optical well. Furthermore, it could be used as a tool to create arbitrary shape potentials [52] for future quantum experiments. Another advantage of working with the hybrid trap is the reduction of the effect of the scattering recoil which has been demonstrated to be the strongest fundamental source of decoherence in optical tweezers [42]. In this thesis, we describe and characterise the original design of a miniature linear

Paul trap suitable for optomechanics experiments with nanoparticles. The oscillator and trap characterisations are realised with a super-resolution technique, which enables to achieve competitive detection sensitivities for those low-frequency oscillators. Among others, we demonstrate that this imaging technique can be used to estimate the nanosphere mass with a 3% uncertainty. This same imaging method is then used at low pressure to measure the gas damping (intrinsic linewidth) of the oscillator with a novel phase sensitive method. This method enables us to trace out slow drifts in the mechanical frequency which are orders of magnitude larger than the intrinsic linewidth. This measurement at low pressure confirms the high-Q potential of levitated nanospheres which is one of the main motivations of the field. The measurement of the ultra-narrow linewidth combined with excess noise estimates at low pressures enables us to place new bounds on standard collapse models along with their dissipative counterparts. The way these bounds are placed in the dissipative case is novel. Rather than measuring an excess noise as usually done, we can place constrains in the parameter space of the models by searching for an excess dissipation rate. Lastly, we demonstrate optomechanical experiments combining the Paul trap and a high-finesse optical cavity. Here, unlike in previous work (see Ref. [45, 46]), the Paul trap does not directly play a role in the cooling mechanism. It is used nonetheless to control the trapping well location within the optical cavity (with $\sim 10\,\mu$m of accuracy). The trapping site is relevant when the optical cavity is pumped with two modes at different frequencies. In conjunction with the intracavity powers of the two modes, it is used to control the ratio between linear and quadratic optomechanical coupling. This enables us to study the dynamics when the quadratic optomechanical interaction dominates over the linear one and among others, demonstrate a highly non-thermal state of motion. Lastly, when operating the system with linear optomechanical coupling, we are able to achieve lower temperatures ($\sim 40\,$mK) than previously reported using a similar cooling scheme and demonstrate stable trapping in an optical cavity down to $\sim 10^{-6}\,$mbar [44].

1.4 Thesis layout

The content of each chapter is briefly summarised below

- In Chapter 2, we provide a theoretical background of the cavity-nanoparticle interaction. Both mechanical oscillator and cavity optical field dynamics are introduced in the classical and quantum regimes. The Hamiltonian describing the nanoparticle-cavity interaction is then given and its different components are explained. Among others, scattering losses, photon recoil and internal temperatures are discussed. Optical classical noise (intensity noise and frequency noise) are then introduced in order to be taken into account in the model of the experiment. Finally, a model of the experiment is given where the linear optomechanical interaction dominates. The expressions of the nanoparticle position and homodyne spectra are detailed with the different noise contributions. Lastly, we discuss technically achievable phonon occupancy as well as corresponding homodyne output spectra.

- In Chapter 3 we review the general Paul trap theory, including Mathieu dynamics and stability diagrams. Two custom original designs are then described. The emphasis is given on the miniature linear Paul trap used in the experiments presented in the subsequent chapters. We detail the calculation of the efficiency parameters, trap depth and effect of voltage noise for this specific design. The loading mechanism with an electrospray alongside a quadrupole guide at a pressure $P = 10^{-1}\,\mathrm{mbar}$ is then finally described. The quadrupole guide when operated as a mass-spectrometer can be used to select specific charge-to-mass ratios.

- In Chapter 4, using a super-resolution imaging method we report sensitivities better than $10^{-16}\,\mathrm{m}^2/\mathrm{Hz}$ with signal-to-noise ratios as good as 10^6. This method can be used to illustrate the excellent force sensitivities of a levitated nano-oscillator, here beyond $1\,\mathrm{aN}/\sqrt{\mathrm{Hz}}$. We compare and discuss different methods to evaluate the nanoparticle mass in the Paul trap. Using the imaging method, previously detailed, we report a method with a 3% uncertainty. Lastly, we discuss the effect of the loading mechanism and the cold cathode pressure gauge on the trap stability. Using over nearly two weeks of uninter-

rupted measurement, we report a competitively low secular frequency drift of 2 ppm/h.

- In Chapter 5 a new method to measure the *true* linewidth of a mechanical oscillator is presented. This is shown to be suitable even when the drifts in its frequency of oscillation are larger than its linewidth. By applying this method to our oscillator we report one of the smallest measured mechanical linewidths to date at room temperature of $81 \pm 23\,\mu$Hz.

- In Chapter 6, we introduce the measurement problem with the possible solution offered by wavefunction collapse models which combine quantum mechanics and classical behaviours at macroscopic scale. Measurements of a levitated nano-oscillator at equilibrium with a bath at $T_b = 293\,$K, and kept at a pressure lower than $10^{-6}\,$mbar, enables us to confirm recently placed bounds in the CSL model. We then use the ultra-narrow linewidth measurements from the previous section to place new bounds in a novel way on dissipative versions of collapse models (CSL and Diósi-Penrose).

- Chapter 7 focuses on the description of the optical set-up mostly used for the experiments presented in Chapter 8. The lasers used for the experiment are characterised with an emphasis on their classical noise budget. In the last two sections, the two cavities used in the experiment are characterised. We introduce a design of filtering cavity with a half-linewidth of $\kappa/2\pi = 2.5\,$kHz to reduce the classical laser noise and evaluate its performance. The level of attenuation applied by this cavity on both laser beams could in theory enable ground state cooling of the oscillator. Finally, we characterise the science cavity, which is used for the experiments with nanoparticles. Among others we report four different methods to measure the linewidth and evaluate the PDH noise floor calibrated in equivalent frequency noise or cavity displacement noise.

- In Chapter 8, we present experimental results of the optomechanical interaction between the levitated nanosphere and the optical cavity. We describe first some attempts at measuring the scattering losses which can be used to estimate the particle polarisability. We demonstrate cooling of the secular motion below

200 mK with feedback on the Paul trap electrodes to minimise the variance of the motion in the transverse direction. By using two optical beams [24, 44], in conjunction with the Paul trap, we demonstrate the versatility of this levitated nano-oscillator which can be operated in regimes dominated by either linear or quadratic optomechanical coupling. We demonstrate cavity cooling in a regime dominated by the quadratic interaction. More importantly, we study the highly non-thermal state of motion created in this nonlinear regime. Lastly, when the linear optomechanical coupling dominates, we demonstrate cavity cooling down to 21 ± 4 mK, improving by more than three orders of magnitude results reported with this scheme [44].

- In Appendix A, we review the well-known PDH cavity locking scheme and detail how the error signal is calibrated. We discuss as well the laser offset-lock and some locking mechanisms used to compensate for slow drifts in the system.

Chapter 2

Theory of the experiment

In this chapter we review the main tools to describe the interaction between a dielectric and an optical field. Firstly, we focus on the harmonic oscillator both in the classical and quantum regimes. Secondly, we provide tools regarding optical fields along with some general information about optical cavities. Combining the two, we discuss the optomechanical coupling between optical field and dielectric. Among others, we examine scattering losses, photon recoil and absorption. In order to describe the system more accurately, we discuss how to incorporate both laser classical intensity noise and frequency noise in the model. The dynamics of both optical field and nanoparticle is then derived in the quantum Langevin formalism. This enables us to quantitatively predict centre-of-mass cooling that can be achieved in this system.

2.1 Mechanical harmonic oscillator

2.1.1 Classical harmonic oscillator

Close to an equilibrium position, a mechanical oscillator such as a levitated nanosphere (trapped either in a Paul trap as described in Chapter 3 or as below in an optical field) can be described as a harmonic oscillator within a very good approximation. In this section, we consider a harmonic oscillator of mass m, mechanical frequency ω_m and viscous damping γ_m. In the presence of external driving forces denoted by $F_{ext}(t)$, the oscillator follows the Newtonian dynamics:

$$\ddot{x} + \gamma_m \dot{x} + \omega_m^2 x = \frac{F_{ext}(t)}{m}\,. \tag{2.1}$$

In the case of a levitated nanoparticle in vacuum, the damping term γ_m is given

by collisions with the surrounding gas molecules. A theoretical expression for the gas damping is [44, 53]

$$\gamma_{\text{gas}} = \frac{6\pi\eta r}{m}\frac{0.619}{0.619+K_n}\left(1+\frac{0.31\,K_n}{0.785+1.152\,K_n+K_n^2}\right), \tag{2.2}$$

where K_n denotes the Knusden parameter, r the particle radius and η the air viscosity. The Knusden number is defined as the ratio between the air mean free path and the particle radius $K_n = \frac{\lambda_{mfp}}{r}$ with $\lambda_{mfp} = \frac{k_B T_b}{\sqrt{2}\pi d^2 P}$ with k_B the Boltzmann constant, P the gas pressure, T_b the bath temperature and d the air molecular diameter. Below a pressure of 10 mbar, which is typical in practice, the gas is in the free molecular flow regime (Knusden parameter satisfying $K_n \gg 1$). In this case, the gas damping is well approximated by [54, 55]

$$\gamma_{\text{gas}} = \frac{(1+\frac{\pi}{8})\bar{c}P\,m_g}{k_B T_b\, r\rho}, \tag{2.3}$$

where the particle mean speed is $\bar{c} = \sqrt{8k_B T_b/m_g\pi}$, ρ the particle density, m_g the mass of the gas molecules (4.84×10^{-26} kg for air).

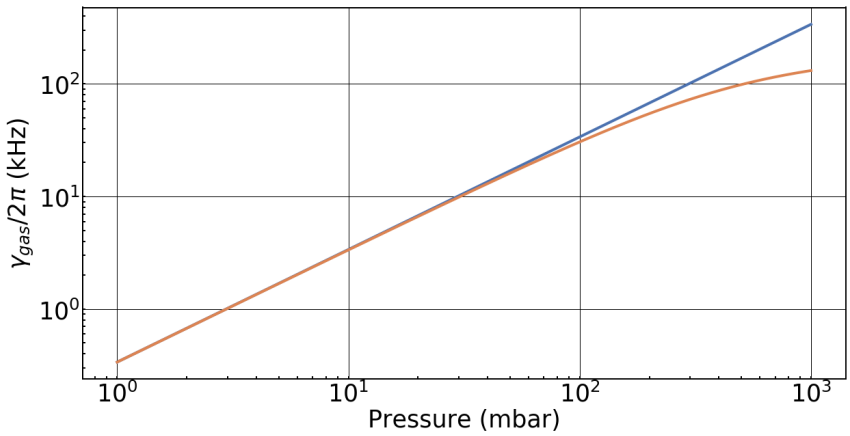

Figure 2.1: Gas damping as a function of pressure. In blue gas damping valid below 100 mbar (Eq. 2.3) and in orange, both at low and higher pressures (Eq. 2.2).

Even in the absence of deterministic forces and technical noise, an unavoidable force exerted on a levitated nanosphere is the thermal Langevin force due to gas collisions. Without this driving force, the amplitude of the particle motion would completely decay, which would be equivalent to an unrealistic coupling to a zero-temperature bath. Following from the equipartition theorem, one has

$\frac{1}{2}m\langle\dot{x}^2\rangle = \frac{1}{2}k_B T_b$ where the brackets $\langle ...\rangle$ denote the statistical average. We can assume the thermal force $F_{th}(t)$ to be a zero-mean stochastic process $\langle F_{th}(t)\rangle = 0$ since this is required to obtain an unperturbed average position of the nanoparticle. By combining those two properties, we obtain the autocorrelation function of the thermal force (fluctuation-dissipation theorem) [56]

$$\langle F_{th}(t)F_{th}(t')\rangle = 2m\,\gamma_m k_B\,T_b\delta(t-t')\,, \tag{2.4}$$

with $\delta(t)$ the Dirac delta function. It is worth noting that the strength of the thermal force directly depends on both bath temperature T_b and damping rate γ_m. The magnitude of this force can therefore be reduced by lowering the pressure or operating the system in a cryogenic environment.

Mechanical oscillators at equilibrium are generally studied in the frequency domain by using the Fourier transform. We define the Fourier transform of a variable $x(t)$ as $x(\omega) = \int_{-\infty}^{\infty} x(t)e^{i\omega t}d\omega$. By applying the Fourier transform to Eq. 2.1, we get $x(\omega) = \frac{F_{th}(\omega)}{m(\omega_m^2-\omega^2-i\gamma_m\omega)} = \chi(\omega)F_{th}(\omega)$ where we have defined the mechanical susceptibility as $\chi(\omega) = (m(\omega_m^2-\omega^2-i\gamma_m\omega))^{-1}$, which quantifies the response of the oscillator to an external driving force. We can define the double-sided power spectral density (PSD) (definition following from the Wiener-Khinchin theorem) of a time domain variable $x(t)$ as $S_x(\omega) = \int_{-\infty}^{\infty}\langle x(t)x(t+\tau)\rangle e^{i\omega\tau}d\tau$. The thermal force noise PSD can be evaluated from its autocorrelation given above as $S_{F_{th}}(\omega) = 2m\,\gamma_m\,k_B\,T_b$. We can then obtain the displacement PSD of the mechanical oscillator driven by thermal noise:

$$S_x(\omega) = |\chi(\omega)|^2 S_{F_{th}}(\omega) = \frac{2\,\gamma_m\,k_B\,T_b}{m((\omega_m^2-\omega^2)^2+\gamma_m^2\omega^2)}\,. \tag{2.5}$$

An experimental PSD of the thermal mechanical oscillators (alongside with theoretical fit) can be seen in Fig. 4.4. The area of the PSD gives the variance of the mechanical motion:

$$\langle x^2\rangle = \frac{1}{2\pi}\int_{-\infty}^{\infty} S_x(\omega)d\omega = \frac{k_B\,T_b}{m\omega_m^2}\,. \tag{2.6}$$

Depending on the value of the Q-factor $Q_f = \frac{\omega_m}{\gamma_m}$, three different regimes can be considered. The under-damped regime $Q_f > 1$, the critically damped regime $Q_f \sim 1$ and the over-damped regime $Q_f < 1$. We can show that the evolution of the variance

of the position of the oscillator in the under-damped regime is [57]

$$\langle (x(t)-x(0))^2 \rangle = \frac{2k_B T_b}{m\omega_m^2}\left(1-e^{-\frac{\gamma_m}{2}t}\left(\cos(\tilde{\omega}_m t)+\frac{\gamma_m}{2\tilde{\omega}_m}\sin(\tilde{\omega}_m t)\right)\right), \tag{2.7}$$

with the effective mechanical frequency $\tilde{\omega}_m = \sqrt{\omega_m^2 - \frac{\gamma_m^2}{4}}$. In the case of the over-damped regime, the cos and sin functions have to be replaced with their hyperbolic counterparts cosh and sinh. In the critically damped regime, the expression of the variance simplifies to $\langle (x(t)-x(0))^2 \rangle = \frac{2k_B T_b}{m\omega_m^2}\left(1-e^{-\frac{\gamma_m}{2}t}\right)$. Lastly, the position autocorrelation functions is:

$$\langle x(t)\, x(0) \rangle = \frac{k_B T_b}{m\omega_m^2} - \frac{1}{2}\langle (x(t)-x(0))^2 \rangle . \tag{2.8}$$

Importantly, it can be seen that the position autocorrelation oscillates at a frequency $\tilde{\omega}_m$, with a decreasing exponential envelope of time constant $2/\gamma_m$. This time is defined as the correlation time and quantifies the timescale over which the motion is unperturbed by stochastic noise.

2.1.2 Quantum harmonic oscillator

The treatment of the quantum mechanical oscillator is similar to the one of the optical field, given in numerous textbooks [58]. The total energy of the quantum system can be written as

$$\hat{H} = \frac{m\omega_m^2}{2}\hat{x}^2 + \frac{\hat{p}^2}{2m}, \tag{2.9}$$

where $\hat{x}$ and $\hat{p}$ represent the position and momentum quantum operators, respectively. Those operators are Hermitian and are therefore observable operators. By definition, the energy is quantised and in the case of a pure harmonic oscillator, is evenly spaced by individual quanta of energy $\hbar\omega_m$. These operators obey the commutation relation $[\hat{x},\hat{p}] = i\hbar$. Following from this commutation relation we can obtain the Heisenberg uncertainty inequality $\Delta\hat{x}\Delta\hat{p} \geq \frac{\hbar}{2}$ where Δ represents the standard deviation of a quantum operator. This inequality shows the trade-off in knowledge in one observable with respect to the other. A natural way of studying quantum harmonic oscillators is by using the non-Hermitian creation $\hat{b}^\dagger$ and annihilation $\hat{b}$ operators which act on a pure Fock state $|n\rangle$ of energy n (where n represents the number of quanta in the system) and increase or decrease by a single quanta the

energy of the oscillator

$$b\,|n\rangle = \sqrt{n}\,|n-1\rangle\,, \quad b\,|0\rangle = 0\,, \tag{2.10}$$

$$b^\dagger\,|n\rangle = \sqrt{n+1}\,|n+1\rangle\,, \tag{2.11}$$

where we have dropped hat symbols $\hat{}$ for simplicity of notations, except for the photon number operator $\hat{n}$ (defined below), to distinguish it from the photon number n. Those operators follow the boson commutation relation $[b, b^\dagger] = 1$ and are related to position and momentum operators as

$$b = \sqrt{\frac{m\omega_m}{2\hbar}}(x + \frac{i}{m\omega_m}p)\,, \tag{2.12}$$

$$b^\dagger = \sqrt{\frac{m\omega_m}{2\hbar}}(x - \frac{i}{m\omega_m}p)\,. \tag{2.13}$$

We can define as well the phonon number operator $\hat{n} = b^\dagger b$ since $|n\rangle$ is an eigenvector of $\hat{n}$ with eigenvalue n: $b^\dagger b\,|n\rangle = n\,|n\rangle$. The Hamiltonian can be rewritten using the creation and annihilation operators as

$$H = \hbar\omega_m\left(b^\dagger b + \frac{1}{2}\right). \tag{2.14}$$

The energy eigenvalues of the Hamiltonian are $E_n = \hbar\omega_m\left(n + \frac{1}{2}\right)$ where $\frac{1}{2}\hbar\omega_m$ denotes the energy of the ground state. Following from Eq. 2.9, this minimum energy of the system can be written in terms of zero-point motion $x_{zpf} = \sqrt{\frac{\hbar}{2m\omega_m}}$ and zero-point momentum $p_{zpf} = \sqrt{\frac{\hbar m\omega_m}{2}}$, respectively. They correspond to the standard deviation of the position and momentum of the oscillator in its ground state. Using typical numbers of the experiment, a single silica nanosphere of 387 nm diameter and density $1850\,\mathrm{kg/m^3}$ has a mass of $5.6\times10^{-17}\,\mathrm{kg}$. We typically operate the system with a mechanical frequency of $\omega_m/2\pi = 50\,\mathrm{kHz}$. In the ground state, the standard deviation of this mechanical mode is 1.7 pm. When coupled to a bath at temperature T_b and at equilibrium, the probability p_n of finding the system in the mode n of energy E_n is

$$p_n = \frac{\exp(-E_n/k_BT_b)}{\sum_n \exp(-E_n/k_BT_b)}\,. \tag{2.15}$$

We can calculate from this expression the average phonon number

$$\bar{n} = \sum_{n=0}^{\infty} n\, p_n = \frac{1}{\exp(\hbar\omega_m / k_B T_b) - 1}\,. \tag{2.16}$$

In the classical limit where $k_B T_b \gg \hbar\omega_m$, this formula simplifies to the well known $\bar{n} = \frac{k_B T_b}{\hbar\omega_m}$. In the case of the levitated nanosphere mentioned above coupled to a bath at 293 K, the mean phonon occupancy is 1.2×10^8. Lastly, the autocorrelation function of the force noise given in the classical regime has to be modified so that the position and momentum operators do not commute in the quantum regime. A full treatment of dissipation in quantum harmonic oscillators coupled to an infinite number of harmonic oscillators can be found in Ref. [3]. In the Markovian limit where the coupling between the bath and the oscillator is assumed to be memoryless, the autocorrelation function is not any more a Dirac delta function and is given by $\langle F_{th}(t) F_{th}(t')\rangle = \hbar\, m\, \gamma_m \int \frac{d\omega}{2\pi} e^{-i\omega(t-t')}\omega \left[\coth\left(\frac{\hbar\omega}{2k_B T_b}\right) + 1\right]$. The classical expression is recovered in the high temperature limit. The quantum Langevin equations of motion read [59]:

$$\dot{x} = \frac{p}{m}\,, \tag{2.17}$$

$$\dot{p} = -m\omega_m^2\, x - \gamma_m\, p + F_{th}(t)\,. \tag{2.18}$$

Lastly, the quantum PSD of the harmonic oscillator can be shown to be [59]

$$S_x(\omega) = \gamma_m x_{zpf}^2 \left(\frac{\bar{n}+1}{(\omega-\omega_m)^2 + (\gamma_m/2)^2} + \frac{\bar{n}}{(\omega+\omega_m)^2 + (\gamma_m/2)^2} \right). \tag{2.19}$$

Interestingly, the PSD of a quantum operator is not necessarily symmetric as it can be seen in the above equation. This is a strong quantum signature as it is a direct consequence of non-commutation of the position and momentum operators. A classical measurement of the mechanical spectrum would symmetrise the PSD shown above. The asymmetric behaviour can nonetheless be preserved depending on the measurement scheme [60].

2.2 Optical cavity field

2.2.1 Classical description - Fabry-Pérot resonator

Optical cavities are notably used in lasers to coherently amplify the stimulated emission process. They have as well been used in numerous physics experiments to take advantage of some of their properties such as their long decay time, the high intensity field or the optical standing wave they can provide. They have been notably used in a key experiment to detect a "single photon without destroying it" with an average photon lifetime of 1 ms [61]. We describe now the standard optical cavity consisting of two partially reflecting mirrors (see Fig. 2.2) [62, 63]. For simplicity, we assume the internal faces only to be reflective. We denote the amplitude reflection and transmission coefficients of the two mirrors by (r_1, t_1) and (r_2, t_2), respectively. The intensity coefficients are defined as $T_i = t_i^2$ and $R_i = r_i^2$ (with $i = 1, 2$). The mirror losses (due to absorption and scattering) are denoted by $\Sigma_i = 1 - R_i - T_i$. We define the input amplitude of the electrical field as E_{in}. The first reflection of the input beam on the input mirror gives a π-phase shift (obtained by energy conservation considerations). The phase shift acquired on each reflection inside the cavity is denoted by $e^{i\delta}$ (its full expression is given below).

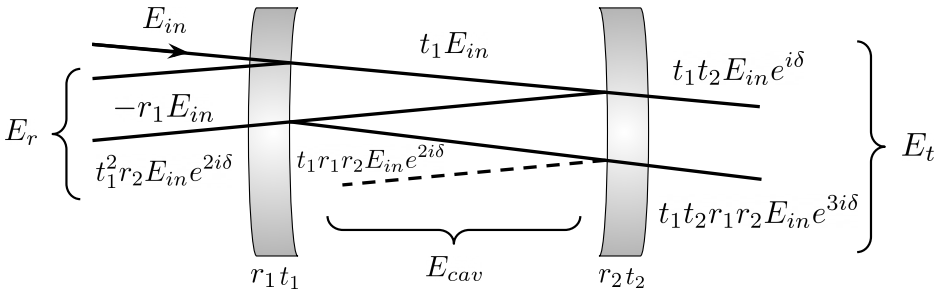

Figure 2.2: Schematic of the transmissions and reflections of an input beam of amplitude E_{in} in an optical cavity. The mirrors are characterised with amplitude reflection and transmission coefficients r_i and t_i, respectively. The reflected input at the input mirror gets a π-phase shift to satisfy energy conservation rules. The phase shift accumulated after half a round-trip is denoted by $e^{i\delta}$. The reflected, intracavity and transmitted fields are denoted by E_r, E_{cav} and E_t, respectively.

When summing up over the different amplitudes we get the intracavity field

$$E_{cav} = \frac{t_1 e^{i\delta}}{1 - r_1 r_2 e^{2i\delta}} E_{in}\,. \tag{2.20}$$

The transmitted field is simply $E_t = t_2 E_{cav} = \frac{t_1 t_2 e^{i\delta}}{1-r_1 r_2 e^{2i\delta}} E_{in}$. The field in reflection is

$$E_r = -r_1 E_{in} + \frac{t_1^2 r_2 e^{2i\delta}}{1-r_1 r_2 e^{2i\delta}} E_{in}\,. \tag{2.21}$$

We can now look in further detail at the ratios between the transmitted and input intensities as well as the reflected and input intensities. We obtain

$$\frac{|E_t|^2}{|E_{in}|^2} = \frac{t_1^2 t_2^2}{1-r_1 r_2^2} \frac{1}{1+B\sin^2(\delta)}\,, \tag{2.22}$$

$$\frac{|E_r|^2}{|E_{in}|^2} = \frac{(\zeta/r_2)^2 + B(1-r_1^2-t_1^2)\sin^2(\delta)}{1+B\sin^2(\delta)}\,, \tag{2.23}$$

where we have defined B and the coupling parameter ζ as

$$B = \frac{4 r_1 r_2}{(1-r_1 r_2)^2}\,, \tag{2.24}$$

$$\zeta = r_2 \frac{r_1 - r_2(r_1^2+t_1^2)}{1-r_2 r_2}\,. \tag{2.25}$$

We can see from the above equations that the condition for resonance is $\delta = m\pi$, with m an integer. As mentioned above, δ corresponds to the phase acquired after half a round-trip. It can be expressed as $\delta = kL$ with k the optical field wave vector and L the cavity length, which gives $\delta = \frac{2\pi\nu}{c} L$ with ν the laser frequency (in Hz). The resonance condition is satisfied for frequencies ν such that $\nu = m\frac{c}{2L}$. The separation between two consecutive resonant longitudinal modes is called the free spectral range (FSR) $FSR = \frac{c}{2L}$. Let us now define the half-linewidth $\delta\nu$ as the frequency at which the transmitted power (equivalently intracavity power) drops by two (Half-Width at Half-Maximum). Another important quantity is the finesse F, defined as $F = \frac{FSR}{2\delta\nu}$. It quantifies how well resolved are two consecutive longitudinal modes. For highly reflective mirrors, we have $\delta\nu \ll FSR$ and $T_i, \Sigma_i \ll 1$. This allows us to introduce the high-finesse approximation, which greatly simplifies the finesse and coupling parameter expressions to

$$F \approx \frac{\pi\sqrt{r_1 r_2}}{1-r_1 r_2} \approx \frac{2\pi}{T_1+T_2+\Sigma_1+\Sigma_2}\,, \tag{2.26}$$

$$\zeta \approx \frac{-T_1+T_2+\Sigma_1+\Sigma_2}{T_1+T_2+\Sigma_1+\Sigma_2}\,. \tag{2.27}$$

With those definitions, we can rewrite Eq. 2.23, in the high-finesse approximation, in terms of intracavity power P_{cav}, transmitted power P_{tr} and reflected power P_r. We denote the frequency detuning between the input field (the laser) and the cavity resonance frequency by $\Delta_o = \omega_l - \omega_{cav}$ (in rad). P_{in} denotes the input power:

$$P_{cav} = T_1 \left(\frac{F}{\pi}\right)^2 \frac{P_{in}}{1+(\Delta_o/\kappa)^2} = (1-\zeta)\frac{F}{\pi}\frac{P_{in}}{1+(\Delta_o/\kappa)^2}\,, \tag{2.28}$$

$$P_{tr} = T_2\, P_{cav}\,, \tag{2.29}$$

$$P_r = \frac{\zeta^2 + (\Delta_o/\kappa)^2}{1+(\Delta_o/\kappa)^2} P_{in}\,. \tag{2.30}$$

Following from Eq. 2.27, $-1 < \zeta < 1$. We can now more easily comment on the physical significance of ζ. Given a cavity finesse and input power, this parameter quantifies the achievable intracavity power. For $\zeta < 0$, the cavity is said to be over-coupled with maximum intracavity power achieved for $\zeta = -1$ in the unrealistic case of a single-sided cavity with no other losses than the input coupler transmission. For $\zeta = 0$, the cavity is said to be critically-coupled which occurs when the input losses are equal to all the other losses. For $\zeta > 0$, the cavity is under-coupled. Moreover, in the case of an over-coupled (under-coupled) cavity, most of the reflected field comes from the cavity field (reflected input field). There is no reflected field in the case of a critically coupled cavity on resonance.

We can estimate the cavity dynamics by looking at the cavity losses after one round-trip of time $t_{trip} = \frac{2L}{c}$: $\frac{dE_{cav}}{dt} = \frac{E_{cav}(t) - E_{cav}(t+t_{trip})}{t_{trip}} = -\frac{c(1-r_1 r_2)}{2L} E_{cav} \approx -\kappa E_{cav}$ where we have defined the cavity decay-rate $\kappa = 2\pi\delta\nu$.

2.2.2 Gaussian beams

Laser beams fail to be accurately described by ray optics as transverse modes are not included. Assuming a small divergence angle along the beam propagation (paraxial approximation), Gaussian beams can be shown to be one solution of Maxwell's equation, which describe laser beams accurately. The envelope of the electric field $u(r,z)$ of the lowest order transverse mode (TEM_{00}) has a Gaussian distribution. Its expression is given below, written in polar coordinates with r the transverse

coordinate and z the direction of propagation [64]:

$$u(r,z) = \frac{w_o}{w(z)} \exp\left(-i\left(k\,z - \Phi(z)\right) - r^2\left(\frac{1}{w^2(z)} + \frac{ik}{2R(z)}\right)\right), \tag{2.31}$$

with w_o the beam waist (defined as the radius at which the amplitude drops by e at the position of the waist $z = 0$), $w(z)$ the beam radius, $R(z)$ the radius of the wave front and $\Phi(z)$ the Gouy phase. These are defined as

$$w^2(z) = w_o^2\left(1 + \left(\frac{\lambda\, z}{\pi w_o^2}\right)^2\right), \tag{2.32}$$

$$R(z) = z\left(1 + \left(\frac{\pi w_o^2}{\lambda\, z}\right)^2\right), \tag{2.33}$$

$$\Phi(z) = \arctan\left(\frac{\lambda z}{\pi\, w_o^2}\right), \tag{2.34}$$

with λ the laser wavelength. Near the cavity waist (quantitatively, for $-z_0 < z < z_0$ with $z_0 = \frac{\pi w_o^2}{\lambda}$), the Gaussian beam is nearly planar and the expression given in Eq. 2.31 can be simplified to

$$u(r,z) = \exp\left(-i\,k\,z - \frac{r^2}{w_o^2}\right). \tag{2.35}$$

In addition, it can be shown that the TEM_{00} mode propagating in an optical cavity of length L and mirror curvatures R (assuming here identical mirrors) has a waist w_c given by

$$w_c = \sqrt{\frac{\lambda}{2\pi}\sqrt{L(2R-L)}}. \tag{2.36}$$

We use in this work an optical cavity $L = 14.6\,\mathrm{mm}$ long with mirror of curvatures $R = 25\,\mathrm{mm}$. This gives a nominal waist $w_c = 62\,\mu\mathrm{m}$. Another important quantity to introduce is the cavity mode volume V_m. It is defined as the volume of the envelope squared of the cavity mode

$$V_m = \int_0^{2\pi}\int_{-L/2}^{L/2}\int_0^{\infty} u(r,z)^2\, r\,dr\,dz\,d\theta = \frac{w_c^2 \pi L}{4}. \tag{2.37}$$

Here we have a mode volume of $4.4 \times 10^{-11}\,\mathrm{m}^3$.

2.2.3 Quantum description

Similarly to the treatment of the quantum mechanical oscillator, the intracavity optical field can be described by creation and annihilation operators $a^\dagger$ and a, respectively. The Hamiltonian of the cavity field, ignoring any dissipation, is $H = \hbar\omega_l \left(a^\dagger a + \frac{1}{2}\right)$. The time evolution of these operators is given by the Heisenberg's equation $\dot{a} = \frac{i}{\hbar}[H, a]$ from which we obtain the evolution

$$\dot{a} = -i\omega_l\, a\,, \tag{2.38}$$

with solutions $a(t) = a(0)e^{-i\omega_l t}$ and $a^\dagger(t) = a^\dagger(0)e^{i\omega_l t}$. We can then define the light amplitude and phase quadrature operators X_1 and X_2 as $X_1 = \frac{a^\dagger + a}{2}$ and $X_2 = i\frac{a^\dagger - a}{2}$, respectively where we have redefined the operators as $a(0) \equiv a$ and $a^\dagger(0) \equiv a^\dagger$. The commutation relations $[X_1, X_2] = \frac{i}{2}$ gives the Heisenberg uncertainty $\Delta X_1 \Delta X_2 \geq \frac{1}{4}$. In the case of the vacuum optical state $|0\rangle$, we can show that the uncertainty in the two light quadratures is $\Delta X_1 = \Delta X_2 = \frac{1}{2}$.

Stimulated emission occurring in lasers can be shown to create coherent states. This optical state is very similar to the vacuum state $|0\rangle$ as it has the same quadrature uncertainties. A coherent state $|\alpha\rangle$ is defined as eigenstate of the annihilation

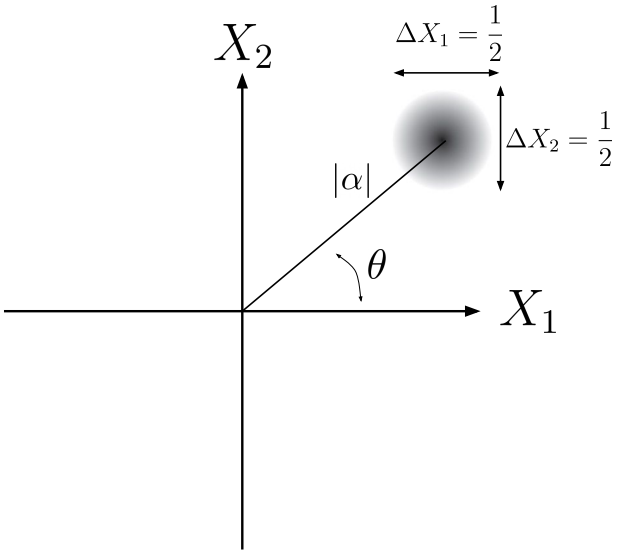

Figure 2.3: Quadratures of a coherent state $||\alpha|e^{i\theta}\rangle$. When the field is demodulated with $\theta = 0$, the X_1 and X_2 quadratures correspond to the amplitude and phase quadrature respectively.

operator a with α a complex number. The stimulated emission process can be modelled by the displacement operator $D(\alpha)$ acting on a vacuum state as [58]

$$|\alpha\rangle = D(\alpha)\,|0\rangle = e^{-\frac{1}{2}|\alpha|^2} \sum_{n=0}^{\infty} \frac{\alpha^2}{\sqrt{n!}}\,|n\rangle\,, \tag{2.39}$$

with $|n\rangle$ the Fock state of n photons. The thermal occupation for the optical field is here negligible: $\bar{n}_{th} = \frac{k_B T_b}{\hbar\omega_l} \ll 1$. We can write α in polar form $|\alpha|e^{i\theta}$ and show that in terms of light quadratures we get $\alpha = \langle X_1\rangle + i\langle X_2\rangle$. The quadratures of a coherent state are shown in phase-space in Fig. 2.3. The expectation values of the photon number operator $\hat{n}$ of the coherent state can be shown to be $\bar{n} = |\alpha|^2$, which directly relates α to the amplitude of the field. Moreover, the standard deviation of the number of photons is $\Delta n = \sqrt{\bar{n}}$. This fundamental uncertainty is called the photon shot noise. The signal-to-noise ratio of the measured number of photons of a coherent state is therefore $\frac{\bar{n}}{\Delta n} = \sqrt{\bar{n}}$ and increases proportionally to the amplitude of the field.

Now, we can look at the dynamical equations of the field within the optical cavity. Exploiting the rotating wave approximation, we can show that the evolution of the annihilation operator a, when including dissipative and driving terms, obeys [3, 65]

$$\dot{a} = -(\kappa - i\Delta_o)a + \sqrt{2\kappa_{in}}(a_{in} + \alpha_{in}) + \sqrt{2\kappa_v}a_v\,, \tag{2.40}$$

where a_{in} and a_v represent the input and vacuum field noise operators, α_{in} the amplitude of the drive, Δ_o the detuning between the input field of frequency ω_l and the cavity resonance frequency ω_{cav}, $\Delta_o = \omega_l - \omega_{cav}$. The input loss rate is here denoted by κ_{in} (it can directly be related to the input transmission coefficient as $\kappa_{in} = cT_1/4L$) and vacuum loss rate by κ_v. Assuming the cavity field is only pumped on the input port, we have $\bar{n}_{in} = |\alpha_{in}|^2$, which is the input flux of photons in s^{-1}. The different uncorrelated white input noise $a_j(t)$ $(j = in, v)$ are described by the correlation functions:

$$\begin{aligned} \langle a_j(t)a_j(t')\rangle = \langle a_j^\dagger(t)a_j^\dagger(t')\rangle = \langle a_j^\dagger(t)a_j(t')\rangle = 0\,, \\ \langle a_j(t)a_j^\dagger(t')\rangle = \delta(t-t')\,. \end{aligned} \tag{2.41}$$

Following from the fact that we are pumping the system with coherent states (which

are eigenstates of the annihilation operators), we can recover the classical dynamics by simply replacing the operator by their expectation values .

2.2.3.1 Homodyne detection

Rather than measuring the field amplitude, one can measure either quadrature of the light field by demodulating the optical signal. This is done in practice by mixing the optical field to be measured, a_1, with an additional reference field of same frequency and controlled phase θ, a_2, called local oscillator as shown in Fig. 2.4. After mixing on a 50:50 beam splitter, the intensity of the two output fields $a_3 = \frac{1}{\sqrt{2}}(a_1 + ia_2)$ and $a_4 = \frac{1}{\sqrt{2}}(i\,a_1 + a_2)$ is measured on two different photodetectors. The resulting photocurrent is then subtracted. Assuming the local oscillator is a strong coherent state, the output signal is proportional to the expectation value of the measured quadrature $X^\theta = \frac{a_1^\dagger e^{-i\theta} + a_1 e^{i\theta}}{2}$. We can show that depending on the phase of θ, we can measure different quadratures of the optical field. If $\theta = 0$ we measure the amplitude quadrature X_1, in phase with the optical field and sensitive to its amplitude fluctuations. In the case of the phase quadrature X_2, we measure the field phase fluctuations.

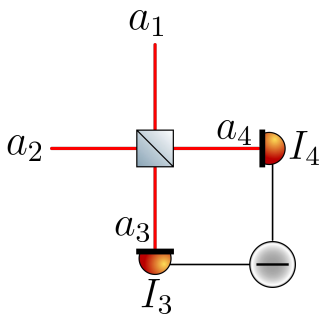

Figure 2.4: Schematic of a balanced homodyne scheme. The field of interest a_1 is mixed on a bean splitter with a strong coherent state a_2 of same frequency (local oscillator). The difference in current between the two photodiodes gives a signal proportional to the expectation value of the quadrature $X^\theta = \frac{a_1^\dagger e^{-i\theta} + a_1 e^{i\theta}}{2}$ which can be adjusted with the phase θ of the local oscillator.

2.3 Dielectric in a cavity

In this section, we study in detail the interaction between a dielectric nanosphere and an optical field.

2.3.1 Optomechanical interaction

In the presence of an electric field, a dielectric object gets polarised. The Hamiltonian of the dipole potential energy interaction reads [24, 27]

$$H_{dipole} = -\frac{1}{2}\int_V d\mathbf{x} P(\mathbf{x}) E(\mathbf{x}), \tag{2.42}$$

with V the sphere volume, $\mathbf{x}$ the spatial coordinate within the sphere, $E(\mathbf{x})$ the electric field given by the optical field and $P(\mathbf{x})$ the polarisation within the sphere. The proportional relationship between the electrical field and the polarisation gives $P(\mathbf{x}) = 3\epsilon_0 \frac{\epsilon_s - 1}{\epsilon_s + 2} E(\mathbf{x})$ with ϵ_0 the vacuum permittivity and ϵ_s the relative permittivity of the nanosphere. Assuming that the nanosphere radius is small in comparison to the wavelength $r \ll \lambda$ we can exploit the Rayleigh-approximation where we assume the nanosphere to be a point-like particle. This is equivalent to consider a constant electric field across the particle evaluated at the nanosphere centre-of-mass position $\vec{x}$ within the cavity field. We discuss the validity of this approximation below. In the Rayleigh regime we can simplify the expression in Eq. 2.42 to

$$H_{dipole} = -\frac{1}{2} 3\epsilon_0 \frac{\epsilon_s - 1}{\epsilon_s + 2} \int_V d\mathbf{x} E^2(\mathbf{x}) \approx -\frac{1}{2}\alpha_p E^2(\vec{x}), \tag{2.43}$$

where we have introduced $\alpha_p = 3\epsilon_0 V \frac{\epsilon_s - 1}{\epsilon_s + 2}$, the nanoparticle polarisability. The amplitude of the electric field in the cavity can be written in terms of creation and annihilation operators as [58]

$$E = \sqrt{\frac{\hbar\omega_{cav}}{2\epsilon_0 V_m}}(a^\dagger + a). \tag{2.44}$$

We get the simplified expression of the Hamiltonian by using $(a^\dagger + a)^2 \approx 2a^\dagger a$ (rotating-wave approximation):

$$H_{dipole} = -\frac{3}{2}\frac{\epsilon_s - 1}{\epsilon_s + 2}\frac{\hbar V \omega_{cav}}{V_m} a^\dagger a \, |u(\vec{x})|^2, \tag{2.45}$$

with $u(\vec{x})$ the cavity mode profile defined in Eq. 2.31. Let us denote $U_o = \frac{3}{2}\frac{\epsilon_s - 1}{\epsilon_s + 2}\frac{V\omega_{cav}}{V_m}$. By neglecting any radial motion for the moment, which is a reasonable approximation if the radial motion of the nanoparticle remains small in comparison

to the cavity waist, we can simplify the Hamiltonian to

$$H_{dipole} = -\hbar U_o a^\dagger a \cos^2(kx)\,, \tag{2.46}$$

with x the centre-of-mass operator of the nanosphere along the cavity axis. The sum of the bare cavity Hamiltonian with the dipole Hamiltonian reads $\hbar\left(\omega_{cav} - U_o\cos^2(kx)\right)a^\dagger a$ where we can identify $-U_o\cos^2(kx)$ as the cavity position-dependent frequency shift. As the particle moves within the fringe it gets more or less polarised which in return shifts the cavity resonance frequency. With only one cavity mode, the particle is trapped at a cavity antinode (bright fringe) where $kx = m\pi$. Around a position of equilibrium x_o, we can simplify the Hamiltonian of the dipole interaction with a Taylor expansion by using the notation $x \to x_o + x$. We have $\cos^2(kx) \approx \cos^2(kx_o) - kx\sin(2kx_o) - k^2x^2\cos(2kx_o)$. Similarly, we can, displace the field amplitude $a \to \alpha_s + a$ with α_s the mean amplitude of the intracavity field. The mean cavity photon number is denoted by $n_{cav} = |\alpha_s|^2$. We obtain the following terms

- $H_{static} = -\hbar U_o a^\dagger a\cos^2(kx_o)$, which corresponds to the static frequency shift. As the particle gets polarised, the conservation of energy translates into a decrease of the cavity resonance frequency, hence the minus sign [24].

- $H_{force} = \hbar U_o|\alpha_s|^2\sin(2kx_o)kx$, which is a constant force acting on the particle.

- $H_{trap} = \hbar U_o|\alpha_s|^2\cos(2kx_o)k^2x^2$ is the trapping potential given by the optical beam. We can identify a trap frequency called *mechanical frequency* $\omega_m = \sqrt{\frac{2\hbar U_o k^2|\alpha_s|^2\cos(2kx_o)}{m}}$. The mechanical frequency is proportional to the cavity field amplitude. It is therefore maximum when the nanoparticle sits at a bright fringe.

- $H_l = \hbar U_o(\alpha_s a^\dagger + \alpha_s^* a)\sin(2kx_o)kx$ gives the linear dispersive optomechanical interaction, i.e., the frequency shift as a function of the linear particle displacement. The linear optomechanical coupling is given by $G_1 = U_o\sin(2kx_o)k$.

- $H_q = \hbar U_o\alpha_s(\alpha_s a^\dagger + \alpha_s^* a)\cos(2kx_o)k^2x^2$ gives the quadratic optomechanical coupling. The quadratic optomechanical coupling is given by $G_2 = U_o\cos(2kx_o)k^2$.

One objective consists in maximising the linear optomechanical coupling to give better cooling rates and detection sensitivity. The coupling is maximum when the average particle position is $x_o = \frac{\lambda}{8}$, which corresponds to an unstable trapping location. When trapped optically, the nanoparticle sits at the antinode of the electric field, $x_o = 0$, where there is no linear optomechanical coupling but maximum quadratic coupling. Therefore, one optical mode is not enough to achieve significant cooling using the linear optomechanical coupling. Three ways have been reported to obtain a non-negligible linear coupling while keeping a high mechanical frequency. The first way uses two optical modes. One more powerful field defines the optical trap and an another weaker one, with a different optical phase, is used to provide some linear coupling [24, 44]. Another method consists in trapping in an optical tweezer to control the particle position within the optical fringe [49, 66]. Lastly, adding a slow (smaller than the mechanical frequency) periodic modulation to the nanosphere mean position allows it to explore regions of larger linear coupling [45, 46] (realised in practice with the Paul micromotion). In order to further increasing the optomechanical coupling, some groups use pure silicon which has a higher permittivity $\epsilon_s \approx 3.4$ than silica $\epsilon_s \approx 2.0$ and gives therefore a larger polarisability [43]. Lastly, the coupling is proportional to the particle volume (since the polarisability is proportional to the volume). A temptation might therefore be to use large nanoparticles but this comes at the price of increasing both scattering cavity losses and recoil heating as discussed in the next section.

So far we have considered nanoparticles in the Rayleigh regime where the particle radius is small in comparison to the wavelength. In our case we use optical fields of wavelength $\lambda = 1064\,\mathrm{nm}$ and a typical particle radius of 194 nm. We are therefore at the edge of the validity of this approximation. The full description taking into account the non-uniformity of the electric field within the sphere is given by the Mie theory [67]. In this case, the frequency shift at an antinode of the field ($x_o = 0$) becomes

$$U_{o,\mathrm{Mie}} = \frac{\pi c}{k^2 V_m} \mathrm{Im}\left[\sum_{n=1}^{\infty} (2n+1)(-1)^{n+1}(a_n + b_n)\right], \tag{2.47}$$

where in the above a_n and b_n are spherical Bessel functions depending on the dielectric constant and the sphere radius [67]. While the frequency shift for our parameters is $U_o/2\pi = 73\,\mathrm{kHz}$ in the Rayleigh approximation, we find $U_{o,\mathrm{Mie}}/2\pi = 67\,\mathrm{kHz}$ using

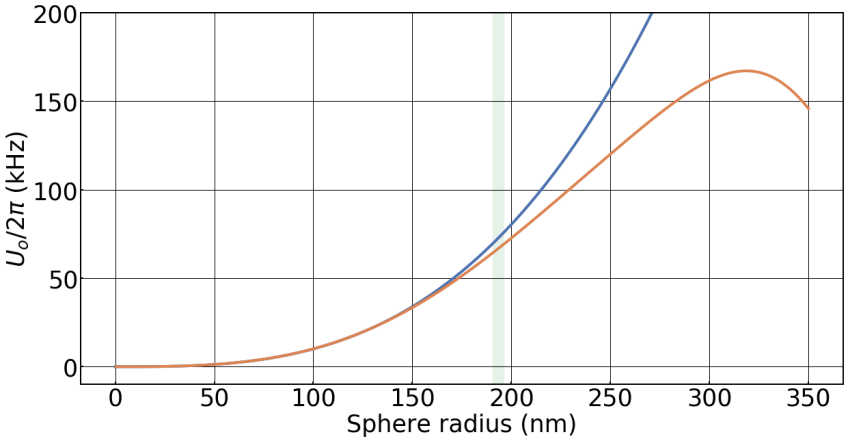

Figure 2.5: Comparison between the static frequency shift given by a nanoparticle as a function of its radius in the Rayleigh (blue) and Mie formalisms (orange). This is calculated for a nanoparticle trapped at the antinode of the electric field ($x_o = 0$), for silica ($\epsilon_s = 2.0$), a cavity mode volume of $4.4 \times 10^{-11}\,\mathrm{m}^3$ and an optical wavelength $\lambda = 1064\,\mathrm{nm}$.

the Mie formalism. We show in Fig. 2.5 the cavity frequency shift U_o as a function of sphere radius, given in both the Rayleigh and Mie formalisms for our typical experimental parameters.

The expression of the linear optomechanical coupling given in the Mie formalism reads as $G_{1,Mie} = |\alpha_s| \frac{\pi c}{k V_m} \sin(2kx_o)\,\mathrm{Im}\left[\sum_{n=1}^{\infty}(2n+1)(-1)^{n+1}(a_n+b_n)\right]$.

2.3.2 Scattering losses

Due to the strong polarisability of silica nanoparticles, photons are scattered out of the nanosphere. This leads to two phenomena, a photon loss in the cavity and momentum kicks to the particle, which are discussed in the next section. The scattering losses, which scale with the volume squared of the particle, are detrimental since they can strongly reduce the effective cavity finesse. In the Rayleigh regime, the scattering losses are given by $\kappa_{sc} = 6\pi^2 \omega_{cav} \frac{V^2}{\lambda^3 V_m} \left(\frac{\epsilon_s - 1}{\epsilon_s + 2}\right)^2 \cos^2(kx_o)$ (half-linewidth), where we have neglected the radial Gaussian envelope of the beam. In the Mie regime, this expression becomes [67]

$$\kappa_{sc,\mathrm{Mie}} = \frac{c\pi}{2k^2 V_m} \mathrm{Re}\left[\sum_{n=1}^{\infty}(2n+1)(1-(-1)^n \cos(2kx_o))(a_n+b_n)\right]. \tag{2.48}$$

For a nanosphere trapped at the antinode, we get $\kappa_{sc}/2\pi = 18\,\mathrm{kHz}$ ($\kappa_{sc,\mathrm{Mie}}/2\pi = 15\,\mathrm{kHz}$ in the Mie formalism) which is significant in comparison to the half-cavity linewidth (typically here between 10 kHz and 150 kHz). We show in Fig. 2.6 the

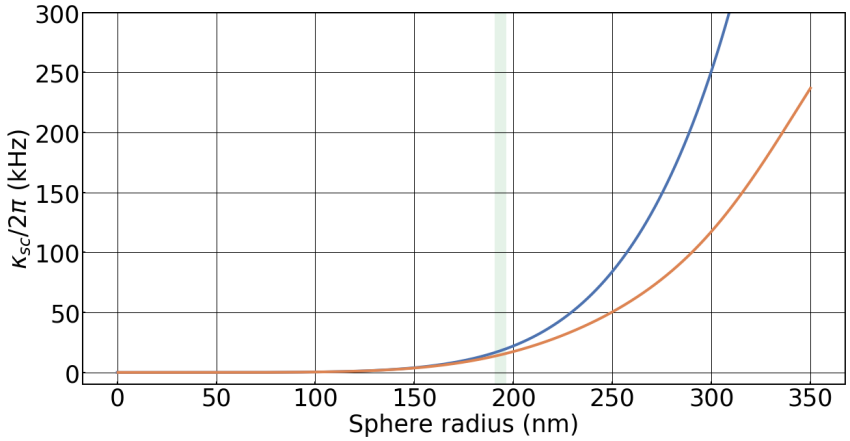

Figure 2.6: Scattering losses (given in half linewidth) for a silica nanoparticle trapped at the cavity antinode, calculated in the Rayleigh formalism (Mie) and shown in blue (orange). The experimental parameters used are the same ones as for Fig. 2.5.

theoretical scattering losses as a function of particle radius in the Mie and Rayleigh regimes.

2.3.3 Photon recoil

Scattered photons give momentum kicks of energy $\hbar k$ leading to a recoil on the nanoparticle. Within the Rayleigh approximation, the scattering follows a dipole pattern $s(\theta) = \frac{3}{8\pi}\sin^2(\theta)$ with θ the angle defined in the transverse plane to the input field propagation, between the direction of interest and the polarisation vector. The recoil is studied here with the assumption of a shot-noise limited beam. When classical laser noise is present (see Section. 2.4), the expression given below of the recoil force noise can be rescaled by comparing the contributions of classical intensity noise to shot-noise in the scattered field. Along the cavity axis, the recoil force noise PSD can be shown to be [42]

$$S_{F_{rc}}(\omega) = \frac{2}{5}\frac{\hbar\omega_l}{c^2}P_{sc}\,, \tag{2.49}$$

with the scattered power $P_{sc} = \sigma_{sc} I_o$ with $\sigma_{sc} = \frac{\alpha_p^2 V^2 k^4}{6\pi\epsilon_0^2}$ the scattering cross-section in the Rayleigh approximation and I_o the intensity at the particle position (in the Mie regime, $\sigma_{sc,\text{Mie}} = \frac{c^2\pi}{\omega_{cav}^2}\text{Re}\left[\sum_{n=1}^{\infty}(2n+1)(1-(-1)^n\cos(2kx_o))(a_n+b_n)\right]$ [67]). We compare the expressions of the scattering cross-section in both formalisms in Fig. 2.7. In the case of the optical cavity, we have $I_o = 2\frac{2P_{cav}}{\pi w_o^2}\cos^2(kx_o)$ with an additional

factor 2 since the cavity mode is a standing-wave rather than a travelling wave. In the case of an optical tweezer (which in a first order approximation can be considered as a Gaussian beam [42]), it is given by $I_{tw} = \frac{P_{tw}k^2\mathrm{NA}^2}{2\pi}$ with P_{tw} the tweezer power and NA the numerical aperture of the beam, which corresponds to the numerical aperture of the objective (typically NA≈ 0.9). One of the advantages of trapping within a cavity field is that for a same trap frequency, the intensity inside the cavity is smaller than the one given by optical tweezers ($62\,\mu$m against sub-micron waist). This leads to higher recoil heating rates when trapping in an optical tweezer in comparison to the cavity.

From the expression of the scattering force noise given above, we can calculate a heating rate. To begin with, the mean energy of a harmonic oscillator follows a Fokker-Planck equation [68]

$$\langle \dot{E} \rangle = -\gamma_m(\langle E \rangle - E_\infty)\,, \tag{2.50}$$

with E_∞, the steady state energy. When writing the energy in terms of quanta $E = n\hbar\omega_m$, we get $\dot{n} = -\gamma_m n + \Gamma$ with a heating rate Γ identified as $\Gamma = \frac{E_\infty}{\hbar\omega_m}\gamma_m$. In the case of the thermal Langevin force (see Eq. 2.6), we have $E_\infty = k_B T_b$, which gives $\Gamma_{th} = \gamma_m \frac{k_B T_b}{\hbar\omega_m}$. Similarly, we can obtain a heating rate for the recoil as $\Gamma_{rc} = \frac{1}{5}\frac{P_{scatt}}{mc^2}\frac{\omega_l}{\omega_m}$. For a silica nanosphere of diameter 387 nm, trapped within a cavity field with a mechanical frequency of $\omega_m/2\pi = 50\,$kHz, we obtain $\Gamma_{rc} = 6.9\times10^3\,\mathrm{s}^{-1}$, a scattered power $P_{sc} = 31\,\mu$W and a scattering force noise $S_{F_{sc}} = 2.6\times10^{-41}\,\mathrm{N}^2/\mathrm{Hz}$

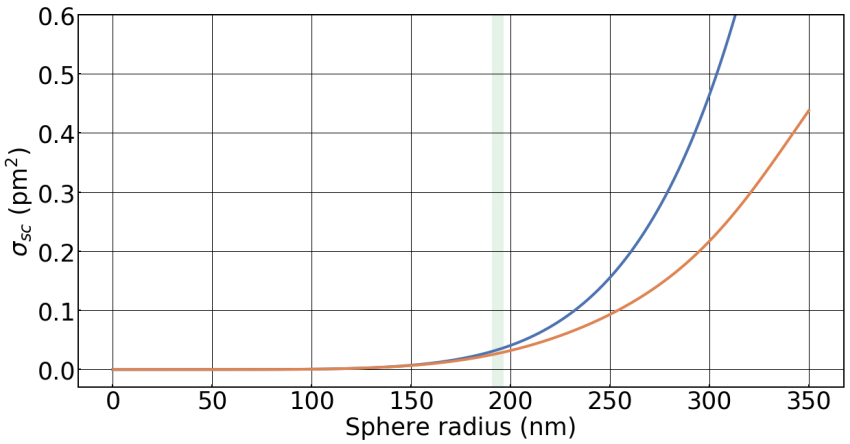

Figure 2.7: Scattering cross section of a silica sphere calculated in the Rayleigh (Mie) regime and shown in blue (orange).

(calculated in the Mie regime). In order, to reduce the effect of the recoil, smaller spheres (typically with diameter smaller than 100 nm) are preferred in tweezers. It has been demonstrated that a nanosphere of 50 nm diameter and mechanical frequency $\omega_m/2\pi = 150\,\text{kHz}$ had a measured recoil close to the nominal one of $\Gamma_{rc} = 16 \times 10^3\,\text{s}^{-1}$ [42]. At pressures lower than $P \sim 10^{-8}\,\text{mbar}$, the recoil should dominate over other fundamental heating mechanisms in the case of the optical tweezer.

2.3.4 Internal temperature

Silica (or silicon) is used by most groups because of its commercial availability as well as its very low absorption in the near-infra-red frequency band. Despite being small, this last effect is not negligible for the particle internal temperature in vacuum, which changes depending on the balance between absorption, black-body radiation and conduction with the surrounding gas. The absorbed power (in the Rayleigh approximation) is given by $P_{abs} = 12\pi \frac{I_o}{\lambda} V \text{Im}\left(\frac{\epsilon_s - 1}{\epsilon_s + 2}\right)$ [24] with $\sqrt{\epsilon_s} = 1.41 + i\,7 \times 10^{-8}$ [69], where the real part corresponds to the refractive index, and the imaginary part to the absorption. Those numbers are given in the case of high purity and amorphous bulk silica. With the parameters given in the previous section, we get $P_{abs} = 55\,\mu\text{W}$, which is a lower bound since calculated for high purity silica. In order to estimate the equilibrium temperature, let us first denote the different heat fluxes by $\dot{Q}_g$, $\dot{Q}_{bb}$ corresponding to conduction and black body emission rates, respectively. We have [24, 37] $\dot{Q}_g = -\frac{\alpha_T \pi r^2 P \bar{c}}{2T_b} \frac{\gamma_s - 1}{\gamma_s + 1}(T_{in} - T_b)$ with α_T the phenomenological accommodation factor $\alpha_T = 0.65$ [70], T_{in} the particle internal

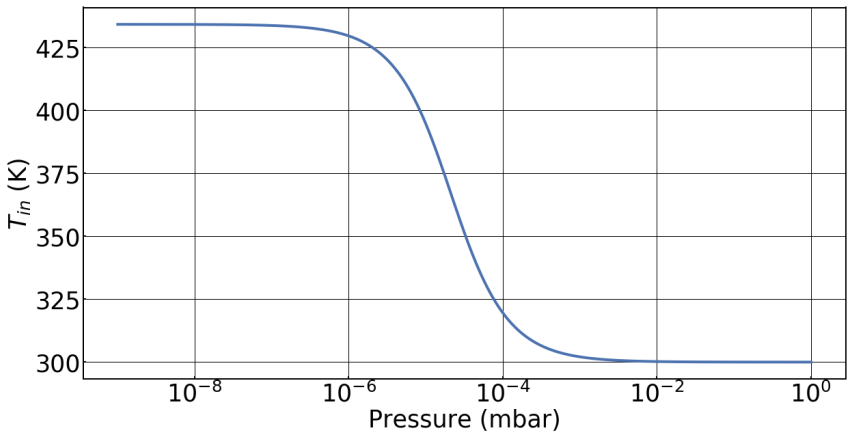

Figure 2.8: Internal temperature of a 387 nm diameter silica nanosphere as a function of pressure. This is calculated for a nanosphere levitated in a cavity with mechanical trap frequency $\omega_m/2\pi = 50\,\text{kHz}$.

temperature, $\gamma_s = 7/5$ the specific heat ratio, P the gas pressure and $\bar{c}$ the gas thermal velocity. The black body emission rate is $\dot{Q}_{bb} = -\frac{74.9}{\pi^2}\frac{Vk_B^5}{c^3\hbar^4}\epsilon_{abs}(T_{in}^5 - T_b^5)$, with $\epsilon_{abs} \approx 0.1$ a coefficient depending on the blackbody emissivity [24]. In Fig. 2.8, we show the theoretical internal temperature as a function of pressure. Two regimes can be noticed, a first regime at pressures higher than $P = 10^{-3}$ mbar, where the coupling with the bath dominates the dynamics and the particle internal temperature remains equal to the bath temperature, and a regime at pressures below $P = 10^{-6}$ mbar where the absorption reaches an equilibrium with black-body radiation. Considering a silica nanosphere optically trapped at a cavity antinode with a frequency $\omega_m/2\pi = 50$ kHz, a lower bound on the final internal temperature at low pressure is 430 K (see Fig. 2.8). The final temperature, considering a higher amount of absorption, is likely to be closer to ~ 1000 K but lower than ~ 2000 K to be compatible with the observation that our nanospheres do not melt, as it would be expected at this temperature [45, 70]. At pressures where conductive cooling becomes negligible, the increase in the internal temperature can lead to a significant change in the bath temperature [70].

2.4 Classical optical noise

2.4.1 Intensity noise

In the discussion above, it has been assumed that the light field was a pure coherent state. In practice, at frequencies below 10 MHz, laser light with optical power $\sim$1 mW is rarely shot-noise limited [17], meaning that the power fluctuations are not given by the shot noise but by classical intensity fluctuations. We can model the classical intensity noise by introducing a real stochastic noise term ϵ, to the drive amplitude and quantum fluctuations $a_{in} + \alpha_{in} \to a_{in} + \alpha_{in} + \epsilon = \tilde{\alpha}_{in}$ [71] where we have introduced the total input field amplitude $\tilde{\alpha}_{in}$. The measured intensity on a photodiode can be defined as the number of photons $i = \tilde{\alpha}_{in}^\dagger \tilde{\alpha}_{in}$ (which is correct in practice when taking the expectation value and up to some experimental constants). After linearising to the first order of the quantum and classical fluctuations, we get $i \approx \alpha_{in}^2 + \alpha_{in}(a_{in}^\dagger + a_{in} + 2\epsilon)$. We can define the power spectral density of the direct detection of the intensity i as $2\pi S_i(\omega)\delta(\omega + \omega') = \frac{\langle i(\omega)i(\omega')\rangle + \langle i(\omega')i(\omega)\rangle}{2}$. This PSD is symmetrised since the measured current is a classical variable [72]. In the case of the quantum fluctuations we have $\langle a_{in}(\omega)a_{in}^\dagger(\omega')\rangle = 2\pi\delta(\omega + \omega')$.

Moreover, we define the classical amplitude field fluctuations noise PSD $S_\epsilon(\omega)$ as $2\pi S_\epsilon(\omega)\delta(\omega+\omega') = \langle\epsilon(\omega)\epsilon(\omega')\rangle$. With those definitions, we get the PSD of the intensity $S_i(\omega) = \alpha_{in}^2(S_{a_{in}}(\omega) + 4S_\epsilon(\omega))$. With typical quantum optics conventions, PSD are normalised to the photon shot noise taken as a reference: $S_{i,n}(\omega) = S_{a_{in}}(\omega) + 4S_\epsilon(\omega)$ with $S_{a_{in}}(\omega) = 1$. This is motivated by the fact that photon shot-noise fluctuations follow $\Delta n^2 = \bar{n}$ with Δn^2 the photon number variance and $\bar{n}$ the average number of photons (see section 2.2.3).

Classical intensity fluctuations can have several origins. A common origin is the fluctuations in the pump diode intensity. Those fluctuations are proportional to the square of the power $\Delta n^2 \propto \bar{n}^2$. We can be quantitative on S_ϵ by looking for an expression of fluctuations satisfying $S_\epsilon = kP_{in}$ with k a constant (and not proportional to the power squared since we are normalised to the shot noise, itself proportional to the mean photon number α_{in}^2). We can define P_o as the input power at which the intensity fluctuations are twice above the shot noise. At this power $P_{in} = P_o$, we get $S_{i,n}(\omega) = 1 + 4kP_o = 2$, from which we get the expression for the classical intensity noise fluctuations of $S_\epsilon = \frac{P_{in}}{4P_o}$. Finally, we can simplify the expression given above of the normalised intensity noise to the mean intensity $S_{i,n}(\omega) = 1 + \frac{P_{in}}{P_o}$.

2.4.2 Frequency noise

Classical frequency noise arises in lasers, among others, because of noise in the frequency tuning actuators. In practice, here, this effect is dominated at frequencies around $\sim 100\,\mathrm{kHz}$ by mechanical noise in the piezo-actuator used to change the laser cavity length, and therefore the laser optical frequency. In an optical cavity, displacement noise caused by vibrations of the cavity mirrors leads to fluctuations of the cavity resonance frequency, which, inside the cavity are indistinguishable from laser frequency noise. In practice, these noise sources can easily overwhelm the laser input intensity fluctuations and lead to excess heating of the centre-of-mass motion of the levitated nanosphere. We can model frequency fluctuations by introducing a noise term $\dot{\phi}$ in the cavity detuning $\Delta_o \to \Delta_o - \dot{\phi}$. In addition to affecting the nanoparticle dynamics as we will show in the next section, this noise increases the noise floor in a phase sensitive detection such as a homodyne detection. We define the frequency noise PSD $S_{\dot{\phi}}(\omega)$ as $2\pi S_{\dot{\phi}}(\omega)\delta(\omega+\omega') = \langle\dot{\phi}(\omega)\dot{\phi}(\omega')\rangle$.

2.5 Model of the experiment

After having given elements to describe the mechanics, the optical field and the interaction between the nanosphere and the optical cavity, we can now discuss the dynamics between the optical field and the nanosphere. We first give the Langevin equations of motion of the system. In some instances the system can be linearised, which is more convenient to study the dynamics, and particularly, cavity cooling. In this case we discuss the contributions of the different noise sources on the nanosphere motion. Lastly, we give expressions of the homodyne spectra which are used in practice to infer information on the nanosphere motion and effective temperature. For simplicity, we only describe the system here with one optical beam, which is enough to characterise both the cooling effects as well as readout. Other optical modes can easily be added. We nonetheless discuss how one other mode (separated by one FSR) can change the mechanical frequency of the nanoparticle.

The Hamiltonian of the system is given below in Eq. 2.51. It is written in the laser rotating frame ω_l where the detuning is defined as $\Delta_o = \omega_l - \omega_{cav}$ with ω_{cav} the bare optical resonance frequency. The first term corresponds to the energy of the optical cavity mode, the second to the particle kinetic energy and the third one to the dipole interaction, discussed in Section 2.3.1. The last two terms correspond to the different dissipative terms (photons leaking and mechanical damping) and laser drive.

$$H = -\hbar\Delta_o a^\dagger a + \frac{p^2}{2m} - \hbar U_o a^\dagger a \cos^2(kx) + H_{diss} + H_{drive}\,. \tag{2.51}$$

2.5.1 Langevin equations

The Heisenberg equations of motion are calculated using the Markov quantum Langevin equation for both mechanical and optical oscillators. The optical field equation is calculated in the rotating wave approximation (neglecting the fast rotating terms at $2\omega_0$) [3, 65]

$$\dot{a} = -(\kappa - i\Delta_o)a + iU_o a\cos^2(kx) + \sqrt{2\kappa_{in}}\,(a_{in} + \alpha_{in}) + \sqrt{2\kappa_v}\,a_v\,, \tag{2.52}$$

$$\dot{x} = \frac{p}{m}\,, \tag{2.53}$$

$$\dot{p} = -\hbar k U_o a^\dagger a \sin(2kx) - \gamma_m p + F_{th}\,. \tag{2.54}$$

The total mechanical losses are represented by γ_m and correspond in practice to the gas damping (see Section 2.1.1). The total optical losses κ is the sum of different contributions corresponding to the cavity losses (scattering, absorption and transmission) and losses due to light scattered off the particle (see Section 2.3.2). The input vacuum fluctuations (corresponding to losses at the input port) are represented by a_{in}. Vacuum fluctuations corresponding to other losses are represented by a_v. The laser drive amplitude is given by α_{in}. In practice, this amplitude can be rewritten in terms of the laser input power P_{in} as $\alpha_{in} = \sqrt{P_{in}/\hbar\omega_l}$. The two different uncorrelated white input noises a_j $(j = in, v)$ are described by the correlation functions given in Eq. 2.41. The mechanical thermal force noise operator is represented by F_{th} (see Section 2.1.2). On top of those fundamental noise, we incorporate classical intensity and frequency noise discussed in Section 2.4. The intensity noise amplitude is represented by ϵ and the frequency noise by $\dot{\phi}$. The optical equation of motion can then be rewritten as

$$\dot{a} = -(\kappa - i(\Delta_o - \dot{\phi}))a + iU_o a\cos^2(kx) + \sqrt{2\kappa_{in}}\,(a_{in} + \alpha_{in} + \epsilon) + \sqrt{2\kappa_v}\,a_v\,. \qquad (2.55)$$

2.5.2 Linearised dynamics

In the case where the particle equilibrium position is not at the antinode and that the particle does not explore nonlinearities of the potential (small amplitude of the motion in comparison to $\lambda/8$), then the dynamics can safely be linearised. If these conditions are not met, this approximation does not hold. The dynamics in this case is discussed in detail in Section 8.4.

The particle motion is linearised the same way as described for the Hamiltonian in Section 2.3.1 with $x \to x_o + x$ where x_o is the nanosphere steady-state position within the optical fringe. In this section we only consider the linear optomechanical coupling. This is valid for a particle mean position $x_o \neq 0$, which, as discussed in previous sections, can be realised with an additional optical mode (see Section 2.5.3). We can introduce the optical field amplitude steady-sate α_s and displace the field amplitude accordingly $a \to \alpha_s + a$ with

$$\alpha_s = \frac{\sqrt{2\kappa_{in}}}{\kappa - i\Delta}\alpha_{in}\,, \qquad (2.56)$$

where we have defined the cavity detuning Δ which includes the static frequency shift given by the nanosphere $\Delta = \Delta_o + U_o \cos^2(kx_o)$. Linearised equations of motion can then be written as

$$\dot{a} = -(\kappa - i\Delta)a - i\dot{\phi}\alpha_s - ikU_o\alpha_s \sin(2kx_o)x + \sqrt{2\kappa_{in}}(a_{in} + \epsilon) + \sqrt{2\kappa_v}a_v\,, \quad (2.57)$$

$$\dot{x} = \frac{p}{m}\,, \quad (2.58)$$

$$\dot{p} = -\hbar k U_o(\alpha_s a^\dagger + \alpha_s^* a)\sin(2kx_o) - m\omega_m^2 x - \gamma_m p + F_{th}\,. \quad (2.59)$$

2.5.3 Two optical modes

Adding another optical mode can easily be achieved following from the above derivations. This is motivated in order to obtain a linear optomechanical coupling, nonexistent otherwise [24, 44]. We consider here two TEM_{00} modes, one FSR apart, with mean intracavity amplitudes for the probe beam (used for probing and cooling) and trapping beam denoted by α_p and α_t, respectively. The particle mean position is given by $x_s = x_i + x_o$ with x_i defined as the position of the intensity maximum of the probe beam (with origin taken at the input mirror) and x_o the particle position within the probe fringe. The phase within the fringe of the probe field is therefore $\phi_p = kx_s$. The phase on the trapping beam is $\phi_t = kx_s + \frac{\pi}{L}x_i$. We indicate with $\mathcal{F}(y,z) = \exp(-2(y^2+z^2)/w_c^2)$ the Gaussian profile of the TEM_{00} cavity mode. The coupled dynamical equations describing the full 3D dynamics are then [73]

$$\begin{aligned}
\dot{a}_j &= -(\kappa - i\Delta_o^j)a_j + iU_o\, a_j \cos^2(kx + \phi_j)\mathcal{F}(y,z) + \sqrt{2\kappa_{in}}(\alpha_{in,j} + a_{in,j}) + \sqrt{2\kappa_v}\, a_{v,j} \\
\ddot{x} &= -\frac{\hbar k U_o}{m}\sum_j a_j^\dagger a_j \sin(2(kx+\phi_j))\mathcal{F}(y,z) - \gamma_m \dot{x} + \frac{F_{th,x}}{m} \\
\ddot{y} &= -y\frac{4\hbar}{m w_c^2}\sum_j a_j^\dagger a_j \cos^2(kx+\phi_j)\mathcal{F}(y,z) - \gamma_m \dot{y} + \frac{F_{th,y}}{m} \\
\ddot{z} &= -z\frac{4\hbar}{m w_c^2}\sum_j a_j^\dagger a_j \cos^2(kx+\phi_j)\mathcal{F}(y,z) - \gamma_m \dot{z} + \frac{F_{th,z}}{m}
\end{aligned} \quad (2.60)$$

where $j = p,t$ indicate the probe and trap fields, γ_m the gas damping, Δ_o^j is the empty cavity detuning, $\kappa = \kappa_{in} + \kappa_v$ is the total cavity half linewidth. Field fluctuations are uncorrelated with the only nonvanishing correlation function given by $\langle a_i(t) a_j^\dagger(t')\rangle = \delta(t-t')\delta_{ij}$ and $F_{th,i}$ is a Brownian stochastic force that arises from

background gas collisions and with a correlation function given by $\langle F_{th,i}(t)F_{th,j}(t')\rangle = 2\,k_B T_b m\,\gamma_m \delta(t-t')\delta_{ij}$, where T_b is the temperature of the background gas. The effective mechanical frequency along the x-axis depends both on the two field amplitudes as well as the well location x_i in the cavity. By defining the intracavity power ratio μ between the two beams as $\mu = |\frac{\alpha_p}{\alpha_t}|^2$, it can be shown that the effective mechanical frequency reads [44]

$$\omega_m^2 = \frac{2\hbar k^2 U_o}{m}|\alpha_t|^2\sqrt{1+\mu^2+2\mu\cos\left(2\frac{\pi}{L}x_i\right)}\,, \tag{2.61}$$

with the equilibrium position x_o satisfying

$$\tan(2kx_o) = -\frac{\sin\left(2\frac{\pi}{L}x_i\right)}{\mu+\cos\left(2\frac{\pi}{L}x_i\right)}\,. \tag{2.62}$$

2.5.4 Position spectra

We follow here the approach detailed in Ref. [74] to calculate the position spectra and study the effect of the optics onto the mechanical oscillator. We only consider one beam as in the previous sections. An additional optical mode can easily be added with a similar treatment. Let us denote $K_o(\omega) = \kappa - i(\Delta+\omega)$. Taking the Fourier transform of the Langevin equation Eq. 2.57, we obtain

$$a(\omega) = \frac{-ikU_o\sin(2kx_s)\alpha_s x(\omega) - i\alpha_s\dot{\phi}(\omega) + \sqrt{2\kappa_{in}}\,(a_{in}(\omega)+\epsilon(\omega)) + \sqrt{2\kappa_v}\,a_v(\omega)}{K_o(\omega)}\,, \tag{2.63}$$

$$x(\omega) = i\frac{p(\omega)}{m\omega}\,, \tag{2.64}$$

$$m(\omega_m^2-\omega^2-i\omega\gamma_m)x(\omega) = -\hbar k U_o\sin(2kx_o)(\alpha_s a^\dagger(\omega)+\alpha_s^* a(\omega)) + F_{th}(\omega)\,. \tag{2.65}$$

One can write the equations for the mechanical motion as

$$\begin{aligned}\chi_{eff}(\omega)^{-1}x(\omega) = {} & B_1(\omega)\left(\sqrt{2\kappa_{in}}\,(a_{in}(\omega)+\epsilon(\omega)) + \sqrt{2\kappa_v}a_v(\omega) + i\alpha_s^*\dot{\phi}\right)\\ & + B_2(\omega)\left(\sqrt{2\kappa_{in}}(a_{in}^\dagger(\omega)+\epsilon(\omega)) + \sqrt{2\kappa_v}a_v^\dagger(\omega) - i\alpha_s\dot{\phi}\right)\,,\end{aligned} \tag{2.66}$$

where

$$B_1(\omega) = \frac{-\hbar k U_o\sin(2kx_o)\alpha_s^*}{K_o(\omega)}\,, \tag{2.67}$$

$$B_2(\omega) = \frac{-\hbar k U_o \sin(2kx_o)\alpha_s}{K_o^*(-\omega)}\,. \tag{2.68}$$

We define the effective coupling rate as $G = \sqrt{2}G_1\alpha_s$ with $G_1 = kU_o\sin(2kx_o)$. Another useful definition is the normalised coupling strength to the zero-point motion: $G_n = G\sqrt{\hbar/m\omega_m}$. The symmetrised position PSD $S_x(\omega)$ is defined as: $2\pi S_x(\omega) = \frac{\langle x(\omega)x(\omega')\rangle + \langle x(\omega')x(\omega)\rangle}{2}$. It consists of five terms corresponding to thermal noise, radiation pressure, intensity, frequency noise and recoil heating contributions.

$$S_x(\omega) = |\chi_{eff}(\omega)|^2 (S_{F_{th}}(\omega) + S_{rp}(\omega) + S_{in}(\omega) + S_{fn}(\omega) + S_{rc}(\omega))\,, \tag{2.69}$$

with the thermal PSD given by $S_{F_{th}}(\omega) = 2k_BT\gamma_m m$ (for the full expression see Section 2.1.2). The expression for the recoil force noise $S_{rc}(\omega)$ is given in Eq. 2.49. The radiation pressure force noise PSD reads

$$S_{rp}(\omega) = \frac{\hbar^2 G^2 \kappa(\Delta^2 + \kappa^2 + \omega^2)}{(\kappa^2 + (\omega+\Delta)^2)(\kappa^2 + (\omega-\Delta)^2)}\,, \tag{2.70}$$

the laser classical intensity noise PSD

$$S_{in}(\omega) = 2\hbar^2 G_1^2 \kappa_{in} S_\epsilon \left| \frac{\alpha_s}{K_o^*(-\omega)} + \frac{\alpha_s^*}{K_o(\omega)} \right|^2, \tag{2.71}$$

and the frequency noise PSD

$$S_{fn}(\omega) = \hbar^2 G_1^2 S_{\dot{\phi}} \left| \frac{-|\alpha_s|^2}{K_0^*(-\omega)} + \frac{|\alpha_s|^2}{K_o(\omega)} \right|^2, \tag{2.72}$$

with S_ϵ and $S_{\dot{\phi}}$ defined in Section 2.4. These two noises are considered here to be white for simplicity. This approximation typically holds for effective mechanical linewidths smaller than $\sim$1 kHz. In the above equation we have identified an effective mechanical susceptibility

$$\chi_{eff}(\omega) = \left(m\left(\omega_m^2 - \omega^2 - i\omega\gamma_m\right) + \frac{\hbar G^2 \Delta}{(\kappa - i\omega)^2 + \Delta^2} \right)^{-1}. \tag{2.73}$$

Finally, from the expression of the susceptibility, one can identify an effective mechanical frequency and damping caused by the optomechanical interaction

$$\omega_{m,eff}(\omega) = \left(\omega_m^2 + \frac{\hbar G^2 \Delta(\Delta^2+\kappa^2-\omega^2)}{m(\kappa^2+(\omega-\Delta)^2)(\kappa^2+(\omega+\Delta)^2)}\right)^{1/2}, \tag{2.74}$$

$$\gamma_{m,eff}(\omega) = \gamma_m - \frac{2\hbar G^2 \Delta\kappa}{m(\kappa^2+(\omega-\Delta)^2)(\kappa^2+(\omega+\Delta)^2)}. \tag{2.75}$$

The shift in the effective mechanical frequency given by the optomechanical interaction is the consequence of the so-called optical spring. Furthermore, the optomechanical interaction changes the effective damping which can be increased or lowered depending on the detuning sign. In the "bad-cavity" regime ($\omega_m/\kappa < 1$), for a red detuning ($\Delta < 0$), the optical spring reduces the mechanical frequency, and the damping is increased, which cools the oscillator. Conversely, a blue detuning increases the mechanical frequency and leads to heating. The final phonon number can be estimated by calculating the position and momentum variances: $\langle \Delta x^2 \rangle = \frac{1}{2\pi}\int S_x(\omega) d\omega$ and $\langle \Delta p^2 \rangle = \frac{m^2}{2\pi}\int S_x(\omega)\omega^2 d\omega$, respectively [74]. From this calculation, the effective number of phonons n_{eff} can be estimated with $\hbar\omega_m\left(n_{eff}+\frac{1}{2}\right) = \frac{m\omega_m^2}{2}\langle \Delta x^2\rangle + \frac{1}{2m}\langle \Delta p^2\rangle$.

2.5.5 Homodyne spectra

As detailed above, the position PSD $S_x(\omega)$ gives useful information regarding the final temperature of the motion and the budget of the different sources of heating. The homodyne spectra adds to this information the detection imprecision noise coming from the shot noise, vacuum losses and additional classical noise. We detail here the expression of the homodyne detection which can be simply adapted to the case of several optical beams. Moreover, the homodyne field is given for the reflected cavity field, as experimentally obtained here in practice. The reflected output field reads $a_{out} = -a_{in} - \epsilon + \sqrt{2\kappa_{in}}a$. We define the homodyne output field a_{out}^{θ} as $a_{out}^{\theta} = a_{out}e^{-i\theta} + a_{out}^{\dagger}e^{i\theta}$ with θ the phase of the local oscillator (see Section 2.2.3.1). With this definition, the homodyne output PSD with the contributions of

the different noise sources reads

$$\begin{aligned} S_{a^{\theta}_{out}} = & S_{a_{in}}\left(|A_1(\omega)|^2+|A_2(-\omega)|^2+2\mathrm{Re}\left[A_1(\omega)A_2(-\omega)e^{-2i\theta}\right]\right) \\ & +S_{a_v}\left(|A_3(\omega)|^2+|A_4(-\omega)|^2+2\mathrm{Re}\left[A_3(\omega)A_4(-\omega)e^{-2i\theta}\right]\right) \\ & +S_{F_{th}}\left(|A_5(\omega)|^2+|A_5(-\omega)|^2+2\mathrm{Re}[A_5(\omega)A_5(-\omega)e^{-2i\theta}]\right) \\ & +S_{rc}\left(|A_5(\omega)|^2+|A_5(-\omega)|^2+2\mathrm{Re}\left[A_5(\omega)A_5(-\omega)e^{-2i\theta}\right]\right) \\ & +S_{\epsilon}\left(|A_6(\omega)e^{-i\theta}+A_6^*(\omega)e^{i\theta}|^2\right) \\ & +S_{\dot{\phi}}\left(|A_7(\omega)e^{-i\theta}+A_7^*(\omega)e^{i\theta}|^2\right), \end{aligned} \tag{2.76}$$

with $S_{a_{in}}$, and S_{a_v} the spectra of different vacuum input ports all equal to 1 with the shot noise normalisation convention. Let us define:

$$A_8(\omega) = \frac{\sqrt{2\kappa_{in}}}{K_0(\omega)}\left(1+i\frac{|\alpha_s|^2\hbar G_1^2\chi_{eff}(\omega)}{K_0(\omega)}\right), \tag{2.77}$$

$$A_9(\omega) = i\frac{\sqrt{2\kappa_{in}}}{K_0(\omega)}\frac{\alpha_s^2\hbar G_1^2\chi_{eff}(\omega)}{K_0^*(-\omega)}. \tag{2.78}$$

With this definition,

$$A_1(\omega) = -1+\sqrt{2\kappa_{in}}\,A_8(\omega), \tag{2.79}$$

$$A_2(\omega) = \sqrt{2\kappa_{in}}\,A_9(\omega), \tag{2.80}$$

$$A_3(\omega) = \sqrt{2\kappa_{v}}\,A_8(\omega), \tag{2.81}$$

$$A_4(\omega) = \sqrt{2\kappa_{v}}\,A_9(\omega), \tag{2.82}$$

$$A_5(\omega) = -i\frac{\sqrt{2\kappa_{in}}}{K_0(\omega)}\alpha_s G_1\,\chi_{eff}(\omega), \tag{2.83}$$

$$A_6(\omega) = A_1(\omega)+A_2(\omega), \tag{2.84}$$

$$A_7(\omega) = i\alpha_s A_8(\omega) - i\alpha_s^* A_9(\omega). \tag{2.85}$$

2.5.6 Parameters discussion

In this section we discuss the minimum phonon occupancy which can be achieved with current and future experimental parameters. Here, we consider two laser beams as discussed in Section 2.5.3. The parameters considered for this case are very close to the ones experimentally used in Section 8.5 and estimated in Chapter 7. We

consider the science cavity input transmission coefficient to be $T_1 = 80\,\text{ppm}$ and total losses $\Sigma = 95\,\text{ppm}$ (particle scattering losses excluded). This corresponds to a cavity half linewidth $\kappa/2\pi = 143\,\text{kHz}$. The trapping (probe) beam has an input power $P_{in} = 0.6\,\text{mW}$ ($P_{in} = 0.2\,\text{mW}$) and detuning $\Delta/2\pi = -10\,\text{kHz}$ (varying detuning), which gives a mechanical frequency $\omega_m/2\pi \approx 55\,\text{kHz}$, see Fig. 2.9(c). The particle position within the cavity is $x_i - L/2 = 0.8\,\text{mm}$, and the pressure of the vacuum chamber is considered to be $P = 5 \times 10^{-6}\,\text{mbar}$. The frequency noise considered for the trapping (probe) beam at 50 kHz is $S_{\dot{\phi}}/(2\pi)^2 = 5 \times 10^{-3}\,\text{Hz}^2/\text{Hz}$ ($S_{\dot{\phi}}/(2\pi)^2 = 2.5 \times 10^{-2}\,\text{Hz}^2/\text{Hz}$). The power at which the laser intensity noise is twice above the shot-noise (for both lasers) is $P_o = 35\,\mu\text{W}$. We show in Fig. 2.9(a), the noise budget of the final phonon occupation number as a function of detuning of the probe beam. With these parameters, a final phonon occupancy $n_{eff} \approx 1000$ is achievable mostly limited by frequency noise and thermal noise.

In order to achieve the ground state, frequency noise, thermal noise, radiation pressure shot noise and classical intensity noise need to be reduced. We present here, reasonable experimental parameters where this could be achieved. We consider now the science cavity input transmission coefficient $T_1 = 30\,\text{ppm}$ and total losses $\Sigma = 5\,\text{ppm}$ (particle scattering losses excluded). This corresponds to a cavity half linewidth $\kappa/2\pi = 29\,\text{kHz}$. The trapping (probe) beam has an input power $P_{in} = 0.6\,\text{mW}$ ($P_{in} = 0.1\,\text{mW}$) and detuning $\Delta/2\pi = -6\,\text{kHz}$ (the probe beam detuning is varied), which gives a mechanical frequency $\omega_m/2\pi \approx 146\,\text{kHz}$, see Fig. 2.9(d). We consider the optimal particle position within the cavity $x_i - L/2 = L/4 = 3.3\,\text{mm}$, which therefore leads to a stronger optical damping. The pressure considered in the vacuum chamber is this time $P = 1 \times 10^{-8}\,\text{mbar}$. The frequency noise considered for the trapping (probe) beam at 150 kHz is $S_{\dot{\phi}}/(2\pi)^2 = 1 \times 10^{-6}\,\text{Hz}^2/\text{Hz}$ ($S_{\dot{\phi}}/(2\pi)^2 = 7 \times 10^{-6}\,\text{Hz}^2/\text{Hz}$). Same classical intensity noise threshold on both beams at $P_o = 100\,\text{mW}$ is considered. We discuss in Section 7.3 how to achieve those noise levels. We show in Fig. 2.9(b), the noise budget of the final phonon occupation number as a function of detuning of the probe beam. With those parameters, a final occupancy $n_{eff} \approx 0.7$ could be achieved, limited this time by the radiation pressure shot noise. Finally, for the two cases considered, we show in Fig. 2.10 the theoretical homodyne spectra in reflection with the main noise contributions. In Fig. 2.10(a),

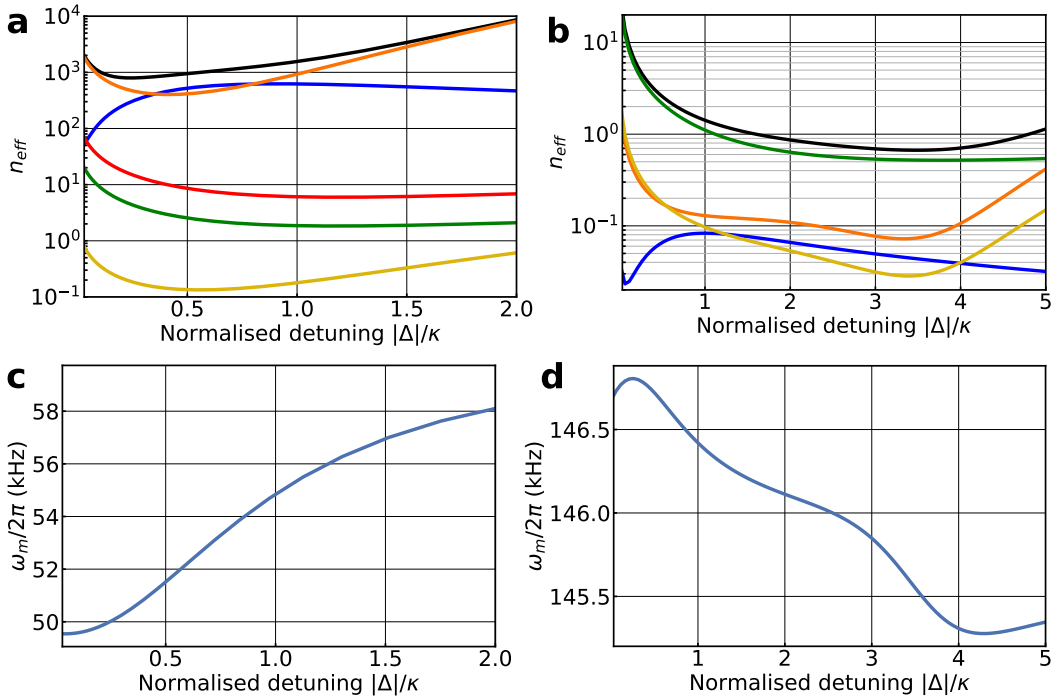

Figure 2.9: (a), (b) Theoretical noise budget given in phonon occupancy as a function of probe beam detuning. The experimental parameters are given in the main text. Total phonon occupancy (black line), thermal contribution (orange), laser frequency noise (blue), classical intensity noise (red), radiation pressure shot noise (green), recoil heating for a shot-noise limited beam (gold). (c), (d) Effective mechanical frequency as a function of probe beam detuning with same experimental parameters as the ones shown in (a) and (b), respectively.

we show the homodyne spectra of the reflected probe beam with same parameters as in Fig. 2.9(a) and with probe beam normalised detuning of $|\Delta|/\kappa = 0.25$. The three main noise contributions in the homodyne PSD (black) are thermal noise (blue), frequency noise from the probe beam (orange) and from the trapping beam (green). The other contributions are not shown. Of particular importance, the effect of frequency noise can be seen both in terms of phonon number occupancy in Fig. 2.9(a) and significant reduction in detection sensitivity as shown in Fig. 2.10(a). In Fig. 2.10(b), we show the homodyne spectra of the reflected probe beam with same parameters as in Fig. 2.9(b) and with probe beam normalised detuning of $|\Delta|/\kappa = 3$. The main contributions to the homodyne PSD are input losses from the probe beam (blue), photon recoil from the trapping beam (orange) and vacuum losses from the probe beam (green).

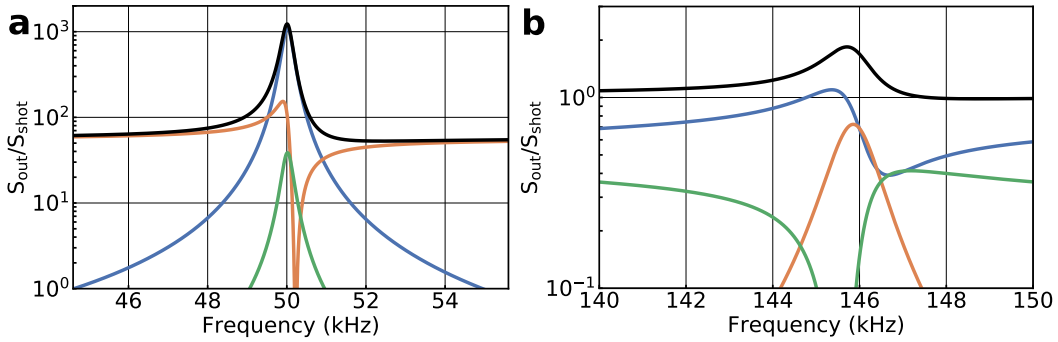

Figure 2.10: Theoretical reflected output homodyne spectra normalised to the shot noise level corresponding to the two cases shown in Fig. 2.9(a) and (b) shown in black. Only the three main noise contributions to the spectra are shown. (a) Thermal contribution is shown in blue, frequency noise from the probe beam in orange and frequency noise from the trapping beam in green. (b) Thermal contribution is shown in blue, noise associated with the input losses on the probe beam in orange and vacuum losses from the same beam in green.

2.6 Summary

To summarise, we have introduced in this chapter theoretical elements to describe the optomechanical interaction between a nanosphere and an intracavity mode. Both theories of the mechanical and optical oscillators were reviewed in the classical and quantum regimes. We were then able to detail the Hamiltonian governing the dipole interaction. Among others, scattering losses, recoil heating and absorption were described. In those experiments where the frequency of interest is low ($\omega_m/2\pi \approx 100\,\mathrm{kHz}$), laser classical noise has to be taken into account. We described how classical intensity noise and frequency noise can be incorporated into the model of the experiment. Then we derived expressions for both light and nanosphere dynamics (Langevin equations) as well as spectra of the particle position and optical field homodyne quadratures. Lastly, we used this model with typical experimental parameters to illustrate among others the need for taking into account laser frequency noise, responsible for both heating of the mechanical motion and lower detection signal-to-noise ratio. Also discussed were reasonable experimental parameters where the ground state could be achieved.

Chapter 3

Paul trap theory and design

Paul traps are a key tool for quantum science and technology [75–77]. They have been utilised for the creation of stable atomic clocks and for the demonstration of important protocols in quantum computation and information [77, 78]. In these traps, atomic and molecular ions can be laser cooled to their ground state and trapped in isolation for weeks. Key to their utilisation has been that a deep and stable low noise electrical potential can be readily created. A growing number of companies are currently using this platform to develop quantum computers[1]. In this chapter we review the general theory of Paul traps. We then discuss our trap architecture that is specifically designed for levitated optomechanics experiments. Finally, we outline the loading procedure which combines electrospray ionisation and a quadrupole guide which delivers a charged nanoparticle to the trap.

3.1 Paul trap theory

Paul traps are used to stably levitate charged objects confined in three dimensions. The first of Maxwell's equations (Gauss's law) states that, in the absence of charge density, the electric field $\boldsymbol{E}$ must follow $\operatorname{div} \boldsymbol{E} = 0$. In order to trap charged objects, the field has to obey $\operatorname{div} \boldsymbol{E} < 0$ which corresponds to the electric field lines pointing towards the trap centre. With this condition, if the charged particle moves away from the trap centre, a force along the electrical field lines will bring it back towards the centre. Since this cannot be achieved with a DC electric field, Wolfgang Paul had the ingenious idea of applying an AC field which creates an equivalent static pseudopotential. Several architectures can be used depending on the experimental needs but all follow similar dynamics (Mathieu dynamics). Here we discuss linear

[1] IonQ, Honeywell, Alpine Quantum Technologies, Universal Quantum...

Paul traps which consist of four electrodes (rods) as the one shown in Fig. 3.1. The trap can be driven either symmetrically or asymmetrically. Symmetric driving corresponds to applying the same AC voltage on two electrodes along a diagonal that is out of phase on the other two. Asymmetric driving corresponds to applying the same AC voltage on two electrodes and keeping the other two at ground. The AC field applied on the rods confines the charged nanoparticles in the radial plane of the trap. DC voltages can be applied on both ends of the trap on so-called endcaps to confine nanoparticles along the trap axis.

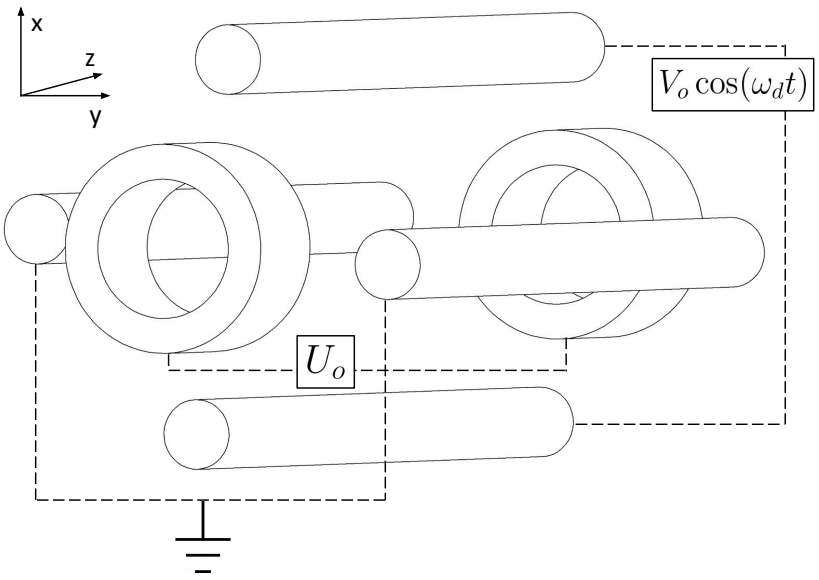

Figure 3.1: Diagram of a linear Paul trap with four electrodes (rods). The same AC voltage of amplitude V_o and frequency ω_d is applied on two opposite rods while the other two are grounded (asymmetric driving). The particle is confined along the z-axis by applying a DC voltage U_o on both endcaps.

3.1.1 Mathieu dynamics

The Mathieu equations are derived here assuming asymmetric driving where a voltage $V_o \cos(\omega_d t)$ is applied on two opposite rod electrodes, where ω_d is the drive frequency. The field close to the trap centre can be approximated as perfectly quadratic. This is in practice modelled and quantified by an efficiency parameter η which can be seen as a quadratic fit to the field near the trap centre [79, 80]. This will be shown in the section below on the trap designs where we calculate the efficiency η of our traps. Within the coordinate axis defined by the trap diagonals (see Fig. 3.1), the voltage $V_{AC}(x, y, t)$ in two dimensions within the quadratic approximation

reads:

$$V_{AC}(x,y,t) = \frac{V_o}{2}\left(1+\eta\frac{x^2-y^2}{r_o^2}\right)\cos(\omega_d t)\,, \tag{3.1}$$

where r_o is the shortest distance between the centre of the trap and the electrodes providing the AC field. A DC voltage U_o is applied on both endcaps to confine the nanoparticles along the z-axis. Similar to the AC field, a geometric efficiency factor κ is used to compare the field to a quadratic one. The distance between the centre of the trap and the endcap electrodes is defined as z_o. The endcaps lead to the DC potential V_{DC}:

$$V_{DC}(x,y,z) = \frac{\kappa U_o}{z_o^2}\left(z^2-\epsilon_t x^2-(1-\epsilon_t)y^2\right). \tag{3.2}$$

The static potential given by the endcap in the transverse direction of the trap is described (in the quadratic approximation of the field) by the ellipticity parameter ϵ_t. Only two parameters (κ and ϵ_t) are needed to describe the field since it has to follow from the condition $\operatorname{div}\boldsymbol{E}=0$ stated above. In the case where the trap is symmetric in the x-y plane we have $\epsilon_t = 0.5$. The Coulomb force $\boldsymbol{F}$ on a particle of charge Q reads

$$\boldsymbol{F}(t) = -Q\nabla\left(V_{AC}(x,y,t)+V_{DC}(x,y,z)\right). \tag{3.3}$$

We can write the Newtonian dynamics along each axis, $i = x,y,z$, in a canonical Mathieu equation form where u_i stands for the amplitude of the motion along the ith direction. We can then define Mathieu stability parameters a_i and q_i that quantify the stability of the particle motion in the trap, given by the AC and DC fields, respectively. It is important to include the effect of stray electric fields E_i as well. We denote the nanosphere mass by m. The canonical Mathieu equation reads

$$\ddot{u}_i + \left(a_i + 2q_i\cos(\omega_d t)\right)\frac{\omega_d^2}{4}u_i = \frac{Q\,E_i}{m}\,, \tag{3.4}$$

with the following expression for the stability parameters along each axis

$$q_x = -q_y = \frac{Q}{m}\frac{2\eta V_o}{r_o^2\omega_d^2} \quad \text{and} \quad q_z = 0\,, \tag{3.5}$$

$$a_x = -\frac{Q}{m}\frac{8\epsilon_t\kappa U_o}{z_o^2\omega_d^2}\,, \quad a_y = -\frac{Q}{m}\frac{8(1-\epsilon_t)\kappa U_o}{z_o^2\omega_d^2} \quad \text{and} \quad a_z = \frac{Q}{m}\frac{8\kappa U_o}{z_o^2\omega_d^2}\,. \tag{3.6}$$

The trapped particle feels an effective ponderomotive pseudopotential $\phi(x,y) = \frac{Q}{4m\omega_d^2}|\nabla V(x,y)|^2$ given by the AC field in the $x-y$ plane [80]. In the common

case of operation where $|a_i| \ll 1$ and $|q_i| \ll 1$, the solution of the above equation can be approximated to [81]:

$$u_i(t) \approx (u_{o,i} + u_{1,i}\cos(\omega_i t + \phi_i))\left(1 + \frac{q_i}{2}\cos(\omega_d t)\right), \tag{3.7}$$

where we have included a phase ϕ_i determined by the initial position and velocity of the nanosphere in the trap and

$$\omega_i \approx \frac{\omega_d}{2}\sqrt{a_i + \frac{1}{2}q_i^2} \quad \text{and} \quad u_{o,i} \approx \frac{Q\,E_i}{m\omega_i^2}. \tag{3.8}$$

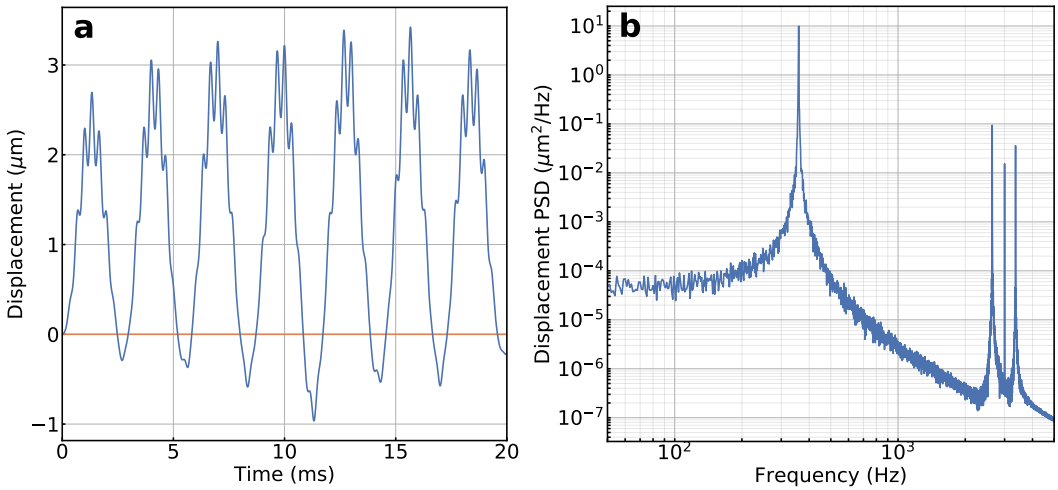

Figure 3.2: (a) Time trace of the position of the nanosphere in one radial direction obtained with a stochastic simulation of the 1-D Mathieu equation. The slow motion of large amplitude corresponds to the secular motion at $\omega_i/2\pi = 358\,\text{Hz}$. The fast oscillations correspond to both micromotion and excess micromotion. For this simulation, the mean position of the particle is offset by an additional DC field of magnitude $10\,\text{V/m}$ to demonstrate the effect of an additional static force. (b) Power spectral density of the displacement. The time trace shown in (a) is a subset of the time trace used to calculate the PSD. The three different motions can clearly be seen: secular motion at ω_i, micromotion at $\omega_i - \omega_d$ and $\omega_i + \omega_d$ and excess micromotion at $\omega_d/2\pi = 3\,\text{kHz}$. It is worth noting that the micromotion has a linewidth identical to the secular motion. The peak corresponding to the excess micromotion has no linewidth as expected since corresponding to a driven motion. The parameters for this simulation are charge-to-mass ratio of $0.7\,\text{C/kg}$, bath temperature of $300\,\text{K}$, mass of $5.6 \times 10^{-17}\,\text{kg}$, stability parameters $a = 0.01$, $q = 0.3$, AC drive frequency $\omega_d/2\pi = 3\,\text{kHz}$ and gas damping $\gamma_m/2\pi = 0.34\,\text{Hz}$ which corresponds to a pressure of $10^{-3}\,\text{mbar}$.

Three different motions arise from the above equation. First, a so-called secular motion (also called macromotion) of amplitude $u_{1,i}$ and frequency ω_i: $u_{1,i}\cos(\omega_i t +$

ϕ_i). This motion is the one given by the AC pseudopotential and is caused by the rotation of the AC field. Along the z-axis it is typically thermal, that is to say incoherent and at equilibrium with the bath temperature T_b. This is also the case for the motion in the radial direction when the condition $|a_i| \leq q_i^2 \, (\text{with} \, i = x, y)$ is satisfied, which leads to $\langle u_{1,i}^2 \rangle = \frac{k_B T_b}{m \omega_i^2}$. The second type of motion is given by $u_{1,i} \frac{q_i}{2} \cos(\omega_i t + \phi_i) \cos(\omega_d t)$, and is called micromotion. The pseudopotential (or macromotion) leads to a periodic excursion of the particle away from the trap centre. This leads to two fast oscillations proportional to the macromotion amplitude $u_{1,i}$ at frequencies $\omega_d + \omega_i$ and $\omega_d - \omega_i$. Lastly, in the case of an additional DC field E_i, the particle's mean position is not in the centre of the AC field which leads to a motion $u_{o,i} \frac{q_i}{2} \cos(\omega_d t)$ called excess micromotion. Those three motions can be seen in both time and frequency domains in the simulations shown in Fig. 3.2. They have been discussed in detail for ion traps since their minimisation is critical in many instances [81]. Indeed, these motions can lead to several undesirable effects such as reduced efficiency in Doppler-cooling or broadening of atomic transitions. Cooling of the thermal secular motion is generally done by combining Doppler-cooling and sideband cooling. The standard micromotion is reduced by cooling the secular motion (since its amplitude is proportional to the secular motion). As mentioned above, the excess micromotion is caused by additional stray fields which perturb the potential. They can be in practice compensated by applying voltages on additional electrodes in order to bring the average position of the particle to the centre of the AC field: $u_{o,i} \to 0$. Similarly, and relevant to the work presented here, excess thermal motion of the nanosphere (macromotion) can lead to an undesired modulation in the experiment. In Section 8.2, we demonstrate cooling of the secular motion by applying feedback on one of the trap electrodes. Furthermore, we apply DC voltages on trap electrodes to reduce the excess micromotion (see Section 4.6.3).

We can now discuss the advantages and drawbacks of using symmetric and asymmetric driving in the linear Paul trap configuration. Driving the trap symmetrically offers the advantage of needing half the voltage to provide an equivalent trap depth. In this case the Mathieu dynamics are identical with an efficiency parameter that is twice higher. The fact that the electrodes are finite in size leads to a ponderomotive potential along the trap axis. While cancelled when using symmetric

driving, it is not the case in the asymmetric case. The main drawback of using symmetric driving is the fact that the phase difference between the two signals needs to be well under control in order to prevent excess micromotion [81]. In most of the work shown below, we use asymmetric driving.

3.1.2 Stability diagran

We now discuss the stability of the Mathieu equations shown in Eq. 3.4 which determines if a charged nanosphere remains trapped. In the case of a linear Paul trap, the radial motion is governed by the Mathieu equation whereas the axial motion is determined by the endcap voltages (in the z-direction we have $q_z = 0$). Whereas this is true in the case of symmetric driving, in the antisymmetric case, this is only a valid approximation when the AC ponderomotive contribution can be shown to be negligible. Depending on the values of the stability parameters in the radial direction, the motion can be stable or unstable [82]. This is typically illustrated in a stability diagram [83] shown in Fig. 3.3(a). The blue region corresponds to values of the a and q parameters which lead to a stable trapped motion. The a parameter needs to be negative to provide stable confinement in the axial direction which corresponds to a positive endcap voltage for a positively charged nanosphere. In practice, a is very small ($|a| < 0.01$) because the effect of the endcap voltages on the effective radial potential is negligible. For the motion to be stable in this case, the q stability parameter must satisfy $0 < q < 0.91$ (see Fig. 3.3(a)). It is worth discussing the operation of the quadrupole trap as a mass-spectrometer. While not relevant to the trap itself, we use a quadrupole guide to assist the trap loading mechanism, discussed in Section 3.3.1. This configuration is the one used in mass-spectrometry to filter out particles depending on their charge-to-mass ratios [84]. The difference of this configuration is to apply the same DC voltage U_1 on two opposite rods. We denote by U_{eff} the effective potential proportional to U_1 corresponding to the quadratic expansion near the trap centre. Since in the mass-spectrometer configuration this potential overcomes the one provided by the endcaps, the a parameters are very well approximated by (assuming $\epsilon_t = 0.5$):

$$a_x = -a_y = -\frac{Q}{m}\frac{4U_{eff}}{r_o^2\omega_d^2}\,. \tag{3.9}$$

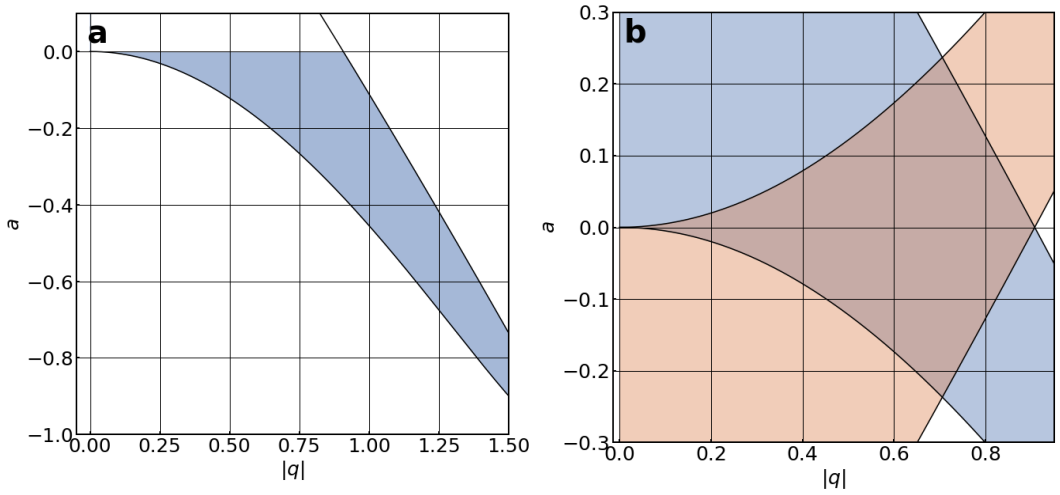

Figure 3.3: (a) Stability diagram of a linear Paul trap. The motion is stable for parameters a and q lying inside the blue region. (b) Stability digram when the trap is operated as a mass-spectrometer. The motion is stable where the blue and orange regions overlap.

We have therefore in this case $a_y = -a_x$ and $q_y = -q_x$ and the stability diagram is therefore made by the overlap of two identical (same as the one shown Fig. 3.3(a)) but opposite diagrams as shown in blue and orange in Fig. 3.3(b). There are several stable regions in this case. The main one corresponds to the area of overlap between the blue and orange regions.

In the above, we have not included the effect of the gas damping γ_m and of the Brownian motion. This makes the set of Mathieu equations (Eq. 3.4) only valid over a time $2/\gamma_m$ which corresponds to the timescale over which the motion loses coherence (see Section 2.1.1). Furthermore, the gas damping can easily be included in Eq. 3.4. A new stability parameter b_i can then be defined as $b_i = a_i - \frac{\gamma_m^2}{\omega_d^2}$ to replace the initial a_i parameter [85]. At pressures lower than 1 mbar we have $|b_i| \ll 1$ and the effect of the damping on the trap stability becomes negligible. At high pressure, this effect dominates and its consequence is to greatly increase the stability domain shown in Fig. 3.3.

3.2 Paul trap designs

In this section, we discuss two main designs of Paul traps for levitated optomechanics experiments. Several criteria were taken into consideration to design those traps. First, to be small enough to fit within an optical cavity that is 14.6 mm long and secondly, to have good control over the position of the nanosphere for compensating

the micromotion. Lastly, a 3-D access to the centre of the trap is required: one for the cavity axis, one for loading and one for direct imaging of the trap. In order to achieve all those requirements, a linear Paul trap consisting of four rod-electrodes as shown in Fig. 3.1 seemed to be the most convenient solution.

3.2.1 Printed circuit board trap

A first design of Paul trap using a printed circuit board (PCB) was reported in Ref. [86]. The advantage of using a PCB is the flexibility given by the printed tracks. In this experiment, NV centres were trapped and detection of the spin state was realised by observing their fluorescence. To achieve greater detection efficiency the trap was designed out of one single board with one rectangular hole in its middle corresponding to the centre of the trap. Tracks on both sides were used to define the field. For our PCB design, we use the same geometry but bring the two PCB on top of each other separated by 1.4 mm, see Fig. 3.4. The two tracks correspond to the rods shown in Fig. 3.1 (the tracks are elongated along the z-axis). The tracks corresponding to the endcaps are the ones elongated along the y-axis. The copper layers have a thickness of 70 μm. The distance between two diagonally opposite AC electrodes is 1.6 mm while the distance between the endcaps is 5.8 mm. The efficiency parameters and geometric factors are $\eta = 0.698$, $\epsilon_t = 1.31$, $\kappa = 0.382$, $r_o = 1.08$ mm and $z_o = 2.99$ mm. Though demonstrating stable trapping, this trap was not used

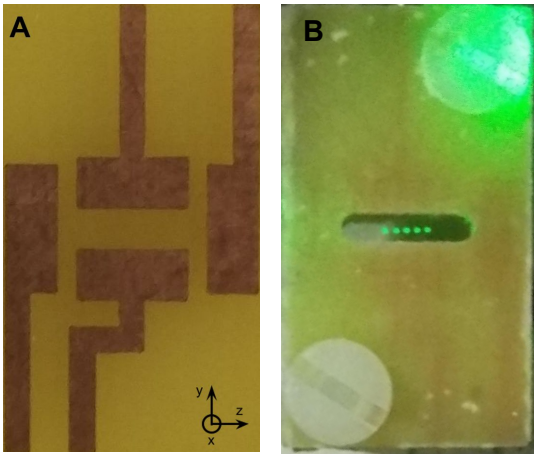

Figure 3.4: (a) Picture of the PCB tracks of one of the two identical boards used for the trap. Two of the four tracks used for the AC field are the ones elongated along the z-direction. The other two electrodes are used as endcaps. (b) Trap formed by placing two identical PCB (shown in (a) with a hole drilled in the middle) on top of each other. The two boards are separated with a spacer 1.4 mm thick. Five nanospheres can be seen in the centre of the trap.

for later experiments. The main drawback of this trap is the fact that the dielectric of the PCB material is too close to the trap centre. Indeed, it is as close as the AC electrodes themselves since the faces normal to the y-axis within the drilled hole are not plated. Because of this, charged nanospheres accumulate on the dielectric surfaces during the loading process which leads to a different equilibrium position of the nanosphere in the trap. After having loaded the trap around ten times it needs to be discarded as too many charges have built up on the dielectric preventing any loading. Similar issues have been reported in the ion trap community where accumulation of ions on the electrodes can have a significant effect on the trapping potential [87].

3.2.2 Miniature linear Paul trap

3.2.2.1 Geometry

In order to still work with a linear Paul trap, while minimising the amount of dielectric material near the centre, we opted for a miniature linear Paul trap. We are still using PCB material but it is kept further away from the trap centre. The PCB is used this time as a trap mount as well as for the electrical connections and endcaps. A schematic diagram of the trap (with the right proportions) is shown in Fig. 3.1 and a picture in Fig. 3.5(a). The four rods constituting the trap are mounted on a printed circuit board (PCB) whose layout is shown in Fig. 3.5 (b) and (c). The stainless steel electrodes of the trap are rods of 0.5 mm diameter which sit into the plated holes of the PCB. One plated through hole on each PCB in the middle of the rods is used as an endcap. The end cap geometry is a ring in order to let the cavity mode go through and therefore be superimposed with the trap axis. The two PCB boards (and therefore the endcaps) are kept at a distance of 7.0 mm. Both the traces and the holes are gold coated to minimise patch potentials [88]. Using a PCB to support the electrodes allows flexibility in making the electrical connections to the rods and keep to a minimum their effect on the potential of the trap. The substrate used here[2] is a ceramic-filled woven glass that is compatible with ultra-high vacuum [89, 90]. The PCB tracks are separated by a distance of at least 225 μm to avoid a voltage breakdown [91] at any pressure with the typical ~ 500 V peak-to-peak AC voltages applied. The efficiency parameters (see next section for

[2]The PCB is a RO4003C by Rogers.

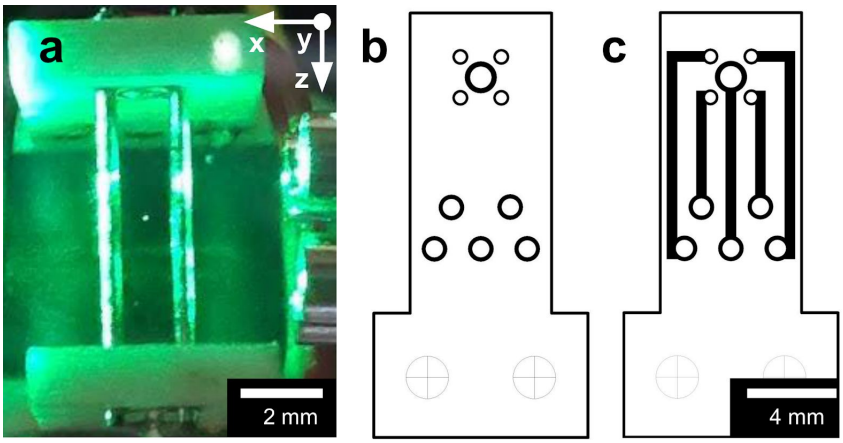

Figure 3.5: (a) An image of the linear Paul trap loaded with a nanoparticle in its centre. (b) The PCB layout of the internal side of the trap. The five holes at the top of the layout are used for the trap connections. The pad in the centre of the five holes is used as an endcap. The other four holes are used as both holders and electrical connections to the four rods constituting the trap. Tracks made out of gold coated copper are shown in black. (c) The PCB layout on the external side of the trap. The connections to the PCB board are realised on the lower part of the PCB using the five lower holes.

calculation) and geometric factors are $\eta = 0.818$, $\epsilon_t = 0.5$, $\kappa = 0.086$, $r_o = 1.1\,\text{mm}$ and $z_o = 3.54\,\text{mm}$.

3.2.2.2 Efficiency parameters

In the previous section we have introduced two efficiency parameters η and κ that quantify how quadratic the potential is near the centre of the trap. We follow here the methods discussed in Ref. [79, 80] to calculate those two coefficients by using finite-element-method simulations. To evaluate η, we carry out a 2D finite element method simulation (FEM) of the potential near the centre of the trap in the transverse direction of the trap, which is shown in Fig. 3.6. The efficiency parameter η is calculated by comparing the potential to a perfect quadrupole potential $\phi(x,y) = \phi_o(x^2 - y^2)/r_o^2$ (for axis definition see Fig. 3.1). Near the centre of the trap, the simulated field $\phi'(x,y)$ can be written as an expansion in cylindrical harmonics where $\phi'(r,\theta) = \sum_{m=1}^{\infty} C_m\phi_{cm} + \sum_{n=1}^{\infty} S_n\phi_{sn}$, with $\phi_{cm} = (r/r_o)^m\cos(m\theta)$ and $\phi_{sm} = (r/r_o)^n\sin(n\theta)$. It can be shown that given the symmetries of the potential distribution, the smallest coefficient different from zero is C_2. This coefficient (and the higher order coefficients) is calculated as the projection of the simulated potential onto the spherical basis: $C_2 = I_{a2}/I_{b2}$ with $I_{am} = \int_{-\pi/4}^{\pi/4}\int_0^{r_o}\phi'\phi_{cm}rdrd\theta$ and $I_{bm} = \int_{-\pi/4}^{\pi/4}\int_0^{r_o}\phi_{cm}^2 rdrd\theta = \pi r_o^2/8(m+1)$. In the case of a perfectly quadrupole field

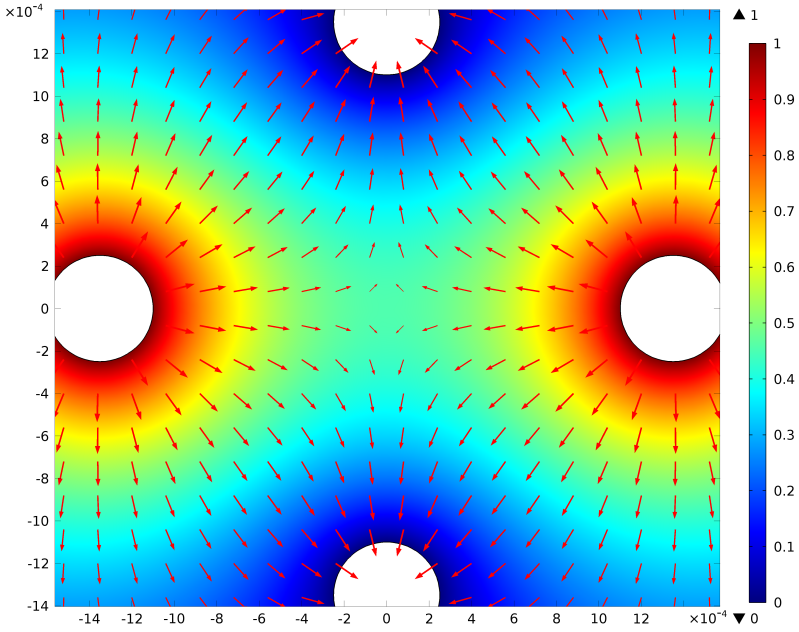

Figure 3.6: 2D-simulation of the voltage in the trap radial plane performed using a finite element method software. The four rods constituting the trap are the four white holes. We apply 1 V (red) to two opposite cylinders and ground (blue) the other two. The local electric field is shown by red arrows (logarithmic scale for the amplitude).

$\phi'(x,y)$, we would get $\eta = C_2 = 1$. Here we obtain $\eta = 0.818$. This value is consistent with a quadratic fit of the pseudopotential near the centre of the trap (see Fig. 3.7(a)). The efficiency parameter κ is more straightforward to calculate since the potential provided by the endcaps is static. A 3D FEM simulation is this time carried out. A simple quadratic fit near the centre of the trap, as shown in Fig. 3.7(b), gives an efficiency parameter of $\kappa = 0.086$ with the convention: $V_{DC}(z) = \frac{\kappa U_o}{z_o^2} z^2$ with $z_o = \sqrt{l_1^2 + l_2^2} = 3.536\,\text{mm}$, with $l_1 = 3.5\,\text{mm}$ corresponding to the distance between the centre of the endcap and the trap centre, and $l_2 = 0.5\,\text{mm}$ the endcap radius.

3.2.2.3 Voltage noise

Voltage noise, which is discussed in great detail by the ion trap community, needs to be assessed as it can lead to motional heating of the nanosphere. Whereas patch potentials can be challenging to assess, the electric field noise given by the different voltage sources can be more easily modelled. By carrying out simulations similar to the ones presented above, one can obtain how the voltage noise on the electrodes is transduced into electric field noise [92]. When considering voltage noise given by one rod only near the centre of the trap and expanded to the first order, we get

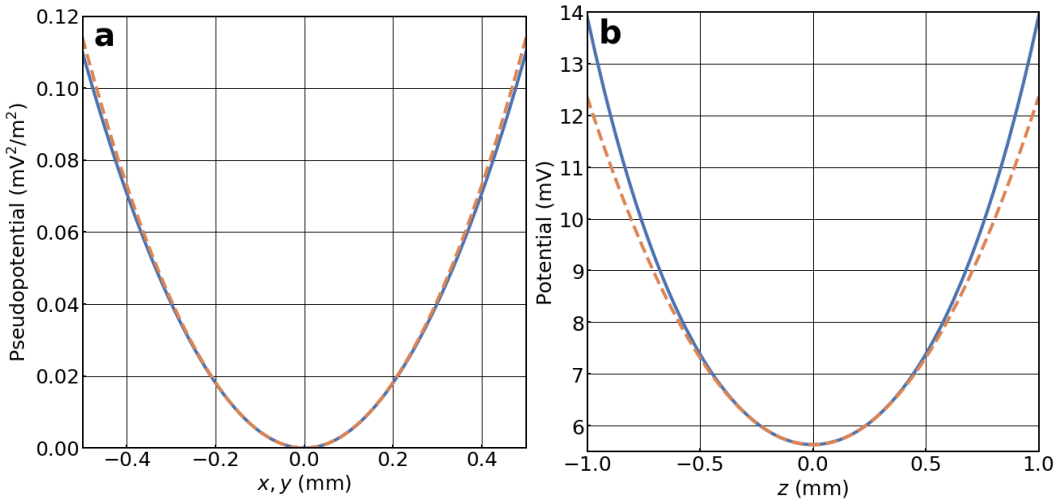

Figure 3.7: (a) Simulation of the pseudopotential in the transverse direction of the trap. The simulation is done in the asymmetric case with 1 V applied on two opposite rods. The ponderomotive pseudopotential envelope $|\nabla V(x,y)|^2$ is shown in blue. The dashed orange line corresponds to a quadratic fit of the potential giving a coefficient $\eta = 0.817$ consistent with the one found with the integration method. Deviations from a pure quadratic potential can be noticed from a distance of 0.3 mm away from the trap. (b) Simulation of the potential along the endcap direction (z-axis) with 1 V applied on both endcaps. A quadratic fit of the potential near the centre of the trap is shown in orange.

$E(x) = V(1/D + \bar{x}/D_1)$ with V the voltage applied on the rod, $\bar{x}$ the particle mean position, $D = 3.3\,\text{mm}$ and $D_1 = -2.9\,\text{mm}^2$ (with the x-axis defined on Fig. 3.1 and $x = 0$ corresponding to the centre of the trap). When the particle is in the centre of the trap, the excess force noise is given by $S_F = Q^2 S_V / D^2$ where S_V is the voltage noise of the source. In the case where the noise sources are correlated on two opposite rods, they cancel each other out in the centre. The first order expansion gives then $E(x) = V|\bar{x}|/D_1$ with $D_1 = -1.5\,\text{mm}^2$. Lastly, we consider the case of correlated noise on both endcaps since we are using the same voltage source for both endcaps. The electric field noise projected onto the axial direction is $E(z) = U\bar{z}/D_1$ with U the same voltage applied on both endcaps and $D_1 = -71\,\text{mm}^2$ (with $z = 0$ corresponding to the centre of the trap).

3.2.2.4 Trap depth

The trap depth can be directly estimated from the simulations shown in the previous section. First in the radial direction, we estimate it by carrying out a simulation of the ponderomotive pseudopotential between the two RF rods of the trap. This corresponds to the x-axis or equivalently to the y-axis as the trap is symmetric

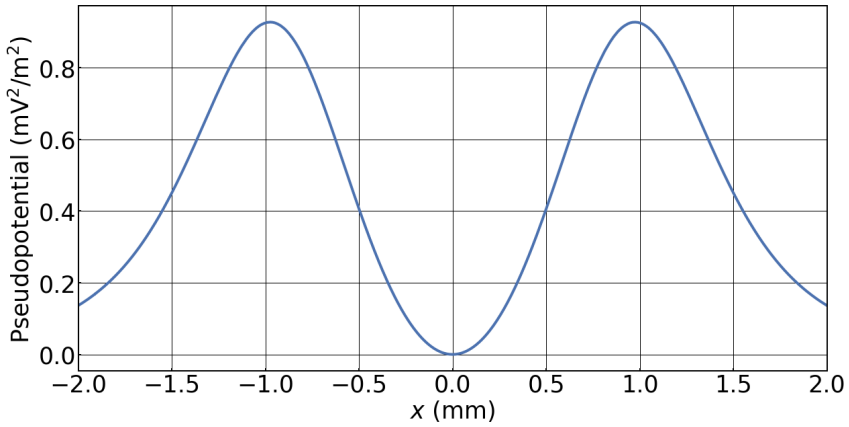

Figure 3.8: Simulated pseudopotential $|\nabla V(x,y)|^2$ along the x-axis. A voltage of 1 V is applied on two diagonally opposed rods.

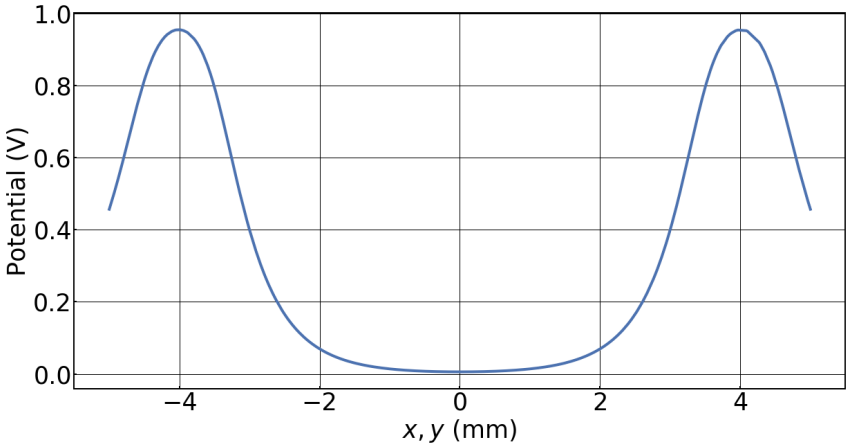

Figure 3.9: Simulated potential provided by the endcaps along the trap axial direction (with 1V applied on both endcaps).

(with this time the axis definition given in Fig. 3.5(a)). The trap depth can then be estimated following from the pseudopotential $\phi(x,y) = \frac{Q}{4m\omega_d^2}|\nabla V(x,y)|^2$. We show the envelope corresponding to the pseudopotential in this trap in Fig. 3.8. We typically trap silica nanospheres of mass $\sim 5\times10^{-17}$ kg with $\sim$200 individual charges. The trap is typically operated with a drive frequency of $\omega_d/2\pi = 3$ kHz and voltage of 500 V(peak-to-peak). This gives us in this case a trap depth in the radial direction of $\sim 10^{-15}\,J \approx 5\times10^3\,eV$. This is equivalent to a velocity of $\sim$ 5m/s or a temperature of 10^8 K. In Fig. 3.9, we show the voltage along the trap axis from which we estimate a trap depth of $\sim 10^{-11}\,J$ with a typical 100 V applied on both endcaps. Lastly, since we are driving the trap asymmetrically, we expect some ponderomotive confinement along the trap axis that is roughly one order of magnitude smaller than

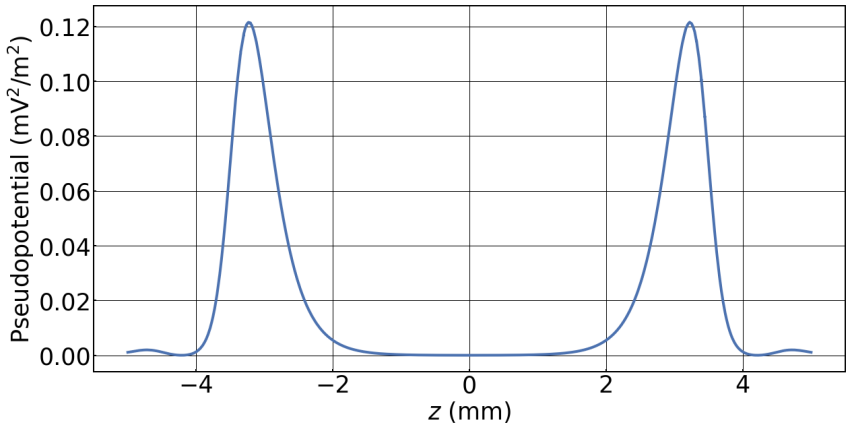

Figure 3.10: Simulated pseudopotential $|\nabla V(x, y, z)|^2$ along the z-axis. A voltage of 1 V is applied on two diagonally opposed rods.

along the radial direction. Given our typical parameters along the trap axis, this ponderomotive potential is overwhelmed by the one provided by the endcaps, as it can be seen in Fig. 3.10.

3.3 Paul trap loading

Reliable loading of nanoparticles is critical to the experiment. Extensive research has been carried out by different groups within the community in order to achieve specific needs such as loading in vacuum, minimising contamination of nanoparticles or controlling the number of charges. Several groups use portable nebulisers where a piezo-actuator pushes liquid through a fine mesh which creates an aerosol. The issue with this method used at atmospheric pressure is the possible contamination of the vacuum chamber and, critically, of the cavity mirrors. This can be overcome by trapping a nanoparticle in an optical tweezer in a first vacuum chamber using the nebuliser, and then transferring it to another optical trap in another vacuum chamber [93]. Another method uses a piezo-disk speaker where nanoparticles are first deposited on its surface and are launched when the speaker is driven on resonance [38]. The attractiveness of this method is that it can be used in medium vacuum ($\sim$1 mbar). Its limitation is that it becomes extremely challenging to launch sub-micron spheres from the speaker as an acceleration of $\sim 2 \times 10^8\,\mathrm{m/s^2}$ is needed to overcome the Van der Walls forces [38, 68]. Furthermore, the number of charges provided with this method is relatively small ($\sim$ 10 individual charges at best) [46]. A recent method has been demonstrated at ultra-high-vacuum where nanoparticles are first

dried on an aluminium foil. The acoustic wave created by a laser pulse applied to the back of the foil transfers enough kinetic energy to the nanospheres to launch them [94]. The Paul trap field is triggered so that it is switched on when particles are in the vicinity of the trap. Alongside the piezo-disk approach, an advantage of this method is that the vacuum chamber is not contaminated with solvents.

3.3.1 Electrospray

We use electrospray ionisation to charge the nanoparticles. This is used widely in mass-spectrometry of smaller particles [95, 96]. It consists in charging a solution containing a mixture of solvent and nanoparticles. When the voltage applied on the solution is high enough, the charges are repelled and the surface tension is overcome, which creates an aerosol. As the solvent evaporates, it leaves charges on the spheres. This method enables us to trap directly at a pressure of $\sim 10^{-1}$ mbar. Here, silica nanospheres are typically suspended in ethanol at a concentration of 10 μg/mL. Prior to loading, the solution is left in an ultrasonic bath for 20 minutes to restore monodispersion of nanospheres. A schematics of the loading process can be seen in Fig. 3.11 and a picture of the set-up is shown in Fig. 3.12. We apply a +1.8 kV voltage on a needle with a 100 μm internal diameter. The polarity of this voltage determines the sign of the overall charge on the nanosphere. We achieve similar charge-to-mass

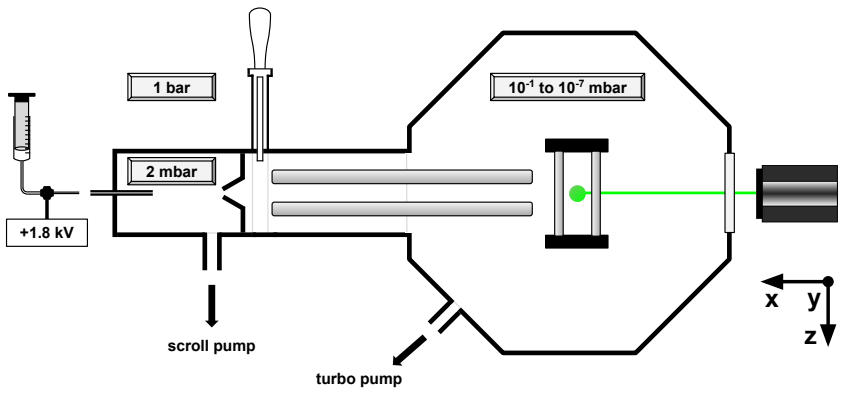

Figure 3.11: Schematic of the loading process. Nanoparticles suspended in ethanol are electrosprayed at atmospheric pressure. The aerosol is entrained into the first pumping stage which is kept at a pressure of 2 mbar. The charged nanoparticles are directed through a beam skimmer and enter the main vacuum chamber, which is kept at a pressure of $\sim 10^{-1}$ mbar during the loading phase. It is then guided inside an electric quadrupole guide towards the trap. The nanoparticle is illuminated with a green diode laser along the x-axis. The motion of the particle is imaged in the x-z plane with a CMOS camera placed along the y-axis (see Chapter 4).

ratios in either case. The aerosol of particles is entrained into a capillary tube that leads directly into a first pumping stage. The capillary is 5 cm long with a 250 μm internal diameter. This first vacuum stage is kept at a pressure of approximately 2 mbar by directly connecting it to a scroll pump. The flux of particles travels through a skimmer with a 0.4 mm aperture. The skimmer isolates the first stage from the main chamber which is initially kept at a pressure of $\sim 10^{-1}$ mbar during the loading phase. Once in the main chamber, some particles are guided through a 20 cm long quadrupole guide and their motion is damped by collisions with the surrounding gas so that the particles have low enough energy to be captured by the Paul trap where further dissipation occurs [97]. Given the experimental parameters, we can estimate the velocity of the air molecules and therefore of the nanoparticles after the entrance capillary. Given that at this pressure the flow is molecular, we estimate the conductance of the tube to be $1.35 \times 10^{-6}\, \bar{p}\, \frac{d_c^4}{l_c}$ (l/s), with the capillary diameter $d_c = 0.25$ mm, length $l_c = 5$ cm and average pressure $\bar{p}$ [98]. We expect the nanospheres to exit the skimmer at a velocity $\sim$100 m/s. At 5×10^{-1} mbar, given our typical trap parameters and charge-to-mass ratio of 0.5 C/kg, the nanosphere will end up with a velocity between 5 and 15 m/s which is the requirement for it to be trapped. A particle with a velocity of ~ 5 m/s has a kinetic energy that corresponds to the effective depth of our trap, as described above. A quadrupole trap (that we

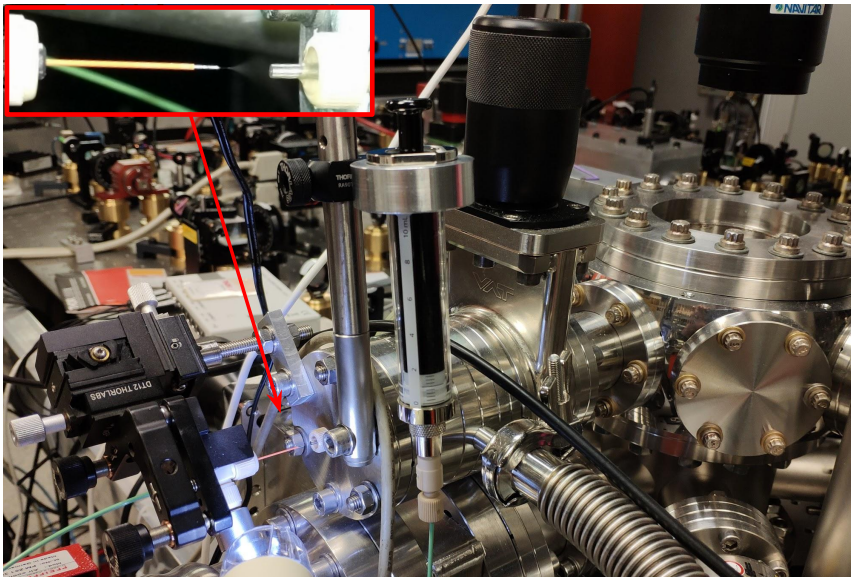

Figure 3.12: Picture of the set-up used for the loading phase. See caption of Fig. 3.11. Inset: Aerosol created by the electrospray.

call guide) is used to increase the flux of particles reaching the trap and can be seen on the right-hand side of the Paul trap in Fig. 3.5 (a). Its end is placed $\sim 3\,\text{mm}$ away from the Paul trap. By operating the guide in a mass filter configuration [84], where a high DC voltage is applied onto two electrodes, one can select more efficiently a given charge-to-mass ratio, as discussed in the next section. Note that since the trap and the guide have different geometries, the effective stability region is further reduced, as discussed in the next section. We typically trap particles with charge-to-mass ratios in the range $0.05 < Q/m < 2\,\text{C/kg}$. Once the trap is loaded, the guide is grounded to avoid any excess micromotion caused by the AC field of the guide. The guide is made of stainless steel rods of 2.5 mm diameter. The distance between the centre of the guide and the rod is the same as the one used for the miniature linear Paul trap $r_o = 1.1\,\text{mm}$, which gives an efficiency parameter of $\eta = 1.0$. We typically apply an AC voltage $V_o = 250\,\text{V}$ at $\omega_d/2\pi = 3.0\,\text{kHz}$ on the trap and guide from the same source[3]. A typical endcap voltage is $100\,\text{V}$ [4].

3.3.2 Charge-to-mass ratio selection

As briefly mentioned above, by operating the guide as a mass spectrometer by applying additional DC voltages on two opposite rods, we can select specific charge-to-mass ratios. Let us consider the trap (as opposed to the guide) stability parameters discussed above. These are given by (the a_i stability parameters are here neglected, since they are typically very small)

$$q_x = -q_y = \frac{Q}{m}\frac{2\eta V_o}{r_o^2\omega_d^2} \quad \text{and} \quad q_z = 0\,. \tag{3.10}$$

The quadrupole guide is operated with a same AC drive voltage. In addition, a DC voltage U_g is applied on two opposite rods. The efficiency parameters of the guide are given by (both trap and guides have same geometric factor $r_o = 1.1\,\text{mm}$.)

$$q_{g,x} = -q_{g,y} = \frac{Q}{m}\frac{2V_o}{r_o^2\omega_d^2}\,, \quad q_{g,z} = 0\,, \tag{3.11}$$

$$a_{g,x} = -a_{g,y} = -\frac{Q}{m}\frac{4U_g}{r_o^2\omega_d^2} \quad \text{and} \quad a_{g,z} = 0\,. \tag{3.12}$$

[3] Wave station 3142 from TeledyneLeCroy is used as signal generator. The signal is then amplified with the high voltage amplifier TREK 2220

[4] Signal provided by MDT694A from ThorLabs.

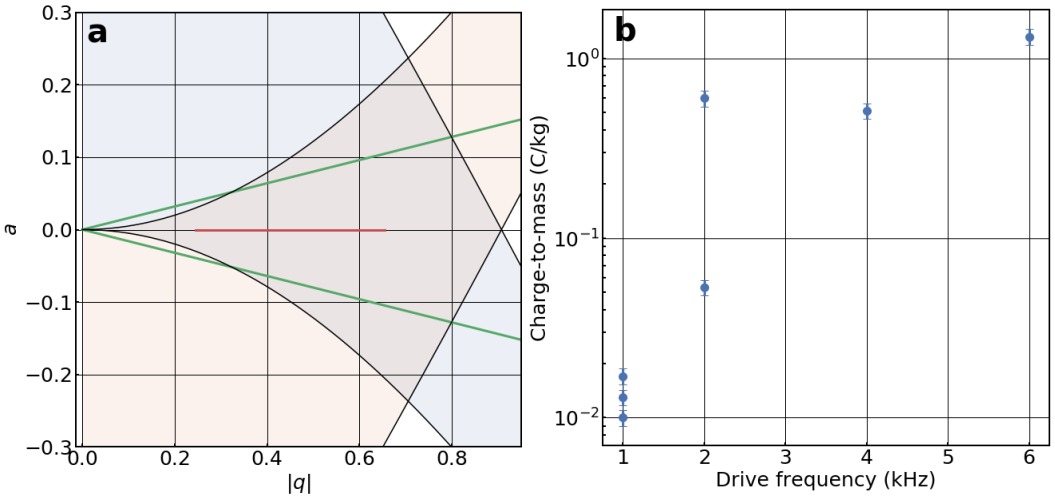

Figure 3.13: (a) Charge-to-mass selection in the quadrupole guide. The green line corresponds to the relationship between a_g and q_g parameters within the quadrupole guide. While with $a = 0$, stable operation satisfies $0 < q_g < 0.98$, here it becomes $0.3 < q_g < 0.8$ (overlap between the green line with the stability diagram), due to the DC offset. The equivalent stability-parameter in the science trap is $q = \eta q_g$ (red line). The parameters used here are $V_o = 250\,\mathrm{V}$, U_g =20 V (DC) and $\omega_d/2\pi = 3.0\,\mathrm{kHz}$. (b) Experimental selection of charge-to-mass ratios by increasing the drive frequency while keeping other trap and guide parameters fixed.

From Eq. 3.12, we can determine that $a_{g,x} = -2U_g/V_o\, q_{g,x}$ and that $a_{g,y} = -2U_g/V_o\, q_{g,y}$. Therefore, a stable charge-to-mass ratio is determined by the overlap of this line and the stable region in the stability diagram as shown by the green lines in Fig. 3.13(a). Lastly, the correspondence between the q parameters of the trap and the guide is $q = \eta q_g$ and is shown in red in Fig. 3.13(a). In the example shown on Fig. 3.13(a), we apply $V_o = 250\,\mathrm{V}$ on both guide and trap at $\omega_d = 3.0\,\mathrm{kHz}$, and U_g =20 V (DC) on two opposite rods of the guide. The effect is to filter the nanospheres with stability parameters $0.3 < q_g < 0.8$, which correspond to charge-to-mass ratios satisfying $0.26 < Q/m < 0.69\,\mathrm{C/kg}$. In Fig. 3.13(b), we show experimentally how to select higher charge-to-mass ratios. Given the fact that the DC offset leads to trapped nanoparticles with stability parameter q_g satisfying $0.3 < q_g < 0.8$, as the trap frequency is increased, for this condition to be met, the charge-to-mass ratio has to be greater.

3.3.3 Loading droplets

While loading the trap, droplets of solvent can be trapped as well as nanoparticles and can remain for hours in low vacuum. In order to ensure that we only observe

bare silica nanoparticles, the pressure is reduced to $\sim 10^{-4}$ mbar right after trapping to increase the evaporation speed. Currently, the pressure can then be reduced in the main chamber down to $\sim 10^{-7}$ mbar and the particles can remain trapped at those pressures for weeks without any cooling (see Chapter 4).

3.4 Summary

To summarise, we have reviewed the general theory of the Paul trap. The motion of a levitated nanosphere in the trap is described by Mathieu equations. Its dynamics can be decomposed in three different motions (secular motion, micromotion and excess micromotion). Two original designs of linear Paul traps for levitated optomechanics experiments have been presented. Calculation of the efficiency parameters in the case of the linear Paul traps were given alongside trap depth and effect of voltage noise. Lastly, we described our loading process which combines the use of an electrospray with a quadrupole guide at a pressure of $\sim 10^{-1}$ mbar. The miniature linear Paul trap introduced here will be characterised in further detail in the next chapter.

Chapter 4

Imaging of a levitated-oscillator and trap characterisation

Many charged nanoparticle traps have been demonstrated but there are few reports characterising their long term stability and noise, which is crucial for applications in quantum optomechanics and for testing fundamental physics [45, 77, 94, 96, 99–102]. Moreover, a precise knowledge of the mass, the number of charges and their stability over time is required. In this chapter, we report on an imaging method suitable to monitor the nanosphere motion. We show how the sensitivity of this technique is improved by more than two orders of magnitude when using super-resolution algorithms. This method is then directly applied to evaluate the force-noise sensitivity of a levitated nanosphere. A precise knowledge of the mass is often required to calibrate the nanosphere effective temperature or force-sensitivity. Different methods to evaluate the mass of the nanosphere in a Paul trap are compared. We discuss as well how the charge-to-mass ratio is estimated. Using the imaging method, we characterise the temperature and frequency stability of the levitated oscillator in the trap. Despite the simplicity of our trap design, we report stability performances comparable to the ones observed in conventional quadrupole traps used with nanoparticles.

4.1 Super-resolution imaging

4.1.1 Imaging the nanoparticle displacement

A distinguishing feature of charged nano-oscillators is their low oscillation frequency, typically in the range of a few Hz to kHz. Detection of small amplitude mechanical motion at these low frequencies is challenging as environmental mechanical noise in the detection chain can swamp measurements of the trapped motion of the nanopar-

ticle. A common approach to measurement of particle displacement uses a difference detection scheme where a laser beam is used to illuminate the particle. The transmitted light modified by scattering from the particle is typically directed onto a quadrant photodiode or alternatively split into two equal components using a mirror such that each component is detected on a separate photodiode. The motion of the particle is observed as an imbalance in the difference between the currents on the photodiodes [41]. While this is relatively noise free at frequencies exceeding 10 kHz, low frequency mechanical noise can induce beam pointing noise which cannot easily be differentiated from the true mechanical motion of the oscillator. We present a very simple and surprisingly sensitive imaging method for measuring low frequency particle displacement which is free of the low mechanical noise observed in split detection methods but yet demonstrates displacement sensitivity of better than $10^{-16}\,\mathrm{m}^2/\mathrm{Hz}$. Optical interferometric detection schemes often offer the best sensitivities in terms of displacement. However, typical sensitivities are often much worst at low frequency. For example, the noise floor of a standard balanced Michelson interferometer can be of the order of $10^{-30}\,\mathrm{m}^2/\mathrm{Hz}$ around 100 kHz but it can easily drop to $10^{-20}\,\mathrm{m}^2/\mathrm{Hz}$ at 100 Hz due to environmental noise affecting the beam paths as well as flicker noise [103]. This difference can be even more pronounced when

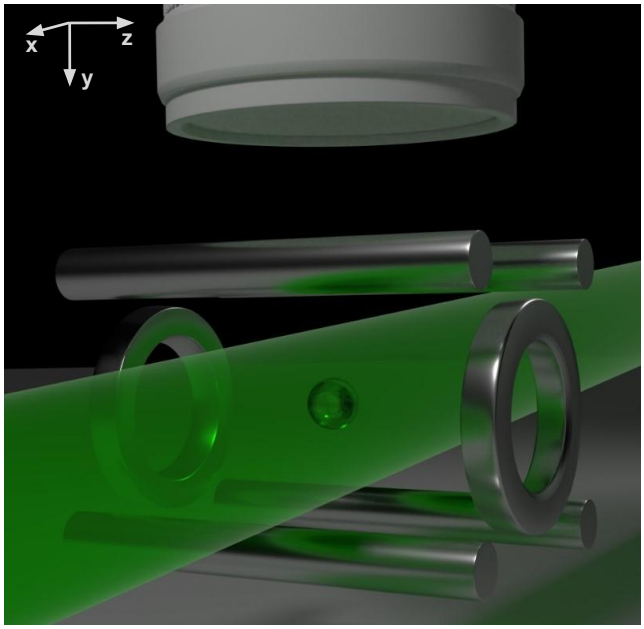

Figure 4.1: Artistic view of the imaging of a silica nanoparticle motion in a Paul trap. The scattered light at 90°coming from a green laser (propagating along the x-axis) is imaged onto a camera (along the y-axis).

dealing with nanoparticle motion due to the intrinsically lower coupling/detection efficiency. Here, we exploit a much simpler detection scheme. The trapped nanoparticle is illuminated with a green laser diode with powers ranging from 10 mW to 40 mW and a beam waist of 250 μm. This is shown schematically in Fig. 4.1 and Fig. 3.11 alongside with the axis definition. The light scattered at 90° is collected by a zoom objective lens[1] mounted on a low cost CMOS camera[2]. We extract the particle position in the x-z plane by finding the coordinates of the pixel of highest intensity.

An example of a time trace for a silica nanoparticle with a mass of 9.6×10^{-17} kg can be seen in Fig. 4.2. The camera sensor has a resolution of 1280 x 1024. A smaller area of interest can be addressed on the sensor allowing an acquisition at a faster frame rate. In our typical configuration we exploit a 50 x 40 matrix that allows to acquire between 800 fps and 1000 fps. The exposure time used ranges from 0.4 to 1.2 ms. It is kept smaller than the sampling time and as high as possible while avoiding blurring of the motion. This, in combination with the simplicity of the algorithm to reconstruct the particle position, allows for a real time acquisition of two time traces corresponding to the particle motion projected onto the coordinates defined by the camera pixel matrix. It is worth noting that the time series is composed of 8 bit integers. Combined with the low sampling rate allows for continuous

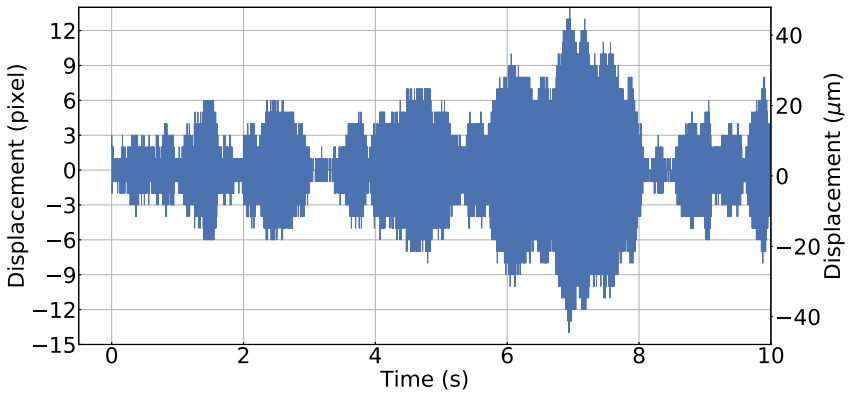

Figure 4.2: Time-trace of the motion along the z-axis of a silica nanoparticle of mass 9.6×10^{-17} kg at 10^{-3} mbar, derived from imaging. The particle position is obtained by considering the pixel of highest intensity. Calibration factor of (3.11 ± 0.03) μm/pixel.

[1]The zoom objective used is a *Zoom 7000* by Navitar. We mount on the objective a focal length lens extender from Edmund optics

[2]The camera used is a $DCC1545M$ by ThorLabs

monitoring of the particle position over very long times without having large data storage requirements.

The secular motion can be easily kept at frequencies lower than 500 Hz, however, it is not possible to avoid aliasing of the micromotion with our typical frame rates. This means that any calibration that is applied to the secular motion cannot be applied to the aliased micromotion. The motion can be described by a damped harmonic oscillator. The single-sided power spectral density (PSD) of the motion along any axis i can be written as: $S_i(\omega) = |\chi(\omega)|^2(S_{F_{th}} + S_F)$ where $S_{F_{th}} = 4k_B T_b m\gamma_m$ is the PSD of the thermal Langevin force while S_F is the PSD of the total force noise due to all other unknown sources. The bath temperature is given by T_b, k_B is the Boltzmann constant, m the mass of the nanoparticle and γ_m the viscous damping due to collisions with residual gas. Finally, $\chi(\omega)$, is the mechanical susceptibility, given by $\chi(\omega) = (m(\omega_i^2 - \omega^2 - i\gamma_m\omega))^{-1}$ where ω_i is the resonant frequency which here corresponds to the secular frequency along the i^{th} axis.

4.1.2 Calibration of the motion

We calibrate the motion of the particle by placing the camera on a translation stage and displacing it by a known amount. Five time traces are taken at different stage positions. By calculating the mean position of the particle for each time trace, we directly map the stage position onto the camera pixel matrix since the particle behaves like a point source. After a simple linear regression, the example shown in Fig. 4.3 gives a displacement per pixel of $(8.75 \pm 0.09)\,\mu$m/pixel. Two independent uncertainties are taken into account. The uncertainty of the fit itself, which only accounts for 0.3%, while the uncertainty in the camera focus stability is 1%. This error is estimated by changing the focus on the trapped particle in a controlled manner. The focus is checked over days to correct for drifts in the camera mount, focus or zoom. Lastly, by ensuring that the residuals of the fit do not increase when the camera is displaced away from the nanoparticle, we ensure that distortions due to the camera objective do not have to be taken into account. This method is competitive for measurements of low frequency oscillators in comparison to methods measuring the particle response to a known force, which can depend on more parameters with larger associated uncertainties [104]. Depending on the position of the zoom, different calibration factors can be obtained.

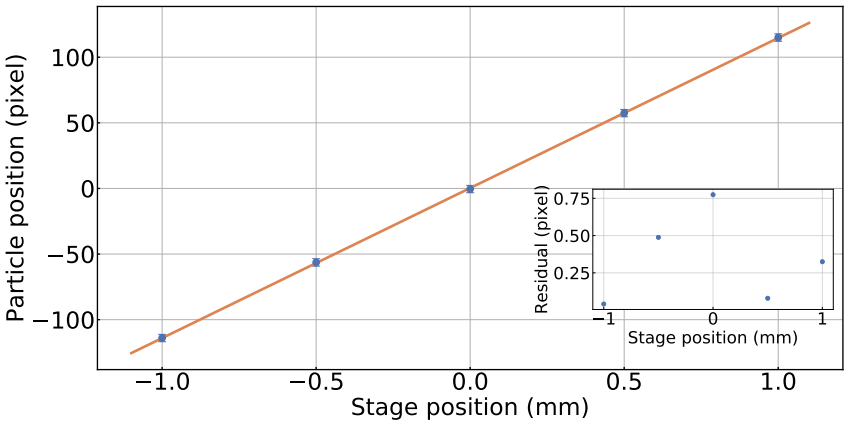

Figure 4.3: The displacement of the nanosphere is calibrated by moving the camera by a known amount. The figure shows the sum of the relative distances of the translation stage positions. The fit is shown in orange with the residuals in the inset. The calibration factor is found to be $(8.75 \pm 0.09)\,\mu$m/pixel.

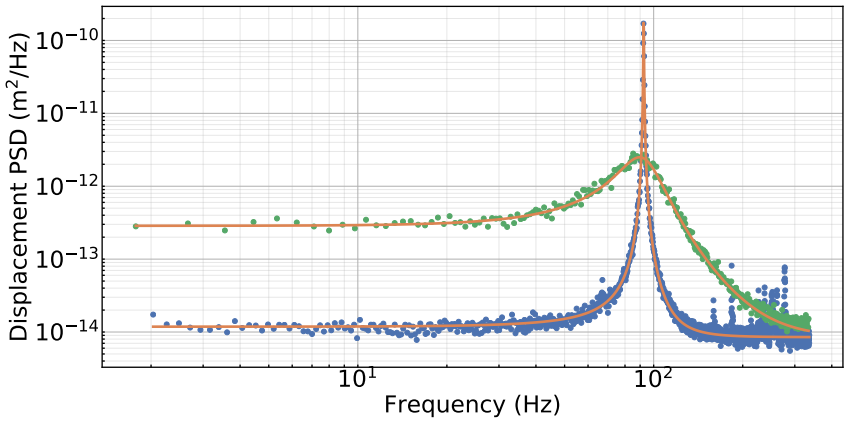

Figure 4.4: Calibrated PSD of the motion of a trapped nanoparticle at 0.10 mbar in green (1.0×10^{-3} mbar in blue) along the z-axis. The secular frequency is 92.5 Hz. The fits of the mechanical susceptibilities are shown in orange. The time trace shown in Fig. 4.2 is a subsection of the time trace used to obtain the spectra shown at 1.0×10^{-3} mbar. Calibration factor of $(3.11 \pm 0.03)\,\mu$m/pixel.

We show an example of a calibrated PSD of the nanoparticle displacement along the z-axis in Fig. 4.4 at two different pressures. Despite the very simple approach, this method provides spectra with high signal-to-noise ratios (SNR). Along with the experimental spectra, we show fit results assuming a total force noise PSD. Down to pressures of the order of $\sim 10^{-3}$ mbar the spectral noise floor is sufficiently low to resolve the susceptibility down to the zero frequency limit.

4.1.3 Low-frequency spectra

The continuous monitoring of the particle motion, allows us to explore the dynamics down to extremely low frequencies. Taking into consideration the longest continuous

stretch of data that lasts almost 3 days at a pressure of $\sim 10^{-5}$ mbar, we obtain the displacement PSD shown in Fig. 4.5. Interestingly, a peak (and its harmonics) is clearly visible corresponding to a period of ~ 1 hour. It is possible to show that this displacement modulation is highly correlated to a modulation of the secular frequency, itself correlated to the temperature drifts in the lab.

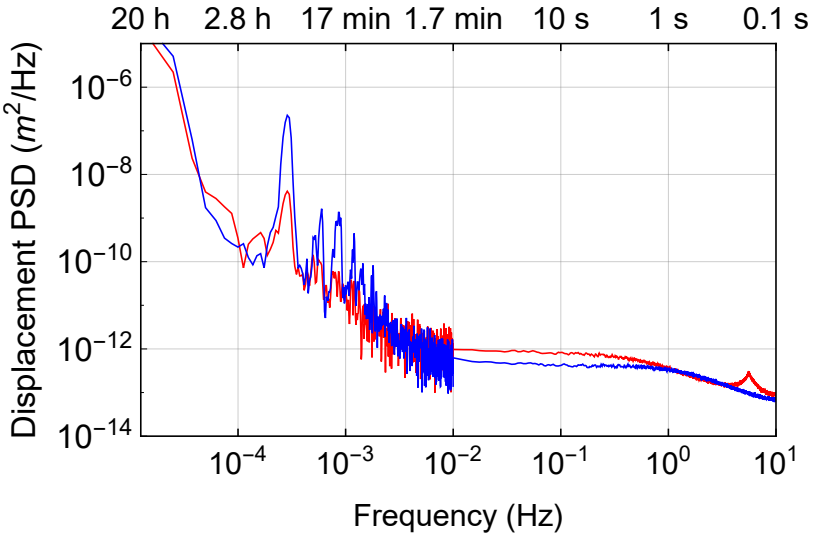

Figure 4.5: Low frequency PSDs calculated from data acquired for almost three days. Red and blue lines represent the PSD along the x and z-axis respectively. The peak around 1 hour corresponds to motion in the trap correlated to temperature fluctuations in the lab. At frequencies above 10^{-2} Hz, the PSD has been averaged with more spectra, which leads to the smoother PSD profiles in this range.

4.1.4 Super resolution measurements

The spectra shown so far in Figures 4.4 and 4.5 have been calculated on time traces where the position of the particle has been determined by finding the pixel of highest intensity. This naive approach enables real time traces by controlling the camera with a software controlled with a Python language library[3]. This is enough to extract basic information such as frequencies and linewidths characterizing the mechanical motion. Applications such as sensing or cooling of the centre-of-mass motion may require higher sensitivities which can be achieved by using super-resolution imaging.

Complex algorithms to obtain sub-pixel resolution is applied in many fields including particle physics [105], chemistry [106] and astrophysics. In the latter case, for

[3] `https://instrumental-lib.readthedocs.io`

example, it was applied to enhance the search for exoplanets [107]. Here, we take advantage of the diffraction limited spot on the camera to extract a sub-pixel particle position, which we call super resolution. The imaged spot of the scattered light can be described with very good approximation by a Gaussian profile, as shown in Fig. 4.6. The beam spot diameter is 3.5 pixels (18 μm). Depending on the exposure time, the number of pixels along a camera axis above the detector noise can range from 1 to 10 pixels. When the signal-to-noise is low, and only the brightest pixel is above the noise floor, the position resolution (given by one pixel) corresponds to 3.1 μm. The quantization noise of the PSD is given by $\frac{\Delta^2}{6f_s}$ with Δ the step size and f_s the sampling frequency [108]. In this case, we expect and find $2{\times}10^{-15}\,\mathrm{m}^2/\mathrm{Hz}$ (see Fig. 4.8). At the other extreme, when the signal-to-noise is sufficiently high, we can utilise the full dynamic range of the camera, the position resolution can be estimated by using the standard error of the mean of the Gaussian distribution. The

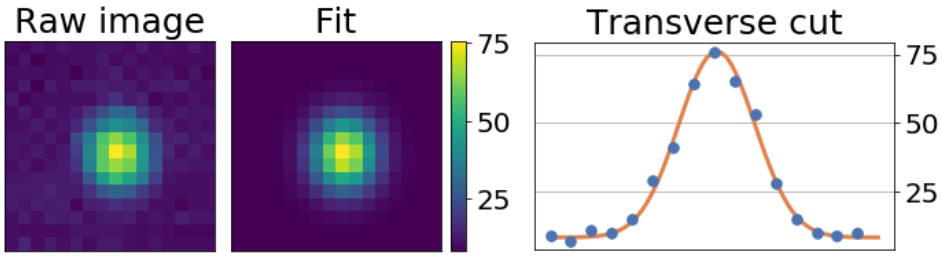

Figure 4.6: Raw camera frame, fit and transverse cut of the imaged scattered light (with both fit (in orange) and intensity values). The frames are acquired at 803 fps with an exposure time of 1.2 ms.

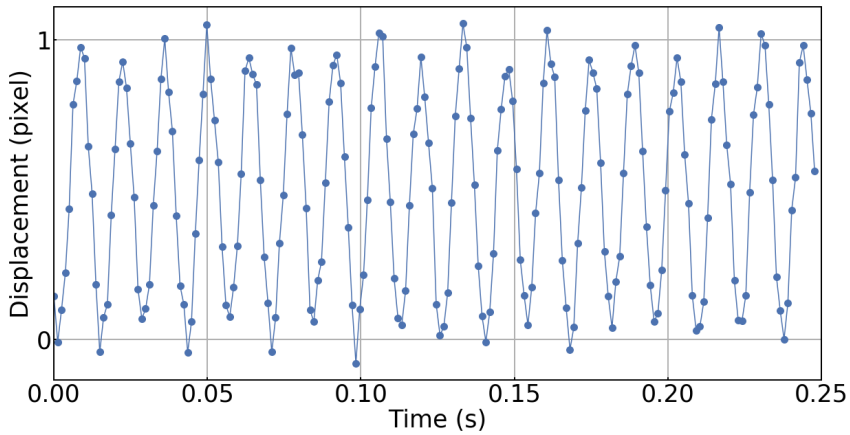

Figure 4.7: Resolution enhancement obtained by fitting a Gaussian distribution to find the particle position on each frame. Time-trace of the motion along the z-axis obtained with the resolution enhancement showing sub-pixel resolution.

number of samples for each pixel is given by its intensity value when the noise floor is subtracted from the image. In this case, for the 10 pixels above the noise floor, the equivalent sample size is 1000, which gives a position resolution of 0.06 pixel. This corresponds to a particle position resolution of 0.3 μm and a PSD noise floor of $7\times10^{-18}\,\mathrm{m}^2/\mathrm{Hz}$. Fitting the image with a two-dimensional Gaussian profile increases the sensitivity by more than two orders of magnitude as it can be seen in Fig. 4.8, where we plot a comparison between PSDs with and without the resolution enhancement for both trap directions. These spectra were taken at a pressure $\sim 10^{-6}$ mbar for a particle with a charge-to-mass ratio of 0.1 C/kg. The secular frequencies along the z, x and y-axis are 72.1, 258.5 and 266.2 Hz respectively. A trap ellipticity slightly different from the nominal one of $\epsilon_t = 0.5$ removes the degeneracy on the x and y-axes, which are easily resolved at this pressure. The peak in the PSD at 298 Hz corresponds to the aliasing of the excess micromotion at the AC drive frequency of 1.1 kHz.

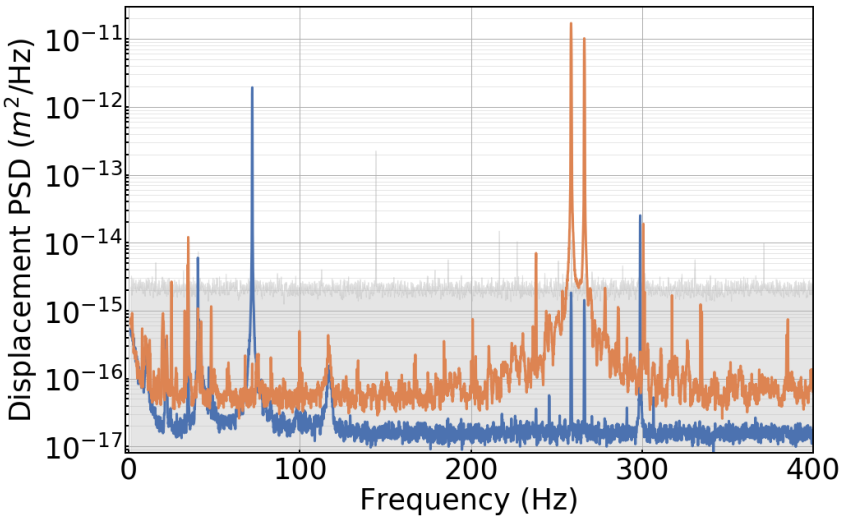

Figure 4.8: PSD of the particle displacement with super resolution imaging. Blue and orange lines refer to the motion along the z and x-axis respectively. The grey shaded area shows the noise floor when the algorithm finds the intensity maximum to obtain the particle position.

The three factors which can be improved in the measurements presented here are the sensitivity, the acquisition rate and the fitting speed of the algorithm used to determine the particle position. The sensitivity of the measurements can easily be improved by increasing the magnification. The secular frequencies were limited here to 500 Hz by the acquisition rate. In order to directly detect higher secular

frequencies and avoid aliasing, it is possible to use cameras with higher pixel clocks (i.e., $\sim 500\,\mathrm{MHz}$ against $\sim 40\,\mathrm{MHz}$ here), opening the possibility of getting frame rates as high as 4 kHz. Furthermore, fluorescence correlation spectroscopy techniques [109] could be used in the case of fluorescing nanoparticles such as YLF crystals doped in Yb^{3+} [110]. This could lead to frame rates of tens of kHz. Recent single-photon avalanche diode (SPAD) cameras have been operated up to 300 kfps [111].

While here the time traces without subpixel resolution are in real time, the data with super-resolution are obtained by post-processing the video. Indeed, the fitting routine used was too slow to keep acquiring data at ~ 800 frames per second (fps). It should nonetheless still be possible to acquire real time position traces with very high frame rates by running the fitting algorithm on a graphics processing unit (GPU). Gaussian fits or better algorithms can then achieve fit speeds ~ 100000 fits/s for a $10\,\mathrm{x}\,10$ pixel matrix [112, 113].

4.2 Nanoparticle force sensitivity

Given its low mass and small damping rate, a levitated nanosphere in vacuum is a sensitive force sensor. The super-resolution enhancement can be used to increase the force sensitivity bandwidth too. We show an example in Fig. 4.9 which compares

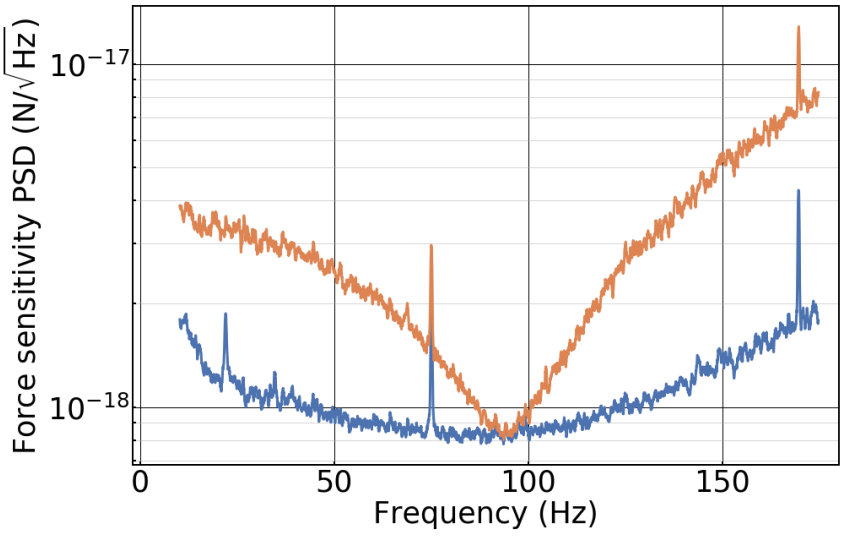

Figure 4.9: Force-noise sensitivity of a silica nanoparticle with a mass of 9.6×10^{-17} kg at 7.4×10^{-5} mbar along the z-axis. The orange curve corresponds to the force-noise sensitivity obtained without the super-resolution enhancement. The blue one is obtained on the same acquisition but using the super-resolution. This increases the 3 dB bandwidth, centred around 90 Hz, from 21 Hz to 112 Hz.

the force sensitivity of a silica nanoparticle with a mass of 9.6×10^{-17} kg levitated at 7.4×10^{-5} mbar. The super-resolution and the brightest pixel method for extracting the particle position are shown. The super resolution method enables us to increase the 3 dB force-noise sensitivity bandwidth from 21 Hz to 112 Hz. The sensitivity peaks at $(8.2\pm0.6)\times10^2\,\mathrm{zN}/\sqrt{\mathrm{Hz}}$. At this pressure, the force noise contribution from the Brownian motion, and therefore the lowest achievable limit without other noise, is $\sqrt{S_{F_{th}}}=(6.3\pm0.3)\times10^2\,\mathrm{zN}/\sqrt{\mathrm{Hz}}$. The force noise sensitivity, $\sqrt{S_F}$, shown in Fig. 4.9 is calculated from the displacement PSD $S_z(\omega)$ as $\sqrt{S_F(\omega)}=\frac{\sqrt{S_z(\omega)}}{|\chi(\omega)|}$ with $\chi(\omega)$ the mechanical susceptibility defined above. The mechanical susceptibility depends on the mass, independently measured, as well as the damping and the secular frequency, obtained by fitting a displacement PSD from an independent data set. This approach provides a good estimate of the force sensitivity, however, a more rigorous analysis can be obtained exploiting Wiener filter theory [114].

4.3 Particle size estimation

Different methods can be used to estimate the size (or mass) of the nanoparticles loaded into the trap with different accuracies [66, 99, 100, 103, 115–117]. We

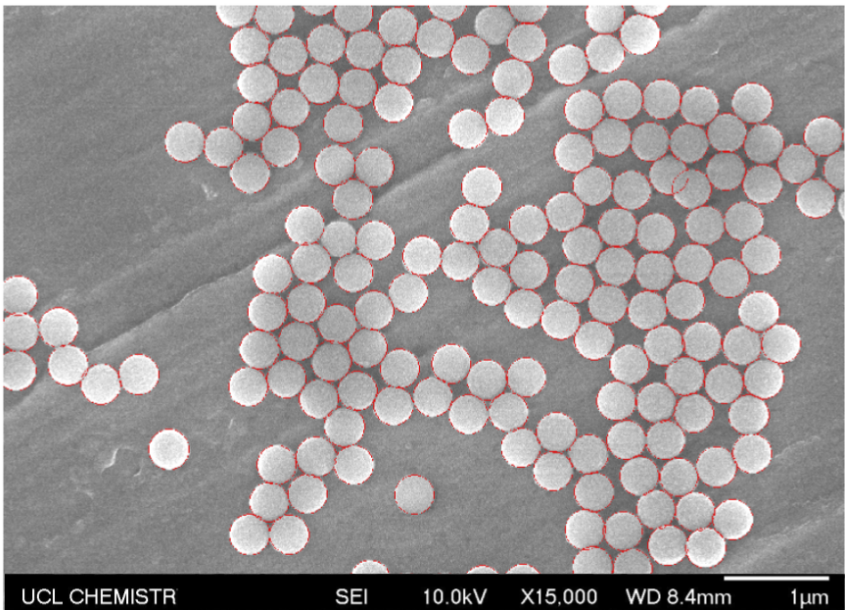

Figure 4.10: SEM image of silica nanosphere of nominal radius of (194 ± 5) nm. The sample is prepared with a gold coating layer of ∼1 nm to increase its conductivity and improve the image quality. The spheres are fitted with circles by using the Hough transform. The edges are detected and are shown in red. Those circles are then fitted to find out the radius size of each particle.

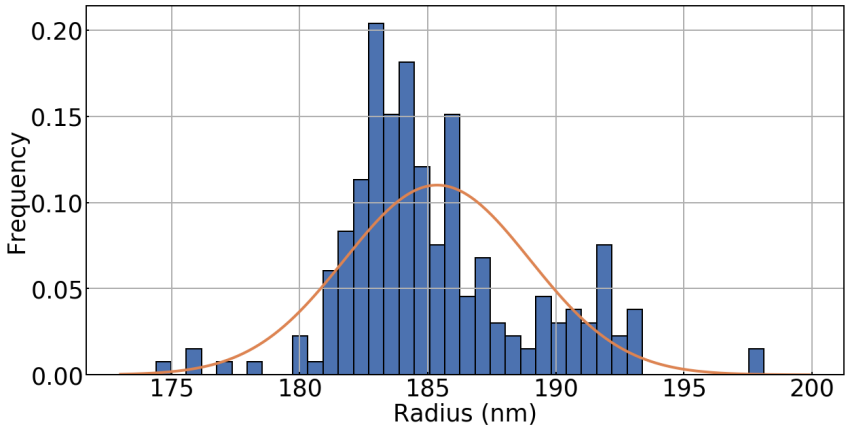

Figure 4.11: Particle size distribution from SEM imaging for nanoparticles of nominal radius (194 ± 5) nm. This distribution combines the result of two SEM images. One is shown above. We find over 223 spheres an average radius (186 ± 4) nm.

use commercial silica nanospheres by *microParticles GmbH* with nominal density of $1850\,\mathrm{kg/m^3}$ and nominal radius of (194 ± 5) nm. A scanning electron microscope (SEM) image of the particles used is shown in Fig. 4.10. We find a radius of (186 ± 4) nm from a sample of 223 imaged nanoparticles after fitting circles by using the Hough transform which transforms an image into edges.

4.3.1 Gas damping

The particle size can be roughly determined by evaluating the gas damping as a function of pressure. This is done by measuring the linewidth of the displacement PSD. It is then fitted to the expected gas damping law in the free molecular flow regime. Here $\gamma_{\mathrm{gas}} = \frac{(1+\frac{\pi}{8})\bar{c}Pm_g}{k_B T_b r \rho}$, where the particle mean speed is $\bar{c} = \sqrt{8k_B T_b/m_g/\pi}$, r and ρ the particle radius and density, respectively, k_B the Boltzmann constant, P, m_g and T_b correspond to gas pressure, the mass of the gas molecules and the bath temperature, respectively [54, 55]. The bath temperature T_b can be assumed to remain at 293 K independently from both the centre-of-mass motion and the internal temperature of the nanosphere [118] (see Section 2.3.4). This gives a radius of (199 ± 57) nm by assuming a nominal density of $1850\,\mathrm{kg/m^3}$ and a spherical shape (see Fig. 4.12). The main uncertainty contribution is due to the pressure measurement (30%, specified by the manufacturer). On top of its large uncertainty, this method has a few drawbacks. It requires the knowledge of the density, which can significantly vary for silica nanospheres [119]. Furthermore, it only works for spheres and it can therefore be challenging to differentiate a single sphere from a cluster.

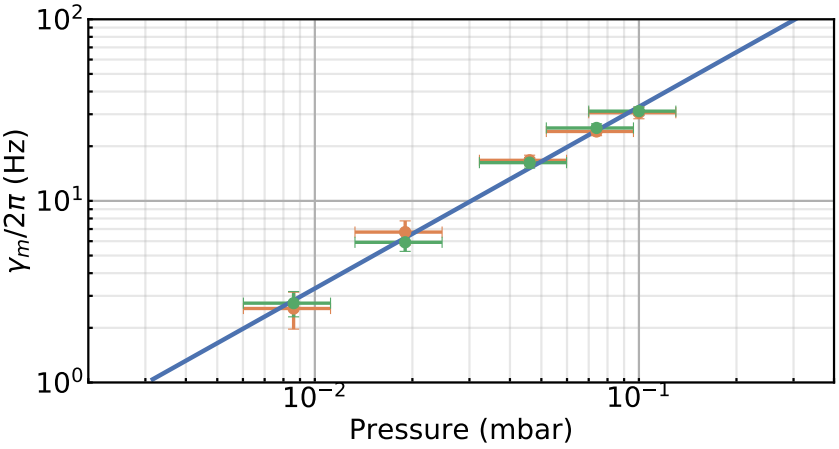

Figure 4.12: Gas damping as a function of pressure. Linewidth measurements from spectra are shown in orange and green corresponding respectively to the damping along the x and z-axis. The fit is shown in blue. The radius found is (199 ± 57) nm assuming a density of $1850\,\mathrm{kg/m^3}$ and a spherical shape.

Indeed, in the case of two particles joined together such as a nanodumbbell, the expected linewidth is numerically shown to be smaller by 8 % compared to a sphere (independently from the size of the spheres and assuming a stochastic rotational motion of the dumbbell) [54], which is comparable to the statistical uncertainty of the measurement shown here. In comparison, a change in mass by a factor 2 for a spherical object corresponds to a reduction in linewidth by 21 %, which is easier to measure. It is therefore challenging to differentiate a nanodumbbell from a single nanosphere in a Paul trap with this method. It can be more easily differentiated when the alignment with respect to the trap axis is well defined, such as in an optical tweezer [120].

4.3.2 Charge jumps

In a Paul trap, a more attractive method to determine the mass is to measure it from the secular frequency shifts due to charge jumps [99, 116]. For a number of charges larger than ~ 50, the secular frequency along the x-axis can be approximated as $\omega_x \approx \frac{\omega_d}{2\sqrt{2}} q_x$ (see Eq. 3.6 and 3.8). The frequency shift given by one electron becomes $\delta\omega_x = \frac{|e|\,V_0\,\eta}{\sqrt{2} m \omega_d r_o^2}$ where e is the elementary charge. While we have monitored a constant number of charges for days, it can be changed (mostly increased in our case) by leaving the pressure gauge on [121], which gives a typical charging rate of ~ 7 charges/hour. Other ways of charging nanoparticles include using an electron gun [116] or a UV light source [103]. The jumps in the secular frequency can be

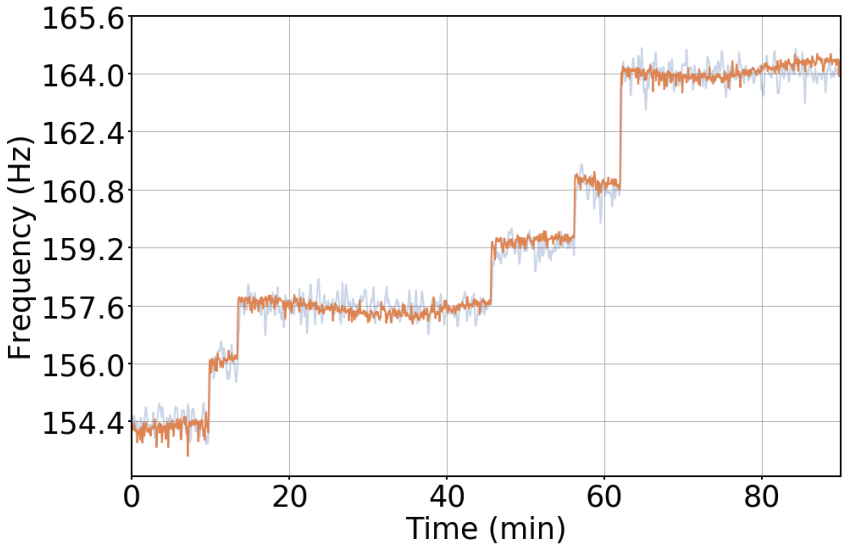

Figure 4.13: Nanosphere mass measurement inferred from charge jumps. Secular frequencies along the x and z-axis (z-axis rescaled) are monitored and shown respectively in orange and blue. A grid with constant separation of 1.59 Hz is added to the plot. It corresponds to the frequency shift given by one elementary charge. From the average frequency shift 1.59 ± 0.07 Hz, we estimate the mass to be $(9.6 \pm 0.9) \times 10^{-17}$ kg. The measurement was taken at 4.6×10^{-4} mbar with the pressure gauge on. The AC drive was 500 V (peak-to-peak) at 3.0 kHz and 90.0 V on the endcaps.

seen in Fig. 4.13. Assuming that the smallest frequency jump corresponds to a change of a single elementary charge, we measure a mass of $(9.6 \pm 0.9) \times 10^{-17}$ kg. Two strong motivations to use this method are that thermal equilibrium of the centre-of-mass motion with the bath is not required and no knowledge over the density is needed. The systematic error in the mass uncertainty comes from the trap fabrication tolerances of $\pm 50\,\mu$m in both the relative position of the holes and their diameter. This gives an uncertainty of 4 % on r_o. The statistical error accounts for 4 % and therefore the overall error on the mass is 9 %. The statistical error on the secular frequency shifts is quite high (4 %). This is due to the drifts in secular frequencies and to charges accumulating on the PCB due to the pressure gauge when left on. When the pressure gauge is turned off drifts as small 2 ppm/h were measured (see section 4.6). Using this method, statistical uncertainties as small as 100 ppm with systematic uncertainty of 1 % have been demonstrated in mass-spectrometers [99, 116].

4.3.3 Thermal equilibrium

The mass of the particle can also be estimated by assuming thermal equilibrium at 293 K with the bath. We verify in the next section the validity of this assumption. However, it is reasonable because the very low intensity (40 W/cm^2 against 10 MW/cm^2 for a typical optical tweezer) used to illuminate the particle is not sufficient to increase its internal temperature [118]. Moreover, these measurements are taken at a high pressure (10^{-2} mbar) where the heat transfer to the surrounding gas is more efficient. At this pressure, thermal noise dominates over other sources of noise e.g. electrical noise. Following from the equipartition theorem, at thermal equilibrium, $\frac{1}{2}k_B T_b = \frac{1}{2}m\omega_i^2\langle i\rangle^2$, where $\langle i\rangle$ is the standard deviation of the motion along the i^{th}-axis. This measurement offers the smallest uncertainty over the different mass measurements used here (3 %) with $m = (9.5 \pm 0.3) \times 10^{-17}$ kg. The mass was obtained after averaging 16 measurements. The total error is composed of a 1 % statistical error and a 3 % systematic error that takes into account the temperature uncertainty of 2 %, an error of 1 % on the frequency and of 2 % on the variance of the displacement given by the calibration method. The uncertainty on this measurement could easily be reduced down to 2 % by using a more precise temperature sensor. Another method, combining the thermal equilibrium assumption with a known force excitation has been demonstrated in Ref. [117]. It would however require a precise knowledge of the number of charges to be applied here.

4.3.4 Nanodumbbells

Fig. 4.14 summarises the different measurements described above. The measurements in blue and orange correspond to the measured mass obtained from thermal equilibrium. Those measurements are taken at a pressure of 1.0×10^{-2} mbar, with different camera magnifications and on two different days to check stability of the mass over time. The calibration used for the data in blue (orange) is (8.35 ± 0.08) μm/pixel ((3.11 ± 0.03) μm/pixel). The green region corresponds to the uncertainty of the mass measurement (with one standard deviation) given by the charge jumps (see Fig. 4.13). As the particle size distribution, obtained from the SEM images, is narrow and that there is good agreement between the two mass measurements, we have good confidence that this nanoparticle is a nanodumbbell, which can easily form from two particles held by Van der Waals forces [120]. Indeed, assuming a nomi-

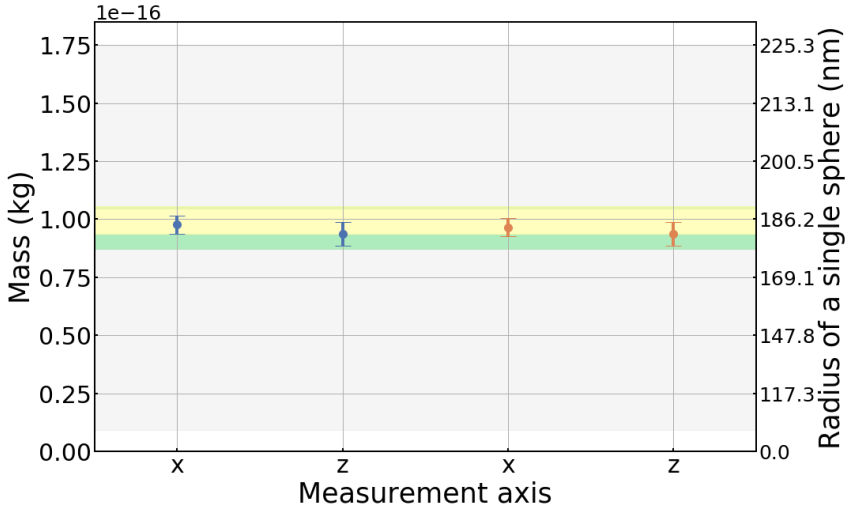

Figure 4.14: Compilation of different mass measurements. The measurements in blue and orange are obtained by assuming thermal equilibrium of the motion at 293 K with the displacement calibrated with the camera. The measurements are taken on two different days at a pressure of 1.0×10^{-2} mbar. The calibration constant for the measurements in blue (orange) is $(8.35\pm0.08)\,\mu$m/pixel ($(3.11\pm0.03)\,\mu$m/pixel). The grey and green regions correspond to the uncertainty of the mass measurements (one standard deviation) with the linewidth measurement (see Fig. 4.12) and from the charge jumps (see Fig. 4.13), respectively. The yellow region corresponds to the mass estimated of two nanospheres from the SEM image, assuming a nominal density of 1850 kg/m^3 (see Fig. 4.10 and 4.11). The equivalent estimated averaged radius of the spheres forming the nanodumbbell is shown on the scale on the right-hand side, assuming a nominal density of 1850 kg/m^3.

nal density of 1850 kg/m^3 (provided by the manufacturer), a nanodumbbell made of spheres of radius (186 ± 4) nm gives a mass of $(9.9\pm0.8)\times10^{-17}$ kg (yellow region), which agrees very well with the different mass measurements. The density found when considering the mass given by the charge jumps with the size found on the SEM images gives (1781 ± 196) kg/m^3. Lastly, the grey region corresponds to the expected mass given by the linewidth measurement assuming a cluster of two particles [54]. Those different measurements demonstrate the lack of reliability of the linewidth measurement in a Paul trap, as we have to guess the particle shape. Indeed, if we assume the particle to be spherical, we measure a radius of 199 nm and if we assume a nanodumbbell made of two identical spheres, we estimate the radius (of one nanosphere) to be 182 nm, which corresponds to a relative error in mass of 35 %. The equivalent radii for a single sphere of the nanodumbbell are shown in Fig. 4.14.

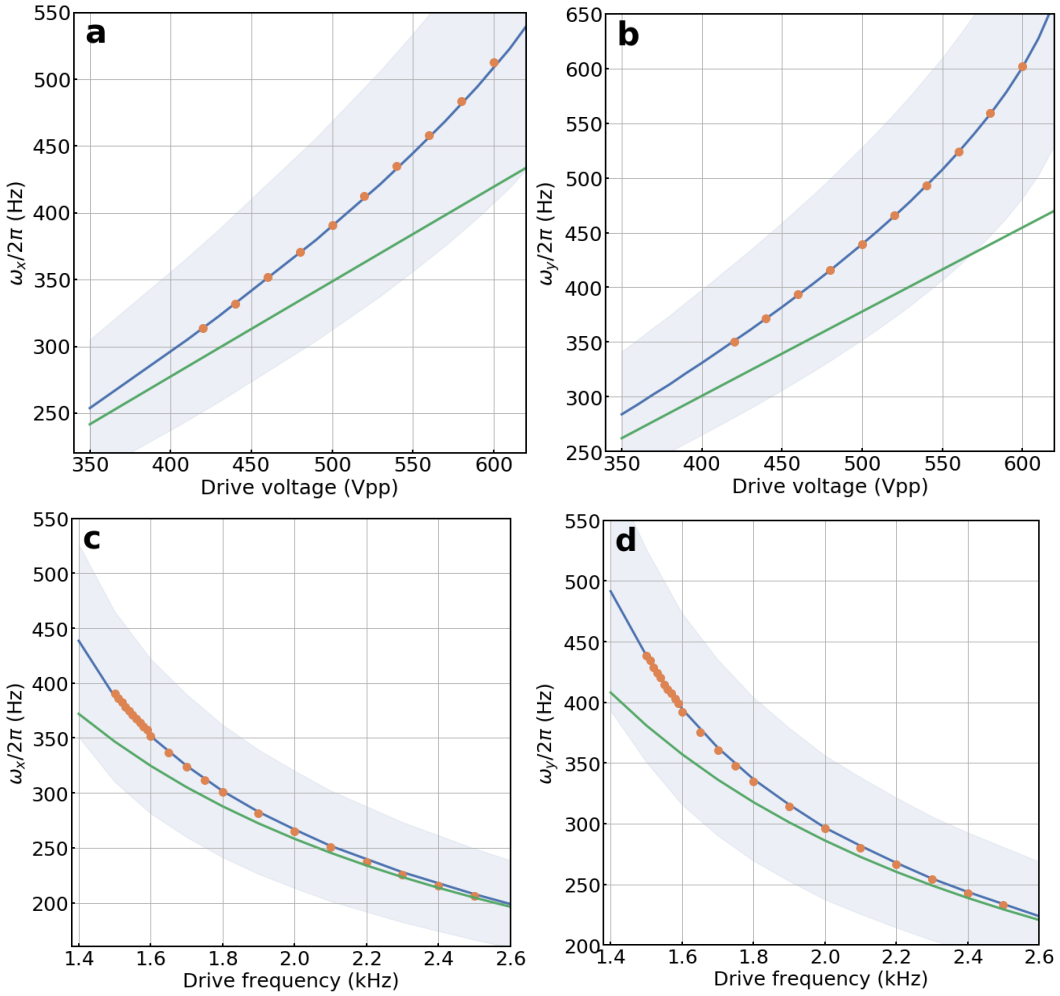

Figure 4.15: Measurement of the radial secular frequencies ω_x and ω_y as a function of drive voltage and drive frequency. The fit to the data is shown in blue. The blue area corresponds to the uncertainty on the secular frequency due to the geometrical uncertainty. The green line corresponds to the expected secular frequency in the small q approximation (see Eq. 3.8). The charge-to-mass ratio founds from panel (a) to (d) are (0.198±0.040), (0.2145±0.043), (0.214±0.043) and (0.197±0.039)C/kg, respectively.

4.4 Charge-to-mass evaluation

We have discussed different ways of estimating the mass of the nanoparticles in a Paul trap. Another important property is the nanosphere number of charges. One way of estimating it is to use the knowledge of the trap geometry and measure the secular frequencies as a function of trapping parameters such as drive voltage, frequency or endcap voltage. We show here an example by using the PCB Paul trap described in Section 3.2.1. As can be seen in Eq. 3.8 and Eq. 3.6, when varying the trap frequency ω_d or the drive amplitude V_o, the transverse secular frequencies only

depend on the geometry parameter r_o and efficiency parameter η. We can show with a simulation that an error on r_o will give a negligible error on η, typically ten times smaller in relative error. For this design the uncertainty on the distance from the trap centre to the rods r_o was 10% and therefore gives an uncertainty of 20% on the charge-to-mass measurement. Measuring the charge-to-mass ratio by varying the endcap-voltage is more reliable since z_o has a smaller associated error: 5%. As for η, the error on the efficiency parameter κ is negligible. The error on the charge-to-mass is therefore 10%.

In Fig. 4.15, we look at the radial frequencies as a function of drive voltage V_o and drive frequency ω_d. An interesting feature of these figures is that we explore a rather large area of the stability parameter, namely for a stability parameter q from 0.2 to 0.7 (see Eq. 3.6). This enables us to verify that the dynamics of the Paul trap matches well the theory. Furthermore, the small q approximation shown in Eq. 3.8 is not valid. In order to fit the data, we have to simulate directly the Mathieu equations Eq. 3.4. The expected secular frequency in the small q approximation is shown in green on those figures. The four estimations of the charge-to-mass ratio are compatible. The average charge-to-mass ratio obtained is $(0.206\pm0.041)\,\mathrm{C/kg}$. In Fig. 4.16, we measure the axial secular frequency as a function of endcap voltage U_o. We find a charge-to-mass ratio of $(0.178\pm0.018)\,\mathrm{C/kg}$ compatible with the previous measurement.

4.5 Centre-of-mass temperature

4.5.1 Temperature estimation

We use the mass measurement from the charge jumps above to estimate the centre-of-mass temperature. The temperature is estimated at different pressures without any active cooling mechanism on the particle by integrating the PSD numerically. It is shown in Fig. 4.17 with the motion calibrated with the camera. The blue (orange) data correspond to the motion along the x (z-axis). Here, we obtain a motion in thermal equilibrium with the bath ($(282 \pm 25)\,\mathrm{K}$) down to $\sim 10^{-4}\,\mathrm{mbar}$ in the z-axis and to less than $\sim 10^{-5}\,\mathrm{mbar}$ in the x-axis. However, excess force noise increases the effective temperature of the centre-of-mass motion at lower pressures. We estimate the excess force-noise in Section 5.4. Despite the increasing temperature at low pressures as much as $\sim 10^4\,\mathrm{K}$, the particle can be kept for weeks at $10^{-7}\,\mathrm{mbar}$,

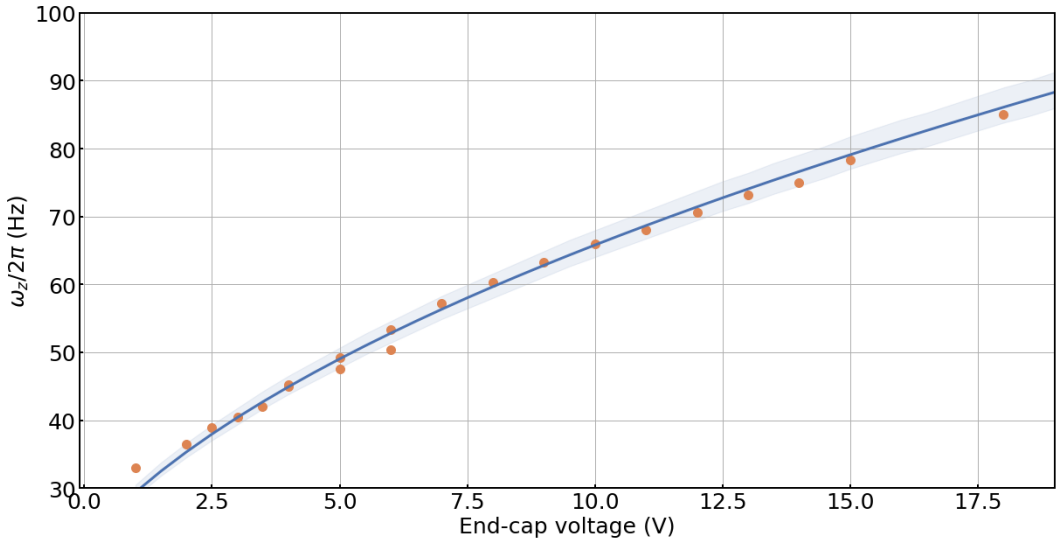

Figure 4.16: Measurement of the axial secular frequency ω_z as a function of endcap voltage. The fit to the data is shown in blue. The blue area corresponds to the uncertainty on the secular frequency due to the geometrical uncertainty. The measured charge-to-mass ratio is (0.178±0.018)C/kg.

as its temperature remains smaller than the equivalent trap depth of $\sim 10^7$ K. It was possible to observe thermal motion at the bath temperature $T_B = 293$ K down to $\sim 8 \times 10^7$ mbar when applying voltages on compensation electrodes to place the mean position of the nanoparticle in the centre of the AC field (see Sections 4.6.3 and 6.3).

4.5.2 Temperature stability

We are also interested in the stability of the effective temperature of the oscillator over time, as well as the optimum time over which this measurement should be made. In Fig. 4.18 we show the relative Allan deviation of the temperature $\sigma_T(\tau)/T_o$ at different pressures. The Allan deviation is a tool widely used for sensors and first applied to atomic clocks to quantify the stability of a frequency standard. We define the relative Allan deviation of a variable T as $\sigma_T(\tau)/T_o$ with T_o the averaged value of T and $\sigma_T(\tau)$ the Allan deviation [122].

$$\sigma_T^2(\tau) = \frac{1}{N-1} \sum_{k=1}^{N-1} \frac{1}{2} \left(\bar{T}_{k+1}^{(\tau)} - \bar{T}_k^{(\tau)} \right), \tag{4.1}$$

where $\bar{T}_k^{(\tau)}$ corresponds to the time average value of T inside N-1 intervals of varying length τ with N, such that $N\tau$ corresponds to the total measurement time. The

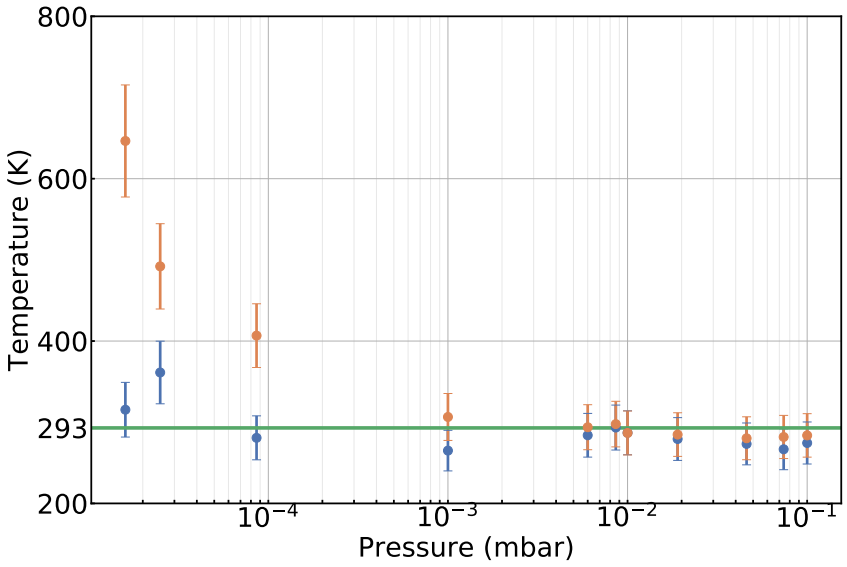

Figure 4.17: Centre-of-mass temperature of the trapped particle as a function of pressure (without cooling). The temperature along the x-axis (z-axis) is shown in blue (orange). The motion is thermal ((282 ± 25) K) down to $\sim 10^{-4}$ mbar along the z-axis and to less than $\sim 10^{-5}$ mbar along the x-axis. The temperature of the room at 293 K is indicated in green.

Allan variance quantifies the stability of the system over time by effectively showing the optimal value of time needed to estimate a variable, here the temperature. The measurements in blue (orange) are taken at 1.6×10^{-5} mbar monitored for 23 hours along the x-axis (z-axis). We also show measurements at 7.2×10^{-2} mbar in green

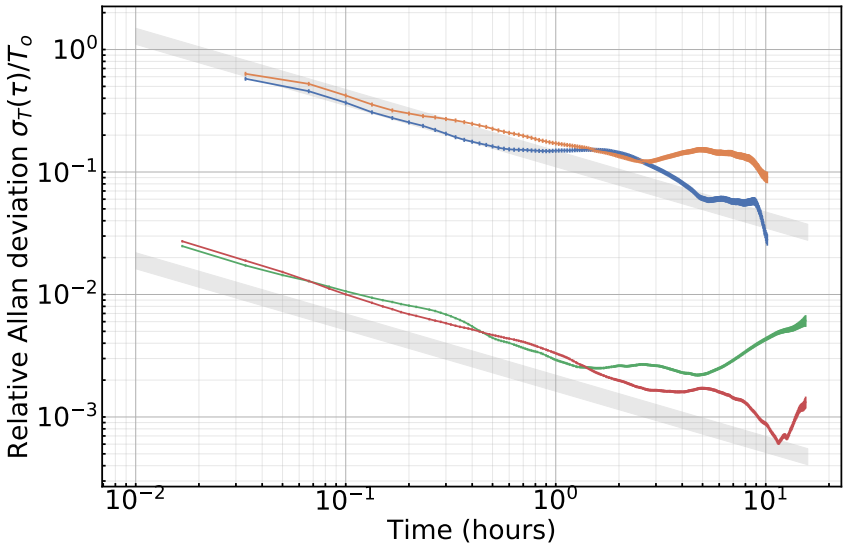

Figure 4.18: The relative Allan deviation of the temperature at 1.6×10^{-5} mbar along the x-axis (z-axis) is shown in blue (orange) and at 7.2×10^{-2} mbar in green (red). Theoretical curves of the expected Allan deviation are shown in gray.

(red) along the x-axis (z-axis). By acquiring statistics, a small error bound, called the standard error of the mean, (smaller than the standard deviation) can be placed on any mean value of normally distributed variable, namely $\sigma/\sqrt{n}$ with n the number of independent samples and σ the standard deviation of the distribution. This formula can be applied to the temperature measurement of a thermal oscillator and can be shown to be $\sqrt{\frac{2}{\gamma\tau}}$ (relative Allan deviation) [104]. It takes on average a time $2/\gamma$ for two samples to be independent (see Section 2.1.1). Therefore at high pressure, not much time is required to have enough statistics to evaluate accurately the temperature. At low pressure, more time is required. In the first part of the plot, the Allan deviation corresponds to the standard error of the mean. More statistics enables us to place a smaller error bound on a given measurement. After some time, the confidence bound increases due to experimental drifts. This time corresponds to the stability time of the variable. Here, we estimate temperature stabilities of a few hours, limited by drifts in the electrical potential. In comparison, stability over 100 seconds range has been reported in optical tweezers, which were believed to be limited by the optical stability of the trap as well as its nonlinearities [104, 117]. Similar stability of ~ 100 s were reported as well in other high frequency optomechanical systems [114].

4.6 Paul trap characterisation

In this section, we study the stability of the Paul trap potential by measuring the secular frequencies as well as the particle position over time. We show that the Paul trap stability depends on several parameters such as the trapping mechanism, the pressure gauge and the material used for the trap itself.

4.6.1 Stray fields due to the ion gauge and the electrospray loading mechanism

The creation of ions by the vacuum gauge leads to charging of the nanoparticle and changes in the trap potential. This leads to temporal changes in secular frequency as well as in the particle's mean position. The gauge therefore needs to be turned off for stable measurements. We monitor the secular frequencies ω_x and ω_z for almost one week when the gauge is turned on and off (see Fig. 4.19 (a)). Both of these secular frequencies show very similar behaviour except initially, right after loading

the trap. When the gauge is on, they follow an almost monotonic increase. The stable region shown in Fig. 4.19 (b) occurs when the pressure gauge has been turned off. To some extent, it is possible to separate the change in number of charges from a change in the potential. To do this we measured the charge-to-mass ratio at different times ($t = 15$, 90 and 137 hours) by changing the endcap potential and measuring the resulting frequency shift. The results are shown in Fig. 4.19 (a) and (b) along with the respective fits which give an increasing charge-to-mass ratio. We find 0.10 C/kg, 0.16 C/kg and 0.18 C/kg (10% standard error), from bottom to top. However, an additional stray potential needs to be accounted for, in order to obtain a reasonable agreement with the data. This offset directly quantifies the stray field along the z-axis as it corresponds to the minimum amount of endcap voltage needed to trap the particle which is ideally 0 V (see Fig. 4.19 (b)). Here, a positive voltage is needed (8.8, 2.7 and 1.5 V, respectively).

Stray fields are also due to solvent droplets reaching the dielectric support of the trap during the loading phase. If the electrospray is kept in operation for sufficiently long times, the stray field can become quite strong even allowing for trapping in the z-direction without any additional endcap potential and providing a trap frequency in this axis of the order of ~ 100 Hz. To verify this description we inverted the sign of

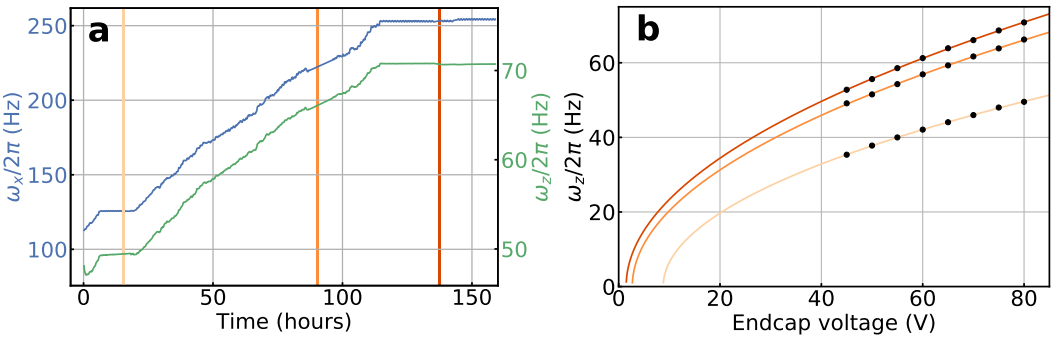

Figure 4.19: (a) Measurements of secular frequencies monitored over 6 days. $\omega_x/2\pi$ is shown on the left ordinate (blue dataset), $\omega_z/2\pi$ on the right one (green dataset). The three colour bands mark the time at which the charge-to-mass ratios were measured and are shown in Fig. 4.19 (b). (b) Fits of the charge-to-mass ratios at different times by changing the end-cap voltage and monitoring the secular motion along the z-axis. The different times correspond to 15, 90 and 137 hours, with charge-to-mass ratios of 0.10 C/kg, 0.16 C/Kg and 0.18 C/kg, respectively, shown going from lighter to darker colours. The stray field is anti-trapping (negative effective potential for a positively charged particle) as it needs to be compensated with a positive voltage to trap the particle. The strength of this stray field decreases over time.

the high voltage for the electrospray needle for a given time, to neutralise the charge build-up, to then go back to the usual configuration. As expected we found that in such a situation, the stray field given by the electrospray is anti-trapping; meaning more endcap potential is needed to trap the particle, as it is shown in Fig. 4.19 (b). Furthermore, its strength is slowly decreasing as mentioned above.

4.6.2 Potential stability

Right after turning the ion gauge off, we have observed an exponential decay in the trapping field with a time constant of approximately 10 hours. This characteristic time, consistently measured over tens of traces is likely to be due to the dielectric material used. Dielectric surfaces should therefore be kept in any trap as far as possible from the nanoparticle. Some of the charging effects during the loading phase could be mitigated by using both a bent and longer guide, or by using a loading mechanism free of solvent [94, 99]. In Fig. 4.20 (a), we show the stability of the secular frequencies along the x and z-axis right after turning the pressure gauge off. The exponential rise along the z-axis has a characteristic time of 10.7 hours. A very periodic modulation (period of $\sim$30 mins) can be seen in the secular frequency along the x-axis. This modulation is correlated to changes in the temperature of the room as shown in Fig. 4.20 (b), and is fully attributable to temperature induced changes in the amplitude of the signal generator, high voltage amplifier and other electronics used to provide the trapping AC field. This corresponds to a slow modulation of approximately 1 V (peak to peak) in the amplitude of the signal applied to the trap electrodes (0.2% of the applied signal). Those drifts could easily be reduced with a better temperature stabilisation. In Fig. 4.20 (c), we show the average position in the x-z plane over time for the same data as shown in Fig. 4.20 (a). One sample corresponds to 2.5 mins. The time is shown with a colour gradient, starting with black at $t = 0$, and ending in yellow at $t = 23$ hours. Correlations can be seen between the drifts in the secular frequency along the z-axis and the motion along the same axis. The same can be noticed along the x-axis. This shows that the same potential drifts are responsible for both changes in the mean position of the nanoparticle in the trap as well as its secular frequencies. Lastly, we show in Fig. 4.20 (d) the relative Allan deviation $\sigma_\omega(\tau)/\omega_o$ of the two secular frequencies monitored for 23 hours with ω_o the averaged frequency. The Allan deviation is calculated on the frequency time

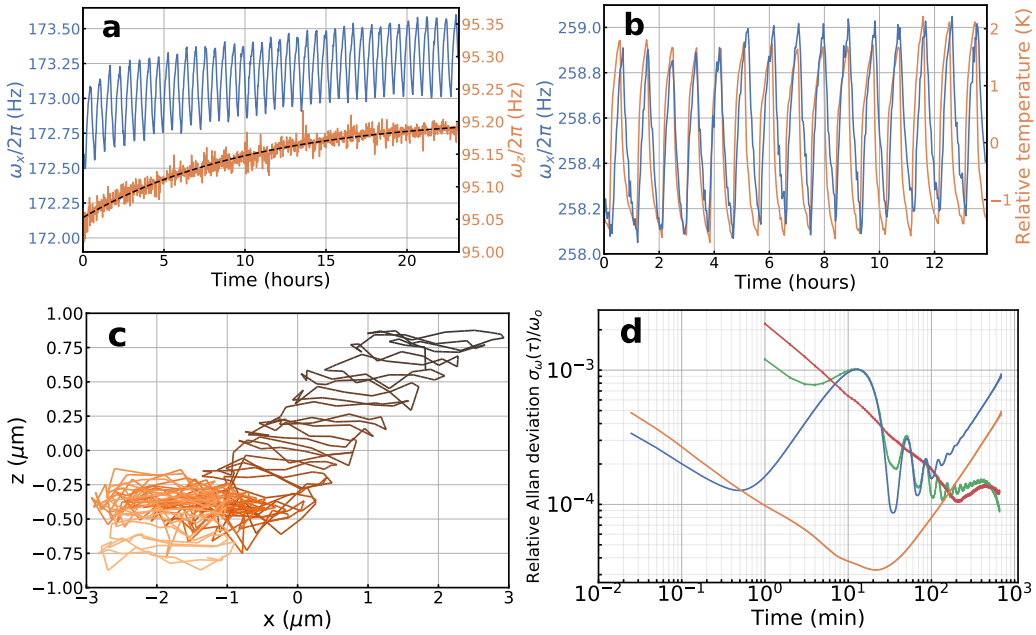

Figure 4.20: (a) Measurement of the secular frequency over time along the x (z-axis) is shown in blue (orange) while keeping the particle at a pressure of 1.6×10^{-5} mbar. The measurements are taken right after turning the pressure gauge off. An exponential rise of 10.7 hours is fitted along the z-axis (fit shown in black dotted lines). (b) A plot of the temperature drifts of the room (in orange) and of the secular frequency (in blue) along the x-axis at the same time. (c) Measurements of the drifts of the particle mean position over time (from dark colours to light ones) in the trap along the x and z-directions for the same data set as the one shown in (a). (d) The relative Allan deviation of the secular frequency along the x-axis (z-axis) is shown in blue (orange) at 1.6×10^{-5} mbar and in green (red) at 7.2×10^{-2} mbar. *Note:* The data shown in (a), (c) and (d) at 1.6×10^{-5} mbar are from the same data set with the same particle as the one characterised in Section 4.3.

traces shown in Fig. 4.20 (a). We get in this case a frequency stability of more than 20 min with a relative uncertainty on the frequency of ∼30 ppm along the z-axis (orange line) and with overall drifts of 60 ppm/h. Along the x-axis (blue line), we recover the periodicity (∼30 mins) also shown in Fig. 4.20 (a), as the frequency periodically gets closer to its initial value. We show in Fig. 4.20 (d) the stability of the frequency along the z-axis (x-axis) at 7.2×10^{-2} mbar. These data cover 32 hours of continuous acquisition that started 33 hours after having turned off the pressure gauge, to ensure a better stability. As expected, longer optimal times of at least 5 hours were obtained. The optimum time is likely to be even longer since the drifts are not yet limiting the Allan deviation. Furthermore, the behaviour above 500 mins is likely to be caused by aliasing of the frequency fluctuations.

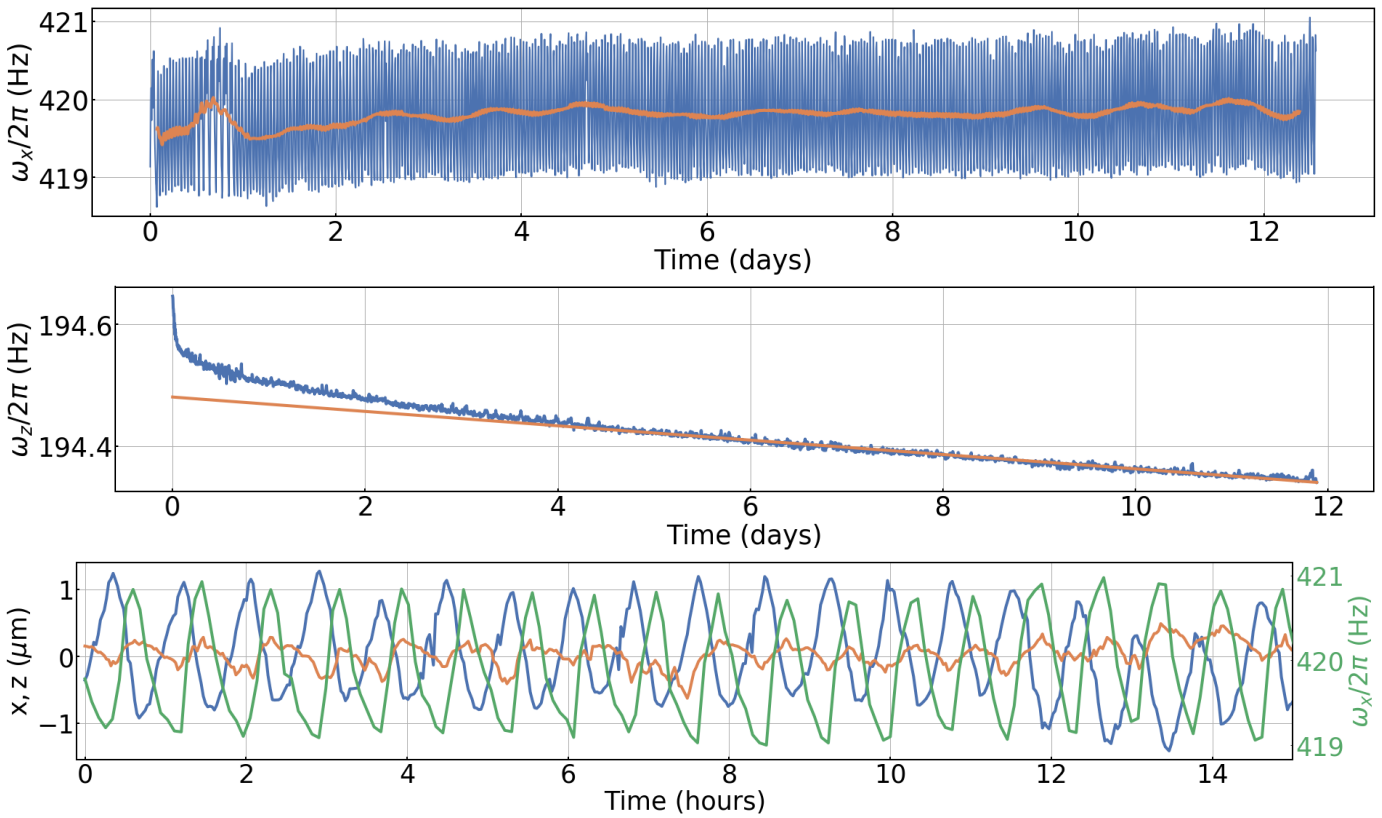

Figure 4.21: Continuous monitoring of the secular frequencies and the particle position over more than twelve days at a pressure of 8.7×10^{-7} mbar. (Top) Secular frequency along the x-axis, in blue. In orange, same averaged over 3.6 hours. (Middle) Secular frequency along the z-axis. Drifts of 2.4 ppm/h are measured between the 4th and 12th day (fit in orange). (Bottom) Motion of the particle along the x-axis (z-axis) in blue (orange) and secular frequency along the x-axis in green. This set is a zoom of the above figure starting at day 9.9. This particle is a single nanosphere of measured mass of $(5.0\pm0.1)\times10^{-17}$ kg with (216 ± 22) individual charges. *Trap parameters:* AC drive of 500 V (peak-to-peak) at 3.0 kHz and endcaps of 120 V.

Lastly we were able to monitor the nanosphere motion and secular frequencies over more than twelve days as shown in Fig. 4.21 demonstrating a constant number of charges. The pressure gauge was turned off at the beginning of the time trace. Frequency stability as good as 2.4 ppm/h is obtained (see Fig. 4.21(Middle)). This demonstrates, that despite the use of a dielectric and the different stray fields mentioned above, a competitive frequency stability can still be achieved [99]. Moreover the position stability in two directions is smaller than $\sim 2\mu$m (see Fig. 4.21 (bottom)). This is satisfying for our optomechanical experiments since those drifts have to be kept smaller than the cavity waist of 62 μm by at least one order of magnitude to reduce the amount of alignment required of the relative trap and cavity positions.

4.6.3 Micromotion compensation

As discussed above, stray fields due to imperfections of the electrodes, ions created by the pressure gauge and both charges and charged nanoparticles accumulated during the loading phase, modify the potential. This effect can locally be modelled by a DC electric field as described in Section 3.1.1. This causes the particle average position to be different from the actual AC centre of the field and causes excess micromotion which can be seen in the PSD of the motion with a peak at the drive frequency as shown in Fig. 3.2(b). Those DC fields in the radial direction of the trap are compensated by adding DC voltages on two of the four rods of the trap (on one AC electrode and one DC electrode). The most effective method found is to

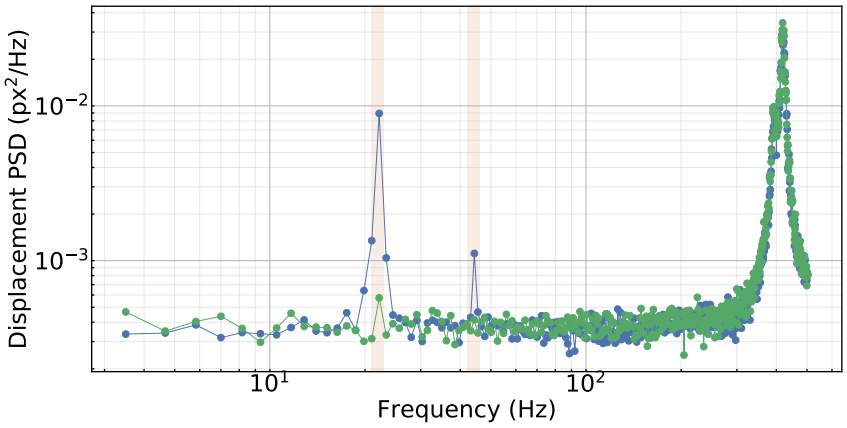

Figure 4.22: Compensation of the micromotion. PSD of the particle displacement along the x-axis at 6.3×10^{-2} mbar. In blue before compensating the micromotion, in green after compensation. The camera frame rate is 1011.67 fps and the micromotion, (at the drive frequency of 3 kHz) is seen aliased at 22 Hz and its first harmonic at 44 Hz.

adjust the DC compensation voltages so that the nanosphere remains at the same position while changing the trap stiffness (by changing the AC amplitude). The particle average position can be monitored at the same time by using the imaging method discussed above. We show a PSD of the motion of the nanosphere with and without compensation of the micromotion in Fig. 4.22. As it can be noticed, by applying DC voltages on two adjacent RF electrodes, we can correct for the spurious electric fields and bring the nanosphere mean position to the effective RF centre of the field. By doing so, we reduce the excess micromotion which can be seen in the PSD in the reduction of the peaks at the micromotion and its harmonics (in practice here, seen at aliased frequencies). We typically apply $\sim$2 V on both compensation electrodes and while using the camera we are able to optimise the micromotion with a voltage resolution on the electrodes down to $\sim 10\,\mathrm{mV}$.

4.7 Summary

To summarise, we have demonstrated an imaging method for low-frequency oscillators. This method can be improved by using super-resolution algorithms which enable us to demonstrate displacement sensitivities better than $10^{-16}\,\mathrm{m}^2/\mathrm{Hz}$. This technique was then applied to estimate a force sensitivity for our levitated nano-oscillator better than $\sim 1\,\mathrm{aN}/\sqrt{\mathrm{Hz}}$. Precise knowledge of the mass and number of charges might be relevant to many experiments to calibrate the temperature or the force-noise sensitivity for instance. We have discussed different methods to estimate the mass. A common method consists in measuring the gas damping as a function of pressure. Unfortunately, this method has the drawback of depending on the knowledge of the particle shape and density. Smaller uncertainties in the mass estimation were obtained by monitoring charge jumps in the secular frequency. Lastly, by using the imaging method we obtain a mass uncertainty of $\sim$3%. The knowledge of the trap geometry can be used to estimate the nanosphere charge-to-mass and therefore the number of charges on the nanosphere. The imaging technique was then used to monitor temperature and frequency stability of the nanosphere. This enables us to quantify the stability of the trap over time as well as study the effect of the loading mechanism and pressure gauge on the trapping potential. After more than 12 days of continuous measurement we were able to report a frequency stability of $\sim 2\,\mathrm{ppm/hr}$ similar to those reported with mass-spectrometers loaded with

nanoparticles [99]. In the next chapter, we use the imaging method presented here to measure ultra-narrow mechanical linewidths.

Chapter 5

Ultra-narrow linewidth levitated nano-oscillator

A fundamental property of any oscillator is its linewidth and mechanical quality factor Q. Narrow linewidths in the microHertz regime and mechanical Q-factors as high as 10^{12} have been predicted for levitated systems [24]. This motivates studying those systems in the quantum regime since this means that the lifetime of a quantum state of the mechanical state would be of the order of $\sim 3 \times 10^5$ s for an oscillator with frequency of oscillation at 100 kHz. However, the poor stability of these oscillators over long periods, coupled with their tendency to operate in anharmonic/non-linear regimes has prevented direct measurement of the predicted narrow linewidths in high vacuum. For many levitated systems, the measured linewidths deviate from those predicted even at moderate vacuum in the 10^{-4} to 10^{-5} mbar range [41, 104, 115]. The reduction of noise introduced by the levitating fields is a key challenge for achieving a stable oscillator. A fundamental limiting noise for optical levitation is the recoil of photons from the levitation laser itself [42], while internal heating via absorption of laser light leads to motional heating [118]. In contrast, a charged nanoparticle that is levitated using electrodynamic fields within a Paul trap, is an attractive levitated system as it is free from recoil induced heating as only low light intensities are required for detection. In addition, large well depths in excess of 5×10^3 eV (see Section 3.2.2.4) allow operation of the trap in the harmonic regime, even for temperatures exceeding 300 K. We demonstrated in the previous chapter that the charge on a levitated nanosphere in the Paul trap was stable over many weeks of measurement allowing stable oscillation frequencies limited only by the

noise and drifts in the applied electric fields and environmental disturbances.

Here we report on a levitated nanoparticle oscillator operating at pressures down to 10^{-7} mbar in a room temperature environment. We outline the application of a phase sensitive detection method that allows us to remove the small residual variations in the trapping potential over the very long timescales required to measure an ultra-low linewidth of $(81 \pm 23)\,\mu$Hz. This is one of the narrowest linewidths measured for a mechanical oscillator alongside recent works with larger particles [123, 124] and paves the way for future precision experiments using levitated systems. We also characterise the important noise sources for this oscillator and outline a means to achieve even lower linewidth measurements and higher Q-factors.

5.1 Linewidth measurement

For this experiment a single nanosphere of 230 nm radius was used in the miniature linear Paul trap introduced in Section 3.2.2. The position of the particle as a function of time was determined from fast imaging of the particle illuminated by a low intensity laser beam ($20\,\mathrm{W/m^2}$, see Section 4.1 for more detail). Using the camera, we track the motion along two axis. The z-axis is defined along the Paul trap axis and the x-axis, which corresponds to the projection of one of the radial motions (see Fig. 4.1 for axis definition). This low intensity guarantees that the particle is not perturbed and that the internal temperature remains close to 300 K (see Section 2.3.4). Additionally, shot noise recoil heating from the probe beam is also negligible (see Section 2.3.3). At relatively high pressures the damping rate can be accurately measured, even for large particles (i.e. $\sim 130\,\mu$m). However, as the pressure is reduced, it becomes increasingly difficult to perform accurate direct measurements. There are many examples in the literature demonstrating a saturation of the linewidth for levitated systems [41, 104, 115]. Spectral estimation requires continuous monitoring for time scales much longer than the correlation time ($2/\gamma_m$, see Section 2.1.1) with the implicit requirement that the drifts $\delta\omega_i$ in the trap frequency ω_i are smaller than the linewidth γ_m ($\delta\omega_i \leq \gamma_m$). On the other hand, for long correlation times, time-resolved techniques, which consist in measuring the relaxation time of the system, are usually preferred [94]. However, this approach requires driving the particle to large amplitudes in order to achieve a good signal-to-noise ratio which could lead to particle loss and, more often, to the exploration of highly non-linear

regions of the trap potential.

The frequency stability in our trap is of the order of $\delta\omega_o/\omega_o = 0.003$ over a time scale of an hour. This is dominated by thermal drifts in the electronics that supply the electrode voltages as well as slowly varying stray fields (see Section 4.6.2). At the lowest pressures, this frequency drift is much larger than the expected linewidth. Furthermore, the behaviour along the two axis is significantly different. Along the trap axis (z-axis in Fig. 3.1) the resonance (mean frequency $\omega_z/2\pi = 97\,\text{Hz}$) goes through a slow smooth drift, while in the orthogonal direction (x-axis, mean frequency $\omega_x/2\pi = 185\,\text{Hz}$) there is an additional periodic modulation of $\delta\omega_x/2\pi = 0.25\,\text{Hz}$ with a period of roughly an hour. This can clearly be seen in Fig. 5.1, where we show the displacement PSD along both axes at two different pressures ($P = 10^{-4}\,\text{mbar}$ (red curves) and $P = 2\times10^{-5}\,\text{mbar}$ (blue curves)). The effect of the frequency drift/modulation in the x-axis is evident by the flattening of the spectral profile. Even along the z-axis, where the PSD is not strongly perturbed, the conventional spectral approach yields a reliable linewidth measurement only at higher pressures.

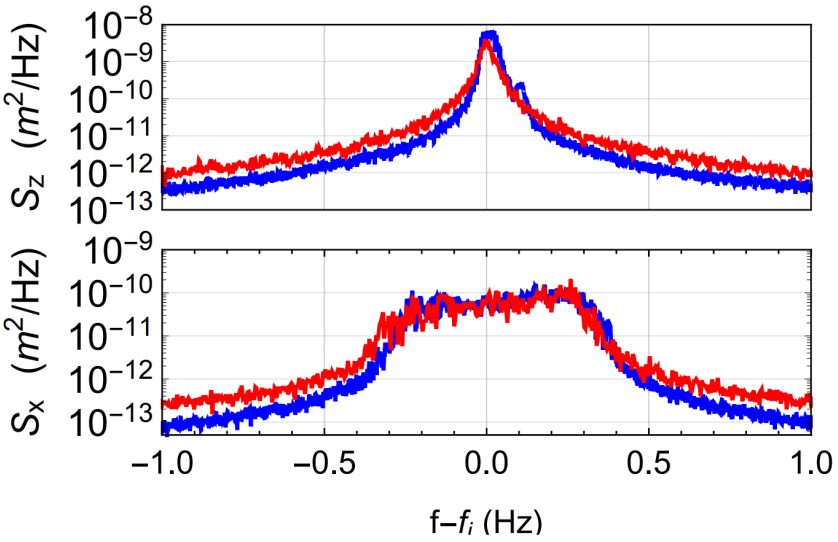

Figure 5.1: Displacement PSD of a trapped nanoparticle along the two degrees of freedom monitored. The PSDs refer to two pressures $P = 10^{-4}\,\text{mbar}$ (red) and $P = 2\times10^{-5}\,\text{mbar}$ (blue). The linewidth measured exploiting the R^2 spectra are respectively $(28.5\pm0.7)\,\text{mHz}$ and $(7.5\pm0.5)\,\text{mHz}$.

5.2 Numerical phase-sensitive detection

We remove the problems related to the trapping potential stability by implementing a numerical phase sensitive detection. To this end, it is convenient to move to a frame rotating at the mechanical frequency ω_i. The motion $u_i(t)$ along any axis, i, can be decomposed into two quadratures $X_i(t)$ and $Y_i(t)$ according to $u_i(t) = X_i(t)\cos(\omega_i t) + Y_i(t)\sin(\omega_i t)$. This approximation neglects fast rotating terms at $2\omega_i$, however, it is well known that this is a very good approximation for high-Q oscillators for which changes of the quadratures amplitude happen adiabatically with respect to the potential. To simplify the notation, we consider only one degree of freedom and denote its resonance frequency by ω_o. If $\gamma_m \ll \omega_o$, the dynamical equations for the slowly varying quadratures are [114]

$$\dot{X} + \frac{\gamma_m}{2} X = \frac{1}{m\omega_o} f^{(1)}, \tag{5.1}$$

$$\dot{Y} + \frac{\gamma_m}{2} Y = \frac{1}{m\omega_o} f^{(2)}, \tag{5.2}$$

where $f^{(k)}$ are stochastic force terms with autocorrelation functions $\langle f^{(k)}(t) f^{(j)}(t')\rangle = \delta_{kj}\delta(t-t')S_F/2$, assuming a delta-correlated force noise F, with PSD S_F, driving the oscillator. The spectra of the two quadratures are then $S_X(\omega) = S_Y(\omega) = \frac{S_F}{2(m\omega_o)^2}\frac{1}{\omega^2+\gamma_m^2/4}$. Experimentally, these PDSs are obtained by implementing a numerical lock-in amplifier, where we demodulate the displacement signal $u_o(t)$ at a frequency ω_{LO} and filter out the fast varying components at $2\omega_o$. The two quadratures are still affected by changes of the trap frequencies or by a frequency difference between ω_o and the reference rotation ω_{LO}; if $\omega_o = \omega_{LO} + \delta\omega_o$ their spectrum will be given by a low frequency Lorentzian peak centred at $\delta\omega_o$. Of course, any time dependence of ω_o will be mapped on $\delta\omega_o$ leading to a broadened peak and a linewidth estimation that is incorrect or impossible. However, frequency drifts or offsets are removed if we look at the amplitude quadrature $R = \sqrt{X^2+Y^2}$. This can be understood with a simple heuristic argument. Let us consider an almost sinusoidal signal $u(t) = A(t)\cos(\omega_o t + \phi(t))$ with a slowly varying amplitude and phase. After demodulation and low pass filtering the two quadratures will be

$$X(t) = \frac{1}{2}A(t)\cos(\phi(t)), \tag{5.3}$$

$$Y(t) = -\frac{1}{2}A(t)\sin(\phi(t)), \tag{5.4}$$

as long as $|\frac{d\phi(t)}{dt}| \ll \omega_o$, i.e., adiabatic phase fluctuations. The amplitude quadrature is then given by $R(t) = \sqrt{X(t)^2 + Y(t)^2} = A(t)/2$ which is unaffected by the slow phase fluctuations $\phi(t)$. Obtaining an analytical expression for the amplitude quadrature spectrum $S_R(\omega)$ is not trivial, however, neglecting the time dependence of ω_o, it is possible to evaluate analytically the PSD of $S_{R^2}(\omega)$ which is given by [125]

$$S_{R^2}(\omega) = \frac{8}{\gamma_m}\frac{1}{\omega^2 + \gamma_m^2}\left(\frac{S_F}{2m^2\omega_o^2}\right)^2. \tag{5.5}$$

Importantly, Eq. 5.5 holds even for an oscillator with a slowly varying resonance as can be shown numerically and as we demonstrate experimentally in the following.

In contrast to what was shown in the previous section, the linewidth can be determined from the PSD of R^2 as shown in Fig. 5.2(a), (b) and (c) for different pressures along the x-axis. Also shown is a fit to the data using Eq. 5.5. The smallest linewidth measured is $(81 \pm 23)\,\mu$Hz (fit shown in Fig. 5.2(c)). The linewidth follows the expected behaviour from gas collisions very well despite the frequency modulation that was clearly visible in the conventional PSDs in Fig. 5.1(bottom). We point out that the modulation in the secular frequency $\delta\omega_x$, at the lowest pressure, is 2500 times larger than the linewidth γ_m. This illustrates the utility of this method for

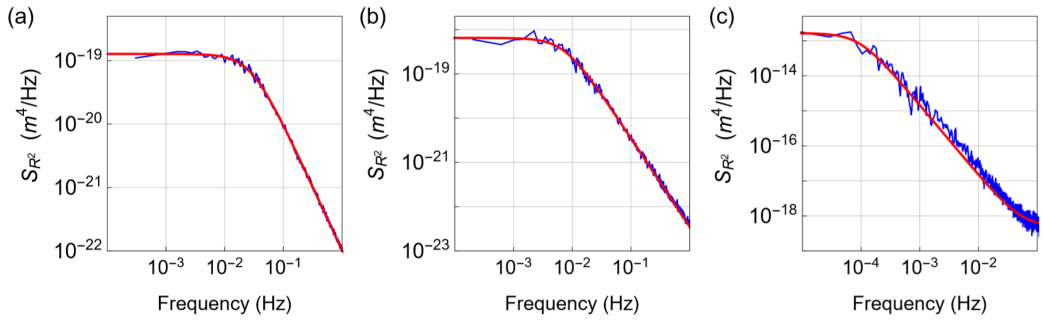

Figure 5.2: Panels (a), (b) and (c): PSD of the square amplitude quadrature for the motion along the x-axis along with a fit following Eq. 5.5 for different pressures $P = 9\times10^{-5}$, 2×10^{-5} and 3×10^{-7} mbar, respectively.

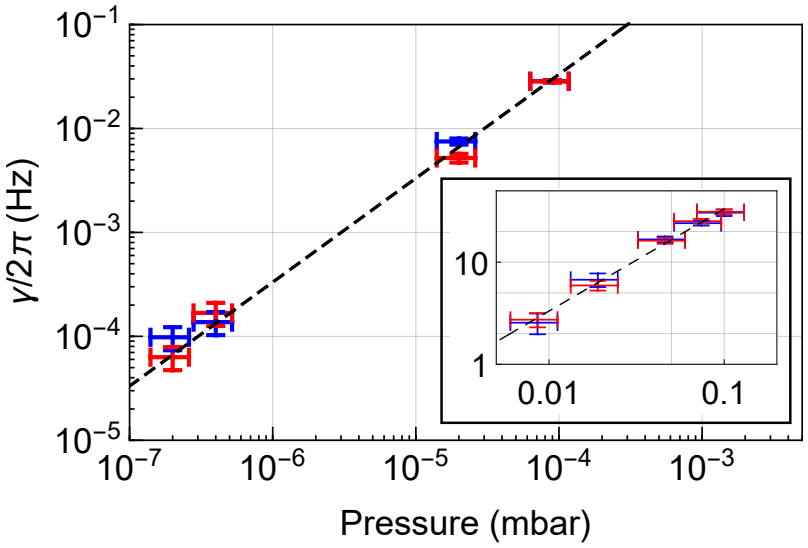

Figure 5.3: Measured linewidths as a function of pressure along both x-axis (blue) and z-axis (red) obtained from the R^2 spectra. Inset: linewidth measured at high pressure by standard spectral analysis. The dashed line is a fit of the expected $\propto P$ behaviour. Only the data in the inset have been used for the fit.

extracting narrow linewidths in the presence of slow, large modulation and drifts in the trap frequency. To test the accuracy of this approach, we can compare the linewidths obtained from the R^2 spectra to the ones obtained from the conventional method consisting of directly fitting the PSD. This last method works only at high pressures because of the frequency drifts, but the linear fit can be extrapolated down to low pressures. This is shown in Fig. 5.3 where the linewidths along the two monitored axes are fitted separately. All the low pressure measurements are consistent with the expected behaviour.

Our nanoscale oscillator, with a Q-factor of 2.3×10^6, compares well with the highest Q-factors ever reported for relatively low frequency oscillators, particularly for operation at room temperature. On a similar experimental system, a Q-factor of 1.5×10^5 has been previously demonstrated [94]. A Q-factor of 1.3×10^7 was later reported for a particle of $27\,\mu$m radius at $P = 5.7 \times 10^{-5}\,$mbar and kept at $4\,$K [124]. For clamped oscillators, the most notable ones are balanced torsional oscillators [126] where Qs of almost 10^6 are reached for higher oscillation frequencies of a few kHz. A single-crystal silicon oscillator has demonstrated a linewidth of $\sim 500\,\mu$Hz at $300\,$K [127] and a Q-factor of 4×10^7. For all clamped systems, however, only a very limited number of normal modes have such high Q-factors. This is in stark

contrast with the levitated case described here where all three translational degrees of freedom of the oscillator experience the same dissipative forces, while the internal modes are completely decoupled as the lowest modes have frequencies greater than GHz [128].

5.3 Bounds on excess damping

The linewidth as a function of pressure, averaged between the two degrees of freedom, are fitted with a simple line, i.e., $\gamma_m = \gamma_{\text{exc}} + k\,P$, to allow the estimation of a possible excess damping γ_{exc} due to additional dissipative mechanisms other than gas damping. The fit is shown in Fig. 5.4 along with the 95% confidence bands. With the same confidence level we find $\gamma_{\text{exc}}/2\pi = (18 \pm 30)\,\mu$Hz which is consistent with zero, confirming that only gas damping is affecting the particle dynamic.

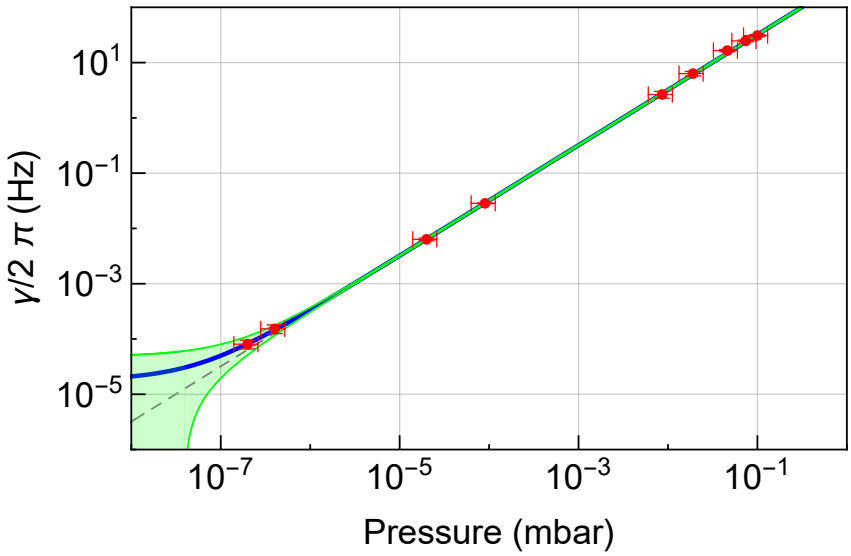

Figure 5.4: Linewidths averaged over the two degrees of freedom measured and with a linear fit (blue) and 95% confidence bands (green). Also shown is the fit assuming no excess damping (dashed-grey)

5.4 Paul trap noise

We show in Fig. 5.5 (a), (b) and (c) histograms of the amplitude quadrature at different pressures. They correspond to the well known Rayleigh distribution $\mu(r,\sigma_i) = r/\sigma_i^2 e^{-r^2/2\sigma_i^2}$ with mean and variance given by $\langle\mu\rangle = \sqrt{\pi/2}\sigma_i$ and $\sigma_\mu^2 = (4-\pi)\sigma_i^2/2$, respectively [129]. Indeed, the X and Y quadratures of a thermal state are normally distributed with zero-mean and are independent. In this case, it can be shown that the amplitude quadrature variable $R = \sqrt{X^2+Y^2}$ follows a

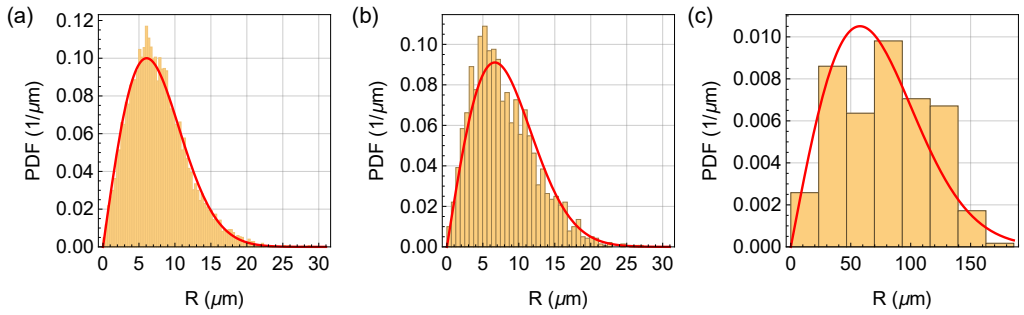

Figure 5.5: Panels (a), (b) and (c): Probability density functions (PDF) of the amplitude quadrature R for the same respective datasets as in Fig. 5.2. A fit to the distribution is shown in red. Each dataset corresponds to a continuous acquisition close to one day.

Rayleigh distribution [129]. If the motion along the i-axis is in thermal equilibrium with the environment we simply have $\sigma_i^2 = k_B T_b / m\omega_i^2$, which is the usual thermal variance for an harmonic oscillator. The three data sets have a similar total observation time of the order of one day. This implies that the number of statistically independent points significantly drops when the pressure is reduced to the minimum value. The number of independent samples goes from approximately 10000 at $P = 9 \times 10^{-5}$ mbar to 100 at $P = 3 \times 10^{-7}$ mbar as can clearly be observed in Fig. 5.5 (a) and (c). We exploit the properties of the Rayleigh distribution to verify that the sample size is big enough to be representative of the distribution. The first two moments allow an estimation of the motional variance which can be compared with each other. Specifically, at $P = 9 \times 10^{-5}$ mbar we have $\Delta\sigma_i / \langle\sigma_i\rangle = 0.005$ while at $P = 3 \times 10^{-7}$ mbar we find $\Delta\sigma_i / \langle\sigma_i\rangle = 0.08$ which is in line with what is expected (with $\langle\sigma_i\rangle$, the mean of the σ_i values calculated over independent sets of R values and $\Delta\sigma_i$ the standard deviation of the σ_i values). Indeed, the relative difference of the two estimators should scale as the square root of the sample size. It is clear, from both the PSD spectra and the Rayleigh distributions of Fig. 5.2 and 5.5, that the variance of the stochastic motion increases as the pressure is reduced. This behaviour is also shown as an increase in the effective temperature as the pressure is reduced in Fig. 5.6.

Here we plot the effective temperature (see Chapter 4) along both trap axes as a function of pressure. This calibration does not rely on the assumption of thermal equilibrium at room temperature but exploits the absolute calibration available from

using the camera (see Section 4.1.2). For the high pressures ($P > 10^{-3}$ mbar), the mean effective temperature is $\langle T \rangle = (293 \pm 3 \pm 25)$ K, where the systematic error comes from the uncertainty in the mass measurement. The excess force noise leads to an increase in effective temperature that varies inversely with pressure. A fit to the average temperature on the two axes gives $T_{eff} = 293(1 + 7.3 \times 10^{-6}/P)$. We obtain a value for the excess force noise from the PSD of $S_F \approx 1 \times 10^{-38}\,\mathrm{N^2/Hz}$. For the nanoparticle illuminated by the detection beam, the back action due to photon recoil is approximately $4 \times 10^{-43}\,\mathrm{N^2/Hz}$ (see Section 2.3.3) which is insignificant compared to the thermal noise of $10^{-40}\,\mathrm{N^2/Hz}$ at 10^{-7} mbar. This excess noise is consistent with a measured voltage noise from the high voltage amplifier amplifier used to drive the AC electrodes[1] $\sqrt{S_V} \approx 200\,\mu\mathrm{V}/\sqrt{\mathrm{Hz}}$ and a nanoparticle position in the transverse direction of the trap of $\sim 100\,\mu$m (consistent with observation when the particle position is not centred in the transverse direction of the trap as described in Section 4.6.3). The voltage was then evaluated using the formula described in Section 3.2.2.3 in the case of correlated noise (correlated since identical noise on both AC electrodes) for a particle with an estimated number of 80 elementary charges.

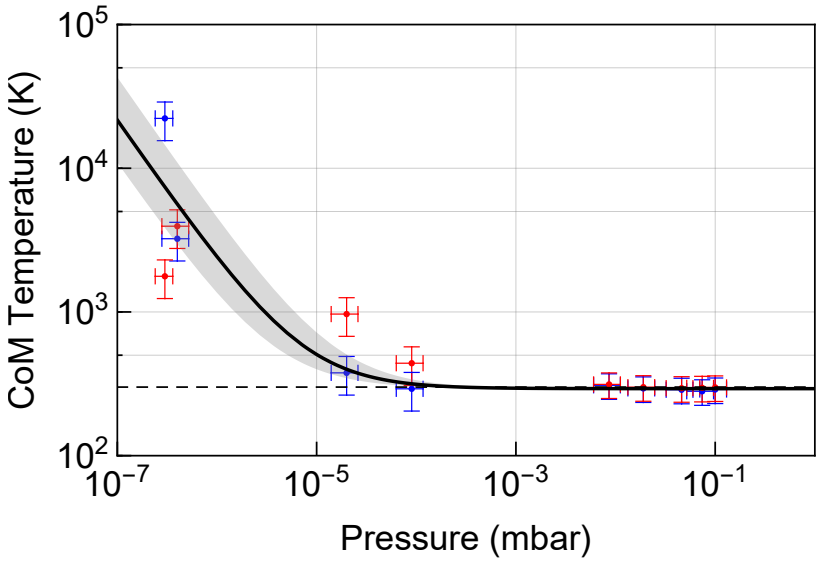

Figure 5.6: Centre-of-mass effective temperature as a function of pressure along both x-axis (blue) and z-axis (red). The average between the two degrees of freedom is fitted assuming a $1/P$ contribution that would rise from a white nonthermal force noise. A 3 dB temperature increase occurs at $P = 7.3 \times 10^{-6}$ mbar. Dashed grey line marks the measured room temperature of 293 K.

[1] Voltage noise of the Trek 2220 below 10 kHz.

5.5 Summary

To summarise, we have demonstrated a novel phase-sensitive technique to measure the intrinsic linewidth of an oscillator with varying frequency. This method can be applied to any oscillator with high Q-factor and frequency drifts or, conversely, phase fluctuations $\phi(t)$ satisfying $|\frac{d\phi(t)}{dt}| \ll \omega_o$ with ω_o the oscillator frequency. Though frequency drifts can be mitigated, requirements on the electronics to maintain a stable secular frequency in a Paul trap down to $\sim 10\,\mu$Hz would be complex. This method was demonstrated to measure a linewidth of $\sim 80\,\mu$Hz corresponding to a Q-factor of 10^6 and dissipation solely provided by gas damping. In the case where the nanosphere would be trapped optically with a trap-frequency of $\sim 100\,$kHz, this would have corresponded to a Q-factor of 10^9. In the next section, we apply those results to dissipative collapse models. This demonstrates the utility of the method discussed here for future precision experiments that aim to test the macroscopic limits of quantum mechanics [36, 37]. We use as well this method in Chapter 8 to estimate the total effective damping given by the sum of the gas damping and optical damping provided by the optomechanical interaction.

Chapter 6

Testing wavefunction collapse models with a levitated oscillator

The measurement postulate in quantum mechanics is in stark contrast with the linear Schrödinger equation since inconsistent with each other. Moreover it introduces a clear distinction between a microscopic scale obeyed by the laws of quantum mechanics and a classical macroscopic one, where the interaction with a quantum system is dictated by the measurement postulate. This postulate, needed to be consistent with observations, has been validated in numerous experiments and has enabled the development of quantum technologies which are directly relying upon it [130–132]. Wavefunction collapse models offer a phenomenological way of unifying both Schrödinger equation and measurement postulates. We use our current oscillator to confirm recently placed bounds on the most studied model: Continuous Spontaneous Localisation (CSL). Finally, we use the narrow linewidth measurements demonstrated in Chapter 5 to place new bounds in a novel way on the dissipative CSL and Diósi-Penrose models.

6.1 The measurement problem

Quantum mechanics, and its subsequent theories, is to this day the most validated physical theory [133]. The measurement of the electron magnetic moment has been shown to be in agreement within 11 digits of the theoretical prediction [134]. Moreover, no physical theory has been tested as much as quantum theory given its peculiar and distinctive behaviour. This leads the scientific community to a reasonable feeling of *faith* towards it as Roger Penrose states [133]. This feeling of *faith* is comforted by the *Copenhagen interpretation* of quantum mechanics where the wave-

function is viewed as a mathematical tool rather than a real entity. The collapse of the wavefunction, i.e. the action of the measurement process upon the wavefunction is a needed postulate which is in stark contrast with the linearity of quantum mechanics. Furthermore, it implicitly introduces different physical scales as the interaction between a quantum system and a larger system performing the measurement follows the measurement postulate rather than the Schrödinger dynamics. The contradiction between the linearity of quantum mechanics and the collapse process is disconcerting and has puzzled the main founders of quantum physics. A famous example is Schrödinger's cat. Heisenberg reported Schrödinger to have said "If all this damned quantum jumping were really here to stay then I should be sorry I ever got involved with quantum theory" [135]. According to Dirac, quantum theory is only at its preliminary stage [136]. Decoherence and the introduction of the density matrix by von Neumann has enabled precise calculations taking into account the effect of the environment on a quantum system. Rather than a pure state, when the environment is traced out, the system is described by a mixed state with a probability mixture of different measurement outcomes. While this is in practice a great tool, this formalism does not solve in any way the measurement problem as the predicted probability mixture needs to be updated once the measurement is performed [137, 138]. At this point, new theories or interpretations are needed. A popular theory (and very attractive from a science fiction prospective) is the many world interpretation which states that superpositions are not observed since they branch out in different worlds [139]. Another idea, and directly relevant to the work presented here, is the idea of collapse models where the quantum dynamics provided by the Schrödinger equation is modified with the slightest possible modifications to preserve the original quantum behaviour at a microscopic level while leading at the macroscopic one to the well-observed effective collapse of the wave-function.

6.2 Continuous Spontaneous Localisation model

The most studied collapse model is Continuous Spontaneous Localisation (CSL) [140–143]. It modifies the Schrödinger dynamics to become

$$d|\psi_t\rangle = \Bigg[-\frac{i}{\hbar}\hat{H}dt + \frac{\sqrt{\gamma}}{m_0}\int d\mathbf{x}\left(\hat{M}(\mathbf{x}) - \langle\hat{M}(\mathbf{x})\rangle\right) dW_t(\mathbf{x}) \\ -\frac{\gamma}{2m_0^2}\int\int d\mathbf{x}d\mathbf{y}G(\mathbf{x}-\mathbf{y})\left(\hat{M}(\mathbf{x}) - \langle\hat{M}(\mathbf{x})\rangle\right)\left(\hat{M}(\mathbf{y}) - \langle\hat{M}(\mathbf{y})\rangle\right)\Bigg]|\psi_t\rangle\,, \tag{6.1}$$

where γ is the collapse strength and m_0 the nucleon mass. The usual Schrödinger equation can be seen on the left hand side of the first line. Stochastic and non-linear terms are added to the dynamics. The stochastic term prevents superluminal signaling while the nonlinear term breaks the linearity of the Schrödinger equation and accounts for the localisation of the wavefunction. In this model, the collapse occurs in space (in the position operator basis). The nonlinear behaviour can be seen in the product in the second line. The stochasticity is introduced with a random Wiener process with zero mean, delta correlated in time and spatially distributed as a Gaussian distribution $\langle dW_t(\mathbf{x})dW_s(\mathbf{y})\rangle = \delta(t-s)G(\mathbf{x}-\mathbf{y})$ with $G(\mathbf{x}-\mathbf{y}) = \frac{1}{(4\pi r_C)^{3/2}}\exp[-\mathbf{x}^2/4r_C^2]$. In Eq. 6.1, $\hat{M}\mathbf{x} = m\hat{a}^\dagger(\mathbf{x})\hat{a}(\mathbf{x})$ refers to the mass density operator. Two important parameters characterise the model. The rate $\lambda = \frac{\gamma}{(4\pi r_C^2)^{3/2}}$ determines the rate of the collapse. The correlation length r_C determines the size of a superposition at which the collapse occurs. If a nucleon spatial superposition is much smaller than r_C, then the collapse is very unlikely to occur and other decoherence processes are more likely to be observed. On the other hand, if the superposition of a single nucleon is macroscopic (of a size much larger than r_C) then it collapses at a rate λ. The description so far only accounts for one single nucleon and places limits on the size of its possible spatial superposition. When it comes to an object constituted of many nucleons, the effective collapse rate of the centre-of-mass is amplified and can be shown to become $\Lambda = \lambda n^2 N$, with λ the previously described collapse rate of a single nucleon, n the number of nucleons contained in a sphere of radius r_C and N the number of such spheres [144]. This amplification mechanism, though with no known underlying origin, could therefore account for the fact that superpositions of a "large" object have not been observed to date. The two parameters characterising the model, λ and r_C, have to be found

experimentally. A standard procedure by GRW has been to consider $r_C = 10^{-7}\,\mathrm{m}$ [145], with the intuition that this scale is halfway between the human smallest scale ($\sim 0.1\,\mathrm{mm}$) and the inter-atomic scale ($\sim 10^{-10}\,\mathrm{m}$). At this value, a collapse of $\lambda = 10^{-16}\,\mathrm{s}^{-1}$ was considered, motivated by the hypothesis that only close to the macroscopic scale, the collapse mechanism would dominate over other phenomena. Another guess for the individual collapse rate at the same scale of $r_C = 10^{-7}\,\mathrm{m}$ was considered by Adler where $\lambda = 10^{-8}\,\mathrm{s}^{-1}$ [144]. With this much stronger value, the collapse becomes effective at mesoscopic scales where quantum physics measurements, and therefore wave-function collapse could occur. The CSL model is by definition experimental and exploration of the parameter space constrains possible values of both parameters. Two ways have been used to explore validity of possible parameters: directly (through matter wave interferometric measurements) and indirectly (with non-interferometric measurements). Interferometric methods consist in observing the coherence time of a given spatial superposition. The record (in size) of successful matter wave interferometry so far has been with a molecule consisting of more than 2000 atoms and weighting $\sim 4\times10^{-23}\,\mathrm{kg}$ [146]. Considering $r_C = 10^{-7}\,\mathrm{m}$, this experiment places the following constraint on the collapse rate $\lambda < 10^{-7}\,\mathrm{s}^{-1}$. Studies of the CSL dynamics formulated in Eq. 6.1 showed that the CSL stochastic behaviour leads to a stochastic force noise [147]. It can be shown that the white force noise PSD on a homogeneous sphere is given by [37] (single-sided PSD)

$$S_{CSL} = \frac{6\hbar^2 r_C^2 m^2}{m_0^2 r^6}\left[1 - \frac{2r_C^2}{r^2} + e^{-\frac{r^2}{r_C^2}}\left(1 + \frac{2r_C^2}{r^2}\right)\right], \tag{6.2}$$

where r and m are the particle radius and mass, respectively. Analysing force noises can therefore be used to place constraints on the CSL model. We use this method in the next section to place some experimental bounds on the CSL model.

6.3 Bounds on the CSL model

In this section, we use data of the particle motion at $8.6\times10^{-7}\,\mathrm{mbar}$ to estimate an excess force noise (additional to thermal force noise), with possible origin attributed to the force noise induced by the wavefunction collapse. This force noise is estimated given the thermal force noise, evaluated with the measurements of the linewidth, bath temperature and nanosphere mass.

Better control over the particle mean position along the transverse direction of the trap (see Section 4.6.3) enabled better cancellation of correlated Paul trap noise. In this case, at a pressure of 8.6×10^{-7} mbar, the motion was still thermal in both transverse and axial directions (same data set as the one shown in Fig. 4.21). This is in agreement with the expected voltage noise on the compensation electrodes of $S_V = 1\mu V/\sqrt{\text{Hz}}$. The nanosphere has an estimated 240 elementary charges which leads to an expected force noise of $S_F \approx 5 \times 10^{-40}\,\text{N}^2/\text{Hz}$. The thermal force noise from a bath at 293 K given the mechanical damping measured (see Fig. 6.1(right)) is $S_{F_{th}} \approx 10^{-39}\,\text{N}^2/\text{Hz}$, and should therefore be the main force noise contribution. We measure (from the area), an average temperature in the transverse direction of $T = (292 \pm 29)\,\text{K}$ where the uncertainty comes from the Allan deviation similarly to what is shown in Fig. 4.18, and in the axial direction of $T = (328 \pm 33)\,\text{K}$. This value is obtained after averaging over 11.2 days. We show in Fig. 6.1(left) the position distribution of the oscillator along the x-direction (from the same data set). A Gaussian fit to this distribution gives a temperature $T = (281 \pm 28)\,\text{K}$. In Fig. 6.1(right) we show a fit of the R^2 spectra of the motion along the x-direction (obtained after averaging over 11.2 days). The fit gives a value for the damping rate of $\gamma_m/2\pi = (259 \pm 26)\,\mu\text{Hz}$. The same fit along the axial direction gives $\gamma_m/2\pi = (279 \pm 28)\,\mu\text{Hz}$. The temperature can be as well estimated from the integral of the R^2 spectra and gives $(312 \pm 31)\,\text{K}$. The temperature measurement can be used in conjunction with the linewidth measurement to place a bound on excess noise above the thermal noise. Among those three measurements (in good agreement), we use the one averaged over the integrals of the PSD: $T = (292 \pm 29)\,\text{K}$. Taking into account that the experiment is performed at room temperature $T_b = (293 \pm 2)\,\text{K}$, we get an excess temperature along the x-axis smaller than $T_{\text{exc}} = 61\,\text{K}$ with a 95% confidence. An excess force noise therefore needs to be smaller than $S_{\text{exc}} = 4m\gamma_m k_B T_{\text{exc}} = 3.6 \times 10^{-40}\,\text{m}^2/\text{Hz}$.

When attributing this excess noise to CSL noise by using Eq. 6.2, we can exclude the λ and r_C parameters as shown as the blue area for this specific measurement in Fig. 6.2. The mechanical frequencies at which this excess noise is probed are $\omega_x/2\pi = 420\,\text{Hz}$ and $\omega_z/2\pi = 149\,\text{Hz}$. This improves bounds at similar frequencies placed by LIGO experiment, shown as a yellow line [148] (frequency band ranging

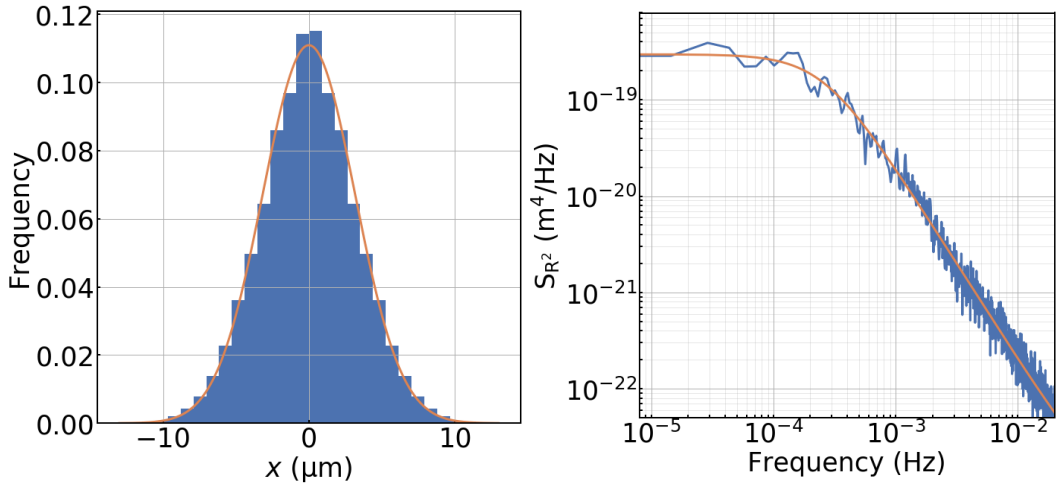

Figure 6.1: (left) Histogram of the oscillator position along the x-axis acquired over 11.2 days of measurement. The oscillation frequency is $\omega_x/2\pi = 420\,\text{Hz}$. The nanosphere has an estimated mass of $5.6 \times 10^{-17}\,\text{kg}$. In orange is shown a Gaussian fit of the distribution which gives an effective temperature $T = (281 \pm 28)\,\text{K}$. (right) R^2 spectra of the motion along the x-axis (spectra obtained with 14 averages). The fit (in orange) gives a linewidth $\gamma_m/2\pi = (259 \pm 26)\,\mu\text{Hz}$ consistent with the measured pressure of $8.6 \times 10^{-7}\,\text{mbar}$. The effective temperature estimated from the square root of the integral is $T = (312 \pm 31)\,\text{K}$.

from $\sim 50\,\text{Hz}$ to $\sim 1\,\text{kHz}$). A recent similar experiment excluded further bounds as shown in orange [123] ($\sim 10\,\text{Hz}$ oscillator). Another experiment with a cantilever (frequency of 8 kHz) and cooled to milliKelvin temperatures exclude even more the parameter space (brown line)[149]. This last measurement, has been extended with a specifically designed load, (frequency of 3 kHz) enabling further improvements over the parameter space (red area) [150]. At milli-Hertz frequencies, the LISA pathfinder experiment can exclude the area shown in green [148]. Additional heating from cold atoms enables to exclude the region shown in grey [151]. Other bounds tested at very high frequencies are shown in dashed purple and dashed red. The former is inferred by measuring the emission spectrum of Neptune [152]. The latter is inferred after analysing the X-ray spectrum from a Germanium sample [153]. Lastly, lower bounds are shown in black. Those values are excluded after theoretical considerations which would otherwise be in contradiction with the human experience of the macroscopic world [154]. The work presented here paves the way for using levitated nano-oscillators to test the CSL model. Further reduction of the voltage noise would enable the nanosphere to remain thermal at lower pressure (and lower bath temperature). At a pressure of $10^{-13}\,\text{mbar}$, and bath temperature of $T_b =$

300 mK, a thermal motion would give an upper bound of $\lambda \approx 10^{-12}\,\mathrm{s}^{-1}$ at $r_C = 10^{-7}$. In order to achieve those bounds, a very careful analysis of the noise contribution of the detection on the oscillator will be required, as detailed in theory in Ref. [37]. Moreover, mitigation of vibrational noise at those low frequencies will be critical.

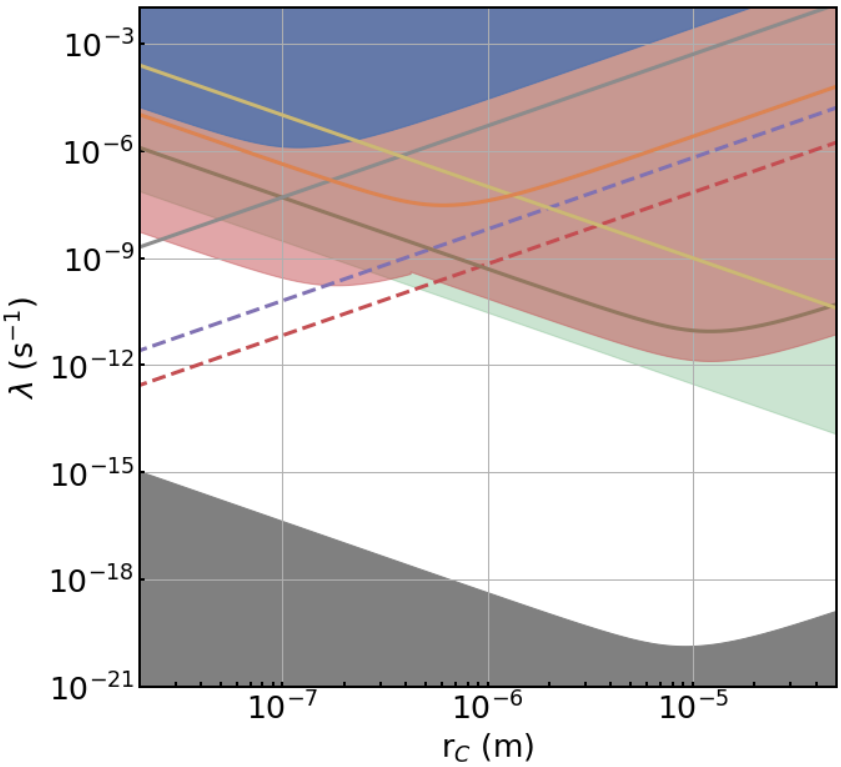

Figure 6.2: Current upper and lower bounds of exclusion of the CSL parameter space with non-interferometric measurements. This experiment excludes the CSL parameters within the blue area. Assuming the CSL force noise to be white, the remaining possible values to-date lie within the white area defined between the black area, green and red-dotted curve. They correspond to bounds provided by theoretical arguments [154], the LISA pathfinder experiment [148] and the X-ray spectrum from a Germanium sample [153], respectively. The other upper bounds correspond to experimental results given by LIGO in yellow [148], microspheres in orange [123], cantilever in brown and red area [149, 150], cold atoms in grey [151] and from the emission spectrum of Neptune in purple [152].

6.4 Bounds on dissipative collapse models

We now describe the use of our narrow linewidth oscillator, coupled with our ability to predict the simple variation of damping with pressure, to put new limits on two dissipative models for wavefunction collapse. This includes the dissipative continuous spontaneous localisation (dCSL) [155] and the dissipative Diósi-Penrose model (DP) [156]. Both the conventional CSL and DP models are not energy conserving

and dissipative versions have been proposed to remove the energy divergence due to the standard white CSL force noise. The additional dissipation determines a finite equilibrium temperature for any given system and an additional parameter T_{dCSL} is introduced which characterises the temperature of the collapse noise. In the dCSL framework, the force noise is no longer white, and for a nanoparticle it has a spectral density [157] $S_{\rm dCSL}(\omega) = \hbar^2\eta_{\rm dCSL}[1+\kappa^2 m^2(\gamma_t^2+\omega^2)]$, where $\gamma_t = \gamma_m + \gamma_{\rm dCSL}$ is the total damping rate and $\kappa = \gamma_{\rm dCSL}/2\hbar\eta_{\rm dCSL}$. In the limit of an infinite temperature the standard CSL is recovered. In the dCSL model the collapse strength, $\eta_{\rm dCSL}$, for a spherical particle of radius r and homogeneous density ρ is given by [157]

$$\begin{aligned}\eta_{\rm dCSL} =& \frac{3\lambda r_C^2 m^2}{(1+\chi_{\rm C})\, r^4 m_0^2}\Bigg[1 - \frac{2r_C^2\,(1+\chi_{\rm C})^2}{r^2} \\ &+ e^{-\frac{r^2}{r_C^2(1+\chi_{\rm C})^2}}\left(1+\frac{2r_C^2\,(1+\chi_{\rm C})^2}{r^2}\right)\Bigg],\end{aligned} \tag{6.3}$$

where m is the total mass of the system, m_0 is the nucleon mass, $\chi_{\rm C} = \hbar^2/(8m_a k_B T_{\rm dCSL} r_C^2)$, and $T_{\rm dCSL}$ is the thermalisation temperature. In the limit of no dissipation, $T_{\rm dCSL} \to \infty$, we have $\chi_{\rm C} \to 0$, and thus one recovers the collapse strength of the standard CSL model, $\eta_{\rm dCSL} \to \eta_{\rm CSL}$. On the other hand, in case of strong dissipation when $a \ll r_C(1+\chi_{\rm C})$, we obtain an approximate expression

$$\eta_{\rm dCSL} = \frac{m m_a \lambda r_C}{2a^3 m_0^2 (1+\chi_{\rm C})^2}\min\left[1, \frac{r^3}{r_C^3(1+\chi_{\rm C})^3}\right], \tag{6.4}$$

where m_a is the average mass of a nucleus ($\simeq$ average atomic mass), and a is the lattice constant [147]. Finally, the dissipation rate is given by $\gamma_{\rm dCSL} = \eta_{\rm dCSL} 4 r_C^2 \chi_{\rm C}(1+\chi_{\rm C}) m_a/m$.

The DP model has a structure quite similar to the CSL with the main difference being that the scale of the collapse strength is set by the gravitational constant G, thus introducing a stronger connection to gravity for the collapse mechanism. As this thesis is being written, the standard DP model has been ruled out [158]. The standard DP model is also not energy conserving, and a dissipative version has been proposed [156]. Since the collapse strength is fixed, the dissipative DP (dDP) model is characterised by only two parameters, namely, the temperature of the collapse noise $T_{\rm dDP}$ and a cut off distance R_0 which plays a similar role as r_C in the dCSL

model. The calculation for the dDP model, under the assumption of a homogeneous sphere, can be carried out similarly as for the dCSL model. Specifically, we find the following collapse strength:

$$\begin{aligned}\eta_{\mathrm{dDP}} =& \frac{Gm_a^2}{\sqrt{\pi}r^6\hbar}\Bigg[\sqrt{\pi}r^3\mathrm{Erf}\left(\frac{r}{R_0(1+\chi_0)}\right)\\ &+(1+\chi_0)R_0\Bigg\{r^2\left(e^{-\frac{r^2}{(1+\chi_0)^2R_0^2}}-3\right)\\ &+2(1+\chi_0)^2R_0^2\left(1-e^{-\frac{r^2}{(1+\chi_0)^2R_0^2}}\right)\Bigg\}\Bigg],\end{aligned} \tag{6.5}$$

where $\chi_0 = \hbar^2/(8m_a k_B T_{\mathrm{dDP}} R_0^2)$, and T_{dDP} is the thermalisation temperature. In the limit of no dissipation, $T_{\mathrm{dDP}} \to \infty$, we have $\chi_{\mathrm{dDP}} \to 0$, and the collapse strength of the standard DP model is recovered, $\eta_{\mathrm{dDP}} \to \eta_{\mathrm{DP}}$ [147]. Using a lattice model for the crystal structure we obtain an approximate formula for the case of strong dissipation, $a \ll R_0(1+\chi_0)$, given by

$$\eta_{\mathrm{dDP}} = \frac{Gmm_a}{6\sqrt{\pi}a^3\hbar}\min\left[1, \frac{r^3}{R_0^3(1+\chi_0)^3}\right]. \tag{6.6}$$

The damping rate for the dDP model is given by $\gamma_{\mathrm{dDP}} = \eta_{\mathrm{dDP}} 4R_0^2\chi_0(1+\chi_0)m_a/m$.

The CSL and DP family of models share many common features, among which the amplification of the collapse strength with the size of the system [156], as discussed in the previous section. Such an amplification mechanism is supposed to accomplish a dual task: on the one hand, agreement with the quantum mechanical predictions for very small systems, and on the other hand, that classicality emerges for large systems [159]. The amplification mechanism has its origin in microscopic derivations where the centre-of-mass dynamics of a bulk material is obtained starting from the dynamics of nucleons or nuclei. In the present case this is reflected in geometrical factors η_{dCSL} and η_{dDP} that describe the effect of the intensive and extensive properties of the system on the centre-of-mass dynamics. In the above formulae we have chosen the nuclei as the building blocks of the models, motivated by considerations about gravity in the Newtonian regime [160]. However, one could also postulate that the centre-of-mass motion is always in the single-particle form. In particular, one can require that the centre-of-mass dynamics depends only on

the total mass m of the system, but not on other intensive or extensive properties of the bulk system. This latter choice is suggestive of a hypothetical underlying theory of spontaneous collapse models, which includes notions of Einstein's General relativity [161]. In this latter case, one has that the collapse strengths are given by $\eta_{\mathrm{dCSL}} = \frac{\lambda m^2}{2m_0^2 r_C^2 (1+\chi_C)^5}$ and $\eta_{\mathrm{dDP}} = \frac{Gm^2}{6\sqrt{\pi}\hbar R_0^3 (1+\chi_0)^3}$, and the dissipation rates are obtained by replacing m_a with m and a with r in the corresponding formulae. The CSL and DP family of models usually discussed in the literature predict that the collapse strength for the centre-of-mass dynamics depends on the intensive and extensive properties of the bulk material, such as composition and shape. This is the version we consider for dCSL. On the other hand, we can also consider the dDP model in the single-particle version, which depends only on the total mass of the system, but not on any other property of the system. In the following, we consider this latter version of the dDP model, while our experiment does not put significant bounds on the former one.

Here we exploit a new and completely different approach to place bounds on the dissipative versions of those collapse models. We compare the theoretical predictions for the damping due to the collapse mechanisms to our measurements of extremely narrow linewidth presented in the previous section. This allows us to place significant constraints on the dCSL and dDP models. For the levitated oscillator the damping rate is well defined by the collisions with the surrounding gas and has a linear dependence with pressure. This allows us to extrapolate its value at zero pressure (see Fig. 5.4) and attribute it to the collapse process. We find an upper limit for the damping rate due to the collapse mechanisms of $\gamma_{\mathrm{dCSL}}/2\pi \leq 48\mu$Hz at the 95% confidence level which is compared to the predictions from the models. Exploiting this upper limit we derive new bounds for dCSL which are shown in Fig. 6.3(left). These new bounds assume different dCSL temperatures. When $T_{\mathrm{dCSL}} = 1$ K our bounds are comparable to existing ones [162]. However, when T_{dCSL} is reduced to 10^{-7} K [157] the excluded parameter space is significantly increased reaching a minimum collapse $\lambda \simeq 10^{-14}$ s^{-1} for an $r_C = 1.5\,\mu$m. Remarkably, for these values the force noise sensitivity required to place an equivalent bound on both CSL and dCSL is $\sim 10^{-50}\,\mathrm{N}^2/\mathrm{Hz}$ which would be achievable only for a thermal particle at a pressure of $\sim 10^{-15}$ mbar (assuming the same particle size). The excluded parameter

space for the dDP model in the single-particle version is shown in Fig. 6.3(right). The value for R_0 originally proposed by Diósi is excluded on an extremely wide temperature range from 10^{-10} K to 10^{10} K while at the GRW value the exclusion is limited to very unrealistic T_{dDP} values. A value considered reasonable is the cosmic microwave background (CMB) temperature [157]; in this case the excluded R_0 goes from 10^{-18} m to 10^{-12} m. Interestingly, the excluded region has no upper bound and extends to T_∞ for increasingly smaller values of R_0.

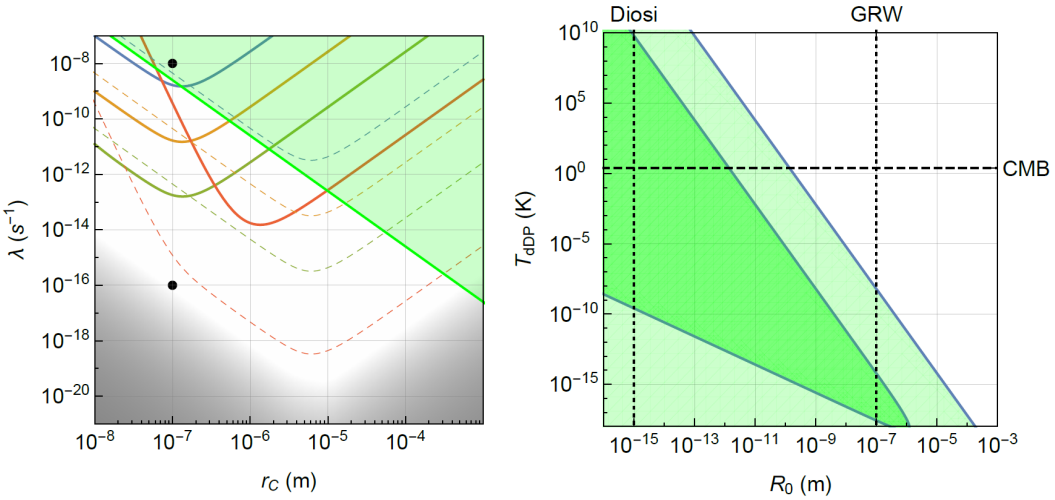

Figure 6.3: Experimental bounds on dissipative collapse models. (left) Exclusion region for the dCSL parameters λ and r_C. Continuous lines: upper bounds from current line width measurements for a 231 nm radius silica particle at 3×10^{-7} mbar for different values of T_{dCSL}: 1 K (blue), 10^{-2} K (yellow), 10^{-4} K (green) and 10^{-7} K (red). The dashed lines are the expected improved bounds from future measurements on a 10 μm radius silica particle; same colour code for T_{CSL}. The green region corresponds to upper bound from LISA pathfinder [148, 162, 163] and the grey region is the lower bound from theoretical arguments [154, 164]. The black markers refer to the Adler [144] (top) and GRW [145] (bottom) values. (right) Exclusion region for the single-particle dDP model. The darker green corresponds to the bounds from the current experiment. The lighter green region is the expected improved bounds from future measurements on a 10 μm radius silica particle. We chose to limit the temperature to the lowest conjectured value of 10^{-18} K associated with Hawking radiation from a supermassive black hole [165, 166]. CMB marks the cosmic microwave background temperature.

6.5 Summary

The measurement problem has puzzled many physicists starting with the founders of quantum mechanics themselves. We have introduced collapse theories which are popular phenomenological models to account for quantum mechanics at the smallest scales and collapse of the wavefunction at the macroscopic one. By placing bounds

on the excess force noise of our thermal levitated nano-oscillator at 8×10^{-7} mbar, we were were able to confirm recently excluded parameters in the CSL model (exclusion for $\lambda > 10^{-6}\,\mathrm{s}^{-1}$ at $r_C = 10^{-7}\,\mathrm{m}$ for $\sim 1\,\mathrm{kHz}$ oscillator). This work paves the way for further experiments at lower pressures with levitated oscillators. With a thermal oscillator at equilibrium with a bath at $T_b = 300\,\mathrm{mK}$ and at a pressure of 10^{-13} mbar, exclusion of $\lambda > 10^{-12}\,\mathrm{s}^{-1}$ could be demonstrated at $r_C = 10^{-7}\,\mathrm{m}$ [37]. Moreover, by using the narrow linewidth of this oscillator (measurements discussed in Chapter 5), we have placed new constraints on two dissipative wavefunction collapse models, namely the continuous spontaneous localisation and the Diósi-Penrose in the single-particle version. By utilising lower noise electronics, and a larger mass oscillator which can be incorporated in this system, we expect to be able to provide even more stringent limits in the future. Considering a $10\,\mu$m radius silica particle, and measuring a linewidth an order of magnitude smaller than measured here, would have a significant impact. In the case of the dCSL it would allow us to almost entirely exclude the λ-r_C parameters subspace for the lowest T_{dCSL} [154, 164]. In the case of the dDP, we could exclude R_0 values almost two orders of magnitude larger at the CMB temperature. Achieving these objectives will require an improvement of the current electronics but nothing beyond the current state of the art.

Chapter 7

Optical set-up

In this chapter, we describe the main optical components used to perform the experiments discussed mostly in Chapter 8. We first describe the general optical layout of the experiment and then focus on characterising the classical intensity noise, and the frequency noise of the laser, which is of crucial importance for the experiment. Finally, the last two sections consist of the characterisation of the two cavities used in the experiment. In the last section, we evaluate the sensitivity performances of the PDH error signal of the science cavity used in Chapter 8 to detect the nanoparticle motion.

7.1 Optical layout

In this section we discuss the general optical layout of the cavity experiment shown in Fig. 7.1. In the following sections, each component is discussed in further details. Two optical cavities are used for the experiment: the science cavity where the nanoparticle is trapped, cooled and monitored, and the filtering cavity used to filter out laser classical noise. In order to perform the experiment, we use two different lasers. One is locked to the science cavity and the other one is offset phase-locked to the first with control over its frequency detuning. Either of the two lasers can be used to trap the nanoparticle. By using two lasers separated in frequency by one free-spectral-range (FSR), which corresponds to 10.3 GHz, we avoid any undesirable beat frequency close to the mechanical frequency of the nanoparticle. Furthermore, we can take advantage of having two modes of different frequencies to tune the ratio between linear and quadratic optomechanical couplings as discussed in Section 8.3.

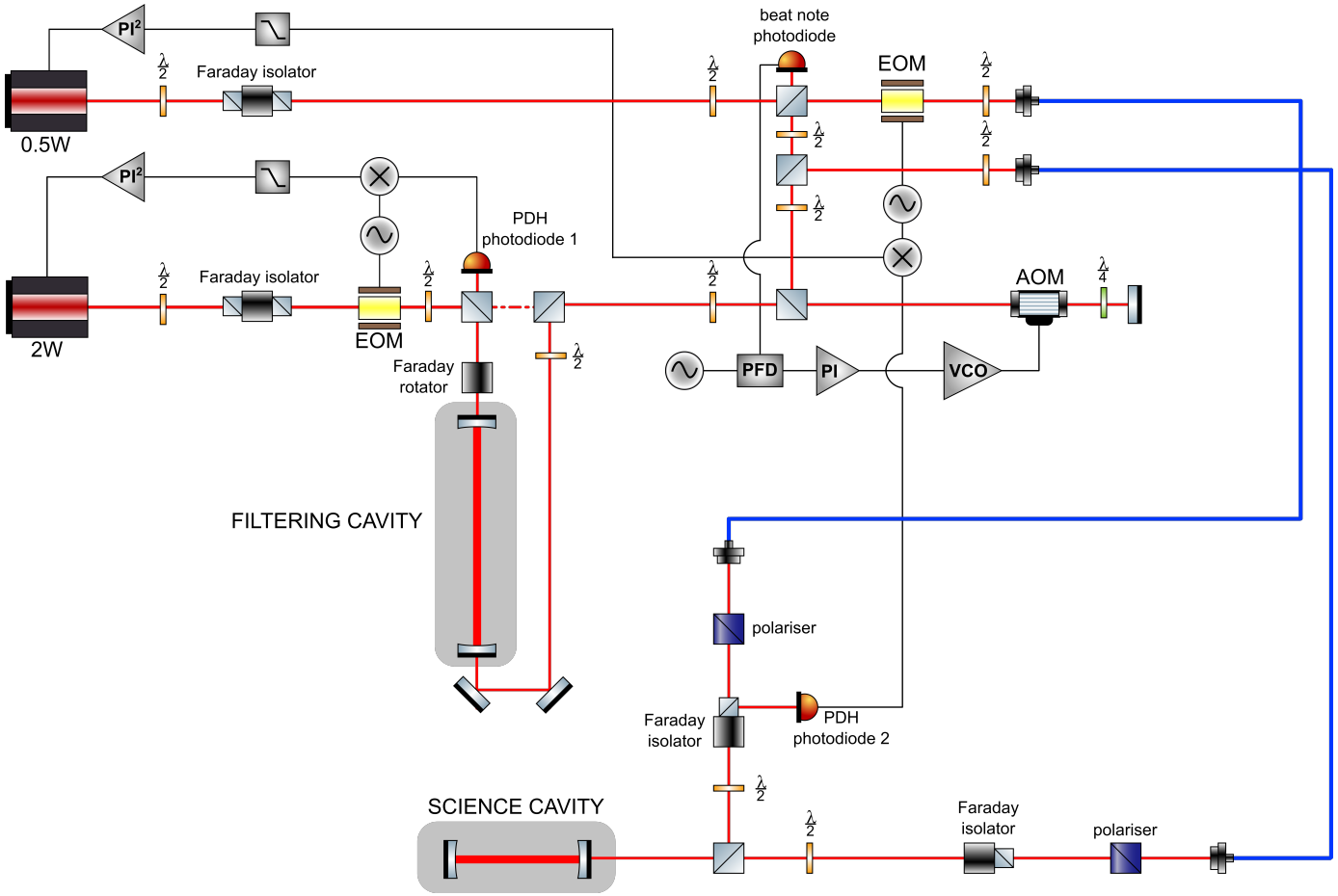

Figure 7.1: Simplified optical layout of the experiment. Laser beams are shown in red, polarisation-maintaining single-mode fibres in blue, and electrical connections in black. EOM: electro-optic modulator. AOM: acousto-optic modulator. PDH: Pound-Drever-Hall. PFD: phase frequency detector. VCO: voltage-controlled oscillator. PI: proportional gain and integrator. PI^2: proportional gain and double integrator.

Both cavities are locked with a standard Pound-Drever-Hall (PDH) technique described in Section A.1. The filtering cavity can be used to filter laser noise of the 2 W beam or can be bypassed (in this case, the laser path is shown by the red dotted line in Fig. 7.1). Both paths are well overlapped (the fringe visibility of the overlapped paths is 92 %) in order to reduce alignment when using either configurations. The frequency difference between the two lasers is measured by monitoring their beat frequency on a photodiode. The offset lock loop is then closed on an acousto-optic modulator (AOM) in a double-pass configuration. When the filtering cavity is bypassed, the loop can be closed either on the AOM or on the laser piezoelectric actuator which is otherwise used for the PDH locking.

Polarisation-maintaining optical fibres are used to decouple the beam preparation (phase and frequency modulations), corresponding to the upper part of the layout in Fig. 7.1, from the science cavity mode-matching, shown in the lower part. This gives a great amount of flexibility to work on one part of the experiment without interfering with the other one. In addition to this flexibility, using single-mode fibres enables us to reach high mode-matching efficiencies to the science cavity, which are above 90 %.

The optical table is isolated from the floor with vibration dampers[1]. This provides -40 dB/decade of isolation above the resonance frequency of ~ 2 Hz.

7.2 Lasers

We use two Mephisto lasers operating at an optical wavelength $\lambda = 1064$ nm with nominal powers of 500 mW and 2 W. The piezoelectric-actuator gains of both lasers have been measured by using an electro-optic modulator (EOM) to add sidebands at 8 MHz to the carrier optical frequency. By ramping the laser frequency and detecting the reflected cavity field (or the transmitted field) we can measure the frequency shift between the carrier and the sidebands, from which we can estimate the laser piezoelectric-actuator gain. We measure a gain of (2.16 ± 0.01) MHz/V for the 500 mW laser and (1.87 ± 0.02) MHz/V for the 2 W laser. Both laser gains have a nominal tuning range of ± 130 MHz and a bandwidth of $\sim$100 kHz. The laser optical frequency can be further tuned by changing the gain medium temperature. The nominal temperature gain is -3 GHz/K, with a tuning range of 30 GHz (which gives

[1] Newport I-2000 Stabilizer Series

us enough flexibility to operate the two lasers one FSR apart) and bandwidth of $\lesssim 1\,\text{Hz}$. This tuning range is mode-hope free over $\sim 9\,\text{GHz}$. In the following sections we evaluate the intensity and frequency noise of the lasers.

7.2.1 Classical intensity noise

The shot-noise is a direct consequence of the corpuscular nature of light when detected on a photodiode. It is characterised with Poissonian statistics satisfying $\Delta n^2 = \bar{n}$ where Δn^2 is the variance in the number of photons and $\bar{n}$ is the average number of photons (see section 2.2.3). When detected on a photodiode, the consequent current fluctuations satisfy $\langle \Delta i^2 \rangle = 2e\bar{i}\,\Delta f$ (Schottky formula, in A^2) with $\bar{i}$ the average current output of the photodiode, e the elementary charge and Δf the detection bandwidth. As a consequence, the PSD of a shot-noise limited beam leads to a voltage PSD of $S_{shot} = 2eP\mathcal{R}G^2$ (single-sided PSD) expressed in V^2/Hz with $\mathcal{R}$ and G the photodiode responsivity and gain, respectively. In practice, with optical powers of the order of $\sim$1 mW and frequencies smaller than 10 MHz, most lasers are not shot-noise limited [17], meaning that the classical fluctuations in the number of photons overwhelm the quantum noise. This classical noise has different origins and statistics. At low frequencies it mainly comes from fluctuations in the electrical current of the pump diode and acoustic noise. At higher frequencies, solid-state lasers generally have relaxation oscillations which is a signature of the fluctuations

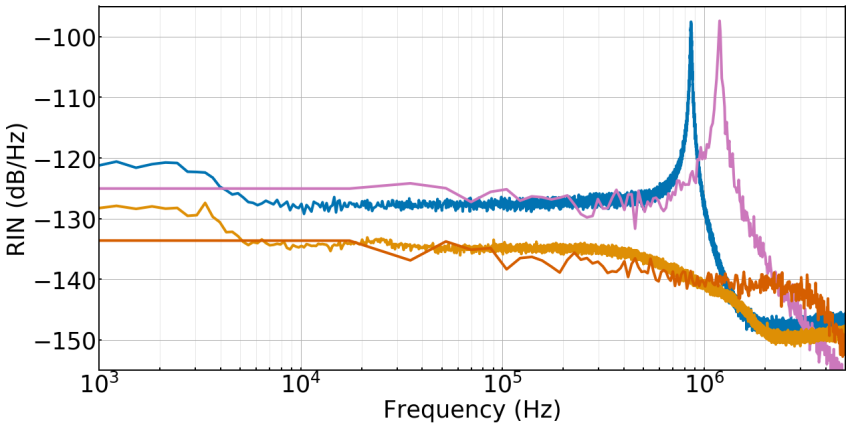

Figure 7.2: Relative intensity noise measurement (RIN) shown in blue (yellow) with (without) activation of the built-in noise eater. This measurement is made with an input optical power of $P_{in} = 217\,\mu\text{W}$. The measurements in pink and orange were taken by the manufacturer for this same exact laser. The main difference with the measurement taken by the manufacturer is the relaxation oscillations frequency, which can be explained by different laser settings (diode current and temperature).

in the steady state of the system. The laser we are using has a built-in feedback mechanism (noise eater) to reduce the amplitude of the relaxation oscillation peak (see Fig. 7.2). Classical intensity noise can simply be evaluated by direct detection on a photodiode. It is generally expressed in relative intensity noise (RIN) defined as $\frac{\langle \Delta P^2 \rangle}{\bar{P}^2}$ with P the optical power. The point of this definition is to obtain a constant RIN as a function of laser power since the classical fluctuations follow $\Delta n^2 \propto \bar{n}^2$. This definition therefore only applies at power where the noise is dominated by classical fluctuations. Our goal is to compare those classical fluctuations to the quantum ones. We characterise this with a threshold optical power P_o introduced in Section 2.4.1.

In order to roughly evaluate P_o, we measure the laser intensity noise on a photodiode[2] with parameters provided by the manufacturer ($\mathcal{R}$ and G). Measurements are taken with three optical powers P_{in} (1.05 mW, 506 μW and 217 μW). From 50 to 150 kHz, the PSD has a white spectral profile with an average value S_{tot} of $6.0\times10^{-13}\,\mathrm{V^2/Hz}$, $1.7\times10^{-13}\,\mathrm{V^2/Hz}$ and $1.8\times10^{-14}\,\mathrm{V^2/Hz}$, respectively. This is well above the detection noise floor of $1.6\times10^{-15}\,\mathrm{V^2/Hz}$. We can then evaluate P_o as $S_{shot}P_{in}/S_{tot}$. For those three powers, we get an average value $P_o = (33 \pm 9)\,\mu\mathrm{W}$. As mentioned above, classical intensity noise can be expressed in RIN, which is shown in Fig. 7.2 at $P_{in} = 217\,\mu\mathrm{W}$, alongside measurements performed by the manufacturer for this same laser.

Another method to detect classical intensity noise consists in measuring the voltage noise fluctuations given by a photodiode output[3] as a function of optical power. We show in Fig. 7.3 the variance of the photodiode voltage fluctuations (PSD integrated between 50 kH and 200 kHz with dark noise subtracted) as a function of optical power on the photodiode. As expected we obtain a parabolic characteristic of the dependency of classical intensity noise as a function of optical power.

7.2.2 Classical frequency noise

Laser frequency noise arises because of mechanical and voltage noise in the laser piezoelectric-actuator which changes the laser optical cavity length and imparts fre-

[2]InGaAs photodiode PDA10DT from ThorLabs. Responsivity at 1064 nm of $\mathcal{R} = 0.23\,\mathrm{A/W}$ and nominal gain $G = 15\,\mathrm{kV/A}$.

[3]InGaAs photodiode PDA10CF from Thorlabs. Measured gain and responsivity product of 4.6 kV/W. Maximum voltage output of 10 V.

quency fluctuations. Those fluctuations cannot be measured in an interferometer with arms of equal length as they would be in phase. In order to detect those fluctuations, a large length imbalance between the two interferometer arms is necessary. We show in Fig. 7.4 the schematics of the set-up used to measure the frequency noise. It consists of a polarisation Michelson interferometer with a large length imbalance of 20 m made by a 10 m long polarisation-maintaining single-mode fibre. The interference fringes are then detected on a balanced photodiode.

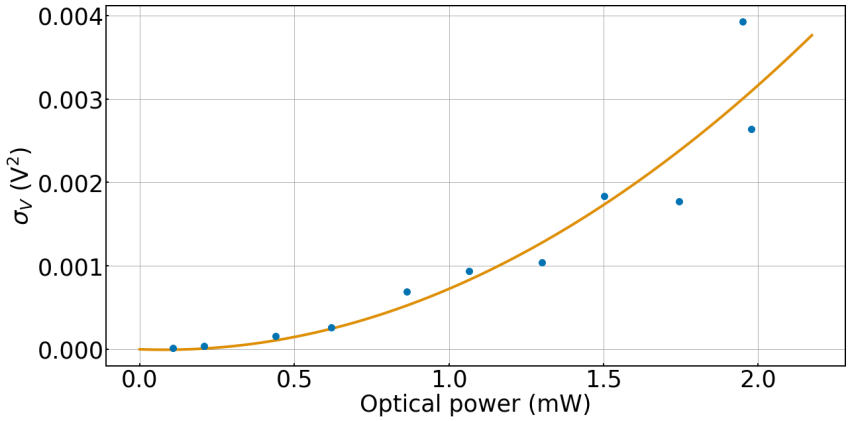

Figure 7.3: Variance of the photodiode voltage fluctuations (integrated between 50 kHz and 200 kHz) as a function of optical power on the photodiode (blue) along with parabolic fit (orange). The quadratic behaviour is a clear signature of classical intensity noise. This is to be compared with Fig. 7.10 where the beam is shot-noise limited.

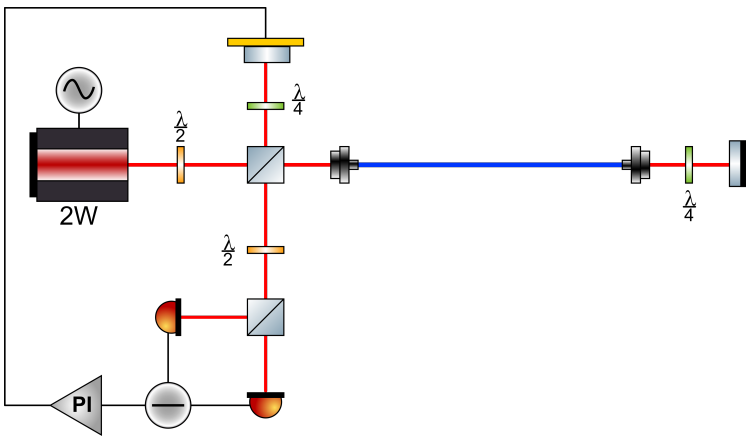

Figure 7.4: Schematics of the delay line interferometer used to measure laser frequency noise. The sensitivity of the measurement is proportional to the length imbalance between the interferometer arms. In practice, we use a single-mode polarisation-maintaining optical fibre as one of the interferometer arms. The frequency noise is measured on a balanced photodiode. Fluctuations in the interferometer path length are compensated by applying feedback on a mirror mounted on a piezoelectric-actuator.

The physics of the measurement can be explained by considering a coherent frequency noise modulation of amplitude K and frequency ω_n [167]. Before being recombined on a beam splitter, the two amplitudes can be written as $\frac{A}{2}\cos(\omega_l t + \frac{K}{\omega_n}\cos(\omega_n t))$ and $\frac{A}{2}\cos(\omega_l(t-\tau) + \frac{K}{\omega_n}\cos(\omega_n(t-\tau)))$ where A denotes the initial amplitude of the beam before the first beam splitter, ω_l the laser frequency and τ the delay between the two interferometer arms. The intensity (ignoring DC terms) on the photodiodes is $I \propto \frac{A^2}{4}\cos\left(-\omega_l\tau + 2\frac{K}{\omega_n}\sin(\frac{\omega_n\tau}{2})\sin(\omega_n(t-\frac{\tau}{2}))\right)$. As expected for an interferometer, the sensitivity is maximum for a phase $\phi = -\omega_l\tau = \frac{\pi}{2}$ where we can linearise the above expression to $I \propto \frac{A^2}{4}\tau K \frac{\sin(\omega_n\tau/2)}{\omega_n\tau/2}\sin(\omega_n(t-\frac{\tau}{2})) \approx \frac{A^2}{4}\tau K \sin(\omega_n(t-\frac{\tau}{2}))$. The AC component of the intensity measured on the balanced detector is therefore directly proportional to the frequency noise amplitude K. Furthermore, we can notice that the sensitivity of the measurement is directly proportional to the time delay τ and therefore to the interferometer length imbalance. The sensitivity of the measurement can be maximised by ensuring that the interferometer is operated at $\phi = \frac{\pi}{2}$. Slow fluctuations in the path length are actively compensated by using a mirror mounted on a piezoelectric-actuator[4]. The

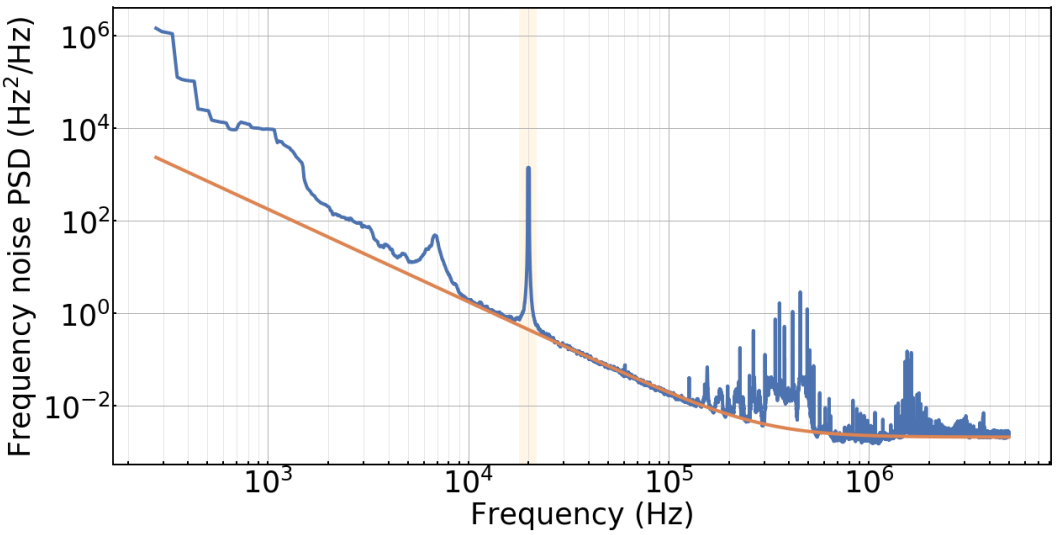

Figure 7.5: Frequency noise measurement of the 2 W Mephisto laser from Coherent. A tone is applied on the laser piezoelectric-actuator at 20 kHz to calibrate the frequency noise with the knowledge of the laser gain of 1.87 MHz/V. The phenomenological behaviour of the frequency noise is shown in orange corresponding to $S_{\dot{\phi}}/(2\pi)^2 = \frac{1.8\times10^8}{f^2}$ Hz^2/Hz.

[4]HPCh10/12-6/2 from Piezomechanik GmbH

phase difference between the two optical paths ϕ is kept at $\phi = \frac{\pi}{2}$ by using a servo[5] (proportional gain and single integrator) and a high voltage amplifier fed on the piezoelectric-actuator (lock bandwidth $\sim 3\,\mathrm{kHz}$).

We show a measurement of the frequency noise in Fig. 7.5. The intensity difference between the two photodiodes is converted into a voltage through the load resistance from which we obtain a PSD in V^2/Hz. We drive the laser piezoelectric-actuator with a calibration tone of 20 mV (peak-to-peak) at 20 kHz from which we can directly convert the PSD initially in V^2/Hz into $\mathrm{Hz}^2/\mathrm{Hz}$ with the knowledge of the laser piezoelectric-actuator gain of 1.87 MHz/V. We find a frequency noise behaviour following the expected $1/f^2$ slope: $S_{\dot{\phi}}/(2\pi)^2 = \frac{1.8\times10^8}{f^2}\,\mathrm{Hz}^2/\mathrm{Hz}$ (shown in orange), in very good agreement with the manufacturer specifications. The noise structures around 400 kHz can be attributed to the mechanical modes of the laser piezoelectric-actuator. The $1/f^4$ slope at frequencies smaller than 10 kHz can be attributed to acoustic noise in the interferometer. The measurement was carried with a power in the optical fibre of $\sim$1 mW. Two photodiodes[6] were mounted in a custom amplifier for this measurement.

As discussed in Chapter 2, for a non-vanishing detuning, frequency noise is transduced within the cavity into intensity noise. This intensity noise, typically orders of magnitude above the photon shot noise, can significantly affect cavity experiments. Furthermore, it reduces the signal-to-noise ratio of a phase sensitive detection. We can demonstrate that frequency noise dominates the amplitude quadrature of the cavity spectra over classical intensity noise by comparing them with a theoretical model. The intensity of the reflected field $I_r(\Delta_o)$ as a function of detuning Δ_o follows (see Eq. 2.30):

$$I_r(\Delta_o) \propto \frac{\zeta^2 + (\Delta_o/\kappa)^2}{1 + (\Delta_o/\kappa)^2}\,. \tag{7.1}$$

Fluctuations in the amplitude quadrature given by classical intensity noise are given by (see Section 2.5.5)

$$S_{in}(\Delta_o,\omega) \propto S_\epsilon \left| -2 + \frac{2\kappa_{in}}{\kappa + i(\Delta_o - \omega)} + \frac{2\kappa_{in}}{\kappa - i(\Delta_o + \omega)} \right|^2 . \tag{7.2}$$

[5] LB1005-S from Newport
[6] InGaAs FPGA10 from ThorLabs

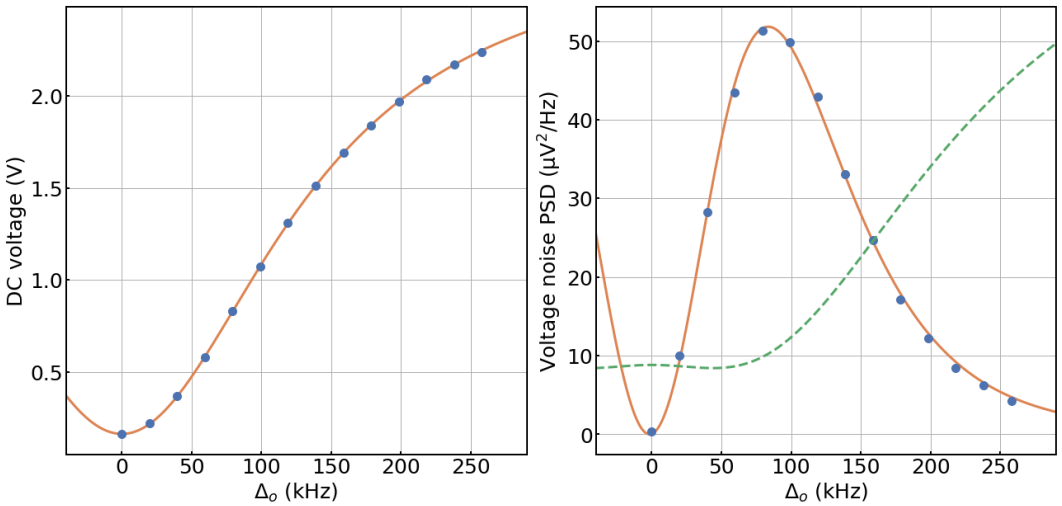

Figure 7.6: (left) DC voltage as a function of detuning of the reflected field measured on a photodiode (blue data points). A fit of the cavity susceptibility (orange) gives a half-linewidth $\kappa/2\pi = (138 \pm 1)\,\mathrm{kHz}$. (right) Voltage noise PSD of the photodiode output of the intensity fluctuations of the reflected beam as a function of detuning (blue) (measured at the same time as the data shown on the left). The PSD are evaluated around 50 kHz. A fit of the amplitude quadrature of the frequency noise is shown in orange. The estimated half-linewidth is $\kappa/2\pi = (138 \pm 1)\,\mathrm{kHz}$. The theoretical shape of the contribution of classical intensity noise to the PSD is shown in green dotted line and is valid up to a proportional factor.

Whereas, fluctuations in the amplitude quadrature given by frequency noise are given by (see Section 2.5.5)

$$S_{fr}(\Delta_o,\omega) \propto S_{\dot{\phi}} \left| i\alpha_s \frac{\sqrt{2\kappa_{in}}}{\kappa + i(\Delta_o - \omega)} - i\alpha_s^* \frac{\sqrt{2\kappa_{in}}}{\kappa - i(\Delta_o + \omega)} \right|^2 , \tag{7.3}$$

$$\alpha_s = \frac{\sqrt{2\kappa_{in}}}{\kappa - i\Delta_o}\alpha_{in} . \tag{7.4}$$

We show this measurement using the science cavity (operated with a half-linewidth $\kappa/2\pi = (141 \pm 1)\,\mathrm{kHz}$) and two lasers. The 500 mW laser is locked on resonance with a PDH lock (see Section A.1). The second laser (2 W Mephisto) is locked to the first one with an offset lock (discussed in Section A.3). The detuning Δ_o between this second laser and the cavity resonance frequency can be precisely controlled. We measure the reflected intensity field of this second laser on a photodiode. In Fig. 7.6(left), we show the DC average on the photodiode as a function of detuning. The data is fitted with Eq. 7.1 (we fit the amplitude, offset in the detuning, coupling parameter ζ and cavity half-linewidth κ). We measure a half-linewidth $\kappa/2\pi =$

(138 ± 1) kHz. In Fig. 7.6(right) we show the voltage PSD of the photodiode output (measured at the same time than the DC average and evaluated at ~ 50 kHz), with a fit of the fluctuations given by frequency noise (orange). Similarly to Fig. 7.6(a), we fit the data with the shape of the fluctuations given by frequency noise (we fit the amplitude, offset in the detuning, and cavity half-linewidth κ). We find $\kappa/2\pi = (138 \pm 1)$ kHz. We also show the theoretical shape (correct up to some proportional factor) of the fluctuations given by intensity noise (green dotted line). The shape of the fluctuations, in very good agreement with the fit, is a clear signature that frequency noise dominates the output quadrature PSD over classical intensity noise, at the frequency at which the fluctuations are considered.

7.3 Filtering cavity

The aim of the filtering cavity is to reduce laser frequency noise. As discussed in Chapter 2, frequency noise drives the nanosphere and therefore increases the minimum achievable phonon number. We use a custom-made 40 cm long optical cavity, which can be shown to behave as a first order low pass filter (with a cut-off frequency equal to its half-linewidth $\kappa/2\pi$), to reduce this noise. In practice, the filtering cavity also reduces the classical intensity noise.

7.3.1 Design

In order to be useful, the cut-off frequency of the filtering cavity needs to be at least one order of magnitude smaller than the frequency of interest to provide sufficient frequency noise attenuation (here the nanoparticle mechanical frequency $\omega_m/2\pi$ is typically between 50 kHz and 100 kHz). Levitated oscillators have typically smaller mechanical frequencies than clamped oscillators ~ 10 MHz. This makes the technical requirements on the filtering cavity much more stringent. Indeed, the higher the frequency of interest, the less frequency noise or intensity noise to be corrected, which therefore relaxes requirements for an ultra-narrow cavity [17]. The cavity holder presented here is designed out of a single INVAR rod (41 cm long), leaving the two cavity mirrors 40 cm apart (see Fig. 7.7). The cavity holder is placed on TORLON feet (25 mm tall, diameter of 19 mm) which is a high quality thermal isolator exhibiting mechanical properties similar to metals. The mirrors are directly placed in contact with the INVAR rod. They are kept in place with an aluminium

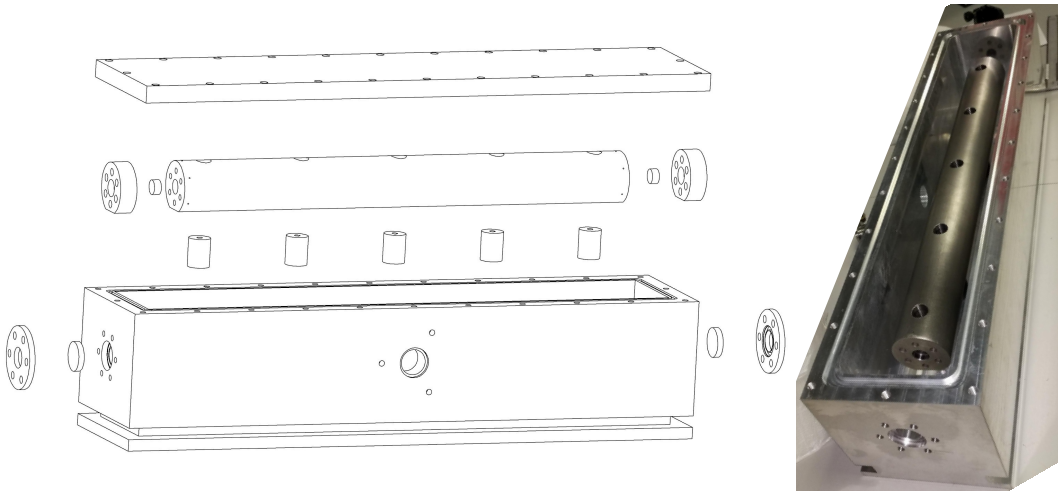

Figure 7.7: (left) Exploded view of the filtering cavity. The cavity holder is designed from an INVAR rod, with a hole machined in its centre. Cavity mirrors are kept in place with aluminium caps. The cavity holder sits inside an aluminium vacuum chamber and is thermally isolated from the chamber with 5 TORLON feet. (right) Picture of the cavity holder in the aluminium vacuum chamber.

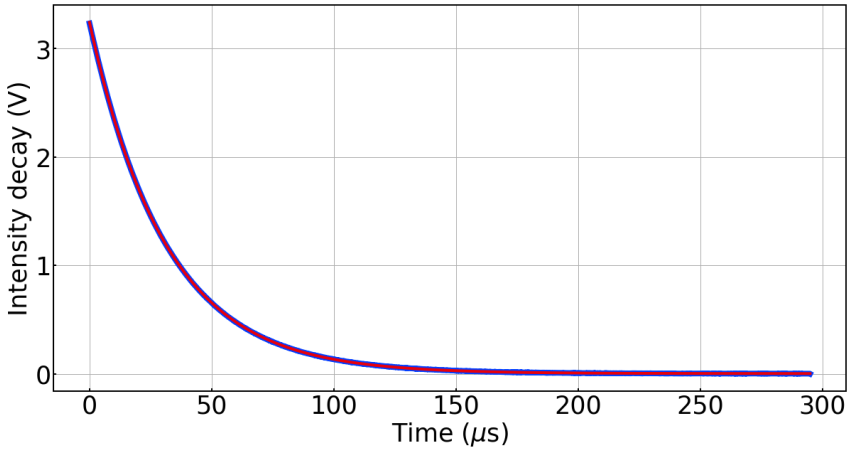

Figure 7.8: Intensity decay (ring-down) measurement of the filtering cavity shown in blue (fit in red). The ring-down time is $\tau = 31.22\,\mu$s, which gives a cavity half-linewidth of $\kappa/2\pi = 2549\,$Hz.

cap and are mechanically isolated from the cap with an O-ring. Both cavity holder and TORLON feet are placed within a custom-made aluminium vacuum chamber in order to isolate the cavity holder from thermal drifts and acoustic noise. The pressure inside this vacuum chamber is kept at $\sim 10^{-3}\,$mbar with a scroll pump and could be lower with a turbo pump. The nominal mirrors from LayerTec have a quoted transmission coefficient of $T = 40\,$ppm (no uncertainty quoted) and radii of curvatures of 600 mm. The measured transmission coefficients of the two mirrors are $T_1 = (13 \pm 1)\,$ppm and $T_2 = (11 \pm 1)\,$ppm and total losses $\Sigma = 61\,$ppm. The half-

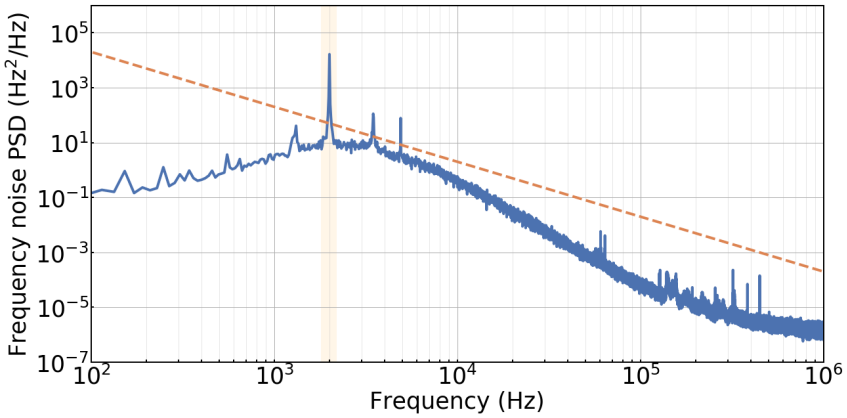

Figure 7.9: PSD of the PDH error signal of the filtering cavity calibrated in effective frequency noise (blue). The initial frequency noise is shown in orange (slope obtained from the measurement shown in Fig. 7.5). The filtering effect of the cavity is seen above 2.5 kHz leading to a $1/f^4$ slope. Below 2 kHz, the two integrators in the feedback loop (both with a corner frequency of 2 kHz) correct the frequency noise fluctuations leading to a f^2 slope. The calibration peak can be seen at 2 kHz.

linewidth is measured after fitting 8 intensity ring-downs, which gives an average half-linewidth $\kappa/2\pi = (2497 \pm 10)$ Hz (see Fig. 7.8).

7.3.2 Frequency noise attenuation

As mentioned above, the filtering cavity behaves as a first order low-pass filter for frequency noise. This filtering effect can be seen in Fig. 7.9 where we show a calibrated PDH error PSD of the filtering cavity. The cavity locking takes care of frequency noise fluctuations below 2 kHz. Above 2.5 kHz the expected frequency noise slope of $1/f^4$ is measured (product between the frequency noise slope and the attenuation effect given by the filtering cavity). At 100 kHz, we observe more than two orders of magnitude of attenuation. Using this filtering cavity on both lasers would enable to achieve the frequency noise levels quoted in Section 2.5.6 and could therefore in theory be sufficient to achieve cooling to the ground state of the centre-of-mass motion.

7.3.3 Intensity noise attenuation

The filtering cavity, which behaves as a first order low-pass filter, attenuates classical intensity noise and frequency noise. We show in Fig. 7.10 a measurement of the intensity noise (variance of the photodiode voltage noise integrated between 50 kHz and 200 kHz with dark noise subtracted) from the transmitted beam of the filtering cavity as a function of optical power. In this case, the filtering cavity was operated

with a different output mirror with a transmission coefficient of 80 ppm leading to a measured half-linewidth of 6.7 kHz. Regarding fluctuations at 125 kHz (mean frequency of the integration window considered), we expect the power at which the beam noise is twice above the shot noise to occur at $P_o \approx 11$ mW. This measurement is taken in exactly the same experimental conditions and photodiode[7] as the one shown in Fig. 7.3, but this time after the filtering cavity. As expected, since the optical powers measured are smaller than ∼5 mW, the voltage noise variance is proportional to the optical power, which is a clear signature of a shot-noise limited beam.

7.4 Science cavity

In this section we characterise the science cavity, used for experiments with nanoparticles in Chapter 8.

7.4.1 Design

The cavity, 14.6 mm long, consists of two mirrors of radii of curvatures of 25 mm. The cavity is therefore operated in the very stable near-confocal regime with theoretical cavity beam waist of 62 μm (Eq. 2.36). The mirror holder is designed out of INVAR in order to reduce drifts in length due to temperature variations. It sits on a double

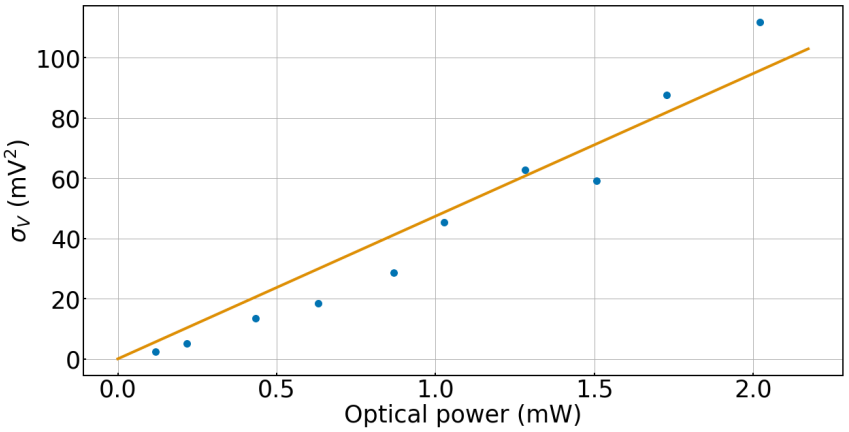

Figure 7.10: Variance of the photodiode output voltage fluctuations (integrated between 50 kHz and 200 kHz) of the transmitted beam from the optical cavity as a function of optical power. The proportional behaviour as a function of optical power, is a signature of a shot-noise limited beam (here demonstrated below an optical power of ∼2 mW). This is to be compared with Fig. 7.3

[7] InGaAs photodiode PDA10CF from Thorlabs. Measured gain and responsivity product of 4.6 kV/W. Maximum voltage output of 10 V.

suspension stage which is discussed below. The mirror holder has a cylindrical shape with openings in the three directions. One cavity mirror is directly glued onto an INVAR cylinder which is then clamped within the cavity holder. The other mirror is glued on a ring piezoelectric-actuator[8] itself glued on a cylindrical holder. This design enables the mirrors to be removed and placed back very easily without entirely losing the mode matching alignment. Since the free spectral range (FSR) is quite large (10.3 GHz), the piezoelectric-actuator gives some flexibility over the tuning between the cavity and the lasers. As mentioned in section A.4, when the filtering cavity is used, feedback can be applied on it. By applying a voltage ranging from 0 to 150 V, we can tune the cavity resonance frequency by more than one FSR.

The waist can actually be measured experimentally by trapping a nanosphere within the Paul trap itself. The Paul trap is placed on a 3D linear translation stage (see Chapter 3 and Fig. 7.14) and we can therefore control the transverse position of the nanosphere with respect to the cavity mode. By imaging the nanosphere scattered light (which is proportional to the field intensity) while moving the translation stage we can reconstruct the beam intensity profile. We show two measurements in

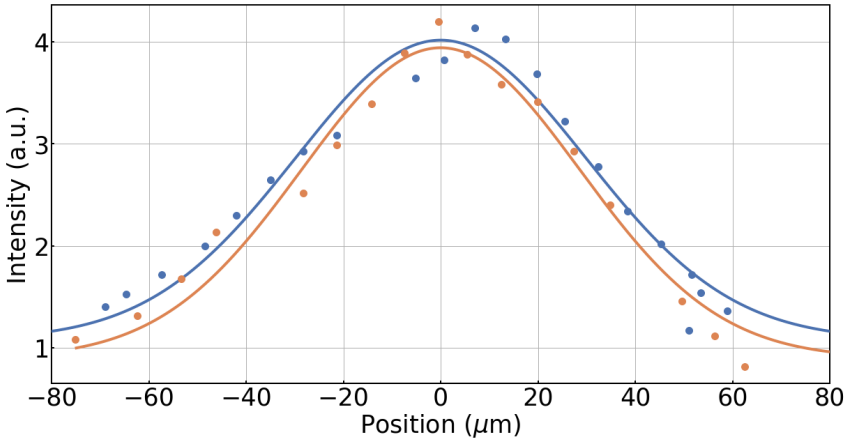

Figure 7.11: Two cavity waist measurements, (data points) along with fits (continuous lines) obtained by imaging the scattered light as a function of the nanoparticle position. The blue (orange) data set gives a waist of $(60 \pm 6)\,\mu$m ($(57 \pm 6)\,\mu$m) and are consistent with the expected value of $62\,\mu$m. The intensity is obtained after integration over the camera pixel matrix. More information regarding the position calibration as well as the imaging technique can be found in Chapter 4.

[8] HPCh 150/12-6/2 from Piezomechanik GmbH

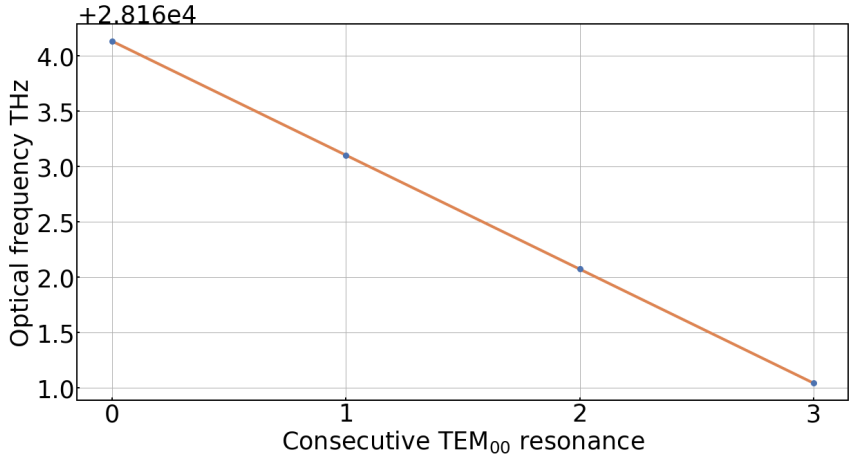

Figure 7.12: Free spectral range measurement of the science cavity. The optical frequency of four consecutive longitudinal modes are measured with a wavemeter. We find FSR=(10.30 ± 0.01) GHz which gives a cavity length L=(14.57 ± 0.01) mm.

Fig. 7.11, where the intensity value is obtained after integration over the camera pixel matrix. Fits give waist values of $(60 \pm 6)\,\mu$m and $(57 \pm 6)\,\mu$m, consistent with the expected value of $62\,\mu$m.

The cavity length was estimated by measuring the optical frequency of four consecutive longitudinal modes (see Fig. 7.12). The frequencies were measured with a wavemeter[9] with a resolution of 0.1 ppm. We measure a cavity length $L = (14.57 \pm 0.01)$ mm or equivalently $FSR = (10.30 \pm 0.01)$ GHz.

7.4.2 Mechanical suspensions

In order to provide a stable cavity locking, mechanical suspensions might be required to decouple the optical cavity from acoustic noise in the ground or in the optical table. The main requirement is to reduce the noise within the cavity half-linewidth, which depending on the set of mirrors used can be as small as $\kappa/2\pi = 7.5$ kHz for the science cavity. Mechanical suspensions were designed by Dr Antonio Pontin with this number in mind. The design is inspired from the one used in the AURIGA gravitational wave detector [168] and relies on the use of C-shaped springs (see Fig. 7.14). The cavity holder sits on an INVAR platform itself sitting on two isolation stages (see Fig. 7.14). The motivation in using this peculiar shape is to provide equivalent attenuation in the three directions. Each stage gives an attenuation factor of -40 dB/decade (power) above the mass-spring resonances at ∼1 kHz. In Fig. 7.13

[9] HighFinesse/Angstrom WS Ultimate 30

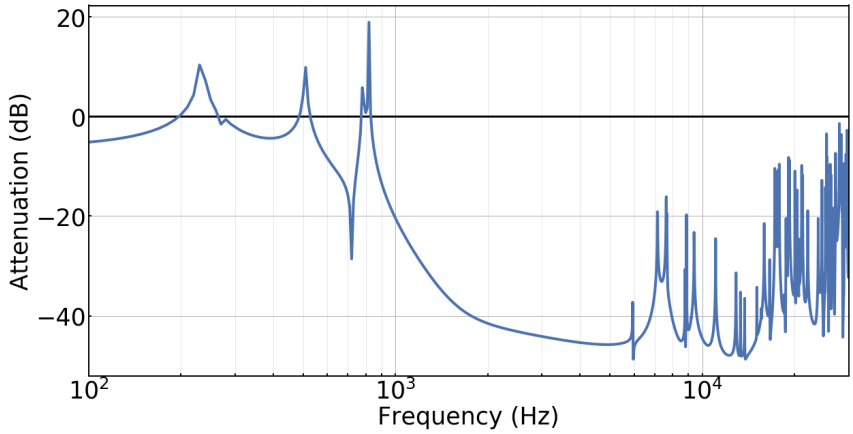

Figure 7.13: Simulated attenuation provided by the double stage suspensions in the cavity length, given a white vertical displacement excitation at the base of the isolation stages. Spring-mass modes can be seen below 1 kHz above which a roll-off of -80 dB/decade can be noted. Internal mode frequencies can be seen above 5 kHz. Simulation carried out by Dr Antonio Pontin.

we show a simulation of the amplitude squared of the relative displacement between the two mirrors as a function of a white excitation in the vertical direction applied at the base of the isolation stage. An attenuation larger than 40 dB can be seen between 1 kHz and 6 kHz. Above 5 kHz, the internal structural modes can be seen. Though the linewidth of the science cavity is slightly larger than the filtering cavity one, the difference by one order of magnitude in length between the two cavities makes the resonance frequency more sensitive to cavity displacement fluctuations by one order of magnitude, therefore relaxing requirements for the filtering cavity.

7.4.3 Finesse measurements

Two sets of mirrors are at our disposal depending on the finesse at which we want the science cavity to be operated at. The mirrors are 4.0 mm thick with 7.75 mm diameter and a 25 mm radius of curvature. They have on the flat surface an anti-reflection coating. *Set 1* of very high finesse cavity mirrors (and very high quality!) was produced by Advanced Thin Films with nominal transmission coefficients of 5 ppm. We measure a transmission coefficient of (2.8 ± 0.5) ppm. *Set 2* was produced by LaserOptik GmbH (fused silica substrates and coating provided by the same company). The quoted transmission was (80 ± 20) ppm. The mirror was measured to have a transmission coefficient of (85 ± 3) ppm with estimated losses of ~ 80 ppm. In *configuration 1*, we use two mirrors from *set 1*. In *configuration 2*, we use one mirror from *set 2* as input mirror and one from *set 1* as the output, in order to

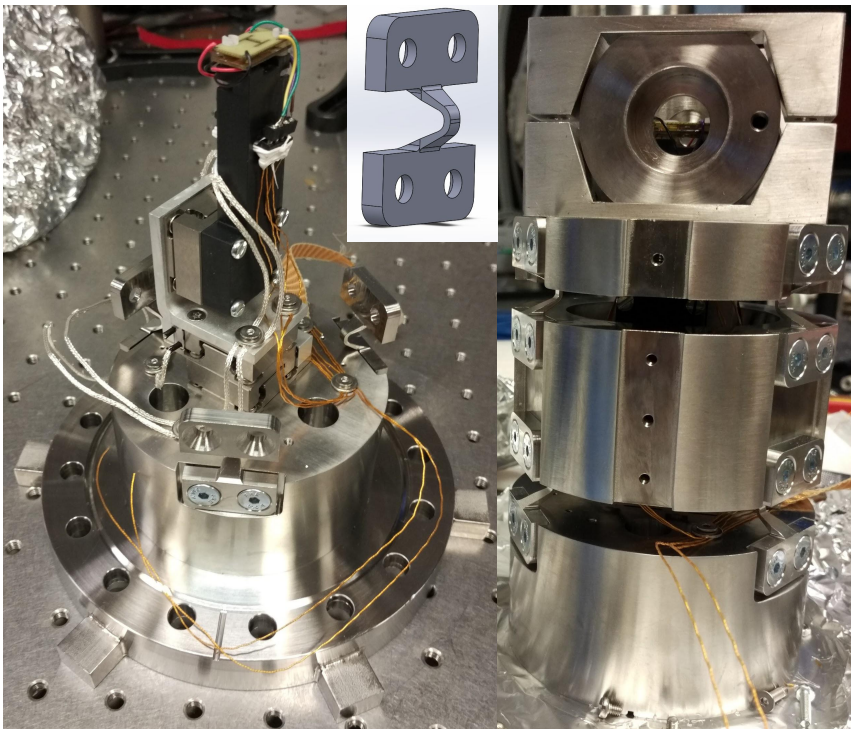

Figure 7.14: (left) The Paul trap (PCB version shown in here), discussed in Chapter 3, is decoupled from the isolation stages. It sits on a 3D-printed piece (black), itself mounted on a 3D-translation stage. (Inset) CAD design of the C-spring. (right) Picture showing on top the cavity holder along the cavity axis. The mirrors are mounted in the two circular openings. The cavity holder sits on two suspension stages. Each stage is isolated with three C-springs.

operate the cavity at a lower finesse. In this case, we measure a half-linewidth of (142.5 ± 0.2) kHz.

In the following section we show four different finesse measurements for *configuration 1*, since it is more challenging to perform than for *configuration 2*. One standard method is a ring-down measurement. The cavity is locked and then unlocked. The cavity transmission, directly proportional to the intracavity power is detected on a photodiode. The measured decay rate is related to the cavity linewidth (see Chapter 2). Another method consists in sweeping the input beam frequency and measure the cavity transmission (or reflection). In the case of a high-finesse cavity, if the sweep frequency is too fast (quantitatively, faster than the cavity decay rate), a ringing phenomenon can be seen as shown in Fig. 7.16. The ringing comes from beating between the intracavity field and the input field [169]. In this case, the cavity dynamics is described with a time dependent detuning ($\Delta_o = \Delta_1 t$) to take into account the frequency sweep of the input beam or conversely of the cavity

detuning. We denote the input field amplitude by α_{in}. The dynamical intracavity amplitude is then

$$\dot{a}(t) = -(\kappa + i\Delta_1 t)a(t) + \sqrt{2\kappa_{in}}\alpha_{in}\,. \tag{7.5}$$

This differential equation can be solved to give

$$a(t) = \sqrt{2\kappa_{in}}\alpha_{in}\exp\left(-\kappa(t-t_0) - i\Delta_1\frac{(t-t_0)^2}{2}\right)\frac{(1-i)e^{\frac{i\kappa^2}{2\Delta_1}}\sqrt{\pi}\left(i+\mathrm{Erfi}\left[\frac{(1+i)(t-t_0)\Delta_1+(1-i)\kappa}{2\sqrt{\Delta_1}}\right]\right)}{2\sqrt{\Delta_1}}, \tag{7.6}$$

where Erfi is the imaginary error function. A third method takes advantage of the nanoparticle-cavity interaction as discussed in further detail in Section 8.1. Nanoparticles sprayed inside the vacuum chamber might go through the cavity-mode. In this case, the scattering losses are large in comparison to the cavity linewidth (for a 600 nm diameter sphere used here, the scattering losses are $\kappa_{sc}/2\pi = 117\,\mathrm{kHz}$)). This can lead to a drop in the intracavity field followed by a ring-up which can be fitted the same way as a ring-down see Fig. 7.17. The fourth measurement consists of a cavity steady-state sweep. The PDH beam is locked on resonance to the science cavity. The other laser is offset locked and the reference detuning is ramped slowly to prevent any ringing. The transmitted (or reflected) cavity field is directly proportional to the modulus square of the cavity susceptibility.

We show in Fig. 7.15 a single ring-down measurement which gives a half-linewidth $\kappa/2\pi = 7.4\,\mathrm{kHz}$. In practice, the cavity is locked at the edge of the dynamical range of the lock so that, once unlocked, the free-running laser is unlikely

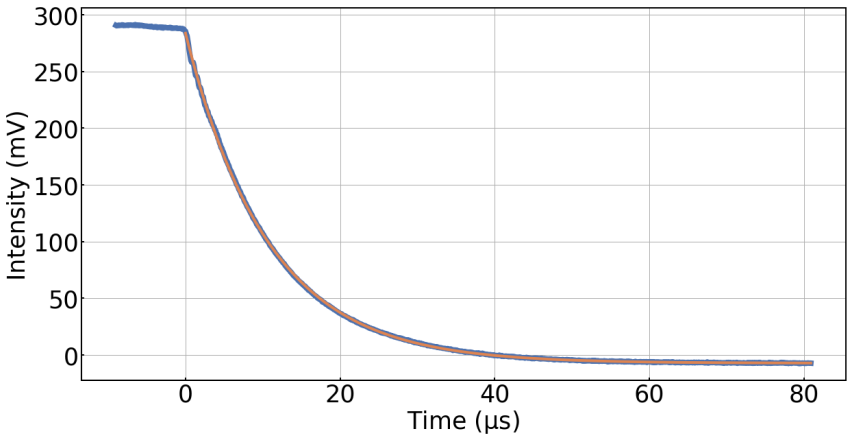

Figure 7.15: Ring-down measurement (data in blue, fit in orange). The measured half-linewidth is $\kappa/2\pi = 7.4\,\mathrm{kHz}$.

to have its frequency getting close to the cavity resonance frequency. In Fig. 7.16, we show a single measurement of ringing decay. The input beam frequency is swept around the cavity resonance frequency (ramp of 7.57 kV/s on the laser piezoelectric-actuator gain leading to a sweep of 16.3 GHz/s). An average over 32 samples gives $\kappa/2\pi = (7.69 \pm 0.07)$ kHz, where the uncertainty is the standard error of the mean. The measurement standard deviation is 0.4 kHz. In Fig. 7.17, we show a ring-up measurement. While keeping the cavity locked, silica beads are injected within the cavity mode leading to an instantaneous change in finesse (due to the scattering losses, see Section 8.1 for more detail). As the particle gets away from the

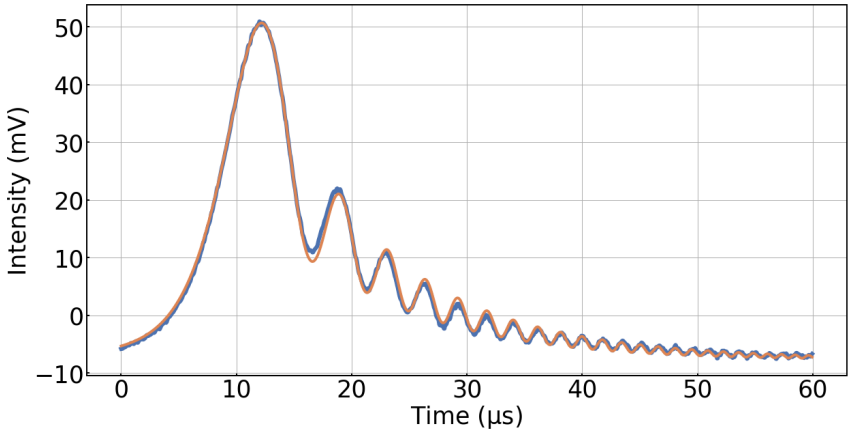

Figure 7.16: Ringing decay to evaluate the cavity linewidth (data in blue, fit in orange). The input beam frequency is swept around the cavity resonance frequency (ramp of 7.57 kV/s on the laser piezoelectric-actuator leading to a sweep of 16.3 GHz/s). The measurement gives a half-linewidth $\kappa/2\pi$ =7.4 kHz.

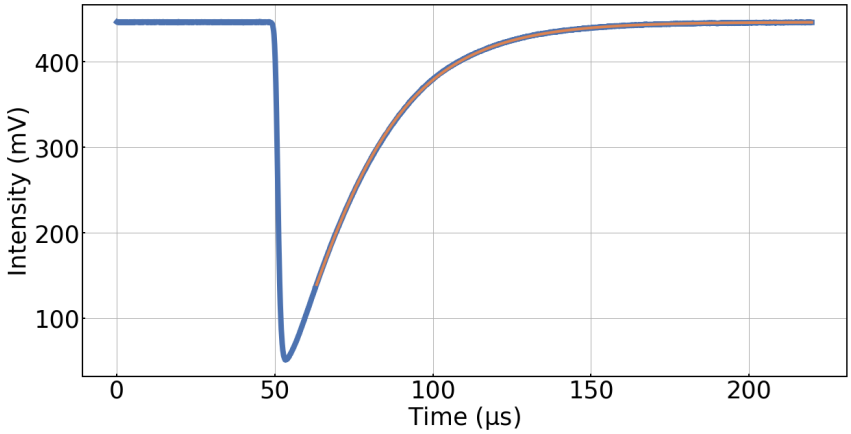

Figure 7.17: Ring-up measurement. While keeping the cavity locked, silica beads are injected within the cavity mode leading to an instantaneous change in finesse. As the particle gets away from the optical mode, the cavity field builds up. Measured half-linewidth of $\kappa/2\pi$ =7.5 kHz.

cavity, the intracavity build-up is measured. An average over 3705 samples gives $\kappa/2\pi = (7.413 \pm 0.001)$ kHz, where the uncertainty is the standard error of the mean. The measurement standard deviation is 0.08 kHz. Lastly, in Fig. 7.18, we show a steady-state sweep measurement, averaged over 64 traces. The input beam frequency is ramped at 64 MHz/s around the cavity resonance frequency and the intensity is measured in transmission. The half-linewidth measured was (10.1 ± 0.1) kHz. The measurement was taken with an input power $P_{in} = 0.12$ mW. This last measurement, though standard, is particularly challenging in the case of a narrow-linewidth cavity. Indeed, the sweep has to be slow enough to prevent any ringing from happening. At the same time, it has to be fast enough not to be blurred by low frequency drifts (temperature and acoustic noise). Lastly, the power has to be kept low enough to prevent thermal instabilities as shown in Fig. 7.18(right). Indeed, as optical power builds up in this high finesse cavity, thermal effects change the effective cavity length.

The first three measurements obtained are compatible with each other. The ring-up measurement gives the best precision with $\kappa/2\pi = (7.41 \pm 0.08)$ kHz (where the error given here is one standard deviation). We evaluate the finesse to be F$\approx$ 700000 with an exceptionally low measured cavity losses of $\Sigma = (3.4 \pm 0.5)$ ppm. After working with nanoparticles for a couple of months, a drop of finesse was

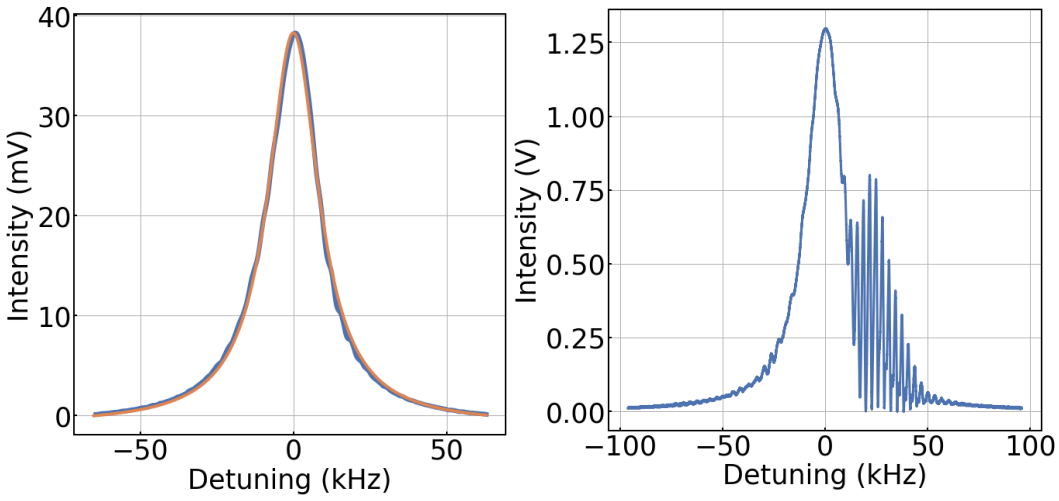

Figure 7.18: (left) Steady-state sweep (64 MHz/s) of the input beam around the cavity resonance frequency (data in blue, fit in orange) averaged over 64 traces. The intensity is measured in transmission. The half-linewidth measured is $\kappa/2\pi = (10.1 \pm 0.1)$ kHz. The measurement is taken with an input power $P_{in} = 0.12$ mW. (right) Same (single trace) with higher input power $P_{in} = 3.8$ mW leading to thermal instabilities.

measured. We illustrate this measurement with our last method used to measure the linewidth, which is a cavity steady-state sweep. The measured change in linewidth of $\Delta\kappa/2\pi \approx 2.6\,\mathrm{kHz}$ corresponds to a change in optical losses by $\Delta\Sigma \approx 3\,\mathrm{ppm}$.

7.4.4 Cavity displacement noise

We show in Fig. 7.19(top) a calibrated PDH spectrum of the high-finesse cavity with *configuration 1* of mirrors as discussed above. A calibration peak is added at 1 kHz to convert the spectrum in frequency noise or equivalently in cavity displacement noise (see section A.2). We show in orange the PDH error signal calibrated in in-loop displacement noise. At 50 kHz, it gives a sensitivity of $2 \times 10^{-35}\,\mathrm{m}^2/\mathrm{Hz}$. The in-loop signal can be converted into an effective input displacement noise, shown in blue (see feedback diagram in Fig. A.2). This is calculated from estimation of the servo gain and integrator corner (here only one integrator of corner frequency 50 kHz is activated). We can check that the estimated amount of displacement noise at low frequency is quantitatively reasonable. A standard model of seismic noise is [168] $S_{\mathrm{seismic}} = \frac{\beta A}{f^4}$ with $A = 10^{-14}\,\mathrm{m}^2/s^4\mathrm{Hz}$ and β which can range from 1 to 100 depending on the location. This seismic noise is then multiplied by the suspension transfer function (see Fig. 7.13) and a first order low-pass filter (with cut-off frequency at $\sim 3\,\mathrm{Hz}$) corresponding to the filtering effect of the optical table suspensions. The phenomenological displacement noise caused by seismic noise (shown in green) agrees with the experimental data within an order of magnitude.

As expected when using the cavity in *configuration 2*, the displacement sensitivity is worst than the one previously discussed. We show in Fig. 7.19(bottom) the displacement sensitivity obtained when using two different Mephisto lasers. The 0.5 W Mephisto gives a much better sensitivity around 50 kHz since it has one order of magnitude less frequency noise at this frequency than the 2 W Mephisto laser. The features around 200 kHz come from mechanical noise of the science cavity ring piezoelectric-actuator. Since the best sensitivity is achieved at 50 kHz, we will choose this bandwidth as the target optical trap frequency in Chapter 8.

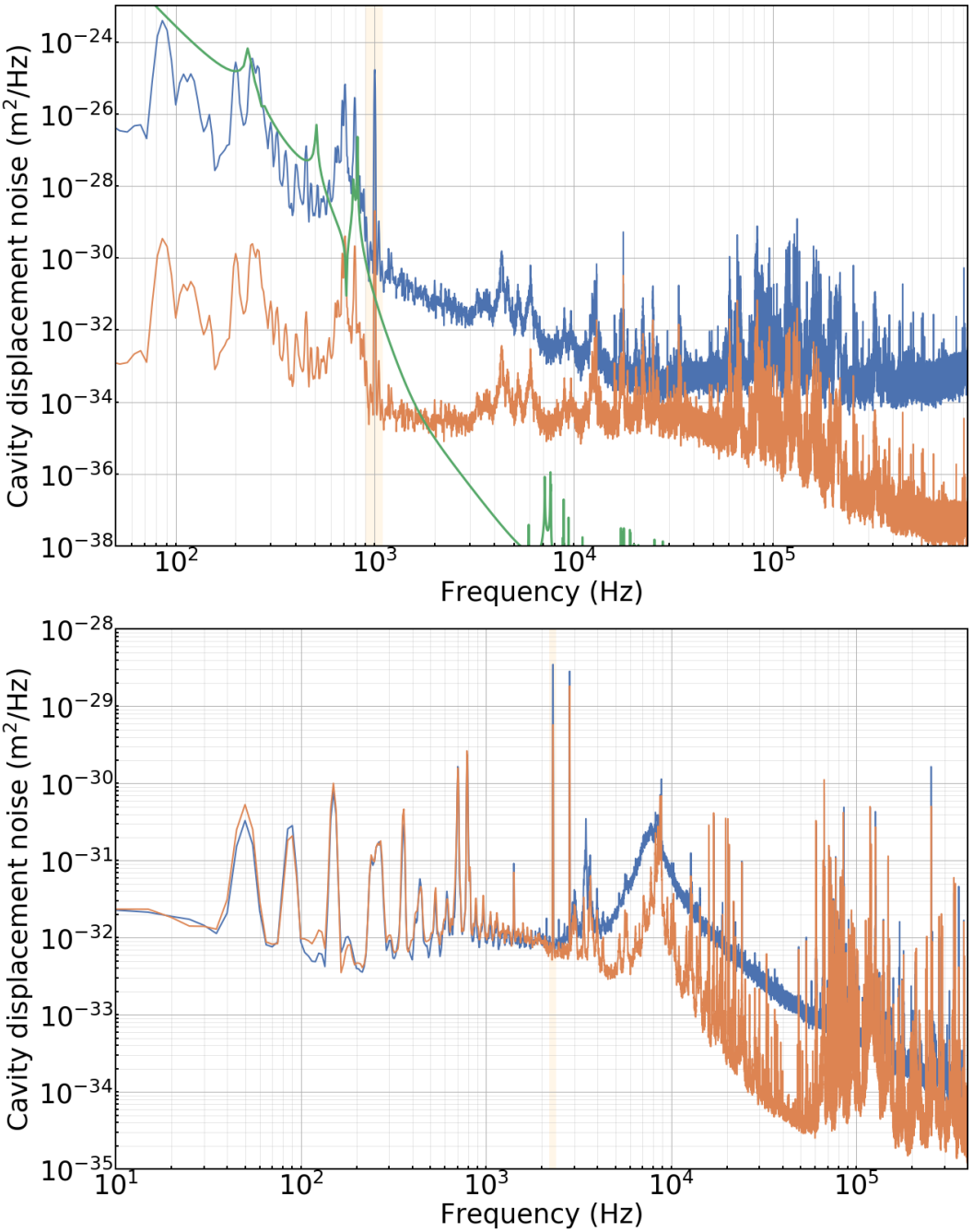

Figure 7.19: (top) Calibrated PDH error signal in effective cavity displacement noise of the high-finesse cavity (*configuration 1* of mirrors). The calibrated PDH error signal is shown in orange. In blue, we show the in-loop noise referenced as an input displacement noise (see Fig. A.2). In green, we show an order of magnitude estimation on the cavity displacement noise (see main text). The calibration tone is added at 1 kHz. (bottom) Calibrated PDH error signal in effective cavity displacement noise of the high-finesse cavity (*configuration 2* of mirrors, cavity linewidth of $\kappa/2\pi = (142.5 \pm 0.2)$ kHz). The calibrated PDH error signal is shown in blue (orange) when locking the cavity with the 2 W Mephisto laser (500 mW Mephisto laser). The calibration tone is added at 2.3 kHz. The two PDH signals were obtained with similar experimental parameters and input optical power of ~ 1 mW.

7.5 Summary

To summarise, we have reviewed the optical set-up used for the experiments mostly described in Chapter 8. After describing the general optical layout, we characterised the classical intensity noise and frequency noise of the laser. In order to filter laser frequency noise, we have presented our original design of filtering cavity and evaluated its behaviour on laser noise. The level of attenuation provided by the filtering cavity applied on both lasers would enable in theory to reach the noise levels required for ground state cooling of the centre-of-mass motion (see Section 2.5.6). Lastly, we presented the design and characterisation of the science cavity used in Chapter 8 to manipulate the motion of levitated nanoparticles.

Chapter 8

Levitated cavity optomechanics in a hybrid electro-optical trap

In this chapter, we study the optomechanical interaction between a levitated silica nanoparticle and an optical cavity mode in a hybrid electro-optical trap consisting of an optical cavity (discussed in Chapter 7) and a Paul trap (discussed in Chapter 3 and 4). The theory relevant to this work has been presented in Chapter 2. In previ-

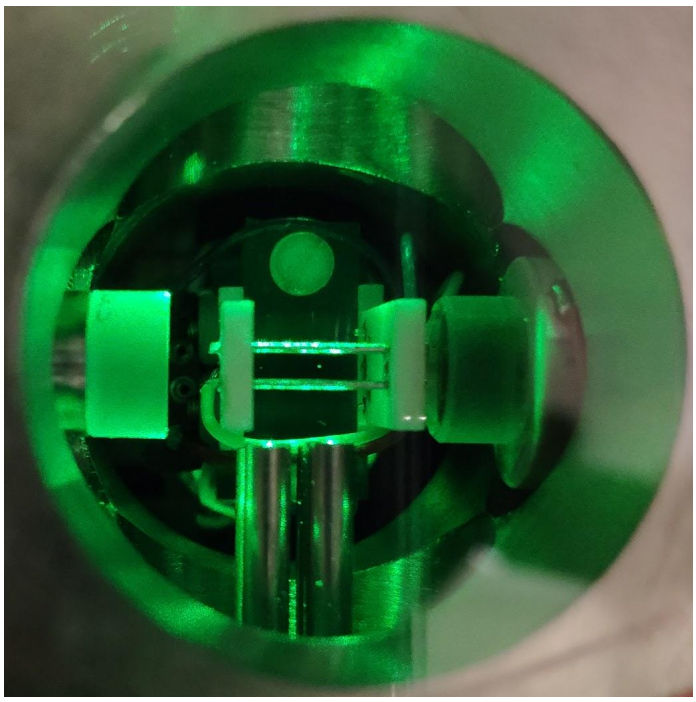

Figure 8.1: Levitated nanosphere (green dot) in the miniature Paul trap and the optical cavity. The cavity mirrors can be seen on both sides of the trap. The mirror on the right-hand side is glued on a piezo-actuator to tune the cavity resonance frequency. The guide used during the loading phase can be seen on the lower part of the picture. The Paul trap is purposely placed closer to one cavity mirror to increase the detection sensitivity (see Section 8.3).

ous works, the Paul trap micromotion has been used to enhance the optomechanical coupling by providing a periodic modulation to the particle mean position [45, 46]. Here, the Paul trap is used to control the trapping optical well location in the cavity (the Paul trap is mounted on a 3D translation stage, see Fig. 7.14), while providing no micromotion to the nanoparticle along the trap axis which corresponds to the Paul trap axis. Except when mentioned otherwise, we use here the *configuration 2* of cavity mirrors (cavity half-linewidth $\kappa/2\pi \approx 140\,\mathrm{kHz}$, see Section 7.4). In the first section, we report measurements of the scattering losses discussed in Section 2.3.2. These are then used to evaluate the particle polarisability. In the second section we report on the cooling of the transverse secular motion with velocity damping on one trap electrode. Depending on the trap operation and the amount of voltage noise, the amplitude of the secular motion can be significant in comparison to the cavity waist and therefore modulate the optomechanical coupling. This effect is greatly reduced by using this active compensation method. In the third section, we discuss the optomechanical dynamics with two optical modes, initially studied in Ref. [24, 44]. Taking advantage of the versatility of this levitated nano-oscillator system, we demonstrate an experimental regime where the quadratic optomechanical coupling dominates over the linear one. To the best of our knowledge, this is the first time that cavity cooling solely provided by quadratic optomechanical coupling is demonstrated. This intrinsic nonlinear dynamics gives rise to a highly non-thermal state of motion which matches well the expected behaviour. As quadratic coupling has a prominent role in proposed protocols to generate deeply nonclassical states, our work represents a first step for producing such states in a levitated system. This system can be operated as well in a regime dominated by linear optomechanical coupling. In this case, we report cooling down to $T_{eff} = (21 \pm 4)\,\mathrm{mK}$, improving previous achieved temperatures by more than three orders of magnitude [44]. This is comparable to recently reported temperatures in the standard optomechanical case (by opposition to coherent scattering [40, 51]) with an optical tweezer and an optical cavity [47].

8.1 Cavity transient dynamics and scattering losses

As we have discussed in Section 2.3.2, nanospheres with radii larger than 150 nm can introduce significant scattering losses when compared to the bare cavity linewidth

(here half-linewidth $\kappa/2\pi \approx 140\,\mathrm{kHz}$). In this section we first demonstrate that by injecting nanoparticles across the cavity mode we can measure the finesse very accurately as shown in Fig. 7.17. Then we report two measurements of the scattering losses, one for a 600 nm (diameter) nanosphere and one for a 387 nm sphere. We then infer from those two measurements the particle polarisability.

8.1.1 Cavity transient behaviour

The dynamics of non-trapped nanospheres crossing an optical cavity mode has been studied in detail in Ref. [43], where cavity cooling has been reported. When neglecting the effect of the cavity on the nanoparticle, the cavity dynamics reads

$$\dot{a}(t) = -\left[\kappa_o + \kappa_{sc,\mathrm{Mie}}(\mathbf{x}(t)) - iU_{o,\mathrm{Mie}}(\mathbf{x}(t))\right] a(t) + \sqrt{2\kappa_{in}}\alpha_{in}\,, \tag{8.1}$$

where $\mathbf{x}(t)$ is the particle position. The expression of the scattering losses and particle-induced frequency shifts can be found in Section 2.3.2 and 2.3.1 (the dependence of those two parameters along the cavity axis is given in Eq. 2.48). Here, while having one beam locked to the cavity (input power $P_{in} = 260\,\mu\mathrm{W}$), we inject nanoparticles (and solvent droplets) through the cavity mode with the loading method discussed in Section 3.3.1 at a pressure $P = 8\times10^{-1}\,\mathrm{mbar}$. The nanospheres

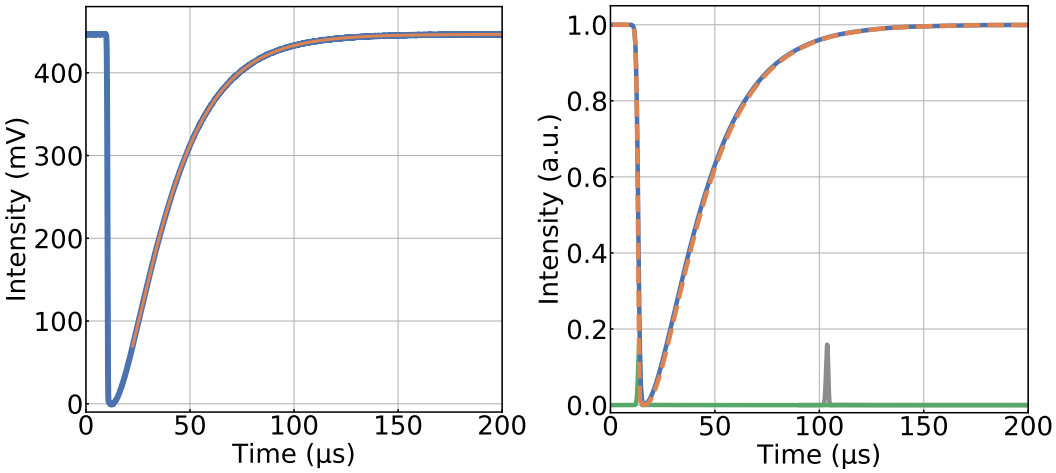

Figure 8.2: (left) Transient cavity dynamics (measured in transmission) of a nanosphere (or solvent droplet) crossing the cavity mode. In orange we show a fit of the ring-up. (right) Theoretical calculation in blue of the cavity transient dynamics as a silica nanoparticle (300 nm diameter) crosses the cavity mode at 25 m/s. The real and imaginary contributions of the cavity field are shown in orange and green, respectively. In grey, at $t = 100\,\mu\mathrm{s}$, we show the imaginary part contribution (same as green) shifted in time for better clarity.

cross the cavity mode at high speed (estimated to be $\sim 10\,\mathrm{m/s}$ see Section 3.3.1) which is assumed to remain constant while crossing the cavity mode. This is a reasonable assumption given the very small interaction time ($\sim 5\,\mu\mathrm{s}$) and the fact that the optical mode is providing negligible cooling or heating. In Fig. 8.2(left) we show the cavity transmission intensity as a nanosphere (or solvent droplet) goes through the optical mode. As the scatterer crosses the beam, the change in finesse makes the intracavity power drop. The event is directly followed by a ring-up which can be fitted to evaluate the cavity linewidth. In Fig. 8.2(right), using Eq. 8.1 we show in blue a theoretical calculation of the intracavity intensity as a silica nanosphere of 600 nm diameter crosses the beam in the transverse direction, in a bright fringe, at 25 m/s. In orange we show the contribution of the real part of the amplitude which is equivalent to neglecting the cavity frequency shift induced by the nanoparticle. In green we show the contribution of the imaginary part. This demonstrates that here, most of the cavity dynamics can be accounted for by the scattering losses. With these experimental parameters, the theoretical calculation matches very well the theory. It is worth noting, that solvent droplets cannot be distinguished here from nanoparticles. Indeed, their speed will be similar and, in both cases, large scattering losses lead to a similar behaviour. This experiment can be used to evaluate the cavity linewidth very accurately as discussed in Section 7.4.3.

8.1.2 Scattering losses

Evaluating the scattering losses introduced by the nanosphere enables us to better estimate the effective cavity linewidth and the optomechanical dynamics. We present here two different measurements consisting in evaluating the linewidth with and without the nanoparticle located in the cavity mode. A first measurement was taken with spheres of 600 nm nominal diameter[1] with the very high finesse cavity (*configuration 1* of mirrors discussed in Chapter 7). Once a particle is levitating in the Paul trap (in this case PCB trap), we can measure the finesse, evaluated here by using the "ringing-decay" method presented in Section 7.4.3. We use for this measurement a single optical beam with input power $P_{in} = 410\,\mu\mathrm{W}$ with its optical frequency scanned at 16.4 GHz/s. In Fig. 8.3(left) we show the cavity transmission measured on a photodiode as a function of time for three different Paul trap

[1] 600 nm silica nanosphere from Corpuscular Inc.

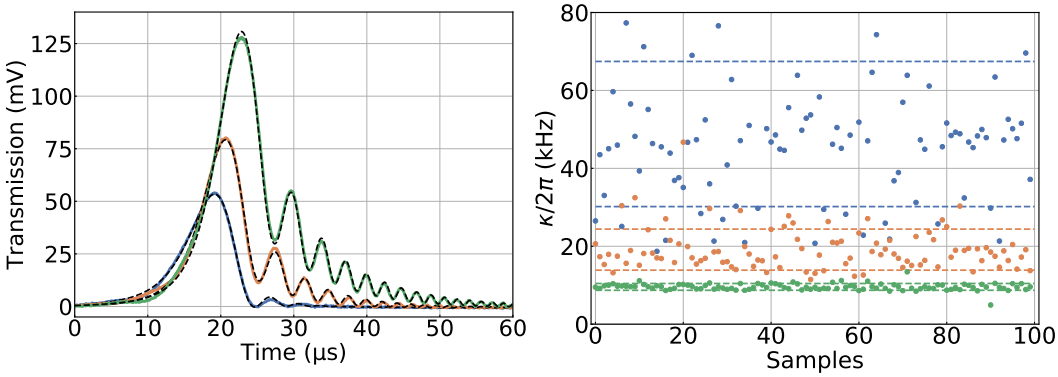

Figure 8.3: (left) Ringing decay to evaluate the cavity linewidth with the nanoparticle at different locations within the cavity mode. In blue it is placed in the centre, orange intermediate position and green away from the cavity mode. Fits are shown in dashed black. (right) Half-linewidth in the three cases mentioned above (same code colour). The dashed lines correspond to one standard deviation. The result of the three measurements are $\kappa/2\pi = (9.57 \pm 0.09)\,\mathrm{kHz}$ (green), $\kappa/2\pi = (19.1 \pm 0.5)\,\mathrm{kHz}$ (orange) and $\kappa/2\pi = (49 \pm 2)\,\mathrm{kHz}$ (blue)

positions. In blue, the trap is aligned such that the nanosphere is located in the centre of the cavity mode. This is realised in practice by moving the trap by small steps ($\sim 10\,\mu\mathrm{m}$) while either maximising the amount of scattered light or measuring the transmitted power (or the linewidth) and minimising (maximising) it. The measurement was taken at a pressure $P = 4.6 \times 10^{-2}\,\mathrm{mbar}$ where the motion is at equilibrium with the bath at $T_b = 293\,\mathrm{K}$. As described in detail in Chapter 4, the particles typically have secular frequencies of $\sim 100\,\mathrm{Hz}$. We therefore expect the secular motion to have a standard deviation of $\sigma_{x,y} \approx 7\,\mu\mathrm{m}$. Therefore, while the particle transverse motion should have a negligible effect (since small in comparison to the cavity waist of $62\,\mu\mathrm{m}$) the nanosphere should travel along the optical direction through many fringes separated by $\lambda/2 = 532\,\mathrm{nm}$. We therefore are measuring on average a half-linewidth $\kappa = \kappa_o + \kappa_{sc}/2$ where κ_o is the bare cavity half-linewidth and κ_{sc} is the scattering losses evaluated when the particle is trapped at a bright fringe. We show in Fig. 8.3(right) the estimated half-linewidth for 100 samples. When the particle mean position is placed sufficiently far away from the cavity centre, we measure a half-linewidth $\kappa/2\pi = (9.57 \pm 0.09)\,\mathrm{kHz}$ compatible with measurements taken with an empty Paul trap. At an intermediate position we measure $\kappa/2\pi = (19.1 \pm 0.5)\,\mathrm{kHz}$ and when the trap is moved so that the particle is located in the middle of the cavity mode $\kappa/2\pi = (49 \pm 2)\,\mathrm{kHz}$. This gives an estimate on the scattering losses of $\kappa_{sc}/2\pi = (79 \pm 4)\,\mathrm{kHz}$. Assuming this nanosphere has a nominal

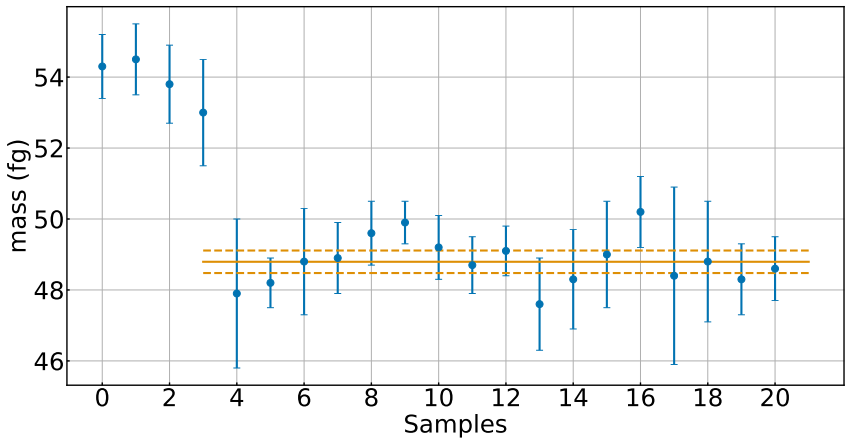

Figure 8.4: Mass measurement of the same nanosphere over two months. Each data point is an average of 8 measurements taken on a same day. Once a portion of the mass has been lost (either by evaporating some remaining solvent within the sphere or burning some impurities), it remains stable. We can estimate the mass (orange line) to be $m = (4.88 \pm 0.03 \pm 0.15) \times 10^{-17}\,\mathrm{kg}$ (where the first uncertainty is statistical and the second systematic). The measurements are typically taken at pressures above $\sim 1 \times 10^{-2}\,\mathrm{mbar}$ and are described in Section 4.3.3.

diameter of 600 nm, we can estimate the dielectric constant as $\epsilon_s = 1.81 \pm 0.02$ from Eq. 2.48. Though this value is much smaller than the nominal value for pure bulk silica $\epsilon_s = 2.1$, it is still compatible with values measured for dehydrated porous Stöber silica nanospheres in vacuum [170].

Most of the data presented in the remaining sections were taken with a same nanosphere with a nominal diameter[2] of 387 nm. After each set of measurements (optical trapping in vacuum below $10^{-4}\,\mathrm{mbar}$) its mass was measured using the imaging method discussed in detail in Section 4.3.3. It can be seen on the fourth sample that once above a power threshold $P_{in} \approx 500\,\mu\mathrm{W}$ at a pressure lower than $\sim 10^{-5}\,\mathrm{mbar}$, the particle lost 10% of its mass. This input optical power corresponds to an intracavity power of $P_{cav} \approx 3.6\,\mathrm{W}$ and an intensity $I_{cav} = 1.2 \times 10^9\,\mathrm{W/m^2}$. This behaviour has been consistently observed with different nanoparticles. After this event, the mass remains stable as it can be seen in Fig. 8.4, regardless of pressure or input power. We estimate the mass of the nanoparticle (after the event) to be $m = (4.88 \pm 0.03 \pm 0.15) \times 10^{-17}\,\mathrm{kg}$ (where the first uncertainty is statistical and the second systematic). Assuming the density quoted by the manufacturer of $1850\,\mathrm{kg/m^3}$, we estimate the radius of this nanosphere to be $r = (185 \pm 2)\,\mathrm{nm}$ in very

[2] 387 nm diameter silica nanosphere from microParticles GmbH

good agreement with the radii measured from SEM pictures (see Fig. 4.11).

We measure the scattering losses for this nanosphere with a similar experimental protocol as the one discussed above. For this measurement we use *configuration 2* of cavity mirrors. Two laser beams are used for this measurement. A first one is locked to the cavity with a PDH scheme. The second beam (probe beam) is offset-locked to the first one and, in addition, its frequency is scanned. In a first measurement, the power of the PDH beam is high ($P_{in} = 295\,\mu$W) so that the particle is optically trapped. The probe beam has an input power $P_{in} = 32\,\mu$W and its frequency is scanned at 7.5 GHz/s. Since the two laser frequencies are kept one FSR apart, when trapping optically the nanosphere in an optical well in the centre of the cavity (location controlled with the Paul trap position), the nanosphere sits at a dark fringe of the probe beam, with therefore negligible losses. This measurement is therefore used as reference to evaluate the bare cavity half-linewidth and we find $\kappa/2\pi = (141.15 \pm 0.05)$ kHz. This measurement is consistent with a linewidth measurement performed just before trapping the particle $\kappa/2\pi = (141.21 \pm 0.01)$ kHz. We can then perform this same experiment with a weak PDH beam ($P_{in} = 9.5\mu$W) so that the particle travels through many fringes. We measure in this case, an effective half-linewidth $\kappa = \kappa_o + \kappa_{sc}/2$. We estimate a half-linewidth $\kappa/2\pi = (146.7 \pm 0.7)$ kHz from which we infer the scattering losses to be $\kappa_{sc}/2\pi = (11.1 \pm 1.4)$ kHz. This gives a dielectric constant $\epsilon_s = (1.98 \pm 0.07)$ for a quoted value by the manufacturer of $\epsilon_s = 2.02$.

A few comments must be given on those two measurements. First, the two dielectric constants differ significantly, which could be explained by the different manufacturer origins for the two different nanoparticle sizes. Second and most important, those measurements are very challenging to perform. As mentioned in Section 2.3.1, when the nanosphere travels through the optical standing wave it not only modulates the cavity losses but shifts the cavity resonance frequency. This leads to a change in the intracavity power which is not instantaneous but occurs on a timescale $1/\kappa$ [43]. Moreover, the measurement accuracy can be affected by drifts in the cavity resonance frequency due to acoustic noise. A better way of performing the last measurement discussed here would be first to trap the particle as we do it in the PDH beam to measure the bare cavity linewidth. We would then keep the

frequency of both beams separated by two FSR so that in the centre of the cavity, the particle sits at the bright fringe of both beams. This way, the particle would remain localised in both cases, reducing intensity modulations caused by the particle travelling through multiple fringes. Unfortunately, this was not implemented since the beat note frequency corresponding to two FSR (20.6 GHz) is larger than the photodiode bandwidth[3].

8.2 Cooling the secular motion in the Paul trap

As mentioned in Chapter 3, cooling the secular motion is critical in ion trap experiments in order to reduce modulations in the transition frequencies. In this case, detection of scattered light modulated by the ion secular motion provides a signal proportional to the ion displacement. Cooling the secular motion was demonstrated using the trap itself by applying a signal proportional to the ion displacement onto the trap electrodes and in phase quadrature [171]. Similar methods have been applied to levitated nanospheres in Paul traps using either parametric feedback cooling (cooling demonstrated down to $\sim 75\,\mathrm{K}$) [96, 172] or velocity damping (down to $\sim 7\,\mathrm{mK}$) [173]. Here we demonstrate cooling of the secular motion in the transverse direction of the trap when the particle (silica sphere of nominal diameter of 387 nm) is trapped optically in the cavity mode (optical trapping frequency of $\omega_m/2\pi \approx 38\,\mathrm{kHz}$). This enables us to reduce modulation at the secular frequency in the optomechanical coupling. Scattered light from the trapping optical field is collected on a photodiode[4] mounted on a objective[5]; a lens is used as well to maximise the collection efficiency. The PSD of the scattered light is shown in blue (orange with feedback) in Fig. 8.5 at a pressure $P = 3 \times 10^{-3}\,\mathrm{mbar}$. The nominal secular frequencies in the transverse plane (measured with green light illumination as described in Chapter 4) are 390 Hz and 475 Hz. With optical trapping, those frequencies are increased to 427 Hz and 508 Hz, respectively. This linear coupling between the trapping beam and the transverse motion arises because of a slight misalignment between the centre of the trap and the cavity mode. Otherwise, only motion at twice the mechanical frequency would be seen since the particle would go over two intensity minima over half a period of oscillation. At high temperature, peaks at the first harmonic can be seen in

[3] EOT ET-3500, bandwidth of 12.5 GHz.
[4] ThorLabs PDA10DT
[5] Navitar 7000

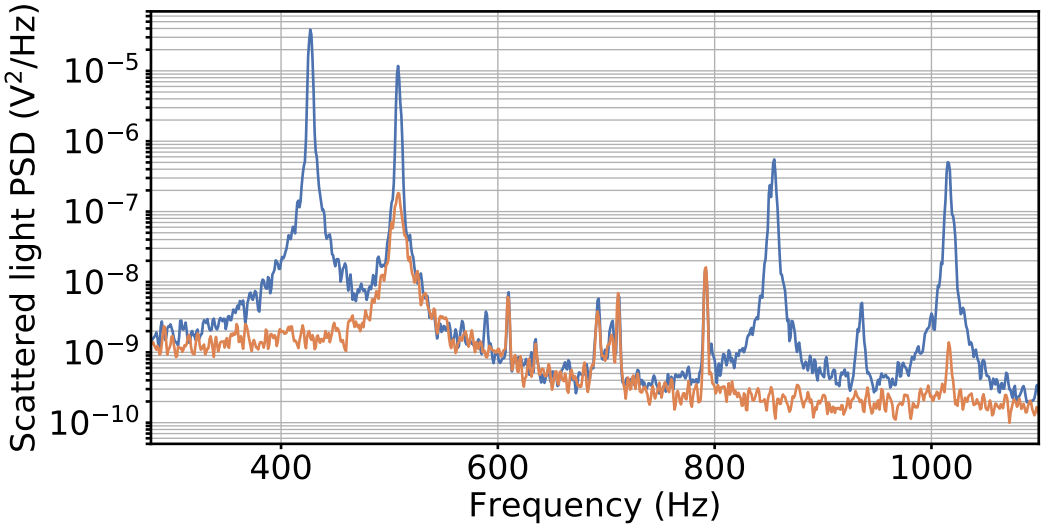

Figure 8.5: PSD of the scattered light from the cavity mode without (with) feedback on the Paul trap electrodes in blue (orange). The two secular frequencies can be seen at 427 Hz and 508 Hz alongside with the first harmonics. The measurement is taken at a pressure $P = 3 \times 10^{-3}$ mbar. The effective temperature is smaller than 200 mK for the mode 427 Hz and (20 ± 12) K for the one at 508 Hz.

Fig. 8.5. In order to apply feedback cooling, this signal is sent to a band-pass filter (first order band-pass filter with high-pass corner frequency at 50 Hz and low-pass corner at 150 Hz). The filter provides a phase shift of -64°and -68°respectively at the two secular frequencies. The signal is then amplified and applied to one of the two grounded electrodes of the trap. The cooling effect on the two secular motions can be seen in Fig. 8.5. As the secular motion in the transverse plane is defined along the diagonals, the secular motion along the feedback electrode is cooled more efficiently. Cooling is still obtained along the other axis because of residual trap ellipticity due to geometrical imperfections and stray fields. Assuming thermal equilibrium of the secular motion when the feedback is off, we estimate the temperature of the mode at 427 Hz to be $T_{eff} \lessapprox 200$ mK (which is an upper bound as the sensitivity is too low to detect the motion) and $T_{eff} = (20 \pm 12)$ K for the mode at 508 Hz. By reducing the thermal variance of the transverse motion we can significantly reduce the modulation in the optomechanical coupling and therefore in the mechanical motion along the cavity axis (defined by the optical trap, $\omega_m/2\pi \approx 38$ kHz). We show the amplitude squared R^2 spectra of the mechanical motion in Fig. 8.6 (see Chapter 5 for more information regarding R^2 spectra) measured in the calibrated PDH error signal and taken at the same time as the data shown in Fig. 8.5. The secular mo-

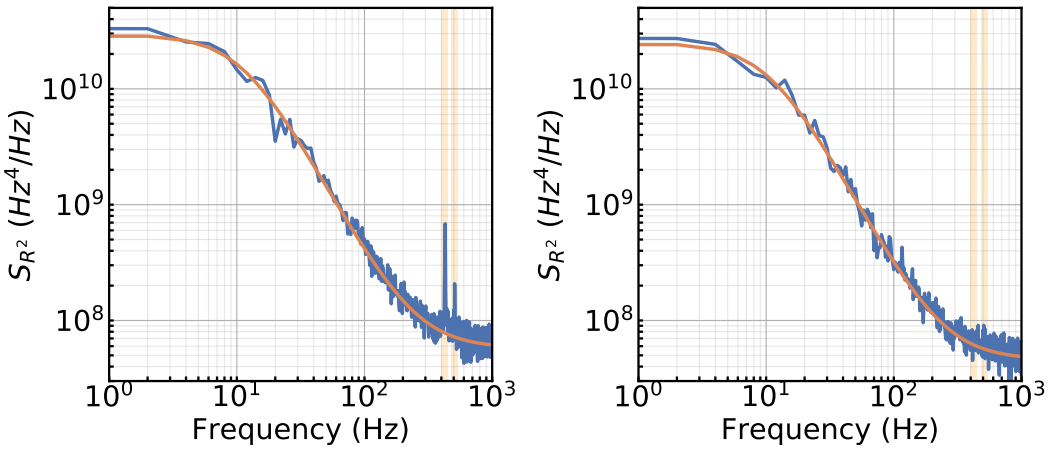

Figure 8.6: PSD of the square amplitude quadrature of the mechanical motion in blue (fit in orange). (left) Without feedback of the transverse secular motion. The secular frequency modulation can be seen at 427 Hz and 508 Hz. (right) With feedback, the modulations given by the secular frequencies are greatly reduced.

tions in the transverse direction lead to a modulation of the mechanical frequency, which can be seen in Fig. 8.6 and disappear with the feedback cooling scheme. This spectral analysis enables us, as well, to check that the feedback scheme does not modify the effective temperature of the motion along the optical direction. Within the measurement uncertainty, the motion is at the same effective temperature in both cases (0.4% of relative difference for 3% of statistical uncertainty on the two temperature measurements).

In Fig. 8.7, we show spectrograms of the PDH error signal (same datasets as the ones used in Fig. 8.6), used to measure the mechanical frequency stability over 20 s. The spectrogram consists of PSDs integrated over 10 ms shown as a function of time with amplitude represented with a logarithmic colour scale. By cooling the secular motion, greater stability in the mechanical frequency is achieved with suppression of the sidebands given by the secular motion. The slow fluctuations here in the mechanical frequency (of the order of 1%) are greatly reduced when cooling the mechanical motion (see Fig. 8.17). This demonstration of feedback cooling works efficiently for pressures between 10^{-2} mbar and 10^{-5} mbar. At higher pressures, the Q-factor is too small to make the feedback effective. At lower pressures, the band-pass filter used is likely not narrow enough, adding too much voltage noise which drives the nanosphere in the transverse direction.

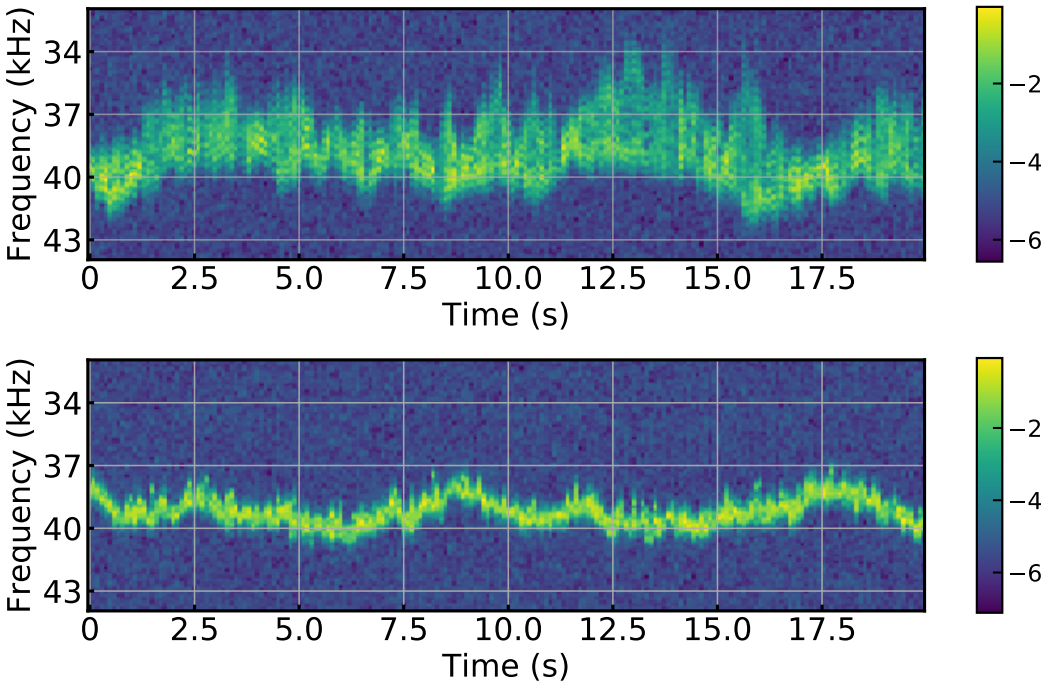

Figure 8.7: Spectrogram of the PDH error signal used to monitor the mechanical frequency. The colour scale is logarithmic for better visibility. (Top) Without feedback, sidebands at the secular frequencies can be seen around the mean mechanical frequency. (Bottom) With feedback on the secular motion, the sidebands are greatly suppressed.

8.3 Levitated optomechanics with two optical modes

In the second part of this chapter, we focus on experiments of the optomechanical interaction arising between a silica nanosphere and an optical field. In this section, we describe the set-up, theoretical approximations and temperature calibration methods. We create our optomechanical system by levitating a highly charged silica nanosphere in a composite potential obtained by overlapping an electrodynamic potential and an optical standing wave. The former provided by a linear Paul trap (see Chapter 3 and 4), the latter resulting from driving a high finesse Fabry-Perot cavity (see Section 7.4). In our typical scenario, the nanoparticle is optically trapped along the main axis by the gradient force in one of the cavity antinodes while radial confinement is guaranteed by the Paul trap potential and the transverse beam profile.

8.3.1 Experimental layout

We show in Fig. 8.8 a simplified schematic overview of our experimental setup (for more detail see Fig. 7.1). Two Nd:YAG lasers with a wavelength of $\lambda = 1064\,\mathrm{nm}$

drive the science cavity with a finesse of $\mathcal{F} = 36000$ (*configuration 2* which gives a half-linewidth of $\kappa/2\pi = 143 \pm 1\,\mathrm{kHz}$). One laser is exploited as a weak probe field and locked to the cavity by implementing a Pound-Drever-Hall (PDH) scheme. The second is used to optically trap the nanoparticle. Its frequency is offset locked to the weak beam, one free spectral range ($FSR = c/2L = 10.27 \pm 0.02\,\mathrm{GHz}$) away and its detuning from the cavity resonance can be precisely controlled. The particle is charged during the loading process by means of electrospray ionisation and captured directly in medium vacuum in the Paul trap (see Chapter 3). We use commercial silica nanospheres of measured mass $m = (4.88 \pm 0.03) \times 10^{-17}\,\mathrm{kg}$ (see Fig. 8.4) and radius $(185 \pm 2)\,\mathrm{nm}$. The trap is mounted on a three-axis translation stage (see Fig. 7.14). This is important for two reasons. First, it allows us to enhance the linear coupling of the probe field by trapping optically away from the cavity centre [44]. Second, it allows us to strongly suppress excess micromotion. Indeed, contrary to previous implementations [45, 46], the dynamics along the cavity axis is ideally micromotion free as long as this axis coincides with the main axis of the Paul trap.

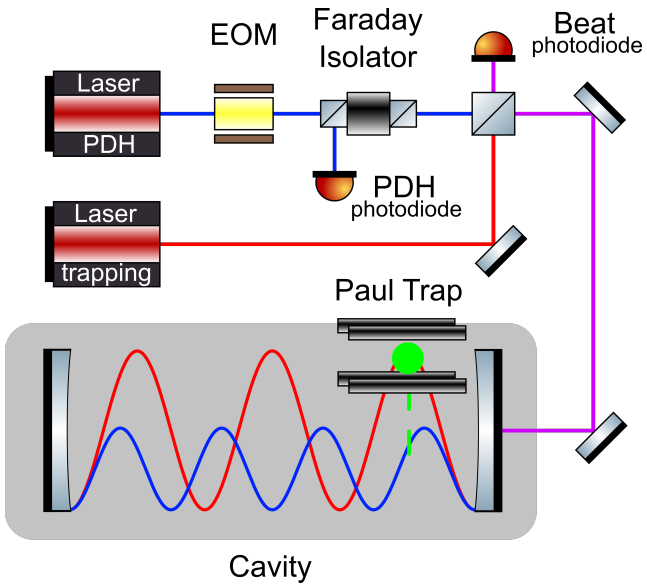

Figure 8.8: Simplified layout of the experiment (see Fig. 7.1 for more detail). A weak probe beam is used to lock the cavity by implementing a PDH scheme. A second beam, generated by a different laser, is used to optically trap the particle. By detecting the beat note of the lasers, the trapping beam is offset phase locked to the PDH beam one FSR apart $\sim 10.3\,\mathrm{GHz}$. The Paul trap, mounted on a three-axis translation stage, is aligned in the cavity transverse direction but kept far from the cavity centre. The trapping site can be controlled with $\sim 10\,\mu\mathrm{m}$ resolution.

We can measure and control the position of the optical trapping site referred to the cavity centre with a resolution of $\sim 10\,\mu$m, mainly limited by the particle thermal variance before optical confinement.

8.3.2 Approximations to the 3D dynamics

The dynamics of the nanoparticle has already been discussed in Section 2.5.3. In the transverse direction, this is a good approximation if the particle's rms amplitude, including both thermal and excess micromotion, remains small compared to the cavity waist. With our typical parameters, secular motion in the transverse direction is almost degenerate with frequencies $\omega_{x,y}/2\pi \simeq 400\,\text{Hz}$. This implies that the thermal rms is of the order of a few microns, i.e., $\sigma_x \simeq \sigma_y \simeq 3.7\,\mu\text{m} \ll w_c$ indicating that the cross coupling is small. Nonetheless, as the particle moves in and out of the Gaussian profile transversely (due to both secular motion and micromotion) there is a small and slow modulation of the coupling along the cavity axis which can lead to a time-dependent optical potential. Since the nanosphere used in this experiment is not a Rayleigh particle, small corrections to the light-particle interaction need to be included according to Mie scattering theory (see Section 2.3.2). A direct consequence is that the rate of photons scattered out of the cavity is no longer negligible as is the associated dissipative coupling. This is taken into account to the first order by modifying the cavity decay rate as $\kappa \to \kappa + \kappa_{sc}$, where κ_{sc} is the scattering induced decay cavity rate. When comparing the experimental results with analytical expectations one needs to consider difficulties in determining some critical parameters. Two examples are worth mentioning, the density of silica nano-spheres can be significantly different from the bulk value of $\rho = 2200\,\text{kg/m}^3$ down to the lowest reported value of $\rho = 1550\,\text{kg/m}^3$ [117]; it has been shown [170] that the dielectric constant of Stöber SiO_2 can be as small as 1.85, depending on temperature and hydration and rarely reaches the bulk value of 2.1. These examples clearly indicate how systematic errors could affect experimental estimates. Finally, quantum backaction, recoil included, could be safely neglected for the parameters explored.

8.3.3 Optical trapping

As the intracavity optical power is increased, a nanoparticle will become optically trapped. The threshold power at which trapping becomes stable depends on the

thermal force noise and therefore on the pressure. For the typical nanospheres we use (387 nm diameter), we observe stable trapping above 20 kHz at a pressure $P \approx 10^{-2}$ mbar. We show in Fig. 8.9 the measured mechanical frequency (trap frequency along the cavity axis) as a function of input power. Here, the trapping beam power is much larger than the power of the other beam and co-trapping can therefore be neglected.

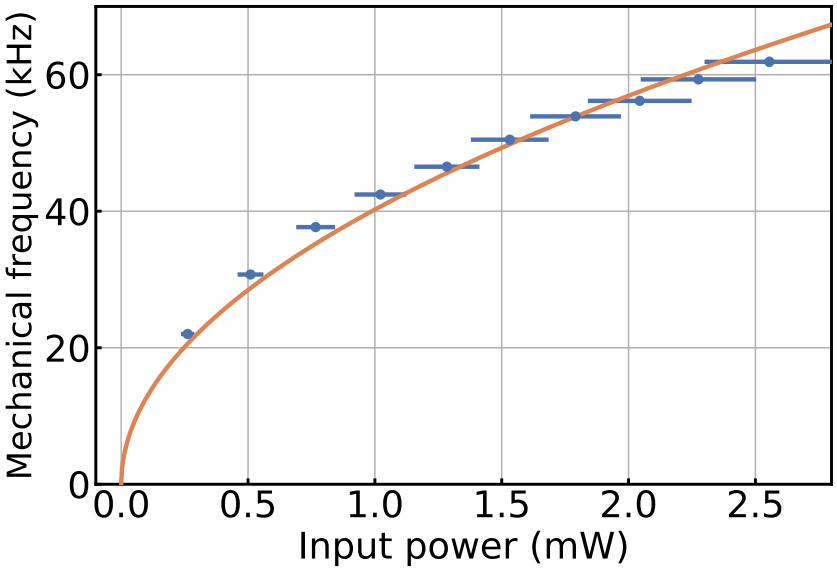

Figure 8.9: Trap optical frequency $\omega_m/2\pi$ as a function of input power (blue). A square-root fit, which corresponds to the expected behaviour, is shown in orange.

8.3.4 Thermometry

The dynamics of the experiment given above can be used to cool the centre-of-mass motion of the nanoparticle. The effective centre-of-mass temperature can be estimated in several ways. A common method assumes a constant bath temperature at $T_b = 293$ throughout the experiment. Though common, this approximation is often valid only at high pressures since absorption can lead to an increase in the bath temperature at lower pressures [70, 118]. Moreover, this method relies on the assumption of a constant coupling throughout the experiment. We discuss now a method not relying on this assumption. We can exploit the measurement of the particle induced optical losses κ_{sc} (see Section 8.1.2), to estimate the particle dielectric constant. With the measured value $\kappa_{sc}/2\pi = (11.0 \pm 1.4)$ kHz and taking into account the uncertainty in the particle radius $r = 1.98 \pm 0.07$, we find $U_o/2\pi = (58 \pm 4)$ kHz. Calibration of cavity spectra in terms of frequency fluctuations can

be performed accurately (see Appendix A.2). Then, we exploit the ratio of the peak area at ω_m and at $2\omega_m$ along with the measured U_o to simultaneously obtain the effective temperature and the distance of the trapping site with respect to the cavity centre, i.e., $\phi_p = \pi/2 + \pi x_i/L$ (see Section 2.5.3). It can be shown that when the nanoparticle displacement spectrum $S_x(\omega)$ is dominated by the thermal noise contribution, the phase quadrature PSD $S_y(\omega)$, around the mechanical frequency ω_m is proportional to $S_y(\omega) \propto G_1^2 S_x(\omega)$. Similarly, around the first harmonic at $2\omega_m$, $S_y(\omega) \propto G_2^2 S_{x^2}(\omega)$, where the expression of the squared-position PSD $S_{x^2}(\omega)$ can be found in Ref. [174]. We define by A_{ω_m} and $A_{2\omega_m}$ the integral in Hz^2 of the peak areas of the phase quadrature PSD $S_y(\omega)$ around the fundamental and first harmonic, respectively. By evaluating the area ratio, and the area of the fundamental, we get the following system of equations

$$\begin{aligned} \frac{k_B T_{eff}}{m\omega_m^2} \frac{k^2}{\tan^2(2\phi_p)} &= \frac{A_{2\omega_m}}{A_{\omega_m}}, \\ \frac{k_B T_{eff}}{m\omega_m^2} k^2 U_o^2 \sin^2(2\phi_p) &= 4\pi^2 A_{\omega_m}. \end{aligned} \tag{8.2}$$

Though this approach avoids any assumption regarding the bath temperature, it cannot be performed at every pressure as for high values, the strong non-linearity of the optical potential leads to an overestimation of $A_{2\omega_m}$, and as the pressure is

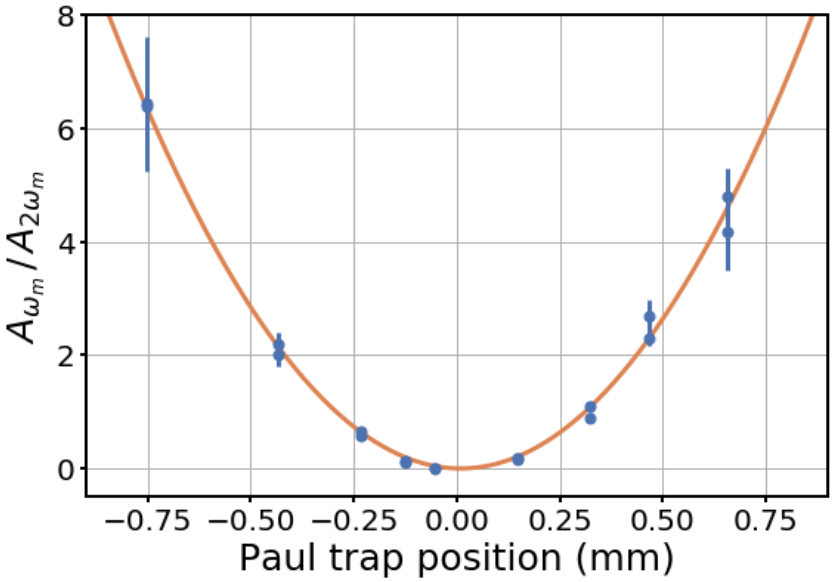

Figure 8.10: Area ratios for the fundamental and first harmonic spectral peaks of the nano-particle motion, along with parabolic fit.

reduced, $A_{2\omega_m}$ quickly falls below the detection noise floor since $A_{2\omega_m} \propto T_{eff}^2$. As such, Eqs. 8.2 is exploited to obtain a calibration coefficient, at intermediate pressure of $P \sim 10^{-2}$ mbar, which is then assumed to be constant as long as the particle is trapped in the same optical well and the lock to the cavity is not lost.

We show in Fig. 8.10 that the peak area ratio $A_{\omega_m}/A_{2\omega_m}$ as a function of the trapping site distance from the cavity centre shows the expected behaviour. Indeed, from Eq. 8.2 we have $A_{\omega_m}/A_{2\omega_m} \propto \tan^2(2\pi x_o/L) \simeq (2\pi/L)^2 x_o^2$. Naturally, to perform this measurement the particle needs to be released from the optical well at each data point, the agreement with the expected behaviour indicates good experimental reproducibility as all other parameters are kept constant. The particle position is monitored by calibrated direct imaging (see Chapter 4). Data shown in Fig. 8.10 has been obtained with a different nanoparticle than the one used in the following sections.

8.4 Quadratic optomechanical coupling

In this section, we operate the system in a regime dominated by the quadratic optomechanical coupling. Nonlinearities are of particular interest in optomechanics [175–179]. For example, the control over the position of ions or levitated nanoparticles within an optical cavity enables tuning between linear and quadratic optomechanical coupling [46, 49, 66, 180]. In membranes, single-photon to two-phonon coupling rates have been demonstrated to reach up to 240 Hz [181–183] paving the way for phonon shot noise measurements [184]. Moreover, to prepare non-Gaussian quantum states some degree of nonlinearity is necessary so that quadratic coupling plays a fundamental role in many proposed protocols to generate, for example, quantum superpositions [185] and Fock states [186, 187]. Levitation of a nanoparticle in a cavity standing wave is particularly favourable to study quadratic coupling, since there is no external elastic potential. The particle is naturally attracted by the optical gradient force toward an intensity maximum where the coupling is purely quadratic. After adapting and simplifying the dynamics presented in Section 2.5.3 to this specific case, we demonstrate a nonlinear coupling strong enough to cool a levitated nanosphere by more than two orders of magnitude. To the best of our knowledge, this is the first time dominant cooling due to this type of coupling in a cavity is reported. Importantly, the resulting oscillator dynamics is equivalent to

that obtained with active parametric feedback [41, 188, 189]. However, as for the comparison between linear cavity cooling and cold damping, the cooling mechanism is passive and does not rely on a position measurement. Finally, we describe the resulting highly nonthermal state of the mechanical motion caused by the nonlinear interaction which compares well with our theoretical description of the experiment.

8.4.1 Nonlinear dynamics

In the following we focus on the centre-of-mass motion (COM) along the cavity axis and assume that the nanoparticle is confined at an antinode of the trapping field. Moreover, we neglect the degrees of freedom in the transverse direction and their coupling to the optical fields. The nonlinear dynamical equation of motion for the oscillator and the optical fields are

$$\begin{aligned} \ddot{x} &= -\omega_x^2 x - \frac{\hbar k U_o}{m}\sum_j a_j^\dagger a_j \sin(2(kx+\phi_j)) - \gamma_m \dot{x} + \frac{F_{th}}{m}\,, \\ \dot{a}_j &= -(\kappa - i\Delta_o^j)a_j + iU_o a_j \cos^2(kx+\phi_j) + \sqrt{2\kappa_{in}}(\alpha_{in,j}+a_{in,j}) + \sqrt{2\kappa_v}\,a_{v,j}\,. \end{aligned} \tag{8.3}$$

8.4.1.1 Duffing and Van der Pol nonlinearities

If we consider a scenario where the probe power is significantly weaker than the trap beam, i.e. $\alpha_{in,p} \ll \alpha_{in,t}$, it is quite immediate to see that upon the usual expansion around the steady state solution to second order of the trigonometric functions in Eq. 8.3, one finds a purely quadratic coupling for the trapping beam with $G_{2,t} = k^2 U_o$ (i.e., $\phi_t = 0$). The probe field has both a linear and quadratic coupling respectively given by $G_{1,p} = kU_o \sin(2\phi_p)$ and $G_{2,p} = k^2 U_o \cos(2\phi_p)$. In these last two expressions the phase is entirely determined by the position x_i of the localisation site referred to the cavity centre, i.e., $\phi_p = \pi/2 + \pi x_i/L$. To gather a clearer understanding of the oscillator dynamics, however, it is more convenient to trace out the cavity rather than linearise, i.e., we want to write an approximate equation of motion for the particle dynamics in the following form

$$\ddot{x} = -\omega_m^2 x\left(1+\epsilon_D x^2\right) - \left(\gamma_m - \omega_m^2 \gamma_{nl} x^2\right)\frac{p}{m} + \frac{F_{th}}{m}\,, \tag{8.4}$$

where ω_m is the optical trap frequency and where we have introduced two additional terms: an elastic Duffing nonlinearity ϵ_D and a Van der Pol nonlinear damping γ_{nl}. The latter corresponds to a dissipation process that becomes more efficient for large

amplitude oscillations. Eqs. 8.3 can be rewritten in the form of Eq. 8.4 by looking at a first order correction to the adiabatic approximation. Neglecting the effect of the probe beam, assuming that $\omega_m/\kappa \ll 1$, and by following the method described in Ref. [190], one finds that

$$\epsilon_D = \frac{2G_2}{\kappa}\frac{\delta}{(1+\delta^2)},\ \gamma_{nl} = \frac{8G_2}{\kappa^2}\frac{\delta}{(1+\delta^2)^2}, \tag{8.5}$$

where $\delta = \Delta/\kappa$ is the normalised hot cavity detuning of the trapping beam and $\omega_m^2 = \frac{2\hbar G_2}{m}|\alpha_{t,s}|^2$ as expected, with $\alpha_{t,s}$ the steady state intracavity field amplitude. Eqs. 8.5 are valid under the additional condition $G_2\langle x^2\rangle \ll \kappa$ which is always satisfied in our experiment. As for linear coupling, the oscillator dynamics depends critically on the detuning sign. For a red detuned ($\delta < 0$) trapping beam the optical potential is softened and dissipation increased while the opposite happens for a blue detuned beam, which can result in dynamical instability. Interestingly, both nonlinear coefficients are power independent, this is a characteristic inherently due to levitation since there is no intrinsic elastic potential.

8.4.1.2 Energy PDF

It is quite convenient, at this point, to move to a reference frame rotating at ω_m and to write the equation of motion for the amplitude[6] $R(t) = \sqrt{x^2 + \dot{x}^2/\omega_m^2}$ and phase $\varphi(t) = -\text{atan}(\dot{x}/\omega_m x) - \omega_m t$ of the oscillator. By performing deterministic and stochastic averaging [191–193], valid in the high Q limit, one obtains two first order differential equations

$$\begin{aligned}\dot{R} &= -\frac{\gamma_m}{2}R + \frac{\omega_m^2\gamma_{nl}}{8}R^3 + \frac{S_{F_{th}}}{4m^2\omega_m^2 R} + \xi = -\frac{d\mathcal{V}(R)}{dR} + \xi,\\ \dot{\varphi} &= \frac{3\omega_m}{8}\epsilon_D R^2 + \frac{1}{R}\chi.\end{aligned} \tag{8.6}$$

Here, ξ and χ are two uncorrelated stochastic variables with correlation function $\langle\xi(t)\xi(t')\rangle = \langle\chi(t)\chi(t')\rangle = (S_{F_{th}}/2m^2\omega_m^2)\delta(t-t')$ and where we introduced the potential $\mathcal{V}(R)$. Eqs. 8.6 allows us to highlight two key aspects. First, the effect of the Duffing term is relegated to the evolution of the phase and has no effect on the energy of the oscillator. Second, the evolution of the amplitude is phase indepen-

[6] where we have used another definition for the amplitude quadrature R in comparison to Chapter 5, see Section 5.2

dent. For this reason, it is possible to write a one dimensional Fokker-Planck (FP) equation which describes the evolution of the probability density function (PDF) $P(R,t)$ of the amplitude. This is given by

$$\frac{\partial}{\partial t}P(R,t) = -\frac{\partial}{\partial R}(D^{(1)}P(R,t)) + \frac{\partial^2}{\partial R^2}(D^{(2)}P(R,t)), \tag{8.7}$$

here, $D^{(n)}$, $n = 1,2$ are the first two Kramers-Moyal coefficients which identify the drift ($n = 1$) and diffusion ($n = 2$) coefficients. From Eqs. 8.6 we have

$$\begin{aligned} D^{(1)}(R) &= -\frac{\gamma_m}{2}R + \frac{\omega_m^2\gamma_{nl}}{8}R^3 + \frac{S_{F_{th}}}{(2m\omega_m)^2 R}, \\ D^{(2)}(R) &= \frac{S_{F_{th}}}{(2m\omega_m)^2}. \end{aligned} \tag{8.8}$$

The steady state solution $P_\infty(R)$ of the FP equation is well known, and in the case of a purely additive noise, it is given by

$$\begin{aligned} P_\infty(R) &= \mathcal{N}\exp\left(\frac{1}{D^{(2)}}\int_0^R D^{(1)}(R')dR'\right) \\ &= \mathcal{N}\exp\left(-\frac{4m^2\omega_m^2}{S_{F_{th}}}\mathcal{V}(R)\right), \end{aligned} \tag{8.9}$$

where the potential $\mathcal{V}(R)$ is given by

$$\mathcal{V}(R) = \frac{\gamma_m}{4}R^2 - \frac{\omega_m^2\gamma_{nl}}{32}R^4 - \frac{S_{F_{th}}}{4m^2\omega_m^2}\ln(R). \tag{8.10}$$

Expressing the steady state solution of the FP equation in terms of energy E rather than amplitude, one readily finds

$$P_\infty(E) = \frac{\mathcal{N}}{m\omega_m^2}\exp\left[-\frac{E}{k_B T_b}\left(1 + \frac{\gamma_{nl}}{4m\gamma_m}E\right)\right], \tag{8.11}$$

where $\mathcal{N}$ is a normalization constant such that $\int_0^\infty P_\infty(E)dE = 1$. Explicitly, we have

$$\mathcal{N} = \frac{\eta\omega_m^2 e^{-1/\beta^2}}{\sqrt{\pi}\beta\,\mathrm{Erfc}(1/\beta)}, \tag{8.12}$$

where we have introduced $\beta = (k_B T_b\eta/m)^{1/2}$ and $\eta = \gamma_{nl}/\gamma_m$. Since the energy distribution is known, all the relevant dynamical parameters can be obtained, e.g., the effective temperature and damping. For a vanishing nonlinear damping Eq. 8.11

becomes the usual Boltzmann-Gibbs distribution. The energy PDF allows us to calculate the effective temperature as the expectation value of the energy, i.e., $T_{eff} = \langle E \rangle / k_B$. For a thermal noise driven oscillator, one readily finds

$$T_{eff} = \frac{2\mathcal{N}T_b}{\eta\omega_m^2\beta}\left[\beta - e^{1/\beta^2}\sqrt{\pi}\,\mathrm{Erfc}\left(\frac{1}{\beta}\right)\right]. \tag{8.13}$$

Another important dynamical parameter is the effective damping γ_{eff}. This is to be interpreted as the equivalent viscous friction that would lead to the effective temperature T_{eff} in Eq. 8.13, i.e., $T_{eff} = T_b\gamma_m/\gamma_{eff}$.

It is important to notice that the coupled dynamics described here are formally equivalent to active parametric feedback, which is commonly used in levitated optomechanics [188, 189]. Indeed, Eq. 8.11 describes the steady state energy distribution of both processes. This should not come as a surprise since in both cases the oscillator dynamic is modified by an optical force proportional to x^2p, i.e., a Van der Pol nonlinear damping. As such, quadratic coupling can also be viewed as passive parametric feedback. Furthermore, Eq. 8.11 represents the classical limit of two phonon cooling in the quantum regime [174].

Finally, we point out that as the pressure is reduced, and the cooling power provided by the quadratic coupling diminishes, additional parameters have to be included in the model. Two in particular; an additional force noise, with spectral density S_F, and a residual linear damping γ_l. The former can arise due to technical excess noise, e.g., voltage noise, but will ultimately be given by backaction and photon recoil. The latter could emerge from a residual linear coupling of the trapping beam or a non-vanishing detuning of the probe field. In such a scenario the energy PDF would be given by

$$P_\infty(E) = \frac{\mathcal{N}}{m\omega_m^2}\exp\left[-\frac{2m(\gamma_m+\gamma_l)}{S_F + 2k_BT_bm\gamma_m}E\left(1+\frac{\gamma_{nl}}{4m(\gamma_m+\gamma_l)}E\right)\right]. \tag{8.14}$$

It is clear that Eq. 8.14 is significantly different from the original PDF, furthermore, the interdependence of the parameters make their experimental determination difficult. At the same time, however, the oscillator dynamic can be richer. For example, a negative γ_l, possible with a blue detuned probe beam, can lead to a dynamical equilibrium due to competing processes.

8.4.2 Results

Here, we present data obtained with a probe and trap beam input power of $2.9\,\mu$W and $830\,\mu$W respectively. The probe is locked near resonance while the trap beam has a nominal red detuning of $\Delta_t/2\pi \simeq -100\,$kHz. For this experiment, the nanosphere is trapped $x_i - L/2 = (803 \pm 25)\,\mu$m away from the centre of the optical cavity to provide a strong linear optomechanical coupling on the probe beam used for read-out of the motion (see Section 2.5.3). This corresponds to the farthest achievable position away from the centre of the cavity in our experiment. The optimum position would be $L/4 = 3.7\,$mm which would provide maximum linear optomechanical coupling. The particle motion is monitored through the PDH error signal since its linear coupling enables us to measure the mechanical motion directly. Spectra at different pressures are shown in Fig. 8.11. It is clear that the oscillator resonance at $\omega_m/2\pi \simeq 51\,$kHz does not converge to a Lorentzian-like peak, as the pressure is reduced, but rather converges to a Gaussian peak. This apparent broadening is due to low frequency intensity fluctuations and by crosscoupling with the motion in the directions perpendicular to the cavity axis. This motion is adiabatically eliminated when moving to the rotating frame as is the case for the Duffing nonlinearity.

The experimental energy distribution can be obtained from the square of the oscillator amplitude $R(t)$ (see Chapter 5). This is shown in Fig. 8.12(a) and (b) at two

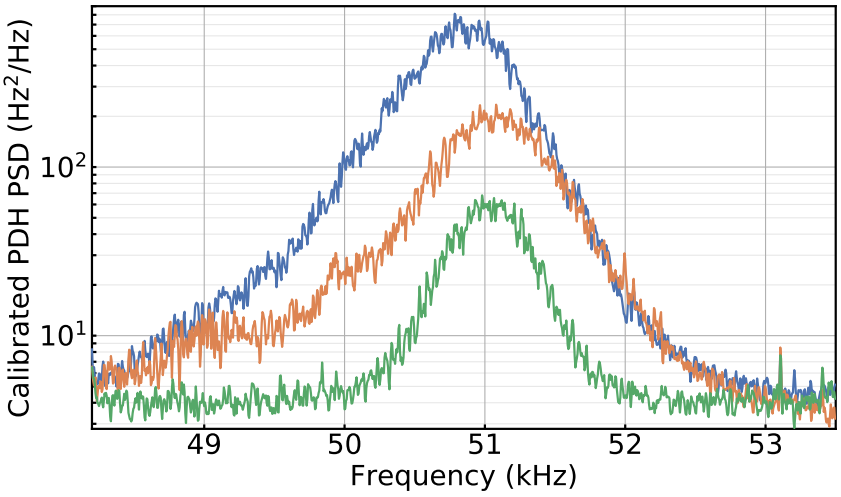

Figure 8.11: Calibrated PSD of the frequency fluctuations induced by the particle motion in the PDH error signal at different pressures. The blue, orange and green PSDs show the particle displacement at pressures of $1.2 \times 10^{-2}\,$mbar, $8.6 \times 10^{-4}\,$mbar and $5.4 \times 10^{-6}\,$mbar, respectively.

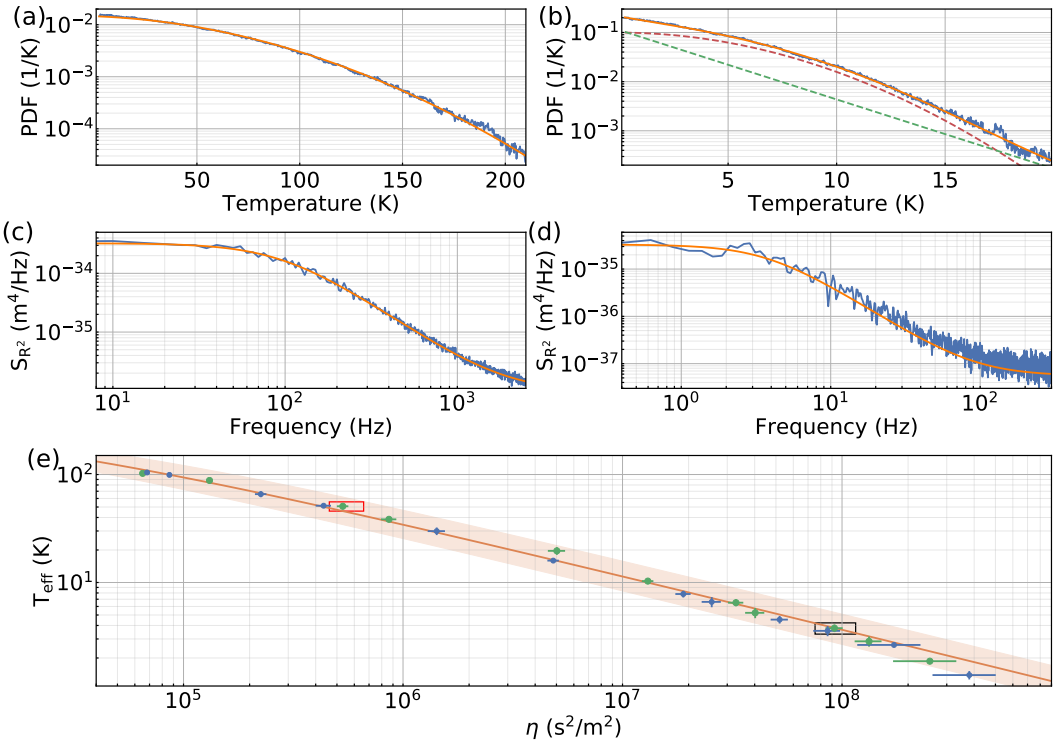

Figure 8.12: Panels (a) and (b): Energy distribution (blue), expressed in units of k_B, for the motion along the x-axis along with a fit (orange) following Eq. 8.11 for different pressures $P = 8.6 \times 10^{-2}$ mbar and 1.6×10^{-4} mbar respectively. In Panel (b) the contribution of the detection noise is included; the corresponding marginal distributions for the motion (red dashed) and noise (green dashed) are also shown. Panels (c) and (d) show the PSD of R^2 corresponding to the distributions in panels (a) and (b) respectively; fits (orange) of the R^2 spectra allow a direct estimation of the energy autocorrelation time constant (see main text); Panel (e): effective temperature as function of fitted parametric gain $\eta = \gamma_{nl}/\gamma_m$ along with an *a priori* analytical estimation (orange line). Shaded region indicates the uncertainty of the theoretical curves due to experimental uncertainty in relevant parameters; blue and green data points correspond to localisation on slightly different optical wells. The red square marks the data point corresponding to panels (a) and (c), the black square to panels (b) and (d).

different pressures where the distributions are expressed in units of k_B, i.e. temperature, for a more intuitive reading. At the higher pressure of $P = 8.6 \times 10^{-2}$ mbar (panel (a)), the deviation from a thermal exponential distribution is immediately recognisable, indeed, the nonlinear damping is much more efficient in suppressing large amplitude fluctuations. At the lower pressure of $P = 1.6 \times 10^{-4}$ mbar (panel (b)) this behaviour is initially less evident. As the motion becomes colder the impact of the detection noise becomes more relevant and it needs to be taken into account. Assuming the noise floor is white and uncorrelated with the motion, its

distribution is again exponential. We fit the experimental data taking into account both processes, the oscillator energy PDF is then recovered by taking the marginal distribution. As the intrinsic gas damping cannot be measured independently, and pressure gauges have a rather low accuracy, we use as a fitting parameter the ratio $\eta = \gamma_{nl}/\gamma_m$ which can be interpreted as a parametric gain. We show in Fig. 8.12 (panel (e)) the experimental effective temperature T_{eff} as a function of η, along with an analytical estimation. The final temperature can be estimated in two ways: from the area of the peak in the probe PSD (calibrated using the area ratio method discussed in Section 8.3.4), as is typical, and from the expectation value of the fitted distribution. The consistency of these two estimates, well within the experimental uncertainty, and the agreement with the analytical expectation, demonstrate that even at the lowest pressure the quadratic coupling is the dominating process in the dynamics.

Another clear signature of the nonlinear damping, is the dependence on pressure of the effective temperature. An approximate expression can be obtained from Eq. 8.13; in the low pressure limit, we have $T_{eff} = (4mT_b/\pi k_B \eta)^{1/2}$. Since η grows inversely proportionally to the pressure, the effective temperature decreases proportionally to the square root of the pressure. This is shown in Fig. 8.13(a) where the experimental observation is compared with an analytical estimation. A direct consequence is that the effective total damping γ_{eff} must have a similar behaviour; in the low pressure limit we have $\gamma_{eff} = \gamma_m (\pi k_B T_b \eta/4m)^{1/2}$. This implies perfect correlation between T_{eff} and γ_{eff} as the pressure is reduced.

A direct estimation of the effective damping can be obtained even in the presence of the Duffing term and of the broadening of the spectral peak, evident in Fig. 8.11. By looking at the PSD of $R^2(t)$ it is possible to obtain information on the energy autocorrelation time constant. PSDs at two different pressures are shown in Fig. 8.12. Although possible for a thermal oscillator (see Chapter 5), calculating an analytical expression for the R^2 PSD when the dynamic is dominated by a nonlinear damping is not trivial. However, it can be shown that modelling the PSD as $S_{R^2}(\omega) = 16\gamma_R a_o^2/(\omega^2 + \gamma_R^2)$ then γ_R allows us to calculate the effective damping. In the absence of non-linear damping, γ_R coincides with the gas damping while $a_o = \sigma_x^2 = k_B T_b/m\omega_m^2$ is the position motional variance. At the same time,

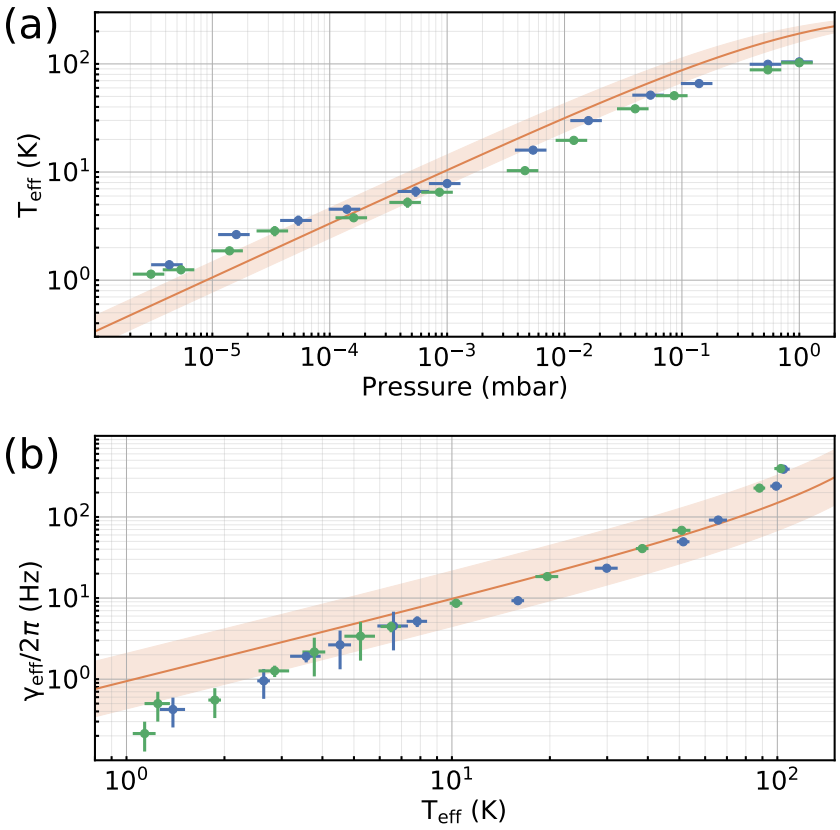

Figure 8.13: Panel (a): The effective temperature as a function of pressure. Panel (b): The measured effective damping as a function of T_{eff}. In both panels blue and green data points correspond to localisation on slightly different optical wells; also shown is an analytical estimation (orange line) with the shaded region indicating the uncertainty of the theoretical curves.

$\sigma^2_{R^2} = 4a_o^2 = 4\sigma_E^2/(m\omega_m^2)^2$ which connects the energy variance to its mean. The simplicity of this last expression stems from the fact that the PDF is exponential, i.e., $\sigma_E = \langle E \rangle$. This is no longer true in the presence of a non-linear damping where the distribution tends to an half-normal distribution and a_o does not directly provide the position variance. Indeed, the quadratic coupling is much more effective in reducing the energy variance than the mean. Interestingly, $S_{R^2}(\omega)$ can still be modelled with $S_{R^2}(\omega) = 16\gamma_R a_o^2/(\omega^2 + \gamma_R^2)$. In this case however we have $\sigma_x^4 = a_o^2\langle E \rangle^2/\sigma_E^2$. This last expression might seem tautological but it allows us to infer the connection between γ_R and the effective damping. Since the area width product must be conserved we can write $\gamma_{eff} = \gamma_R \sigma_E^2/\langle E \rangle^2$. This expression can be shown to hold through numerical simulations even if derived here not in a rigorous way. The effective damping calculated with this method plotted as a function of T_{eff} is shown in Fig. 8.13(b) demonstrating the expected good correlation.

8.5 Linear optomechanical coupling

In the previous section the system was operated in a regime dominated by quadratic optomechanical coupling. The versatility of this levitated oscillator system, in addition to the control over the optical well location provided by the Paul trap, enables us to operate the system in a very different regime where the linear optomechanical coupling dominates. Away from the trap centre, as previously demonstrated, probe and trapping fields have different phases. This was previously used to detect the motion on the weak probe beam given its linear optomechanical coupling. By increasing the power of the red-detuned probe beam, its effect on the nanoparticle rapidly dominates over the dynamics. Indeed, first, the linear optomechanical is much stronger than the quadratic one, second, as the power of the probe beam increases, it pulls the particle equilibrium position away from the antinode of the strong beam (anti-trapping), therefore further reducing the effect of the quadratic coupling. While keeping constant experimental parameters, the pressure in the vacuum chamber is reduced, leading to a lower effective temperature on the nano-oscillator.

8.5.1 Results

The experimental parameters presented here are similar to the ones used in the previous section. The input powers of the probe and trap beams are $610\,\mu$W and $180\,\mu$W, respectively. Unlike in the quadratic case, the trapping beam is used for the PDH scheme. It is locked near resonance while the probe beam has a nominal detuning $\Delta_p/2\pi = -30\,$kHz, slightly smaller than the optimal one, in order to reduce heating from frequency noise (see Fig. 2.9(a)). For this experiment, the nanosphere is trapped $x_i - L/2 = (822 \pm 25)\,\mu$m away from the centre of the optical cavity. The particle motion is monitored in the PDH error signal as well as in the direct detection of the cavity reflected probe optical mode. Spectra at different pressures can be seen in Fig. 8.14. The noise floor level is compatible with the estimated frequency noise of both lasers. Though the frequency noise level is higher on the probe field (2 W Mephisto laser), the optomechanical coupling is ~ 4 times larger on the probe mode, hence a sensitivity ~ 16 times larger. Interestingly, at pressures below $P \approx 10^{-5}\,$mbar (see Fig. 8.14(right)), a dip can be noticed in the noise floor in the right-hand side of the mechanical frequency. This is a clear signature of a classical interference effect mediated by the optomechanical interaction. In the optical cav-

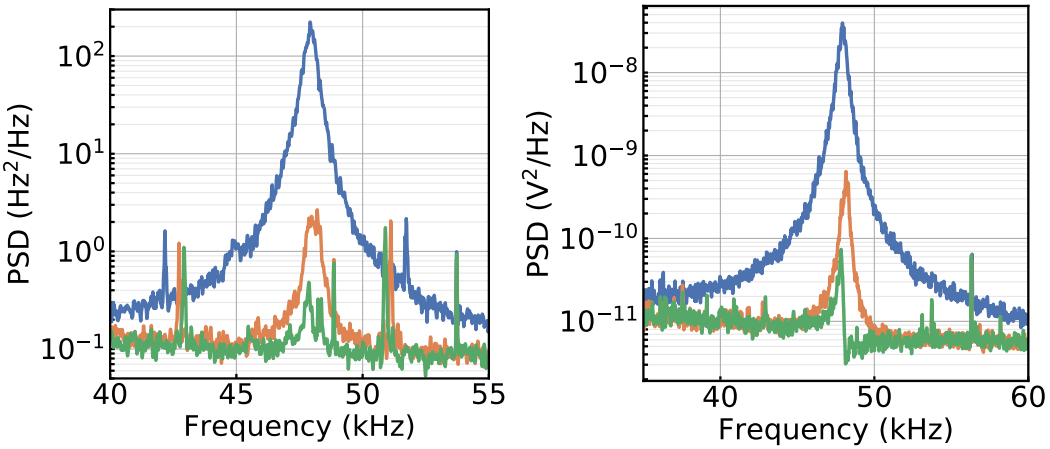

Figure 8.14: (left) Calibrated PSD of the frequency fluctuations induced by the particle motion in the PDH error signal at different pressures. (right) PSD of the intensity fluctuations induced by the particle motion in the probe beam reflection at different pressures. In both cases blue, orange and green PSD show the particle displacement at pressures 1.2×10^{-1} mbar, 1.2×10^{-3} mbar and 4.6×10^{-6} mbar, respectively. Spectra of same colour on both figures were recorded at the same time.

ity, frequency noise of the probe beam is transduced into an intensity noise which drives the levitated oscillator. As a consequence of the optomechanical interaction, this motion modulates the phase of the reflected field which in turn modulates the intracavity field amplitude, hence the interference effect. For a shot-noise limited input with negligible frequency noise fluctuations, this is a well-observed phenomenon which can lead to squeezing of the field fluctuations below the shot-noise level [17].

In Fig. 8.15, we present different effective temperature estimations, T_{eff}, as a function of pressure. The temperature can be estimated from direct integration of the PSD of the PDH error signal (or from the direct detection of the probe field) around the mechanical frequency $\omega_m/2\pi \approx 48\,\text{kHz}$ as shown in red (purple). We use the same method for the calibration as the one presented in the quadratic optomechanical case by considering the area ratio $A_{\omega_m}/A_{2\omega_m}$ at $P = 5.4 \times 10^{-2}\,\text{mbar}$ (see Section 8.3.4). The temperature can as well be estimated as $T_{eff} = \frac{\gamma_m}{\gamma_{eff}} T_b$, where γ_m is the gas damping and T_b is the bath temperature (shown in blue). This method relies on the assumption of a constant bath temperature $T_b = (293 \pm 2)\,\text{K}$ throughout the experiment. The effective damping γ_{eff} is evaluated from the amplitude squared amplitude R^2 spectra (see Chapter 5) of either PDH error signal or direct detection of the probe field (measurements in agreement within 5%). Finally, γ_m is

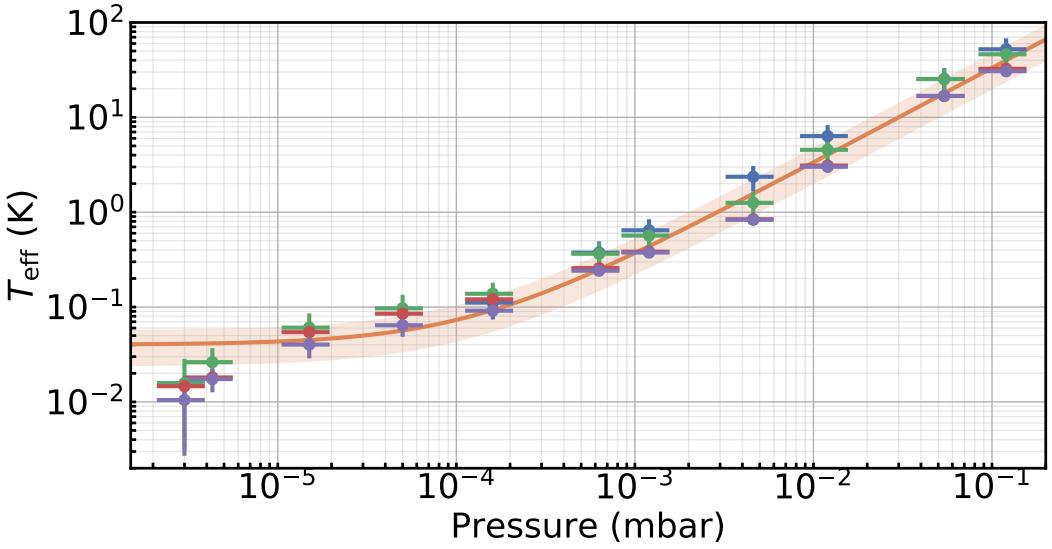

Figure 8.15: Effective temperature as a function of pressure. Red (purple) data points correspond to the temperature estimated from the integration of the PSD of the PDH error signal (direct detection of the reflected trapping field) and calibrated using the area ratio method discussed in Section 8.3.4. Blue data points are temperature estimations from the measured effective damping γ_{eff}. In green we show the temperature estimated from the integral of the reflected trapping field but, unlike purple, calibrated using the temperature estimation given by the effective damping γ_{eff} at $P = 5.4 \times 10^{-2}$ mbar. Also shown is an analytical estimation (orange line) with the shaded region indicating the uncertainty of the theoretical curves.

estimated from the gas damping law (see Eq. 2.3). Though this law relies on the precise knowledge of the experimental parameters and particularly the pressure, the gas damping can be measured independently using the camera (when the particle is not trapped optically) at each pressure given by the pressure gauge (see Chapter 4). We also present the temperature estimated from the integration of the direct detection shown in green, but this time, unlike the purple graph, it is calibrated using the temperature obtained from the effective damping γ_{eff} at $P = 5.4 \times 10^{-2}$ mbar. Lastly, in orange, we show a theoretical estimation of the effective temperature assuming an excess force noise $S_F = 1 \times 10^{-37}\,\text{N}^2/\text{Hz}$. A theoretical estimation, without Paul trap noise, but with similar experimental parameters was discussed in Section 2.5.6. As it can be noticed in Fig. 8.15, at pressures below $\sim 5 \times 10^{-5}$ mbar, the effective temperature saturates, corresponding to an additional effective force noise of $S_F \approx 5 \times 10^{-38}\,\text{N}^2/\text{H}$, leading to a final temperature of ~ 20 mK. This can be explained by two facts. First, the Paul trap and cavity axis are aligned with an accuracy of $\sim 3°$. Therefore, any voltage noise on the trap AC rods will be pro-

jected onto the cavity axis. Given the measured noise of the high voltage amplifier $S_V = 200\,\mu\mathrm{V}/\sqrt{\mathrm{Hz}}$ around 50 kHz and assuming a 3° angle, we expect a force noise $S_F \approx 3 \times 10^{-38}\,\mathrm{N}^2/\mathrm{Hz}$ (see Section 3.2.2.3). Furthermore, co-trapping in the transverse direction due to the optical field could shift the particle equilibrium position away from the Paul trap centre, leading to additional noise in the secular motion (since cancellation of correlated voltage noise only occurs in the Paul trap centre) and possible additional excess micromotion. The average of the different estimators give a final temperature at $P = 3.0 \times 10^{-6}\,\mathrm{mbar}$ of $T_{eff} = (21 \pm 4)\,\mathrm{mK}$. This corresponds to an improvement in the final reached temperature with two optical modes by more than three orders of magnitude, despite the bad-cavity regime [44]. The lowest temperature reported here is similar to the one demonstrated with an optical tweezer and cavity in the standard optomechanical case [47] (by opposition to the coherent scattering case [40, 51]). This final temperature could be improved by one order of magnitude with lower noise electronics and better alignment between the Paul trap and the optical cavity. Furthermore, this measurement was taken without the filtering cavity (see Section 7.3) and without feedback on th secular frequencies (see Section 8.2). Assuming no other technical noise, without the filtering cavity, frequency noise is expected to become a limiting factor at pressures below $P = 10^{-6}\,\mathrm{mbar}$. Nevertheless, it could still be used here to improve the detection sensitivity, particularly at the lowest pressures (see Fig. 8.14).

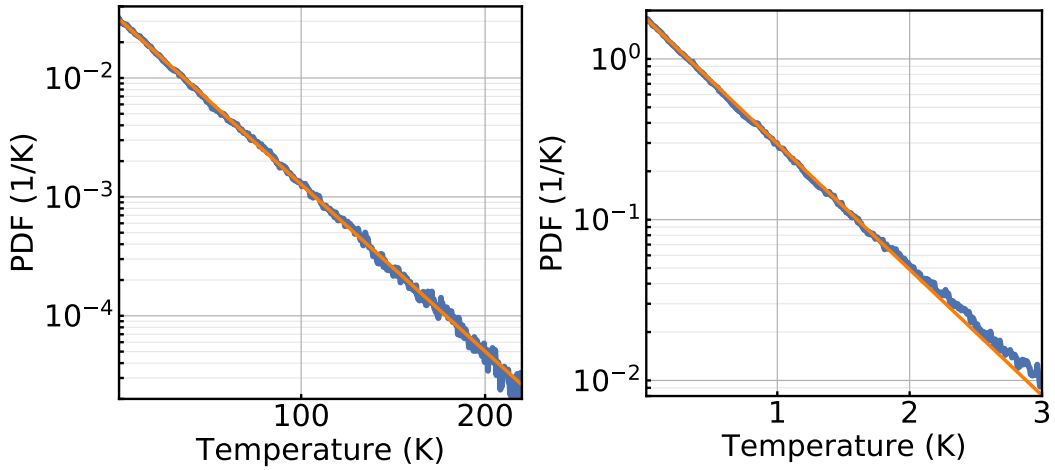

Figure 8.16: Energy distribution expressed in units of k_B, for the motion along the optical direction at different pressures. (left) pressure $P = 5.4 \times 10^{-2}\,\mathrm{mbar}$ (right) pressure $P = 6.3 \times 10^{-4}\,\mathrm{mbar}$.

The energy distribution of the oscillator is thermal (exponential) as expected with this linear cooling process (see Fig. 8.16 to be compared with Fig. 8.12). Lastly, we show in Fig. 8.17, the spectrogram of the direct detection PSD, demonstrating satisfying mechanical frequency stability of the oscillator at different pressures. When cooling the oscillator along the cavity axis, it can be noticed that the frequency is more stable here in comparison to what was shown in Fig. 8.7 (0.2% at $P = 1.2 \times 10^{-1}$ mbar and 0.3% at $P = 6.3 \times 10^{-4}$ mbar). This can be explained among others by the reduction of power modulation caused by the scattering losses (see Section 2.3.2).

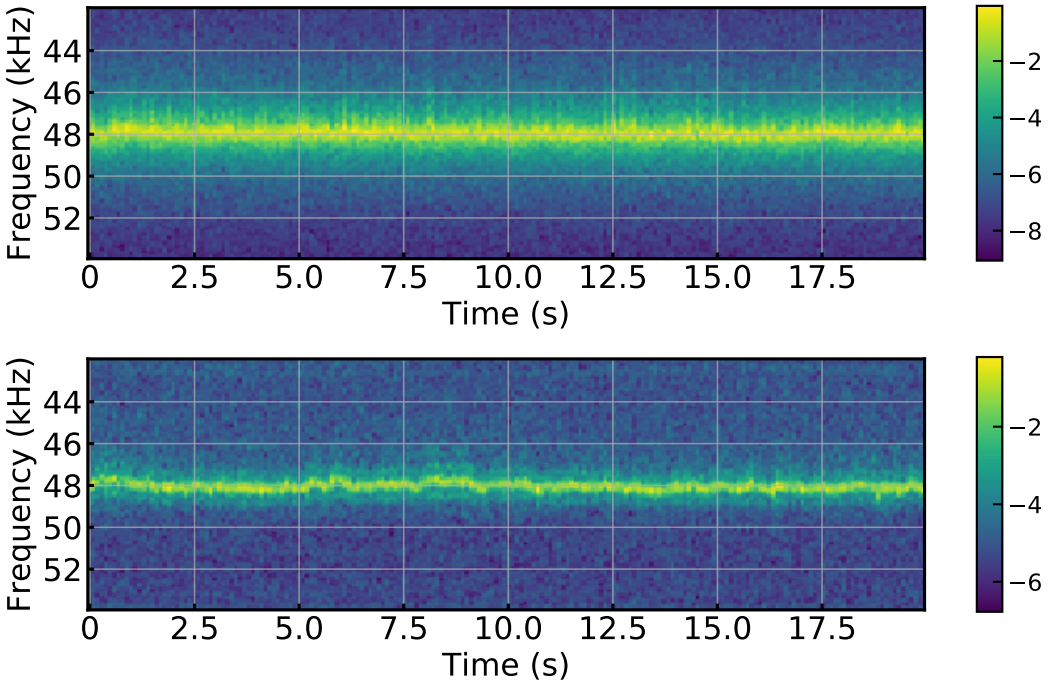

Figure 8.17: Spectrogram of the PSD of the direct detection of the trapping field at different pressures with logarithmic scale, to monitor the stability of the trapping frequency. (bottom) pressure $P = 1.2 \times 10^{-1}$ mbar (right) pressure $P = 6.3 \times 10^{-4}$ mbar.

8.6 Summary

There are few reports of estimation of Stöber silica polarisability as measured here. This is nevertheless a crucial parameter to evaluate accurately the optomechanical coupling as well as the scattering losses. We have reported measurements of those losses by measuring the difference in linewidth with and without a single nanoparticle inside the cavity field. We pointed out that those measurements are challenging

and discussed possible improvements. Inside the optical cavity, with small optical powers, the trapping potential in the transverse direction is predominantly defined by the Paul trap. Depending on the Paul trap parameters and relative position between the optical and trap potential centres, secular motion and excess micromotion can have an amplitude comparable to the cavity waist. In this case, the optomechanical coupling can be modulated which leads to an undesired modulation of the mechanical frequency and cooling rate. The secular motion can be detected in the scattered light of the trapping field. Using this signal, we have demonstrated cooling of the secular motion below $T_{eff} = 200\,\mathrm{mK}$ with a velocity damping feedback scheme applied on a single trap electrode. Modulations in the mechanical frequency were clearly reduced. We have also confirmed that the effective temperature of the motion defined by the optical trap was not affected by the feedback mechanism. By using two optical modes as initially studied in Ref. [24, 44], in conjunction with the Paul trap, this nano-oscillator system demonstrates great versatility for the study of regimes dominated by either quadratic or linear optomechanical coupling. We demonstrate for the first time, to the best of our knowledge, cooling solely provided by quadratic optomechanical coupling. Comparison of the experimental results show good agreement with analytical calculations. This type of passive parametric feedback cooling is analogous to the active feedback cooling in levitated optical tweezers and indeed comparable temperatures are obtained here. The major difference between the two methods is that the cavity automatically applies feedback whereas, conventionally, detection and electronic feedback are required to modulate the potential for active cooling. We have also shown that a highly nonthermal state is produced, which in the quantum regime, would be a highly nonclassical state. In both cases, the cooling rate decreases as the particle is cooled to the bottom of the optical potential. When operating the system in the linear optomechanical regime, we have demonstrated cooling down to $T_{eff} = (21 \pm 4)\,\mathrm{mK}$ limited by technical noise in the Paul trap. By reducing voltage noise in conjunction with using the filtering cavity, near ground state cooling should be achievable (see Section 2.5.6). We report here a final effective temperature lower by more than three orders of magnitude with two optical modes [44]. Furthermore, we demonstrate stable trapping in the optical well of a cavity standing-wave down to $P \sim 10^{-6}\,\mathrm{mbar}$.

Chapter 9

Conclusion and outlook

In this chapter we review the main results presented in this work, both of technical and physical relevance. We discuss then possible short-term improvements and reasonable applications.

9.1 Summary of results

9.1.1 Technical achievements

Several technical achievements have been presented here to be able to manipulate with reliability levitated nanospheres in a low noise environment. After incorporating classical noise in a theoretical model of the experiment, it is clear that it needs to be addressed in order to reach the quantum regime with conventional levitated optomechanics (see Chapter 2). Frequency noise has recently been demonstrated as a limitation to reach ground-state cooling [47]. Here we have demonstrated experimentally that the detection sensitivity in the current set-up was limited by frequency noise (see Chapter 7). In order to further reducing its effect on the signal-to-noise ratio and in spurious heating of the nanosphere, we have designed a filtering cavity with custom original design presented in Chapter 7. With its measured half-linewidth of $\kappa/2\pi = 2.5\,\mathrm{kHz}$, we characterised the attenuation in frequency noise provided. When using the cooling scheme with two adjacent optical modes [24, 44], filtering the frequency noise on both lasers could in theory be sufficient to reach the ground-state of the centre-of-mass motion.

We have characterised a miniature linear Paul trap specifically designed for levitated optomechanics experiments and presented in Chapter 3. Printed circuit boards are used to mount the trap and facilitate electrical connections. The dielectric re-

mains 3.5 mm away from the trap centre therefore reducing the effect of individual charges and charged nanospheres accumulating during the loading phase or when the cold-cathode pressure gauge is on. The trap is small enough to fit in our optical cavity with openings in the centre of the endcaps for the cavity mode. The two other access directions are used for the loading process and for imaging of the nanoparticle. Despite its simple design, we reported in Chapter 4 secular frequency stability of 2 ppm/hr similar to what has been reported in mass-spectrometers loaded with nanoparticles [99]. We have also reported a method combining electrospray loading [96] with a quadrupole guide which enables us to reliably trap charged nanospheres at a pressure of $P = 10^{-1}$ mbar. It is worth noting that the dielectric of the Paul trap acts as a shield which has been protecting efficiently the cavity mirrors during the loading phase.

We have detailed an imaging method in Chapter 4 for low-frequency oscillators such as a levitated nanosphere in a Paul trap. When used in conjunction with super-resolution algorithms we have reported displacement sensitivities better than $10^{-16}\,\mathrm{m}^2/\mathrm{Hz}$. We applied this method to demonstrate the good force-noise sensitivities of levitated nanospheres in vacuum (sensitivity better than $1\,\mathrm{aN}/\sqrt{\mathrm{Hz}}$). This imaging method was used to characterise the Paul trap stability and nanosphere temperature. While estimating the size of the nanosphere with the gas-damping law as function of pressure is highly inaccurate (due to poor knowledge of pressure, particle shape and density uncertainties), we have discussed several alternatives. With the imaging method, we are able to estimate the nanosphere mass with 3% of uncertainty.

High-Q oscillators typically exhibit drifts in their frequency of oscillation as it has been reported here in the Paul trap and more generally in optical traps. The frequency of oscillation is typically very sensitive to potential drifts. We have demonstrated a phase-sensitive method to measure the intrinsic mechanical linewidth of an oscillator, with phase fluctuations (or conversely frequency fluctuations) $\phi(t)$ satisfying $|\frac{d\phi(t)}{dt}| \ll \omega_o$, where ω_o is the oscillator frequency. This method was here illustrated with our levitated oscillator at 8×10^{-7} mbar demonstrating a linewidth as small as $80\,\mu$Hz and drifts three times larger than the linewidth.

With the typical trapping frequency in the cavity presented here ($\omega_m/2\pi \approx 50\,\mathrm{kHz}$), the effective radial frequencies can remain quite low ($\sim 400\,\mathrm{Hz}$). In this case, cooling the radial motion can prevent modulation of the optomechanical coupling and, therefore, of both the mechanical frequency and the cooling rate. We have demonstrated a proof-of-principle velocity damping where scattered light from the cavity trapping mode is fed back to one Paul trap electrode to provide cooling below 200 mK.

9.1.2 Experimental achievements

Levitated optomechanics is at an exciting stage with much progress having been realised over the last decade, including the quantum regime having recently been reached [40, 51]. As mentioned in the introduction, a levitated nanosphere in vacuum is a tremendous platform for studying not only different signatures of quantum mechanics but material science and thermodynamics. Here we report experiments with applications in those different fields. In Chapter 6, we addressed collapse models. These phenomenological models combine the measurement postulate and quantum mechanics to account for a description valid in both the macroscopic and microscopic regimes. The most studied model (CSL) introduces two parameters which determine the size of a quantum superposition r_C at which the collapse rate λ dominates. By placing bounds on the measured excess noise of our levitated oscillator at $8 \times 10^{-7}\,\mathrm{mbar}$, we were able to confirm recent exclusion bounds in the parameter space $\lambda - r_C$. At $r_C = 10^{-7}\,\mathrm{m}$ this experiment excludes collapse rate values $\lambda > 10^{-6}\,\mathrm{s}^{-1}$. Moreover, these studies pave the way for the next generation of platforms to test the CSL model. By operating the system in a cryostat kept at 300 mK, and at pressure $P = 10^{-13}\,\mathrm{mbar}$, exclusion down to $\lambda > 10^{-12}\,\mathrm{s}^{-1}$ could be achieved [37]. In this scenario, a very careful analysis of the detection both in terms of sensitivity and spurious heating will be required as demonstrated theoretically in Ref. [37]. Dissipative variants of the CSL model have been introduced to satisfy conservation of energy. The narrow-linewidth measurement presented here enabled us to bound the excess damping other than provided by ambient gas. This bound has been directly applied, in a novel way, to exclude parameters in two dissipative variants of collapse models, namely CSL and Diósi-Penrose. A significant improvement over those bounds is within reach with lower noise electronics and a sphere

with a 10 μm radius.

Precise evaluation of the silica nanospheres parameters such as mass measurements is a compulsory step in levitated optomechanics experiments [66, 99, 103, 117]. A challenging parameter to evaluate is the particle polarisability. Here, we estimate it by measuring the scattering losses in the cavity, combined with our precise knowledge of the mass. We also discussed a simple improvement to the method, which uses two optical modes with frequency separated by two FSR. This simple improvement would significantly reduce the uncertainty in the measurements presented here.

Using two optical modes [24, 44] in conjunction with the Paul trap provides us with a versatile levitated nano-oscillator system which can be operated either in the quadratic or linear optomechanical regime. To the best of our knowledge, we demonstrate for the first time cooling solely provided by the quadratic optomechanical interaction. More interestingly, this creates a highly nonlinear state of motion, showing good agreement with theoretical calculations. In a regime dominated by linear optomechanical coupling, we demonstrate cooling down to $T_{eff} = (21 \pm 4)\,\mathrm{mK}$ limited by Paul trap noise. This final temperature constitutes an improvement by more than three orders of magnitude with the same cooling scheme [44]. Moreover, the final temperature is similar to what has been reported in standard optomechanics [47]. With better electronics, and by using the filtering cavity presented in Section 7.3, near ground state cooling should be achievable.

9.2 Outlook

The quantum regime has recently been reached by two groups [40, 51]. In both cases nanospheres were trapped in an optical tweezer. In the first case, cooling was provided on a charged nanosphere with a velocity damping scheme. In the other case, cooling was provided with the coherent scattering scheme [48, 49]. These two protocols offer numerous advantages over what has been presented in this work. Nevertheless, a drawback is the scattering recoil which has a larger effect in optical tweezers in comparison to optical cavities (see Section 2.3.3), introducing a higher fundamental heating rate and possible source of decoherence when exploring nonclassical states of motion. For this reason, cooling and trapping in an optical cavity standing-wave might still very well be an interesting alternative.

One of the main advantages of optical levitation in a cavity field lies in the possibility of manipulating the optomechanical coupling from quadratic to linear and vice versa by simply controlling the power ratio between the probe and trapping field. As linear coupling is significantly more efficient than quadratic cooling it should be possible to switch between the two configurations producing two nonequilibrium steady states at different effective temperatures. This is a new tool for exploring nanoscale thermodynamics allowing the measurement of the relative entropy change for testing thermodynamics out of equilibrium and fluctuation theorems [194–196]. An even more intriguing possibility is to exploit a similar protocol where the particle is initialised close to the quantum ground state [51] through linear coupling and then to adiabatically change to a quadratic coupling. Such a scheme may allow squeezing of mechanical motion [174] but also the creation of other nonclassical states by using the nonlinear damping demonstrated here.

There has recently been an increased interest in using Paul traps for experiments using levitated nanospheres [94, 197, 198]. Advantages offered by the Paul trap include a deep and broad potential and the absence of optical fields. This could be used for instance to explore macroscopic superposition with nanorotors [199]. Recent proposals include studying hybrid atom-nanosphere systems where sympathetic cooling of the ion could lead to small ($\sim \mu$K) motional temperatures of the nanosphere [200]. Furthermore, this could directly be used to probe quantum gravity [7]. A similar system could be used as well to detect mechanical superpositions of the nanoparticle [201].

Appendix A

Optical locks

In this appendix, we review and describe the different optical locking mechanisms used in the experiment. We summarise the well-known Pound-Drever-Hall (PDH) method, used here to lock laser frequencies to our two optical cavities. We discuss how the PDH error signal is calibrated in frequency noise (or conversely in cavity displacement noise). We describe then how we implement an offset-phase lock to stabilise one laser frequency to another laser. Lastly, we discuss locking mechanisms used to correct for slow frequency drifts in the experiment.

A.1 Pound-Drever-Hall

In this section we review the Pound-Drever-Hall (PDH) locking method [202]. Temperature drifts and acoustic noise are responsible for fluctuations of the cavity resonance frequency. The PDH technique is a feedback scheme used in order to keep a laser locked to an optical resonance. This is used in practice in this work to lock both science and filtering cavities. The need for a specific method comes from the fact that the amplitude transfer function of the reflected field on resonance has a null derivative and therefore cannot be used as an error signal. A linear slope can nevertheless be obtained by measuring the phase of the reflected field (see Fig. A.1). In order to implement the phase detection, a phase modulation is added to the optical field by means of an electro-optic modulator (EOM). The modulated input field can be written as $E_{in} = E_o e^{i\omega_l t + \beta \sin(\Omega t)}$ with E_o the field amplitude, ω_l the laser frequency, β the modulation depth and Ω the modulation frequency. This frequency modulation creates sidebands on the optical carrier frequency evenly spaced by Ω : $E_{in} = E_o \left(J_0(\beta) e^{i\omega_l t} + \sum_{n=1}^{\infty} \left(J_n(\beta) e^{i(\omega_l + n\Omega)t} - J_n(\beta) e^{i(\omega_l - n\Omega)t} \right) \right) \approx$

$E_o\left(J_0(\beta)e^{i\omega_l t}+J_1(\beta)e^{i(\omega_l+\Omega)t}-J_1(\beta)e^{i(\omega_l-\Omega)t}\right)$ where J_n denotes the Bessel functions. We can simplify this expression by keeping only the first terms in the Bessel function expansion. The reflected field amplitude can be written as $E_r = F(\Delta_o) = \frac{\zeta - i\Delta_o/\kappa}{1+i\Delta_o/\kappa}E_{in}$ with Δ_o the detuning between the input field ω_l and the cavity resonance frequency ω_{cav} and κ the cavity half-linewidth (see Section 2.2.1). The reflected field taking into account the first sidebands is $E_r = E_0\left(F(\Delta_o)J_0(\beta)e^{i\omega_l t}+F(\Delta_o+\Omega)J_1(\beta)e^{i(\omega_l+\Omega)t}-F(\Delta_o-\Omega)J_1(\beta)e^{i(\omega_l-\Omega)t}\right)$. We show the reflected field intensity as a function of detuning in Fig. A.1(left), where we have used a low-pass filter with cut-off frequency smaller than Ω. The fit can be used to evaluate the modulation depth $\beta = 0.73$. The intensity contains constant terms (shown in Fig. A.1(left)) and ones rotating at the frequencies Ω and 2Ω. The reflected beam is measured on a photodiode of response bandwidth larger than Ω. The output voltage is then mixed with a local oscillator of same frequency Ω and phase θ. After mixing and applying a low pass filter, we obtain the PDH error signal $V_{\mathrm{PDH}} \propto \mathrm{Re}\left[F(\Delta_o)F^*(\Delta_o+\Omega)-F^*(\Delta_o)F(\Delta_o-\Omega)\right]\cos(\theta) - \mathrm{Im}\left[F(\Delta_o)F^*(\Delta_o+\Omega)-F^*(\Delta_o)F(\Delta_o-\Omega)\right]\sin(\theta)$. It can be shown that close to the resonance frequency for optical frequencies ω_l satisfying $\omega_{cav}-\kappa<\omega_l<\omega_{cav}+\kappa$, we obtain $V_{\mathrm{PDH}} \propto \mathrm{Im}\left[F(\omega)\right]\sin(\theta)$. When this condition is met, the PDH error signal is linear as a function of detuning. It can be shown to be proportional to the phase of the reflected beam, itself proportional to the detuning and can therefore be used as an error signal to lock the cavity. We show in Fig. A.1(right) a typical PDH error signal along with theoretical fit. The central part, highlighted in orange, corresponds to the linear section of the signal used for locking. The sensitivity of the error signal is maximised for $\theta = \pi/2$ which corresponds to the phase quadrature of the field (here we measure $\theta = \pi/2 + 0.31$). Moreover, the sensitivity is maximised for a modulation depth $\beta = 1.08$ (here we measure β=0.73) roughly corresponding to an equal amount shared between the carrier and the first order sidebands. In practice, we generate the sidebands at frequencies ranging between 4 MHz and 8 MHz. We use as an EOM a $LiTaO_3$ crystal on which we apply a voltage modulation. The modulation signal is either issued from an off the shelf lock box[1] or an FPGA[2]. The RF signals

[1] Vescent D2-125
[2] redpitaya

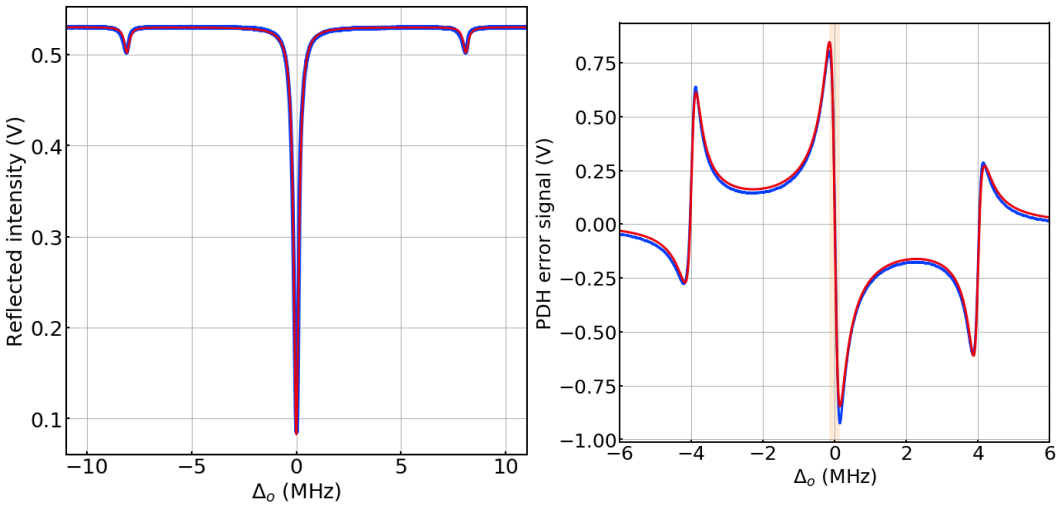

Figure A.1: (left) Reflected intensity (data in blue, fit in red) from the science cavity as a function of detuning. The science cavity here has a half-linewidth $\kappa/2\pi = 130\,\text{kHz}$. Sidebands are obtained at $\Omega/2\pi = 8\,\text{MHz}$ by using an EOM. The fit gives a modulation depth of $\beta = 0.73$. (right) PDH error signal as a function of detuning (data in blue, fit in red). The dynamic range of the lock, shown in orange, corresponds to one full linewidth 2κ. The fit gives a demodulation angle $\theta = \pi/2 + 0.31$. Unlike in (left), the EOM modulation is here at 4 MHz.

are amplified with Mini-circuits amplifiers[3]. In the case of the lock box, we typically apply on the EOM crystal $\sim 30\,\text{V}$ (peak-to-peak) at 4 MHz, when using the FPGA, $\sim 40\,\text{V}$ (peak-to-peak) at 8 MHz. The reflected intensity is detected on a photodiode with a bandwidth large enough to be sensitive at the modulation frequency[4]. The signal is then demodulated either internally in the case of the lock box or with an external mixer otherwise[5]. In both cases we use the lock box[6] as a servo which has two integrators and one proportional gain. Given the output voltage of the lock box and the laser piezo-electric actuator gain, the dynamic range of the PDH lock to the two cavities is $\pm 20\,\text{MHz}$.

A.2 PDH calibration

In this section we discuss how the PDH error signal is calibrated. As discussed above, the PDH error signal quantifies the detuning, when calibrated in Hz, between the input optical frequency and the cavity resonance. It can first be used to evaluate the performance of the lock as well as the frequency noise and/or cavity displacement

[3] ZHL-1-2W-S+
[4] InGaAs PDA10CF from ThorLabs. Bandwidth of 150 MHz.
[5] ZX05-1-S+
[6] Vescent D2-125

noise. Lastly, since the PDH error signal is actually proportional to the phase of the reflected beam, it can be used directly to read out the particle motion as it could be realised in a standard homodyne detection (see Chapter 8). We show in Fig. A.2, a diagram summarising the different components of the feedback loop as well as controlled inputs and noise terms.

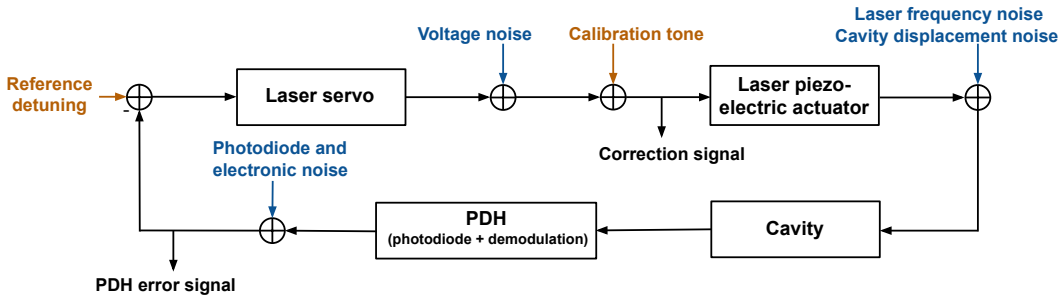

Figure A.2: Feedback block diagram of the PDH lock. Controlled inputs are written in orange. Noise inputs are shown in blue. For the calibration, PDH error signal and correction signal are measured.

The laser servo[7] is used with two integrators of cut-off frequencies ω_1 and ω_2 and a gain G_s. While the frequency of the two integrators is well known, the gain is not known precisely as it is set with a knob. The transfer function of the servo is $H_s(\omega) = G_s \frac{1+i\frac{\omega}{\omega_1}}{i\frac{\omega}{\omega_1}} \frac{1+i\frac{\omega}{\omega_2}}{i\frac{\omega}{\omega_2}}$. The laser piezoelectric-actuator gain G_{PZT} is considered to be white within its working bandwidth $\sim 100\,\mathrm{kHz}$. The cavity behaves as a first order low-pass filter regarding the field frequency. When the PDH error signal is on resonance, it is well approximated (up to a gain) by $H_c(\omega) = \frac{1}{1+i\frac{\omega}{\kappa}}$ with κ the cavity half-linewidth which can be measured accurately (see Section 7.4.3). Lastly, the reflected field is measured on a photodiode and the signal is then demodulated to provide the PDH error signal. This signal depends on several parameters such as optical power, photodiode gain, responsivity, amplitude of the local oscillator in the mixer and possible additional electronic gains. One method of evaluating the PDH overall gain G_{PDH} consists in taking the ratio of the PDH error signal peak-to-peak with the cavity full linewidth 2κ. Here, rather than using this approach which depends on several parameters, a calibration tone is added to the correction signal driving the laser piezoelectric-actuator. We denote the open-loop transfer function as $OL(\omega) = G_{\mathrm{PZT}} G_{\mathrm{PDH}} H_s(\omega) H_c(\omega)$. We denote the calibration amplitude by A

[7] Vescent D2-125

and its frequency by $\omega_{\rm cal}$. We generally choose a calibration frequency smaller than the cavity bandwidth, to minimise calibration errors $\omega_{\rm cal} < \kappa$. The amplitude of the calibration is chosen such that it dominates both PDH error signal and correction signal at the frequency $\omega_{\rm cal}$. In this case, the amplitude square of the PDH error signal $V^2_{\rm PDH}$ at the calibration frequency ω_{cal} is $V^2_{\rm PDH}(\omega_{\rm cal}) = \left|\frac{G_{\rm PZT}G_{\rm PDH}}{1+OL(\omega_{\rm cal})}\right|^2 A^2$. While, the amplitude square of the correction signal $V^2_{\rm corr}$ evaluated at the calibration frequency $\omega_{\rm cal}$ (taken after adding the calibration tone) is $V^2_{\rm corr}(\omega_{\rm cal}) = \left|\frac{1}{1+OL(\omega_{\rm cal})}\right|^2 A^2$. By taking the ratio of those two signals, we can evaluate the PDH gain $G_{\rm PDH}$ with the knowledge of the laser piezoelectric-actuator gain G_{PZT}. The PDH error signal PSD $S_{\rm PDH}(\omega)$ can then be calibrated into an in-loop effective frequency noise $S_{\text{freq noise}}(\omega) = \frac{1}{G^2_{\rm PDH}}|H_c(\omega)|^{-2}S_{\rm PDH}(\omega)$. It can be written as well in terms of effective cavity displacement noise after multiplication by $\frac{L^2}{\nu_L^2}$ with L the cavity length and ν_L the laser frequency.

When the PDH is used to measure the nanoparticle motion, a notch filter is placed at the mechanical frequency on the correction signal to limit actions of the feedback loop on the nanoparticle motion.

A.3 Offset lock

As mentioned above, two lasers are used in the experiment presented in Chapter 8. One is typically locked to the science cavity (500 mW laser) while the second one (2 W laser) is offset locked to the first one. The two lasers are separated in frequency by one free-spectral-range (10.3 GHz) on top of which a small detuning is added (typically $\sim$ 100 kHz). The beat note (visibility of $\sim$ 90 %) between the two lasers is detected on a very high bandwidth photodiode[8]. It is then amplified[9] and its frequency is divided[10] by 8 to be used with standard electronic equipments. An off the shelf offset lock box[11] is used to provide an error signal as well as a correction signal. The offset lock reference signal is provided by a high quality and ultra stable signal generator[12]. The offset lock loop is either closed on the 2 W laser piezoelectric-actuator or on an AOM[13].

[8] EOT ET-3500. Bandwidth of 12.5 GHz
[9] ZVA-183W-S+
[10] HMC494
[11] Vescent D2-135
[12] R&S SMB 100A
[13] Series 3000 by Crystal Technology. Central frequency of 80 MHz.

In the case of the AOM, the error signal has to be converted into a frequency modulation. This is realised by using a low phase noise voltage-controlled oscillator (VCO)[14]. We measure the VCO gain to be $(5.81 \pm 0.06)\,\mathrm{MHz/V}$. We place on the VCO output signal a sharp low pass filter[15] to attenuate higher order harmonics generated by the VCO. The signal is then amplified[16] and sent to the AOM. The AOM is operated in a double pass configuration (efficiency in the double pass $\sim 60\%$) in order to minimise pointing noise, since the refraction angle is frequency dependent. The dynamic range given by the offset lock operated with the VCO and the AOM is $\pm 10\,\mathrm{MHz}$.

A.4 Slow drifts locks

As mentioned above, the dynamic range of both AOM and laser piezoelectric-actuators is $\sim \pm 20\,\mathrm{MHz}$. Furthermore, both cavity resonance frequency and laser frequencies can drift by a significant amount because of temperature fluctuations. Even at constant room temperature, the Mephisto lasers from Coherent have drifts of the order of $\sim 1\,\mathrm{MHz/min}$. The temperature drifts in the two cavities are partially mitigated by using cavity holders designed in INVAR, which has a small linear expansion coefficient of $\sim 1\,\mathrm{ppm/K}$. We can easily calculate the relationship between the drifts in resonance frequency ν and in cavity length L to be $\frac{\Delta L}{L} = \frac{\Delta \nu}{\nu}$. For both cavities, we therefore have $\Delta\nu \approx 300\,\mathrm{MHz/K}$. Lastly, when taking measurements with a nanosphere, we generally change the pressure within the science cavity between $\sim 1\,\mathrm{mbar}$ and $\sim 10^{-7}\,\mathrm{mbar}$. At $1\,\mathrm{mbar}$, the refractive index of air is $1{+}2.7{\times}10^{-7}$. Therefore, lowering the pressure leads to a change in the cavity resonance frequency by $75\,\mathrm{MHz}$. In order to compensate actively for those slow frequency drifts, we use custom feedback with proportional gain and single integrator of small time constant $\sim 1\,\mathrm{Hz}$ on the temperature actuator of both lasers.

When the filtering cavity is used, the offset lock loop is closed on the AOM. Though operated in a double pass configuration, the refracted beam angle still depends on the drive frequency. Due to fibre alignment, this pointing noise can lead to drifts in power up to $\sim 10\%$ at the science cavity input. In order to cancel out

[14] CRBV55FL-0075-0085 from Crystek Corporation.

[15] CLPFL-0100 from Crystek Corporation. 7th order low pass filter with cut-off frequency at 100 MHz

[16] ZHL-1-2W-S+

those drifts, the AOM is operated at a constant mean frequency and the feedback is applied on the science cavity piezoelectric-actuator, leading to the AOM only correcting high frequency fluctuations. Therefore, in this case, the 2 W laser follows the filtering cavity drifts, the AOM is operated at a fixed frequency, and the science cavity length is changed to obtain the desired offset between the two beams. The 500 mW laser follows the science cavity frequency.

Those different locks are robust enough to go multiple times up and down in pressure with the same nanosphere.

Bibliography

[1] B. Henderson. The rebel physicist on the hunt for a better story than quantum mechanics. *The New York Times*, page 36 (2020).

[2] M. Aspelmeyer, T. J. Kippenberg, and F. Marquardt. Cavity optomechanics. *Rev. Mod. Phys.*, **86**, 1391 (2014).

[3] W. P. Bowen and G. J. Milburn. *Quantum Optomechanics*. CRC Press (2015).

[4] K. W. Murch, K. L. Moore, S. Gupta *et al.* Observation of quantum-measurement backaction with an ultracold atomic gas. *Nature Physics*, **4**, 561 (2008).

[5] J. Aasi, B. P. Abbott, R. Abbott *et al.* Advanced LIGO. *Classical and Quantum Gravity*, **32**, 074001 (2015).

[6] J. Bateman, S. Nimmrichter, K. Hornberger *et al.* Near-field interferometry of a free-falling nanoparticle from a point-like source. *Nature Communications*, **5**, 4788 EP (2014).

[7] S. Bose, A. Mazumdar, G. W. Morley *et al.* Spin entanglement witness for quantum gravity. *Phys. Rev. Lett.*, **119**, 240401 (2017).

[8] J. Millen, T. S. Monteiro, R. Pettit *et al.* Optomechanics with levitated particles. *Reports on Progress in Physics*, **83**, 026401 (2020).

[9] F. Acernese, M. Agathos, K. Agatsuma *et al.* Advanced Virgo: a second-generation interferometric gravitational wave detector. *Classical and Quantum Gravity*, **32**, 024001 (2014).

[10] B. P. Abbott, R. Abbott, T. D. Abbott *et al.* (LIGO Scientific Collaboration and Virgo Collaboration). Observation of gravitational waves from a binary black hole merger. *Phys. Rev. Lett.*, **116**, 061102 (2016).

[11] D. Mason, J. Chen, M. Rossi *et al.* Continuous force and displacement measurement below the standard quantum limit. *Nature Physics*, **15**, 745 (2019).

[12] H. J. Kimble, Y. Levin, A. B. Matsko *et al.* Conversion of conventional gravitational-wave interferometers into quantum nondemolition interferometers by modifying their input and/or output optics. *Phys. Rev. D*, **65**, 022002 (2001).

[13] O. Arcizet, P. F. Cohadon, T. Briant *et al.* Radiation-pressure cooling and optomechanical instability of a micromirror. *Nature*, **444**, 71 EP (2006).

[14] T. J. Kippenberg and K. J. Vahala. Cavity optomechanics: Back-action at the mesoscale. *Science*, **321**, 1172 (2008).

[15] J. Chan, T. P. M. Alegre, A. H. Safavi-Naeini *et al.* Laser cooling of a nanomechanical oscillator into its quantum ground state. *Nature*, **478**, 89 (2011).

[16] J. D. Teufel, T. Donner, D. Li *et al.* Sideband cooling of micromechanical motion to the quantum ground state. *Nature*, **475**, 359 (2011).

[17] T. P. Purdy, P.-L. Yu, R. W. Peterson *et al.* Strong optomechanical squeezing of light. *Phys. Rev. X*, **3**, 031012 (2013).

[18] J. Suh, A. J. Weinstein, C. U. Lei *et al.* Mechanically detecting and avoiding the quantum fluctuations of a microwave field. *Science* (2014).

[19] E. E. Wollman, C. U. Lei, A. J. Weinstein *et al.* Quantum squeezing of motion in a mechanical resonator. *Science*, **349**, 952 (2015).

[20] R. Riedinger, A. Wallucks, I. Marinković *et al.* Remote quantum entanglement between two micromechanical oscillators. *Nature*, **556**, 473 (2018).

[21] C. F. Ockeloen-Korppi, E. Damskägg, J.-M. Pirkkalainen *et al.* Stabilized entanglement of massive mechanical oscillators. *Nature*, **556**, 478 (2018).

[22] A. Ashkin, J. M. Dziedzic, J. E. Bjorkholm *et al.* Observation of a single-beam gradient force optical trap for dielectric particles. *Opt. Lett.*, **11**, 288 (1986).

[23] Y. Harada and T. Asakura. Radiation forces on a dielectric sphere in the Rayleigh scattering regime. *Optics Communications*, **124**, 529 (1996).

[24] D. E. Chang, C. A. Regal, S. B. Papp *et al.* Cavity opto-mechanics using an optically levitated nanosphere. *Proceedings of the National Academy of Sciences*, **107**, 1005 (2010).

[25] O. Romero-Isart, M. L. Juan, R. Quidant *et al.* Toward quantum superposition of living organisms. *New Journal of Physics*, **12**, 033015 (2010).

[26] P. F. Barker and M. N. Shneider. Cavity cooling of an optically trapped nanoparticle. *Phys. Rev. A*, **81**, 023826 (2010).

[27] O. Romero-Isart, A. C. Pflanzer, M. L. Juan *et al.* Optically levitating dielectrics in the quantum regime: Theory and protocols. *Phys. Rev. A*, **83**, 013803 (2011).

[28] G. Ranjit, M. Cunningham, K. Casey *et al.* Zeptonewton force sensing with nanospheres in an optical lattice. *Phys. Rev. A*, **93**, 053801 (2016).

[29] A. A. Geraci, S. B. Papp, and J. Kitching. Short-range force detection using optically cooled levitated microspheres. *Phys. Rev. Lett.*, **105**, 101101 (2010).

[30] A. Arvanitaki and A. A. Geraci. Detecting high-frequency gravitational waves with optically levitated sensors. *Phys. Rev. Lett.*, **110**, 071105 (2013).

[31] A. Pontin, L. S. Mourounas, A. A. Geraci *et al.* Levitated optomechanics with a fiber Fabry–Perot interferometer. *New Journal of Physics*, **20**, 023017 (2018).

[32] M. Scala, M. S. Kim, G. W. Morley *et al.* Matter-wave interferometry of a levitated thermal nano-oscillator induced and probed by a spin. *Phys. Rev. Lett.*, **111**, 180403 (2013).

[33] C. Wan, M. Scala, G. W. Morley *et al.* Free nano-object Ramsey interferometry for large quantum superpositions. *Phys. Rev. Lett.*, **117**, 143003 (2016).

[34] C. Wan, M. Scala, S. Bose *et al.* Tolerance in the Ramsey interference of a trapped nanodiamond. *Phys. Rev. A*, **93**, 043852 (2016).

[35] R. Kaltenbaek, M. Aspelmeyer, P. F. Barker *et al.* Macroscopic quantum resonators (MAQRO): 2015 update. *EPJ Quantum Technology*, **3**, 5 (2016).

[36] D. Goldwater, M. Paternostro, and P. F. Barker. Testing wave-function-collapse models using parametric heating of a trapped nanosphere. *Phys. Rev. A*, **94**, 010104 (2016).

[37] A. Vinante, A. Pontin, M. Rashid *et al.* Testing collapse models with levitated nanoparticles: Detection challenge. *Phys. Rev. A*, **100**, 012119 (2019).

[38] T. Li. *Fundamental tests of physics with optically trapped microspheres*. Ph.D. thesis, The University of Texas at Austin (2011).

[39] F. Tebbenjohanns, M. Frimmer, A. Militaru *et al.* Cold damping of an optically levitated nanoparticle to microkelvin temperatures. *Phys. Rev. Lett.*, **122**, 223601 (2019).

[40] F. Tebbenjohanns, M. Frimmer, V. Jain *et al.* Motional sideband asymmetry of a nanoparticle optically levitated in free space. *Phys. Rev. Lett.*, **124**, 013603 (2020).

[41] J. Gieseler, B. Deutsch, R. Quidant *et al.* Subkelvin parametric feedback cooling of a laser-trapped nanoparticle. *Phys. Rev. Lett.*, **109**, 103603 (2012).

[42] V. Jain, J. Gieseler, C. Moritz *et al.* Direct measurement of photon recoil from a levitated nanoparticle. *Phys. Rev. Lett.*, **116**, 243601 (2016).

[43] P. Asenbaum, S. Kuhn, S. Nimmrichter *et al.* Cavity cooling of free silicon nanoparticles in high vacuum. *Nature Communications*, **4** (2013).

[44] N. Kiesel, F. Blaser, U. Delić *et al.* Cavity cooling of an optically levitated submicron particle. *Proceedings of the National Academy of Sciences*, **110**, 14180 (2013).

[45] J. Millen, P. Z. G. Fonseca, T. Mavrogordatos *et al.* Cavity cooling a single charged levitated nanosphere. *Phys. Rev. Lett.*, **114**, 123602 (2015).

[46] P. Z. G. Fonseca, E. B. Aranas, J. Millen *et al.* Nonlinear dynamics and strong cavity cooling of levitated nanoparticles. *Phys. Rev. Lett.*, **117**, 173602 (2016).

[47] N. Meyer, A. d. l. R. Sommer, P. Mestres *et al.* Resolved-sideband cooling of a levitated nanoparticle in the presence of laser phase noise. *Phys. Rev. Lett.*, **123**, 153601 (2019).

[48] D. Windey, C. Gonzalez-Ballestero, P. Maurer *et al.* Cavity-based 3D cooling of a levitated nanoparticle via coherent scattering. *Phys. Rev. Lett.*, **122**, 123601 (2019).

[49] U. Delić, M. Reisenbauer, D. Grass *et al.* Cavity cooling of a levitated nanosphere by coherent scattering. *Physical Review Letters*, **122** (2019).

[50] A. de los Ríos Sommer, N. Meyer, and R. Quidant. Strong optomechanical coupling at room temperature by coherent scattering. *arXiv: 2005.10201* (2020).

[51] U. Delić, M. Reisenbauer, K. Dare *et al.* Cooling of a levitated nanoparticle to the motional quantum ground state. *Science*, **367**, 892 (2020).

[52] H. Pino, J. Prat-Camps, K. Sinha *et al.* On-chip quantum interference of a superconducting microsphere. *Quantum Science and Technology*, **3**, 025001 (2018).

[53] S. A. Beresnev, V. G. Chernyak, and G. A. Fomyagin. Motion of a spherical particle in a rarefied gas. Part 2. Drag and thermal polarization. *Journal of Fluid Mechanics*, **219**, 405 (1990).

[54] J. Corson, G. W. Mulholland, and M. R. Zachariah. Calculating the rotational friction coefficient of fractal aerosol particles in the transition regime using extended Kirkwood-Riseman theory. *Phys. Rev. E*, **96**, 013110 (2017).

[55] P. S. Epstein. On the resistance experienced by spheres in their motion through gases. *Phys. Rev.*, **23**, 710 (1924).

[56] R. Kubo. The fluctuation-dissipation theorem. *Reports on Progress in Physics*, **29**, 255 (1966).

[57] G. E. Uhlenbeck and L. S. Ornstein. On the theory of the Brownian motion. *Phys. Rev.*, **36**, 823 (1930).

[58] C. Gerry and P. Knight. *Introductory Quantum Optics*. Cambridge University Press (2004).

[59] B. Hauer, J. Maciejko, and J. Davis. Nonlinear power spectral densities for the harmonic oscillator. *Annals of Physics*, **361**, 148 (2015).

[60] T. P. Purdy, P.-L. Yu, N. S. Kampel *et al.* Optomechanical Raman-ratio thermometry. *Phys. Rev. A*, **92**, 031802 (2015).

[61] G. Nogues, A. Rauschenbeutel, S. Osnaghi *et al.* Seeing a single photon without destroying it. *Nature*, **400**, 239 (1999).

[62] M. Born and E. Wolf. *Principles of Optics: Electromagnetic Theory of Propagation, Interference and Diffraction of Light (7th Edition)*. Cambridge University Press, 7th edition (1999).

[63] D. Meschede. *Optics, Light, and Lasers*. Wiley-VCH Verlag GmbH & Co. KGaA (2017).

[64] H. Kogelnik and T. Li. Laser beams and resonators. *Appl. Opt.*, **5**, 1550 (1966).

[65] C. W. Gardiner and M. J. Collett. Input and output in damped quantum systems: Quantum stochastic differential equations and the master equation. *Phys. Rev. A*, **31**, 3761 (1985).

[66] U. Delić, D. Grass, M. Reisenbauer *et al.* Levitated cavity optomechanics in high vacuum. *Quantum Science and Technology*, **5**, 025006 (2020).

[67] A. C. Pflanzer, O. Romero-Isart, and J. I. Cirac. Master-equation approach to optomechanics with arbitrary dielectrics. *Phys. Rev. A*, **86**, 013802 (2012).

[68] J. Gieseler. *Dynamics of optically levitated nanoparticles in high vacuum*. Ph.D. thesis, Institut de Ciències Fotòniques (2014).

[69] R. Kitamura, L. Pilon, and M. Jonasz. Optical constants of silica glass from extreme ultraviolet to far infrared at near room temperature. *Appl. Opt.*, **46**, 8118 (2007).

[70] E. Hebestreit, R. Reimann, M. Frimmer *et al.* Measuring the internal temperature of a levitated nanoparticle in high vacuum. *Phys. Rev. A*, **97**, 043803 (2018).

[71] A. Pontin, C. Biancofiore, E. Serra *et al.* Frequency-noise cancellation in optomechanical systems for ponderomotive squeezing. *Phys. Rev. A*, **89**, 033810 (2014).

[72] R. J. Glauber. The quantum theory of optical coherence. *Phys. Rev.*, **130**, 2529 (1963).

[73] T. S. Monteiro, J. Millen, G. A. T. Pender *et al.* Dynamics of levitated nanospheres: towards the strong coupling regime. *New Journal of Physics*, **15**, 015001 (2013).

[74] C. Genes, D. Vitali, P. Tombesi *et al.* Ground-state cooling of a micromechanical oscillator: Comparing cold damping and cavity-assisted cooling schemes. *Phys. Rev. A*, **77**, 033804 (2008).

[75] R. S. Van Dyck, P. B. Schwinberg, and H. G. Dehmelt. Precise measurements of axial, magnetron, cyclotron, and spin-cyclotron-beat frequencies on an isolated 1-mev electron. *Phys. Rev. Lett.*, **38**, 310 (1977).

[76] W. Paul. Electromagnetic traps for charged and neutral particles. *Rev. Mod. Phys.*, **62**, 531 (1990).

[77] D. Leibfried, R. Blatt, C. Monroe *et al.* Quantum dynamics of single trapped ions. *Rev. Mod. Phys.*, **75**, 281 (2003).

[78] A. D. Ludlow, M. M. Boyd, J. Ye *et al.* Optical atomic clocks. *Rev. Mod. Phys.*, **87**, 637 (2015).

[79] R. R. A. Syms, T. J. Tate, M. M. Ahmad *et al.* Design of a microengineered electrostatic quadrupole lens. *IEEE Transactions on Electron Devices*, **45**, 2304 (1998).

[80] M. Madsen, W. Hensinger, D. Stick *et al.* Planar ion trap geometry for microfabrication. *Applied Physics B*, **78**, 639 (2004).

[81] D. J. Berkeland, J. D. Miller, J. C. Bergquist *et al.* Minimization of ion micromotion in a Paul trap. *Journal of Applied Physics*, **83**, 5025 (1998).

[82] M. Abramowitz. *Handbook of mathematical functions, with formulas, graphs, and mathematical tables.* Dover Publications, Inc., USA (1974).

[83] M. Drewsen and A. Brøner. Harmonic linear Paul trap: Stability diagram and effective potentials. *Phys. Rev. A*, **62**, 045401 (2000).

[84] R. E. March. Quadrupole ion traps. *Mass Spectrometry Reviews*, **28**, 961 (2009).

[85] T. Hasegawa and K. Uehara. Dynamics of a single particle in a Paul trap in the presence of the damping force. *Applied Physics B Laser and Optics*, **61**, 159 (1995).

[86] A. Almuqhim. *Development of levitated electromechanics of nanodiamond in a Paul trap.* Ph.D. thesis, University College London (2020).

[87] V. Letchumanan, G. Wilpers, M. Brownnutt *et al.* Zero-point cooling and heating-rate measurements of a single $^{88}Sr^{+}$ ion. *Phys. Rev. A*, **75**, 063425 (2007).

[88] Q. A. Turchette, Kielpinski, B. E. King *et al.* Heating of trapped ions from the quantum ground state. *Phys. Rev. A*, **61**, 063418 (2000).

[89] C. Rouki. Ultra-high vacuum compatibility measurements of materials for the CHICSi detector system. *Physica Scripta*, **T104**, 107 (2003).

[90] L. Westerberg, V. Avdeichikov, L. Carlén *et al.* CHICSi—a compact ultra-high vacuum compatible detector system for nuclear reaction experiments at storage rings. I. General structure, mechanics and UHV compatibility. *Nuclear Instruments and Methods in Physics Research Section A: Accelerators, Spectrometers, Detectors and Associated Equipment*, **500**, 84 (2003).

[91] V. A. Lisovskiy, S. D. Yakovin, and V. D. Yegorenkov. Low-pressure gas breakdown in uniform dc electric field. *Journal of Physics D: Applied Physics*, **33**, 2722 (2000).

[92] L. Deslauriers, S. Olmschenk, D. Stick *et al.* Scaling and suppression of anomalous heating in ion traps. *Phys. Rev. Lett.*, **97**, 103007 (2006).

[93] P. Mestres, J. Berthelot, M. Spasenović *et al.* Cooling and manipulation of a levitated nanoparticle with an optical fiber trap. *Applied Physics Letters*, **107**, 151102 (2015).

[94] D. S. Bykov, P. Mestres, L. Dania *et al.* Direct loading of nanoparticles under high vacuum into a Paul trap for levitodynamical experiments. *Applied Physics Letters*, **115**, 034101 (2019).

[95] J. B. Fenn, M. Mann, C. K. Meng *et al.* Electrospray ionization-principles and practice. *Mass Spectrometry Reviews*, **9**, 37 (1990).

[96] P. Nagornykh, J. E. Coppock, and B. E. Kane. Cooling of levitated graphene nanoplatelets in high vacuum. *Applied Physics Letters*, **106**, 244102 (2015).

[97] R. M. Danell, A. S. Danell, G. L. Glish *et al.* The use of static pressures of heavy gases within a quadrupole ion trap. *Journal of the American Society for Mass Spectrometry*, **14**, 1099 (2003).

[98] A. Chambers. *Modern Vacuum Physics*. CRC Press (2004).

[99] S. Schlemmer, J. Illemann, S. Wellert *et al.* Nondestructive high-resolution and absolute mass determination of single charged particles in a three-dimensional quadrupole trap. *Journal of Applied Physics*, **90**, 5410 (2001).

[100] Y. Cai, W.-P. Peng, S.-J. Kuo *et al.* Single-particle mass spectrometry of polystyrene microspheres and diamond nanocrystals. *Analytical Chemistry*, **74**, 232 (2002). PMID: 11795799.

[101] I. Alda, J. Berthelot, R. A. Rica *et al.* Trapping and manipulation of individual nanoparticles in a planar Paul trap. *Applied Physics Letters*, **109**, 163105 (2016).

[102] H. L. Partner, J. Zoll, A. Kuhlicke *et al.* Printed-circuit-board linear Paul trap for manipulating single nano- and microparticles. *Review of Scientific Instruments*, **89**, 083101 (2018).

[103] B. R. Slezak, C. W. Lewandowski, J.-F. Hsu *et al.* Cooling the motion of a silica microsphere in a magneto-gravitational trap in ultra-high vacuum. *New Journal of Physics*, **20**, 063028 (2018).

[104] E. Hebestreit, M. Frimmer, R. Reimann *et al.* Calibration and energy measurement of optically levitated nanoparticle sensors. *Review of Scientific Instruments*, **89**, 033111 (2018).

[105] T. Bisanz, J. Große-Knetter, A. Quadt *et al.* Subpixel mapping and test beam studies with a HV2fei4v2 CMOS-sensor-hybrid module for the ATLAS inner detector upgrade. *Journal of Instrumentation*, **12**, P08018 (2017).

[106] S. H. Nowak, A. Bjeoumikhov, J. von Borany *et al.* Sub-pixel resolution with a color X-ray camera. *Journal of Analytical Atomic Spectrometry*, **30**, 1890 (2015).

[107] S. T. Bryson, P. Tenenbaum, J. M. Jenkins *et al.* The *Kepler* pixel response function. *The Astrophysical Journal*, **713**, L97 (2010).

[108] B. Widrow and I. Kollár. *Quantization noise: Roundoff error in digital computation, signal processing, control, and communications*. Cambridge University Press (2008).

[109] S. A. Kim, K. G. Heinze, and P. Schwille. Fluorescence correlation spectroscopy in living cells. *Nature Methods*, **4**, 963 (2007).

[110] A. T. M. A. Rahman and P. F. Barker. Laser refrigeration, alignment and rotation of levitated Yb3+:YLF nanocrystals. *Nature Photonics*, **11**, 634 (2017).

[111] G. Gariepy, N. Krstajić, R. Henderson *et al.* Single-photon sensitive light-in-fight imaging. *Nature Communications*, **6** (2015).

[112] Y. Li, M. Mund, P. Hoess *et al.* Real-time 3D single-molecule localization using experimental point spread functions. *Nature Methods*, **15**, 367 (2018).

[113] C. S. Smith, N. Joseph, B. Rieger *et al.* Fast, single-molecule localization that achieves theoretically minimum uncertainty. *Nature Methods*, **7**, 373 (2010).

[114] A. Pontin, M. Bonaldi, A. Borrielli *et al.* Detection of weak stochastic forces in a parametrically stabilized micro-optomechanical system. *Phys. Rev. A*, **89**, 023848 (2014).

[115] T. Li, S. Kheifets, and M. G. Raizen. Millikelvin cooling of an optically trapped microsphere in vacuum. *Nature Physics*, **7**, 527 (2011).

[116] S.-C. Seo, S.-K. Hong, and D. W. Boo. Single nanoparticle ion trap (snit): A novel tool for studying in-situ dynamics of single nanoparticles. *Bulletin of the Korean Chemical Society*, **24**, 552 (2003).

[117] F. Ricci, M. T. Cuairan, G. P. Conangla *et al.* Accurate mass measurement of a levitated nanomechanical resonator for precision force-sensing. *Nano Letters* (2019).

[118] J. Millen, T. Deesuwan, P. Barker *et al.* Nanoscale temperature measurements using non-equilibrium Brownian dynamics of a levitated nanosphere. *Nature Nanotechnology*, **9**, 425 (2014).

[119] S. R. Parnell, A. L. Washington, A. J. Parnell *et al.* Porosity of silica Stöber particles determined by spin-echo small angle neutron scattering. *Soft Matter*, **12**, 4709 (2016).

[120] J. Ahn, Z. Xu, J. Bang *et al.* Optically levitated nanodumbbell torsion balance and GHz nanomechanical rotor. *Phys. Rev. Lett.*, **121**, 033603 (2018).

[121] M. Frimmer, K. Luszcz, S. Ferreiro *et al.* Controlling the net charge on a nanoparticle optically levitated in vacuum. *Phys. Rev. A*, **95**, 061801 (2017).

[122] D. Allan. Statistics of atomic frequency standards. *Proceedings of the IEEE*, **54**, 221 (1966).

[123] D. Zheng, Y. Leng, X. Kong *et al.* Room temperature test of the continuous spontaneous localization model using a levitated micro-oscillator. *Phys. Rev. Research*, **2**, 013057 (2020).

[124] A. Vinante, P. Falferi, G. Gasbarri *et al.* Ultralow mechanical damping with Meissner-levitated ferromagnetic microparticles. *Phys. Rev. Applied*, **13**, 064027 (2020).

[125] Y. Mishin and J. Hickman. Energy spectrum of a Langevin oscillator. *Phys. Rev. E*, **94**, 062151 (2016).

[126] L. Haiberger, D. Jäger, and S. Schiller. Fabrication and laser control of double-paddle silicon oscillators. *Review of Scientific Instruments*, **76**, 045106 (2005).

[127] D. F. McGuigan, C. C. Lam, R. Q. Gram *et al.* Measurements of the mechanical Q of single-crystal silicon at low temperatures. *Journal of Low Temperature Physics*, **30**, 621 (1978).

[128] S. Wheaton, R. M. Gelfand, and R. Gordon. Probing the Raman-active acoustic vibrations of nanoparticles with extraordinary spectral resolution. *Nature Photonics*, **9**, 68 (2014).

[129] A. Papoulis. *Probability, random variables, and stochastic processes*. McGraw-Hill, Boston (2002).

[130] F. Arute, K. Arya, R. Babbush *et al.* Quantum supremacy using a programmable superconducting processor. *Nature*, **574**, 505 (2019).

[131] S.-K. Liao, W.-Q. Cai, W.-Y. Liu *et al.* Satellite-to-ground quantum key distribution. *Nature*, **549**, 43 (2017).

[132] V. Ménoret, P. Vermeulen, N. L. Moigne *et al.* Gravity measurements below 10-9 g with a transportable absolute quantum gravimeter. *Scientific Reports*, **8** (2018).

[133] R. Penrose. *Fashion, Faith, and Fantasy in the New Physics of the Universe*. Princeton University Press (2016).

[134] D. Hanneke, S. Fogwell Hoogerheide, and G. Gabrielse. Cavity control of a single-electron quantum cyclotron: Measuring the electron magnetic moment. *Phys. Rev. A*, **83**, 052122 (2011).

[135] W. Heisenberg. *Physics and Beyond: Encounters and Conversations*. G. Allen & Unwin (1971).

[136] P. A. M. Dirac. The evolution of the physicist's picture of nature. *Scientific American*, **208**, 45 (1963).

[137] A. Bassi and G. Ghirardi. A general argument against the universal validity of the superposition principle. *Physics Letters A*, **275**, 373 (2000).

[138] S. L. Adler. Why decoherence has not solved the measurement problem: a response to P.W. Anderson. *Studies in History and Philosophy of Science Part B: Studies in History and Philosophy of Modern Physics*, **34**, 135 (2003).

[139] H. Everett. "Relative state" formulation of quantum mechanics. *Rev. Mod. Phys.*, **29**, 454 (1957).

[140] G. C. Ghirardi, P. Pearle, and A. Rimini. Markov processes in Hilbert space and continuous spontaneous localization of systems of identical particles. *Phys. Rev. A*, **42**, 78 (1990).

[141] A. Bassi and H. Ulbricht. Collapse models: from theoretical foundations to experimental verifications. *Journal of Physics: Conference Series*, **504**, 012023 (2014).

[142] A. Bassi. Models of spontaneous wave function collapse: what they are, and how they can be tested. *Journal of Physics: Conference Series*, **701**, 012012 (2016).

[143] M. Carlesso and S. Donadi. Collapse models: Main properties and the state of art of the experimental tests. In B. Vacchini, H.-P. Breuer, and A. Bassi, editors, *Advances in Open Systems and Fundamental Tests of Quantum Mechanics*, pages 1–13. Springer International Publishing, Cham (2019).

[144] S. L. Adler. Lower and upper bounds on CSL parameters from latent image formation and IGM~heating. *Journal of Physics A: Mathematical and Theoretical*, **40**, 13501 (2007).

[145] G. C. Ghirardi, A. Rimini, and T. Weber. Unified dynamics for microscopic and macroscopic systems. *Phys. Rev. D*, **34**, 470 (1986).

[146] Y. Y. Fein, P. Geyer, P. Zwick *et al.* Quantum superposition of molecules beyond 25 kDa. *Nature Physics*, **15**, 1242 (2019).

[147] S. Nimmrichter, K. Hornberger, and K. Hammerer. Optomechanical sensing of spontaneous wave-function collapse. *Phys. Rev. Lett.*, **113**, 020405 (2014).

[148] M. Carlesso, A. Bassi, P. Falferi *et al.* Experimental bounds on collapse models from gravitational wave detectors. *Phys. Rev. D*, **94**, 124036 (2016).

[149] A. Vinante, R. Mezzena, P. Falferi *et al.* Improved noninterferometric test of collapse models using ultracold cantilevers. *Phys. Rev. Lett.*, **119**, 110401 (2017).

[150] A. Vinante, M. Carlesso, A. Bassi *et al.* Challenging spontaneous collapse models with ultracold layered force sensors. *arXiv: 2002.09782* (2020).

[151] M. Bilardello, S. Donadi, A. Vinante *et al.* Bounds on collapse models from cold-atom experiments. *Physica A: Statistical Mechanics and its Applications*, **462**, 764 (2016).

[152] S. L. Adler, A. Bassi, M. Carlesso *et al.* Testing continuous spontaneous localization with Fermi liquids. *Phys. Rev. D*, **99**, 103001 (2019).

[153] C. Curceanu, B. C. Hiesmayr, and K. Piscicchia. X-rays help to unfuzzy the concept of measurement. *Journal of Advanced Physics*, **4**, 263 (2015).

[154] M. Toroš and A. Bassi. Bounds on quantum collapse models from matter-wave interferometry: calculational details. *Journal of Physics A: Mathematical and Theoretical*, **51**, 115302 (2018).

[155] A. Smirne and A. Bassi. Dissipative continuous spontaneous localization (CSL) model. *Scientific Reports*, **5** (2015).

[156] M. Bahrami, A. Smirne, and A. Bassi. Role of gravity in the collapse of a wave function: A probe into the Diósi-Penrose model. *Phys. Rev. A*, **90**, 062105 (2014).

[157] J. Nobakht, M. Carlesso, S. Donadi *et al.* Unitary unraveling for the dissipative continuous spontaneous localization model: Application to optomechanical experiments. *Phys. Rev. A*, **98**, 042109 (2018).

[158] S. Donadi, K. Piscicchia, C. Curceanu *et al.* Underground test of gravity-related wave function collapse. *Nature Physics* (2020).

[159] S. Nimmrichter and K. Hornberger. Macroscopicity of mechanical quantum superposition states. *Phys. Rev. Lett.*, **110**, 160403 (2013).

[160] A. Tilloy and L. Diósi. Principle of least decoherence for Newtonian semiclassical gravity. *Phys. Rev. D*, **96**, 104045 (2017).

[161] R. Penrose. On the gravitization of quantum mechanics 1: Quantum state reduction. *Foundations of Physics*, **44**, 557 (2014).

[162] M. Armano, H. Audley, J. Baird *et al.* Beyond the required LISA free-fall performance: New LISA pathfinder results down to 20 μHz. *Phys. Rev. Lett.*, **120**, 061101 (2018).

[163] M. Carlesso, M. Paternostro, H. Ulbricht *et al.* Non-interferometric test of the continuous spontaneous localization model based on rotational optomechanics. *New Journal of Physics*, **20**, 083022 (2018).

[164] M. Toroš, G. Gasbarri, and A. Bassi. Colored and dissipative continuous spontaneous localization model and bounds from matter-wave interferometry. *Physics Letters A*, **381**, 3921 (2017).

[165] S. W. Hawking. Black hole explosions? *Nature*, **248**, 30 (1974).

[166] S. W. Hawking. Particle creation by black holes. *Communications In Mathematical Physics*, **43**, 199 (1975).

[167] O. Llopis, P. H. Merrer, H. Brahimi *et al.* Phase noise measurement of a narrow linewidth CW laser using delay line approaches. *Opt. Lett.*, **36**, 2713 (2011).

[168] M. Bignotto, M. Bonaldi, M. Cerdonio *et al.* New suspension system for the gravitational wave bar detector AURIGA. *Review of Scientific Instruments*, **76**, 084502 (2005).

[169] J. Poirson, F. Bretenaker, M. Vallet *et al.* Analytical and experimental study of ringing effects in a Fabry–Perot cavity. Application to the measurement of high finesses. *J. Opt. Soc. Am. B*, **14**, 2811 (1997).

[170] F. García-Santamaría, H. Míguez, M. Ibisate *et al.* Refractive index properties of calcined silica submicrometer spheres. *Langmuir*, **18**, 1942 (2002).

[171] P. Bushev, D. Rotter, A. Wilson *et al.* Feedback cooling of a single trapped ion. *Phys. Rev. Lett.*, **96**, 043003 (2006).

[172] G. P. Conangla, A. W. Schell, R. A. Rica *et al.* Motion control and optical interrogation of a levitating single nitrogen vacancy in vacuum. *Nano Letters*, **18**, 3956 (2018).

[173] L. Dania, D. S. Bykov, M. Knoll *et al.* Optical and electrical feedback cooling of a silica nanoparticle in a Paul trap. *arXiv: 2007.04434* (2020).

[174] A. Nunnenkamp, K. Børkje, J. G. E. Harris *et al.* Cooling and squeezing via quadratic optomechanical coupling. *Phys. Rev. A*, **82**, 021806 (2010).

[175] W.-j. Gu, Z. Yi, L.-h. Sun *et al.* Mechanical cooling in single-photon optomechanics with quadratic nonlinearity. *Phys. Rev. A*, **92**, 023811 (2015).

[176] H. Shi and M. Bhattacharya. Quantum mechanical study of a generic quadratically coupled optomechanical system. *Phys. Rev. A*, **87**, 043829 (2013).

[177] Z. J. Deng, Y. Li, M. Gao *et al.* Performance of a cooling method by quadratic coupling at high temperatures. *Phys. Rev. A*, **85**, 025804 (2012).

[178] A. Xuereb and M. Paternostro. Selectable linear or quadratic coupling in an optomechanical system. *Phys. Rev. A*, **87**, 023830 (2013).

[179] J. D. P. Machado, R. J. Slooter, and Y. M. Blanter. Quantum signatures in quadratic optomechanics. *Phys. Rev. A*, **99**, 053801 (2019).

[180] T. P. Purdy, D. W. C. Brooks, T. Botter *et al.* Tunable cavity optomechanics with ultracold atoms. *Phys. Rev. Lett.*, **105**, 133602 (2010).

[181] T. K. Paraïso, M. Kalaee, L. Zang *et al.* Position-squared coupling in a tunable photonic crystal optomechanical cavity. *Phys. Rev. X*, **5**, 041024 (2015).

[182] H. Kaviani, C. Healey, M. Wu *et al.* Nonlinear optomechanical paddle nanocavities. *Optica*, **2**, 271 (2015).

[183] C. Healey, H. Kaviani, M. Wu *et al.* Design and experimental demonstration of optomechanical paddle nanocavities. *Applied Physics Letters*, **107**, 231107 (2015).

[184] A. A. Clerk, F. Marquardt, and J. G. E. Harris. Quantum measurement of phonon shot noise. *Phys. Rev. Lett.*, **104**, 213603 (2010).

[185] H. Tan, F. Bariani, G. Li *et al.* Generation of macroscopic quantum superpositions of optomechanical oscillators by dissipation. *Phys. Rev. A*, **88**, 023817 (2013).

[186] T. V. Gevorgyan, A. R. Shahinyan, and G. Y. Kryuchkyan. Generation of Fock states and qubits in periodically pulsed nonlinear oscillators. *Phys. Rev. A*, **85**, 053802 (2012).

[187] S. Rips, M. Kiffner, I. Wilson-Rae *et al.* Steady-state negative wigner functions of nonlinear nanomechanical oscillators. *New Journal of Physics*, **14**, 023042 (2012).

[188] J. Gieseler, R. Quidant, C. Dellago *et al.* Dynamic relaxation of a levitated nanoparticle from a non-equilibrium steady state. *Nature Nanotechnology*, **9**, 358 (2014).

[189] W. Ge, B. Rodenburg, and M. Bhattacharya. Feedback-induced bistability of an optically levitated nanoparticle: A Fokker-Planck treatment. *Phys. Rev. A*, **94**, 023808 (2016).

[190] C. Jiang, Y. Cui, and G. Chen. Dynamics of an optomechanical system with quadratic coupling: Effect of first order correction to adiabatic elimination. *Scientific Reports*, **6** (2016).

[191] R. Stratonovich. *Topics in the theory of random noise, vol. 2.* New York: Gordon Breach (1967).

[192] J. Roberts and P. Spanos. Stochastic averaging: An approximate method of solving random vibration problems. *International Journal of Non-Linear Mechanics*, **21**, 111 (1986).

[193] E. Boujo and N. Noiray. Robust identification of harmonic oscillator parameters using the adjoint Fokker–Planck equation. *Proceedings of the Royal Society A: Mathematical, Physical and Engineering Sciences*, **473**, 20160894 (2017).

[194] D. J. Evans, E. G. D. Cohen, and G. P. Morriss. Probability of second law violations in shearing steady states. *Phys. Rev. Lett.*, **71**, 2401 (1993).

[195] D. J. Evans and D. J. Searles. Equilibrium microstates which generate second law violating steady states. *Phys. Rev. E*, **50**, 1645 (1994).

[196] G. Gallavotti and E. G. D. Cohen. Dynamical ensembles in stationary states. *Journal of Statistical Physics*, **80**, 931 (1995).

[197] T. Delord, P. Huillery, L. Schwab *et al.* Ramsey interferences and spin echoes from electron spins inside a levitating macroscopic particle. *Phys. Rev. Lett.*, **121**, 053602 (2018).

[198] G. P. Conangla, R. A. R. Alarcón, and R. Quidant. Extending vacuum trapping to absorbing objects with hybrid Paul-optical traps. *arXiv: 2005.05486* (2020).

[199] B. A. Stickler, B. Papendell, S. Kuhn *et al.* Probing macroscopic quantum superpositions with nanorotors. *New Journal of Physics*, **20**, 122001 (2018).

[200] A. Hopper and P. F. Barker. A hybrid quantum system formed by trapping atoms in the near-field of a levitated nanosphere. *arXiv: 2005.11662* (2020).

[201] M. Toroš, S. Bose, and P. F. Barker. Atom-nanoparticle Schrödinger cats. *arXiv: 2005.12006* (2020).

[202] E. D. Black. An introduction to Pound–Drever–Hall laser frequency stabilization. *American Journal of Physics*, **69**, 79 (2001).